

# Photoacoustic Spectroscopy for C1-C2 Hydrocarbon Monitoring in Ambient Air



Dissertation

zur Erlangung des Doktorgrades der Naturwissenschaften  
(Dr. rer. nat.)  
der Fakultät für Chemie und Pharmazie  
der Universität Regensburg

vorgelegt von  
**Max Müller**  
aus Regensburg  
im Jahr 2023



Die vorgelegte Dissertation entstand in der Zeit von September 2020 bis Dezember 2023 in Kooperation des Instituts für Analytische Chemie, Chemo- und Biosensorik der naturwissenschaftlichen Fakultät IV - Chemie und Pharmazie - der Universität Regensburg (UR)

und

des Sensorik-Applikationszentrums (SappZ) der Ostbayerischen Technischen Hochschule (OTH) Regensburg.

Die Arbeit wurde angeleitet von: Prof. Dr. Frank-Michael Matysik  
Prof. Dr. Rudolf Bierl

Das Promotionsgesuch wurde eingereicht am: 18.12.2023  
Termin des Kolloquiums: 22.03.2024

Vorsitz des Prüfungsausschusses übernimmt Prof. Dr. Oliver Tepner. Erstgutachter ist Prof. Dr. Frank-Michael Matysik, Zweitgutachter Prof. Dr. Rudolf Bierl und Drittprüfer ist Prof. Dr. Alkwin Slenczka.

Ich möchte mich an dieser Stelle bei allen bedanken, die mich auf dem Wege der Promotion unterstützt und begleitet haben. Im Besonderen bedanke ich mich bei meiner Familie und meiner Freundin Sophia für die ständige Unterstützung und Motivation. Spezieller Dank geht an Dr. Thomas Rück für die zahlreichen Diskussionen, seine Zeit und sein Engagement in den letzten drei Jahren. Ich bedanke mich bei Prof. Dr. Rudolf Bierl und Prof. Dr. Frank-Michael Matysik, für die fachliche Betreuung und Unterstützung. Danke auch an die gesamte Photoakustik Arbeitsgruppe im SappZ. Ein internationaler Dank geht an Dr. Angelo Sampaolo und Dr. Andrea Zifarelli der Polytechnischen Universität Bari, Italien für die sehr gute und fruchtbare Zusammenarbeit. Abschließend bedanke ich mich bei Dr. Jennifer Müller-Williams und Dr. Matthias Lindauer vom Deutschen Wetterdienst für die tatkräftige Unterstützung während der einwöchigen Vergleichsmessungen, sowie bei der Datenauswertung.

Vielen Dank!

I would like to take this opportunity to thank everyone who has supported and accompanied me on the way to my doctorate. In particular, I would like to thank my family and my girlfriend Sophia for their constant support and motivation. Special thanks go to Dr. Thomas Rück for the numerous discussions, his time and commitment in past three years. I would like to thank Prof. Dr. Rudolf Bierl and Prof. Dr. Frank-Michael Matysik, for their scientific supervision and support. Also thanks to the entire photoacoustic group of the SappZ. International thanks go to Dr. Angelo Sampaolo and Dr. Andrea Zifarelli of the Polytechnic University in Bari for the excellent and fruitful collaboration. Finally, I would like to thank Dr. Jennifer Müller-Williams and Dr. Matthias Lindauer from the German Weather Service for their enthusiastic support during the one-week comparison measurements, as well as during the data analysis.

Many thanks!

*"What's measured improves"*  
*(Peter F. Drucker)*



# Contents

<b>List of Figures</b>	<b>ix</b>
<b>List of Tables</b>	<b>xv</b>
<b>Curriculum Vitae</b>	<b>xvi</b>
<b>Oral and Poster Presentation</b>	<b>xvii</b>
<b>Co-authored Publications</b>	<b>xviii</b>
<b>The Author's Original Publications</b>	<b>xx</b>
<b>Declaration of Collaboration</b>	<b>xxiv</b>
<b>1 Introduction</b>	<b>1</b>
<b>2 Theory</b>	<b>11</b>
2.1 Absorption spectroscopy . . . . .	12
2.1.1 Spectral broadening effects . . . . .	14
2.1.2 Spectroscopic measurement techniques . . . . .	17
2.1.3 References . . . . .	23
2.2 Photoacoustic spectroscopy . . . . .	27
2.2.1 Signal generation . . . . .	29
2.2.2 Non-radiative relaxation . . . . .	33
2.2.3 References . . . . .	45

---

<b>3</b>	<b>Experimental</b>	<b>53</b>
3.1	Laboratory setup . . . . .	54
3.1.1	Gas mixing concept . . . . .	54
3.1.2	Electronic setup . . . . .	55
3.2	Light source characterization . . . . .	57
3.3	References . . . . .	60
<b>4</b>	<b>Results and discussion</b>	<b>61</b>
4.1	General information . . . . .	63
4.1.1	Jablonsky diagramm . . . . .	63
4.1.2	Energy transitions . . . . .	64
4.1.3	Molecule parameters . . . . .	67
4.1.4	References . . . . .	68
4.2	[P1] - An algorithmic approach to compute the effect of non-radiative relaxation processes in photoacoustic spectroscopy . . . . .	70
4.2.1	Methods . . . . .	71
4.2.2	Results and discussion . . . . .	75
4.2.3	Conclusion . . . . .	84
4.2.4	References . . . . .	85
4.3	[P2] - Digital Twin of a photoacoustic trace gas sensor for monitoring methane in complex gas compositions . . . . .	88
4.3.1	Theoretical correlations and Digital Twin representation . . . . .	89
4.3.2	Experimental section . . . . .	94
4.3.3	Results and discussion . . . . .	94
4.3.4	Conclusion . . . . .	100
4.3.5	References . . . . .	101
4.4	[P3] - Comparison of photoacoustic spectroscopy and cavity ring-down spectroscopy for ambient methane monitoring at Hohenpeißenberg . . . . .	103

---

4.4.1	Non-radiative relaxation in photoacoustic spectroscopy . . . . .	104
4.4.2	Experimental . . . . .	105
4.4.3	Results and discussion . . . . .	107
4.4.4	Conclusion . . . . .	110
4.4.5	References . . . . .	111
4.5	Multivariate analysis and digital twin modeling: alternative approaches to molecular relaxation in photoacoustic spectroscopy . . . . .	113
4.5.1	Introduction . . . . .	113
4.5.2	Experimental setup for QEPAS detection . . . . .	114
4.5.3	Target features selection . . . . .	115
4.5.4	Partial Least Squares Regression . . . . .	116
4.5.5	Results and disussion . . . . .	118
4.5.6	Conclusion . . . . .	122
4.5.7	References . . . . .	122
4.6	Spectral influences on WM-2f photoacoustic detection . . . . .	125
4.6.1	Alternative representation of WM-2f PAS signal . . . . .	127
4.6.2	Spectral overlap of water with ethane . . . . .	129
4.6.3	Methane absorption pressure deformation . . . . .	132
4.6.4	Conclusion . . . . .	134
4.6.5	References . . . . .	135
4.7	Photoacoustic AM measurements . . . . .	137
4.7.1	References . . . . .	140
<b>5</b>	<b>Summary</b>	<b>143</b>
<b>6</b>	<b>Zusammenfassung in deutscher Sprache</b>	<b>147</b>
	<b>Appendices</b>	<b>151</b>
A	Miscellaneous . . . . .	152

---

A.1	Acoustic resonance modes . . . . .	152
A.2	Ethan absorpction spectrum from different databases	153
A.3	Lock-in amplification . . . . .	154
A.4	Universal equation for heat production rate . .	156
A.5	The effect of pressure on the absorption coefficient	157
A.6	AM PAS spectra of methane for different pressures	158
A.7	Picarro G2301 temperature features with measured CH <sub>4</sub> readings . . . . .	159
A.8	Work flow of the WM-2f FFT analysis . . . . .	160

# List of Figures

2.1	Simulated line intensities of CH <sub>4</sub> (left) and C <sub>2</sub> H <sub>6</sub> (right) for different temperatures in the spectral range investigated in this work. . . . .	13
2.2	Schematic representation of CRDS. . . . .	19
2.3	Double logarithmic representation of the difference in decay time $\Delta\tau$ for an empty and an analyt containing cavity. . . . .	20
2.4	Schematic representation of WMS technique. . . . .	21
2.5	Visualisation of the corresponding signal of WMS spectral scan, after LIA processing of $S_1$ and the first harmonic $S_2$ over an undistorted absorption peak (left graph). . . . .	22
2.6	Schematic representation of the signal generation process in PAS, adapted from [2]. . . . .	27
2.7	Simplified cross-section of a typical $H - type$ PAC, adapted from [58]. . . . .	33
2.8	Lennard-Jones potential, apated from [60]. . . . .	34
2.9	Simplified schematic of the trajectories of molecular collisions for different impact parameters $b_{0-3}$ . Inside the inner, grey highlighted circle with radius $r_m$ only repulsive forces act. The outer circle marks the distance, where the attractive forces start. . . . .	35
2.10	Schematic of a collinear collision between a vibrating $\mathbf{A}^*\mathbf{B}^*$ and a non-vibrating molecule $\mathbf{AB}$ . . . . .	37
2.11	VV transitions from $\nu_a$ to $\nu_b$ resulting in heating of the surrounding $\Delta E_1$ and kinetic cooling $\Delta E_2$ . . . . .	40

2.12	Estimated VV probability of a collision between <b>AB</b> and <b>CD</b> as a function of $\Delta E$ for a energy transition from $\nu_a$ to $\nu_b$ after [72]. . . . .	41
3.1	Simplified schematic of the gas mixing concept used in chapters 4.2, 4.3, 4.7 and 4.6. <b>MFC</b> = mass flow controller. . . . .	54
3.2	Humidification and pressure control concept of the sample gas. . . . .	55
3.3	Schematic of the basic electronic concept used in this work. . . . .	56
3.4	Raw (left) and FFT (right) microphone voltage during ARMS. . . . .	57
3.5	Characterization of the ICL used for WM measurements.	58
3.6	Characterization of the ICL used for AM measurements.	59
4.1	Jablonsky diagram of mid-IR laser excitation of methane, followed by collision-based non-radiative relaxation processes with methane, water, oxygen, nitrogen and carbon dioxide. . . . .	63
4.2	Programming flowchart of CoNRad for computing relaxation dependent PA signals. . . . .	73
4.3	Example of three excited states $A^*(\nu_1)$ , $B^*(\nu_1)$ and $C^*(\nu_1)$ forming a circular reference. . . . .	74
4.4	Theoretical Jablonski diagram for non-radiative relaxation, only considering VT transitions. . . . .	76
4.5	Simulated relative photoacoustic signal amplitudes (upper graphs) and corresponding phase lags (lower graphs) for the theoretical relaxation cascade shown in Figure 4.4.	77
4.6	Relative photoacoustic signal amplitude for higher C concentrations ( $N_{C,max} = 99\%V$ ) simulated for $k_3 = 1 \cdot 10^4$ (blue rhombus), $k_3 = 1 \cdot 10^3$ (red triangles) and $k_3 = 1 \cdot 10^2$ (black squares). . . . .	78

4.7	Measured photoacoustic magnitude (black squares, upper graph) and phase shift $\phi$ (red triangles, lower graph) for 15 ppmV methane diluted in dry nitrogen with rising oxygen content. . . . .	79
4.8	Measured photoacoustic magnitude (black squares, upper graph) and phase shift $\phi$ (red triangles, lower graph) for 15 ppmV methane diluted in nitrogen with rising humidity content. . . . .	80
4.9	Comparison of the measured relative magnitudes resulting from amplitude modulated (AM, blue circles) and wavelength modulated (WM, black squares) methane detection, normalized to the magnitude measured for dry conditions. . . . .	81
4.10	Measured photoacoustic magnitude (black squares, upper graph) and phase shift $\phi$ (red triangles, lower graph) for 15 ppmV methane diluted in a nitrogen, oxygen mixture with rising humidity content. . . . .	82
4.11	Direct comparison of the relative measured photoacoustic data (black circles) from [19] (upper graphs: magnitude, lower graphs: phase shift) with the simulation results from [19] (red solid lines) and the algorithm (CoNRad) presented in this work (blue dashed lines). . . . .	83
4.12	Schematic representation of the circular dependencies of different environmental parameters, i.e., temperature $T$ , pressure $p$ , and gas composition $\Sigma \chi_i$ on certain PA parameters. . . . .	89
4.13	Comparison of experimental and Digital Twin data when successively adding CO <sub>2</sub> to a constant analyte concentration of 15 ppmV CH <sub>4</sub> diluted in N <sub>2</sub> . . . . .	95
4.14	Illustration of how CO <sub>2</sub> addition contrarily affects different system parameters. . . . .	96
4.15	Metrological comparison of the CH <sub>4</sub> concentration readings of the PA sensor based on standard calibration in dry nitrogen (black squares) and Digital Twin compensation (blue half-filled diamonds). . . . .	98

4.16	Comparison of concentration readings after N <sub>2</sub> calibration (black squares) and DT compensation (half-filled blue diamonds) for analyte concentrations of 15 ppmV and 18 ppmV CH <sub>4</sub> at different measuring conditions (see Table 4.5), respectively. . . . .	100
4.17	Overall efficiency of non-radiative relaxation $\epsilon_{\text{relax}}$ at 5055 Hz laser modulation for CH <sub>4</sub> in air with rising humidity content (a). . . . .	105
4.18	Schematic of the experimental setup for the measurement campaign. . . . .	107
4.19	Direct comparison of the methane concentration readings (a), the deviation of the PA sensor compared to the Picarro G2301 (in %) (b) and the water readings (c). . . . .	108
4.20	Absolute difference of CH <sub>4</sub> in ppbV (a) based on raw PA data (red) and after CoNRad compensation (black) with regard to the G2301 reference methane readings. . . . .	110
4.21	Simplified schematic of the experimental setup. The dashed arrows indicate gas flow, the solide arrows indicate electronic signals. . . . .	114
4.22	Absorption cross-section of CH <sub>4</sub> and H <sub>2</sub> O in the spectral range from 2987.25 cm <sup>-1</sup> to 2989.25 cm <sup>-1</sup> at 533 mbar (400 Torr) and 301 K. . . . .	116
4.23	Measured QEPAS spectra for the low (a) and the high (b) CH <sub>4</sub> concentration range. The dashed grey lines indicte the selected on-peak CH <sub>4</sub> peaks, the highlighted grey areas result from the water absorption. . . . .	117
4.24	Direct comparison of the QEPAS measurements (black squares), the DT (blue open squares) and the PLSR predictions (red open triangles). . . . .	119
4.25	Violin plots of the percentage prediction deviation obtained with the DT (blue) and with the PLSR (red). . . . .	120
4.26	Measured QTF frequency response for electrical stimulation (a). The $Q$ -factors for different humidities are plotted on the right side (b). . . . .	121

4.27	Comparison of the DT (black open squares) and PLSR (red open triangles) predictions for the low and the high concentration range. . . . .	122
4.28	Logarithmic representation of the absorption coefficients $\alpha$ for typical fuel gas analysis in the spectral range from 2966.65 to 2975.25 $\text{cm}^{-1}$ . . . . .	126
4.29	Absorption coefficient of ambient methane (2 ppmV) and water (1 %V) concentration, as well as 2 ppmV ethane. . . . .	127
4.30	Schematic of the FFT-based simulation process to quantify PAS signal alteration due to peak deformation. . .	128
4.31	Representation of the effect of non-ideal light sources on the measured absorption spectrum. . . . .	129
4.32	Effect of rising humidity on the photoacoustic $\text{C}_2\text{H}_6$ detection at 2973.57 $\text{cm}^{-1}$ with a modulation depth of $\Delta\tilde{\nu}_{\text{WM}} = 0.174 \text{ cm}^{-1}$ for different $\text{C}_2\text{H}_6$ concentrations. . . . .	130
4.33	Absorption spectra (a) of 1.2 ppmV $\text{C}_2\text{H}_6$ , 0.5 %V $\text{H}_2\text{O}$ and the mixture with an applied IF of 0.174 $\text{cm}^{-1}$ . . . . .	131
4.34	Measured WM-2f spectrum of 15 ppmV $\text{C}_2\text{H}_6$ diluted in $\text{N}_2$ . . . . .	132
4.35	Variation of applied laser modulation depth for 1.2 ppmV ethane and different humidities. . . . .	133
4.36	Measured PA spectra of 3.01 ppmV $\text{CH}_4$ for selected pressures ranging from 1035 mbar to 364 mbar. . . . .	134
4.37	Predicted $\text{CH}_4$ concentration in ppmV based on standard calibration in dry nitrogen (black squares), DT compensation (blue half-filled diamonds) and combination of DT and WM-2f FFT analysis (red triangle). . . . .	135
4.38	Measured absorption spectra (a) normalized for the emitted optical power of ethane, water and methane using AM photoacoustic spectroscopy. . . . .	137
4.39	Measured emission spectra of the ICL temperature controlled to 27 °C for different high currents. . . . .	138

---

4.40	Water-induced signal increase regarding ethane detection at $2967.55\text{ cm}^{-1}$ (a) and $2964.24\text{ cm}^{-1}$ (b), including linear fits (dashed red line). . . . .	139
A1	Schematic representation of the longitudinal, radial and azimuthal acoustic resonances in a cylindrical acoustic resonator. . . . .	152
A2	Ethane absorption coefficient in the spectral range from $2966\text{ cm}^{-1}$ to $2976\text{ cm}^{-1}$ obtained from Molexplorer (black line), HITRAN (blue line) [2] and <i>HITRAN on the web</i> (red line). . . . .	153
A3	Pressure dependency of the absorption coefficient of 15 ppmV $\text{CH}_4$ simulated using <i>HITRAN on the web</i> (left) and Molexplorer (right) database. . . . .	157
A4	Measured methane spectra for different pressures exploiting AM PAS used to obtain the results in chapter 4.6.3 . . . . .	158
A5	Comparison of data acquisition system (DAS), cavity, and etalon temperature (a) of the Picarro G2301 CRDS over time, with the measured percentage deviation (b) and $\text{CH}_4$ reading (c). . . . .	159
A6	Procedure of the WM-2f FFT simulation for 1.2 ppmV ethane in dry nitrogen (a) and for a humidified mixture (b). . . . .	160

# List of Tables

3.1	ICL parameters for WM methane and ethane detection.	59
3.2	ICL parameter for AM methane, ethane and water detection. . . . .	59
4.1	Summary of all 50 collision-based energy transitions (reactions) that have been considered for computing relaxational effects in mixtures containing CH <sub>4</sub> , N <sub>2</sub> , O <sub>2</sub> , H <sub>2</sub> O and CO <sub>2</sub> . . . . .	64
4.2	Listing of the molecular parameters mass $M$ , radii at infinite temperature $r _{T \rightarrow \infty}$ and Sutherland constants $T_V$ [12] . . . . .	67
4.3	Listing of the molecules' vibration details notation, energy $\Delta E$ and degeneracy $n$ . . . . .	67
4.4	Individual reactions and their reaction ratios $k_{1,2,3}$ for the discussed Jablonski diagram (Figure 4.4). . . . .	76
4.5	Measuring conditions for the experiment shown in Figure 4.16. . . . .	99
4.6	Sensitivity of the PA sensor over the five day measurement period. . . . .	109
4.7	MAPE for the DT and PLSR analysis for the low and the high CH <sub>4</sub> concentrations. . . . .	120
4.8	Results of the best linear fits regarding the predicted CH <sub>4</sub> concentrations, including 25 ppmV and 0.11 %V. . . . .	121
4.9	List of the target analytes ( <b>bold</b> ) methane, ethane and propane for fuel gas analysis, including the expected concentration ranges. . . . .	125
4.10	Calibration characteristics for ethane, methane and water in the spectral range shown in Figure 4.38. . . . .	139

## Person

Full name           Max Müller  
E-Mail               max.mueller@oth-regensburg.de  
Date and place of birth   03<sup>th</sup> April 1994 in Regensburg

## Education

02/2021–11/2023   Doctorate at the University of Regensburg  
Faculty of Chemistry and Pharmacy, Institute of Analytical  
Chemistry, Chemosensors and Biosensors  
10/2018–09/2020   Completion of the master study "Electrical and Microsystems  
Engineering", M.Eng.  
10/2014–09/2018   Completion of the bachelor study "Sensor Technology and Ana-  
lytics ", B.Sc.

## Positions and Employment

since 09/2020       Research associate at the Ostbayerische Technische Hochschule  
(OTH) Regensburg  
03/2016–09/2020   Student assistant at the Sensorik-ApplikationsZentrum, OTH  
Regensburg  
Research focus: ultrasonic gas sensing, photoacoustic spec-  
troscopy  
10/2015–02/2016   Internship at Infineon, Batam, Indonesia  
Optical evaluation of a new sawing process in pre-assembly

## Poster presentations

”Digitaler Zwilling eines photoakustischen Methansensors”

M. Müller, T. Rück, S. Jobst, R. Bierl

Presented at the *Dechema Workshop zur Digitalisierung der chemischen Industrie* in 2022 (Frankfurt, Germany)

”The Impact of Spectral Peak Deformations on Mid-Infrared Wavelength Modulated Photoacoustic Hydrocarbon Sensors”,

M. Müller, T. Rück, R. Bierl, F.-M. Matysik

Presented at the *C-PASS* in 2023 (Castellaneta Marina, Italy)

## Oral presentation

”Creating a Digital Twin of a Photoacoustic Gas Sensor for Methane Detection in Complex Gas Matrices”,

M. Müller, T. Rück, S. Jobst, J. Pangerl, R. Bierl, F.-M. Matysik

Presented at the *Optica* in 2022 (Vancouver, Canada)

## Co-authored publications

**”Characterizing a sensitive compact mid-infrared photoacoustic sensor for methane, ethane and acetylene detection considering changing ambient parameters and bulk composition (N<sub>2</sub>, O<sub>2</sub> and H<sub>2</sub>O)”**

J. Pangerl, M. Müller, T. Rück, S. Weigl and R. Bierl

in *Sensors and Actuators B: Chemical*, vol. 352, no. February 2022, p. 130962, February 2022, <https://doi.org/10.1016/j.snb.2021.130962>

**”Scopes and Limits of Photoacoustic Spectroscopy in Modern Breath Analysis”**

S. Weigl, M. Müller, J. Pangerl and T. Rück

in *Springer International Publishing, book series; Bioanalytical Reviews*, vol. 4, no. 2022, p. 101-159, 2022, [https://doi.org/10.1007/11663\\_2022\\_22](https://doi.org/10.1007/11663_2022_22)

**”Aus Licht wird Schall – Photoakustische Spurengasanalyse”**

M. Müller, J. Pangerl

in *Wiley Analytical Science*, no. March 2023, 2023,

<https://analyticalscience.wiley.com/do/10.1002/was.0004000351>

**”A sub-ppbv-level Acetone and Ethanol Quantum Cascade Laser Based Photoacoustic Sensor – Characterization and Multi-Component Spectra Recording in Synthetic Breath”**

J. Pangerl, E. Moser, M. Müller, S. Weigl, S. Jobst, T. Rück, R. Bierl and F.-M. Matysik

in *Photoacoustics*, vol. 30, no. April 2023, p. 100473, April 2023, <https://doi.org/10.1016/j.pacs.2023.100473>

**”Multivariate analysis and digital twin modeling: alternative approaches to molecular relaxation in photoacoustic spectroscopy”**

A. Zifarelli, A.F.P. Cantatore, A. Sampaolo, M. Müller, T. Rück, C. Hölzl, P. Patimisco and V. Spagnolo

in *Photoacoustics*, vol. 33, no. October 2023, p. 100564, October 2023,  
<https://doi.org/10.1016/j.pacs.2023.100564>

## The authors' original publications

Parts that were adapted from the author's publications form the basis of chapter 4. The adapted text parts are indicated by [P1], [P2] and [P3]. This section lists the abstracts of the original publications.

[P1]

### An Algorithmic Approach to Compute the Effect of Non-Radiative Relaxation Processes in Photoacoustic Spectroscopy

M. Müller\*, T. Rück\*, S. Jobst, J. Pangerl, S. Weigl, R. Bierl and F.-M. Matysik

in *Photoacoustics*, vol. 26, no. June 2022, p. 100371, June 2022,  
<https://doi.org/10.1016/j.pacs.2022.100371>

#### Abstract

Successful transfer of photoacoustic gas sensors from laboratory to real-life applications requires knowledge about potential cross-sensitivities towards environmental and gas matrix changes. Multi-dimensional calibration in case of cross-sensitivities can become very complex or even unfeasible. To address this challenge, we present a novel algorithm to compute the collision based non-radiative efficiency and phase lag of energy relaxation on a molecular level (CoNRad) for photoacoustic signal calculation. This algorithmic approach allows to calculate the entire relaxation cascade of arbitrarily complex systems, yielding a theoretical photoacoustic signal. In this work the influence of varying bulk compositions, i.e. nitrogen (N<sub>2</sub>), oxygen (O<sub>2</sub>) and water (H<sub>2</sub>O) on the photoacoustic signal during methane (CH<sub>4</sub>) detection is demonstrated. The applicability of the algorithm to other photoacoustic setups is shown exemplary by applying it to the relaxational system investigated in [1]. Hayden et al. examined the effect of water on photoacoustic carbon monoxide (CO) detection.

---

\*equally contributing author

## References

- [1] J. Hayden et al. “Anomalous Humidity Dependence in Photoacoustic Spectroscopy of CO Explained by Kinetic Cooling”. In: *Appl. Sci.* 10.3 (Jan. 2020), p. 843. ISSN: 2076-3417. DOI: 10.3390/app10030843 (cit. on p. xx).

**[P2]****Digital Twin of a photoacoustic trace gas sensor for monitoring methane in complex gas compositions**T. Rück\*, M. Müller\*, S. Jobst, S. Weigl, J. Pangerl, R. Bierl and  
F.-M. Matysikin *Sensors and Actuators, B: Chemical*, vol. 378, no. March 2023, p.  
133119, March. 2023, <https://doi.org/10.1016/j.snb.2022.133119>**Abstract**

The digitalization of industrial processes requires smart sensor systems. Photoacoustic spectroscopy is well suited for this purpose as it allows for small-sized and low-cost trace gas analysis. However, the method is susceptible to changes in measurement conditions and standard calibration routines often fail to correct for all changes. We therefore created a Digital Twin (DT) of a photoacoustic trace gas sensor for methane and evaluated it regarding variations in gas composition (CH<sub>4</sub>, N<sub>2</sub>, O<sub>2</sub>, CO<sub>2</sub>, H<sub>2</sub>O), temperature and pressure. With a mean absolute percentage error of 0.8 % the accuracy of the sensor after DT compensation significantly exceeds the 24 % achieved based on standard calibration in nitrogen. For the first time, we can fully analytically compute the photoacoustic signal under moderate ambient conditions with an error in the ppbV range by taking a holistic approach. Assuming knowledge of the underlying energy transfer processes, the model of this Digital Twin can be adapted to any microphone based photoacoustic sensor for monitoring any analyte species.

---

\*equally contributing author

[P3]

**Comparison of photoacoustic spectroscopy and cavity ring-down spectroscopy for ambient methane monitoring at Hohenpeißenberg**

M. Müller, S. Weigl, J. Müller-Williams, M. Lindauer, T. Rück, S. Jobst, R. Bierl and F.-M. Matysik

in *Atmospheric Measurement Techniques*, vol. 16, no. September 2023, p. 4263-4270, September. 2023,

<https://amt.copernicus.org/articles/16/4263/2023/>

**Abstract**

With an atmospheric concentration of approximately 2000 parts per billion (ppbV,  $10^{-9}$ ) methane ( $\text{CH}_4$ ) is the second most abundant greenhouse gas (GHG) in the atmosphere after carbon dioxide ( $\text{CO}_2$ ). The task of long-term and spatially resolved GHG monitoring to verify whether climate policy actions are effective is becoming more crucial as climate change progresses. In this paper we report the  $\text{CH}_4$  concentration readings of our photoacoustic (PA) sensor over a 5 d period at Hohenpeißenberg, Germany. As a reference device, a calibrated cavity ring-down spectrometer, Picarro G2301, from the meteorological observatory of the German Weather Service (DWD) was employed. Trace gas measurements with photoacoustic instruments promise to provide low detection limits at comparably low costs. However, PA devices are often susceptible to cross-sensitivities related to fluctuating environmental conditions, e.g. ambient humidity. The obtained results show that for PA sensor systems non-radiative relaxation effects induced by varying humidity are a non-negligible factor. Applying algorithm compensation techniques, which are capable of calculating the influence of non-radiative relaxation effects on the photoacoustic signal, increase the accuracy of the photoacoustic sensor significantly. With an average relative deviation of 1.11 % from the G2301, the photoacoustic sensor shows good agreement with the reference instrument.

## Declaration of Collaboration

Most of the theoretical and experimental scientific work that is presented within this thesis was done independently by the author. In some cases, however, the practical implementation of concepts and the performance of measurements was carried out in collaboration with other researchers. In any case, assistance was guided and supervised by the author. In accordance with § 7 Abs. 3 Satz 3 of *Ordnung zum Erwerb des akademischen Grades eines Doktors der Naturwissenschaften (Dr. rer. nat.) an der Universität Regensburg vom 18. Juni 2009 (Änderungssatzung vom 6. Februar 2014)*, this section gives a detailed declaration of those collaborations.

### ***Gas mixing concept*** ***(section 3.1.1, p.54)***

The concept of the gas mixing system was developed by Thomas Rück and Stefan Weigl. The implementation was carried out by the company INTEGA GmbH (Kirchheim, Germany). The humidification concept was developed and implemented in the gas stream by Stefan Weigl and the author.

### ***Acoustic resonance monitoring system (ARMS)*** ***(section 3.1.2, p.55)***

The electronic concept of the ARMS was developed by Simon Jobst and the author. The programming of the ARMS routine was performed by Simon Jobst. The implementation of the necessary hardware was performed by Simon Jobst and the author.

### ***Light source characterization*** ***(section 3.2, p.57)***

The interband cascade laser (ICL) used for the WM measurements in chapters 4.2, 4.3, 4.4, and 4.6 was characterized and tested by Jonas Pangerl during his master thesis. The group of Prof. Vincenzo Spagnolo from the Polytechnical University of Bari, Italy characterized the ICL used in chapter 4.5. The ICL wavelength characterization for the AM measurements presented in chapter 4.7 was performed by the author.

***CoNRad algorithm***  
***(section 4.2, p.70)***

The mathematical concept of *CoNRad* was developed by the author. The first version of the algorithm used to calculate the relaxation efficiency was programmed by the author. The final version of *CoNRad* was programmed by Thomas Rück in consultation with Simon Jobst and the author.

***Data curation and analysis for [P1]***  
***(chapter 4.2, p.70)***

All experimental work was mainly planned, carried out and evaluated by the author. Thomas Rück was involved in the data curation. Thomas Rück, Simon Jobst, Jonas Pangerl, Stefan Weigl, and Frank-Michael Matysik advised on the conceptualization of the experiments. The results were validated by Simon Jobst, Jonas Pangerl, Stefan Weigl, Rudolf Bierl and Frank-Michael Matysik. All experiments were supervised by Rudolf Bierl and Frank-Michael Matysik.

***Data curation and analysis for [P2]***  
***(chapter 4.3, p.88)***

All experimental work was mainly planned, carried out and evaluated by the author. Thomas Rück was involved in the data curation. Thomas Rück, Simon Jobst, Stefan Weigl, Jonas Pangerl, and Frank-Michael Matysik advised on the conceptualization of the experiments. The results were validated by Simon Jobst, Stefan Weigl, Jonas Pangerl, Rudolf Bierl and Frank-Michael Matysik. All experiments were supervised by Rudolf Bierl and Frank-Michael Matysik.

***Experimental setup for [P3]***  
***(section 4.4.2, p.105)***

The experimental setup for chapter 4.4 was designed by the author and Stefan Weigl, together with Jennifer Müller-Williams and Matthias Lindauer from the German Weather Service.

***Data curation and analysis for [P3]***  
***(chapter 4.4, p.103)***

All experimental work was mainly planned, carried out and evaluated by the author. Stefan Weigl, Jennifer Müller-Williams and Matthias Lindauer advised on the conceptualization of the experiments, as well as

the data curation. The software for the mobile photoacoustic setup was developed by Stefan Weigl in close consultation with the author. The obtained results were validated by Thomas Rück, Simon Jobst, Rudolf Bierl, and Frank-Michael Matysik. All experiments were supervised by Rudolf Bierl and Frank-Michael Matysik.

***Experimental setup for QEPAS measurements***  
***(section 4.5.2, p.114)***

The QEPAS sensor was provided by Thorlabs GmbH (Bergkirchen, Germany). The experimental setup was designed by Aldo Francesco Pio Cantatore in collaboration with Christine Hölzl and Hubert Rossmadl from Thorlabs GmbH.

***Data curation and analysis for QEPAS measurements***  
***(chapter 4.5, p.113)***

Aldo Francesco Pio Cantatore performed the QEPAS measurements, Andrea Zifarelli and Angelo Sampaolo conducted the partial least squares regression (PLSR) analysis, and the author performed the DT analysis. Thomas Rück, Christine Hölzl, Hubert Rossmadl, Pietro Patimisco, and Vincenzo Spagnolo were involved in supervision and validation of the data.

**Funding**

Financial support was received within the scope of the *PreSEDA* research project by the German Government and the Federal Ministry of Economic Affairs and Climate Action (BMWK) - Grant number: 03EN2028A.

Furthermore, the author received financial support within the scope of the *BayWISS - Resource efficiency and materials* from November 2022 until Dezember 2023.

# Chapter 1

## Introduction

In response to the 2020 COVID-19 pandemic, governments globally implemented strict lockdowns to curb the spread of the virus, notably impacting individual transportation and leading to a significant reduction in global traffic [1]. Studies revealed that these lockdowns resulted in a noteworthy reduction of 9 % to 32 % in anthropogenic CO<sub>2</sub> emissions, primarily from burning fewer fossil fuels [2–6]. While such reductions may seem substantial, anthropogenic emissions typically elevate the regional CO<sub>2</sub> background by approximately 1 ppm to 2 ppm [7–10]. Therefore, even a substantial 32 % decrease only translates to a local reduction of 0.64 ppm [10], falling below the typical measurement precision achievable with current satellites. Although weekly or monthly averaging enhances satellite data precision, the ability to detect crucial information about daily variations is lost [11]. Buchwitz et al. thus concluded that more sophisticated analysis techniques are required for current satellite measurements to derive trends related to COVID-19-induced CO<sub>2</sub> changes [10]. Contrastingly, local ground-based monitoring stations in cities could clearly measure the impact of mobility restrictions during lockdown, highlighting the value of such monitoring networks [12, 13].

This is especially relevant when considering methane, the second most abundant greenhouse gas. Several studies have identified a relatively small fraction of high-emission point sources, with high emission rates ( $>100 \text{ kg h}^{-1}$ ), responsible for approximately 60 % to 90 % of total methane emissions [14–16]. State-of-the-art satellites, e.g. *GHGSat-C1* and *GHGSat-C2*, are expected to detect emissions above  $100 \text{ kg h}^{-1}$  [16, 17], making them suitable for identifying large emitters globally. However, ground-based measurements, in cities such as Paris, Hamburg, and Utrecht, revealed cumulative ground-level emissions below the detection limit of satellites [18, 19]. These type of measurements, while not being able to account for emissions above their respective measurement heights, proved valuable in identifying previously unknown yet relevant methane sources [20, 21]. Thus, a combination of satellite-based measurements and precise ground sensors is essential to identify all relevant sources and sinks.

The World Meteorological Organization (WMO) Report No. 255 outlines international standards for the precision of greenhouse gas measurements to model the global carbon cycle and understand the role of greenhouse gases in climate change [22]. For methane, the precision goal is defined as 2 ppb, well below the precision of current satellites, which provide 40 ppb precision or 2 % of the background [23]. The WMO emphasizes the expansion of greenhouse gas monitoring networks with accurate, precise, and cost-effective sensors to complement satellite data with long-term, in situ observations to mitigate variations induced by weather conditions or the albedo field and gather crucial knowledge about atmospheric processes and thus support science- and data-based decision-making.

While ground-based sensors detected a decrease in urban CO<sub>2</sub> emissions during COVID-19 lockdowns, methane data showed an increase from 2020 to 2021, which was partly attributed to lockdown-unaffected factors like increased rainfall in the tropics and the high elevations of the northern hemisphere [24–26]. In the analysis of the methane cycle not only sources, but also natural sinks, such as the oxidation by

the hydroxyl radical (OH) in the troposphere must be considered [27, 28]. The OH radical is produced by photochemical reactions with water vapor, nitrogen oxides (NO<sub>x</sub>) and stratospheric ozone [27, 29–32]. As NO<sub>x</sub> emissions were significantly reduced by the lockdown regulations and the resulting restriction of mobility, the OH methane sink was weakened [33–35]. The complexity of the methane cycle highlights the importance of precise monitoring techniques to understand natural sources, sinks, and anthropogenic influences. Highly precise, well-calibrated devices deployed at baseline sites, i.e. regions not affected by natural sources or sinks, offer the optimal approach for long-term monitoring of the global greenhouse gas burden, aligning with the WMO’s advocacy for further research in mobile sensors [22]. Numerous research groups recognize this need, publishing articles on mobile trace gas sensors for environmental monitoring. Techniques range from laser-based methods, such as cavity ring-down spectroscopy (CRDS) [18, 36–39] and quantum cascade laser absorption spectroscopy [40–43], to Fourier-transform spectrometers using the sun as light source [44, 45] and larger devices based on selected ion flow tube mass spectrometry (SIFT-MS) [46]. Furthermore, several cities have already established monitoring networks in recent years, based on expensive CRDS devices [47, 48], but also utilizing low-cost sensors [49, 50] to improve the resolution of atmospheric greenhouse gas monitoring.

An alternative approach which has already produced promising results regarding ppbV (parts per billion, 10<sup>-9</sup>) level GHG detection in laboratory is photoacoustic spectroscopy (PAS). Elefante et al. developed a methane sensor based on a quantum cascade laser (QCL) emitting at 1297.5 cm<sup>-1</sup> and reached a limit of detection (LoD) of 18 ppbV with a lock-in time ( $\tau_{LIA}$ ) of 100 ms [51]. Using distributed feedback (DFB) lasers emitting in the near-infrared region Xiao et al. and Gong et al. obtained LoDs for methane of 4.9 ppbV ( $\tau_{LIA} = 81$  s) and 9 ppbV ( $\tau_{LIA} = 500$  s), respectively [52, 53]. While the previous sources utilized a single light source for methane detection, Giglio et al. employed a laser array consisting of 32 QCLs, with which the spectral range from 1190 cm<sup>-1</sup> to 1340 cm<sup>-1</sup> could be excited [54]. The methane concentration was calculated from the area underneath the measured spectrum and the LoD was determined to be 200 ppbV for  $\tau_{LIA} = 10$  s. Sub-ppbV detection limits of 0.6 ppbV ( $\tau_{LIA} = 90$  s) and 0.065 ppbV ( $\tau_{LIA} = 30$  s) have already been achieved in literature, utilizing an interband cascade laser (ICL) and an optical parametric oscillator (OPO) laser system, respectively [55, 56].

This thesis specifically addresses the advantages and challenges of photoacoustic methane and ethane detection in the mid-infrared spectral region, with a focus on addressing limitations in the reliability of analyte detection due to acoustic, spectral, and relaxation effects. The thesis also provides and discusses potential solutions, which are evaluated in the laboratory, and field-tested for monitoring ambient methane against a reference instrument.

## References

- [1] P. M. Forster et al. “Current and future global climate impacts resulting from COVID-19”. In: *Nat. Clim. Chang.* 10.10 (Oct. 2020), pp. 913–919. ISSN: 1758-678X. DOI: 10.1038/s41558-020-0883-0 (cit. on p. 2).
- [2] Z. Liu et al. “Near-real-time monitoring of global CO<sub>2</sub> emissions reveals the effects of the COVID-19 pandemic”. In: *Nat. Commun.* 11.1 (Oct. 2020), p. 5172. ISSN: 2041-1723. DOI: 10.1038/s41467-020-18922-7 (cit. on p. 2).
- [3] C. Le Quéré et al. “Temporary reduction in daily global CO<sub>2</sub> emissions during the COVID-19 forced confinement”. In: *Nat. Clim. Chang.* 10.7 (July 2020), pp. 647–653. ISSN: 1758-678X. DOI: 10.1038/s41558-020-0797-x (cit. on p. 2).
- [4] Y. Tohjima et al. “Detection of fossil-fuel CO<sub>2</sub> plummet in China due to COVID-19 by observation at Hateruma”. In: *Sci. Rep.* 10.1 (Oct. 2020), p. 18688. ISSN: 2045-2322. DOI: 10.1038/s41598-020-75763-6 (cit. on p. 2).
- [5] R. L. Ray et al. “What is the impact of COVID-19 pandemic on global carbon emissions?” In: *Sci. Total Environ.* 816 (Apr. 2022), p. 151503. ISSN: 00489697. DOI: 10.1016/j.scitotenv.2021.151503 (cit. on p. 2).
- [6] A. Kumar et al. “Impact of COVID-19 on greenhouse gases emissions: A critical review”. In: *Sci. Total Environ.* 806 (Feb. 2022), p. 150349. ISSN: 00489697. DOI: 10.1016/j.scitotenv.2021.150349 (cit. on p. 2).
- [7] J. Hakkarainen et al. “Direct space-based observations of anthropogenic CO<sub>2</sub> emission areas from OCO-2”. In: *Geophys. Res. Lett.* 43.21 (Nov. 2016). ISSN: 0094-8276. DOI: 10.1002/2016GL070885 (cit. on p. 2).
- [8] J. Hakkarainen et al. “Analysis of Four Years of Global XCO<sub>2</sub> Anomalies as Seen by Orbiting Carbon Observatory-2”. In: *Remote Sens.* 11.7 (Apr. 2019), p. 850. ISSN: 2072-4292. DOI: 10.3390/rs11070850 (cit. on p. 2).
- [9] F. Chevallier et al. “Local Anomalies in the Column-Averaged Dry Air Mole Fractions of Carbon Dioxide Across the Globe During the First Months of the Coronavirus Recession”. In: *Geophys. Res. Lett.* 47.22 (Nov. 2020). ISSN: 0094-8276. DOI: 10.1029/2020GL090244 (cit. on p. 2).
- [10] M. Buchwitz et al. “Can a regional-scale reduction of atmospheric CO<sub>2</sub>; during the COVID-19 pandemic be detected from space? A case study for East China using satellite XCO<sub>2</sub> retrievals”. In: *Atmos. Meas. Tech.* 14.3 (Mar. 2021), pp. 2141–2166. ISSN: 1867-8548. DOI: 10.5194/amt-14-2141-2021 (cit. on p. 2).
- [11] A. Agustí-Panareda et al. “Modelling CO<sub>2</sub> weather – why horizontal resolution matters”. In: *Atmos. Chem. Phys.* 19.11 (June 2019), pp. 7347–7376. ISSN: 1680-7324. DOI: 10.5194/acp-19-7347-2019 (cit. on p. 2).
- [12] A. J. Turner et al. “Observed Impacts of COVID-19 on Urban CO<sub>2</sub> Emissions”. In: *Geophys. Res. Lett.* 47.22 (Nov. 2020). ISSN: 0094-8276. DOI: 10.1029/2020GL090037 (cit. on p. 2).

- [13] G. Nicolini et al. “Direct observations of CO<sub>2</sub> emission reductions due to COVID-19 lockdown across European urban districts”. In: *Sci. Total Environ.* 830 (July 2022), p. 154662. ISSN: 00489697. DOI: 10.1016/j.scitotenv.2022.154662 (cit. on p. 2).
- [14] A. R. Brandt et al. “Methane Leaks from Natural Gas Systems Follow Extreme Distributions”. In: *Environ. Sci. Technol.* 50.22 (Nov. 2016), pp. 12512–12520. ISSN: 0013-936X. DOI: 10.1021/acs.est.6b04303 (cit. on p. 2).
- [15] R. M. Duren et al. “California’s methane super-emitters”. In: *Nature* 575.7781 (Nov. 2019), pp. 180–184. ISSN: 0028-0836. DOI: 10.1038/s41586-019-1720-3 (cit. on p. 2).
- [16] D. J. Jacob et al. “Quantifying methane emissions from the global scale down to point sources using satellite observations of atmospheric methane”. In: *Atmos. Chem. Phys.* 22.14 (July 2022), pp. 9617–9646. ISSN: 1680-7324. DOI: 10.5194/acp-22-9617-2022 (cit. on p. 2).
- [17] J.-F. Gauthier. “The Importance of Matching Needs to Satellite System Capability when Monitoring Methane Emissions from Space”. In: *2021 IEEE Int. Geosci. Remote Sens. Symp. IGARSS*. IEEE, July 2021, pp. 687–690. ISBN: 978-1-6654-0369-6. DOI: 10.1109/IGARSS47720.2021.9555123 (cit. on p. 2).
- [18] S. M. Defratyka et al. “Mapping Urban Methane Sources in Paris, France”. In: *Environ. Sci. Technol.* 55.13 (July 2021), pp. 8583–8591. ISSN: 0013-936X. DOI: 10.1021/acs.est.1c00859 (cit. on pp. 2, 3).
- [19] H. Maazallahi et al. “Methane mapping, emission quantification, and attribution in two European cities: Utrecht (NL) and Hamburg (DE)”. In: *Atmos. Chem. Phys.* 20.23 (Dec. 2020), pp. 14717–14740. ISSN: 1680-7324. DOI: 10.5194/acp-20-14717-2020 (cit. on p. 2).
- [20] T. R. Scarpelli et al. “A global gridded (0.1° × 0.1°) inventory of methane emissions from oil, gas, and coal exploitation based on national reports to the United Nations Framework Convention on Climate Change”. In: *Earth Syst. Sci. Data* 12.1 (Mar. 2020), pp. 563–575. ISSN: 1866-3516. DOI: 10.5194/essd-12-563-2020 (cit. on p. 2).
- [21] A. Forstmaier et al. “Quantification of methane emissions in Hamburg using a network of FTIR spectrometers and an inverse modeling approach”. In: *Atmos. Chem. Phys.* 23.12 (June 2023), pp. 6897–6922. ISSN: 1680-7324. DOI: 10.5194/acp-23-6897-2023 (cit. on p. 2).
- [22] World Meteorological Organization (WMO). *20th WMO/IAEA Meeting on Carbon Dioxide, Other Greenhouse Gases and Related Measurement Techniques (GGMT-2019)*. Tech. rep. 2019, p. 151 (cit. on pp. 2, 3).
- [23] D. Jervis et al. “The GHGSat-D imaging spectrometer”. In: *Atmos. Meas. Tech.* 14.3 (Mar. 2021), pp. 2127–2140. ISSN: 1867-8548. DOI: 10.5194/amt-14-2127-2021 (cit. on p. 2).

- [24] D. S. Stevenson et al. “COVID-19 lockdown emission reductions have the potential to explain over half of the coincident increase in global atmospheric methane”. In: *Atmos. Chem. Phys.* 22.21 (Nov. 2022), pp. 14243–14252. ISSN: 1680-7324. DOI: 10.5194/acp-22-14243-2022 (cit. on p. 2).
- [25] S. Peng et al. “Wetland emission and atmospheric sink changes explain methane growth in 2020”. In: *Nature* 612.7940 (Dec. 2022), pp. 477–482. ISSN: 0028-0836. DOI: 10.1038/s41586-022-05447-w (cit. on p. 2).
- [26] L. Feng et al. “Methane emissions are predominantly responsible for record-breaking atmospheric methane growth rates in 2020 and 2021”. In: *Atmos. Chem. Phys.* 23.8 (Apr. 2023), pp. 4863–4880. ISSN: 1680-7324. DOI: 10.5194/acp-23-4863-2023 (cit. on p. 2).
- [27] S. Kirschke et al. “Three decades of global methane sources and sinks”. In: *Nat. Geosci.* 6.10 (Oct. 2013), pp. 813–823. ISSN: 1752-0894. DOI: 10.1038/ngeo1955 (cit. on p. 3).
- [28] M. Rigby et al. “Role of atmospheric oxidation in recent methane growth”. In: *Proc. Natl. Acad. Sci.* 114.21 (May 2017), pp. 5373–5377. ISSN: 0027-8424. DOI: 10.1073/pnas.1616426114 (cit. on p. 3).
- [29] M. J. Prather. “Lifetimes and eigenstates in atmospheric chemistry”. In: *Geophys. Res. Lett.* 21.9 (May 1994), pp. 801–804. ISSN: 0094-8276. DOI: 10.1029/94GL00840 (cit. on p. 3).
- [30] O. Wild et al. “Indirect long-term global radiative cooling from NO<sub>x</sub> Emissions”. In: *Geophys. Res. Lett.* 28.9 (May 2001), pp. 1719–1722. ISSN: 00948276. DOI: 10.1029/2000GL012573 (cit. on p. 3).
- [31] D. S. Stevenson et al. “Radiative forcing from aircraft NO<sub>x</sub> emissions: Mechanisms and seasonal dependence”. In: *J. Geophys. Res. Atmos.* 109.D17 (Sept. 2004). ISSN: 0148-0227. DOI: 10.1029/2004JD004759 (cit. on p. 3).
- [32] J. Weber et al. “Minimal Climate Impacts From Short-Lived Climate Forcers Following Emission Reductions Related to the COVID-19 Pandemic”. In: *Geophys. Res. Lett.* 47.20 (Oct. 2020). ISSN: 0094-8276. DOI: 10.1029/2020GL090326 (cit. on p. 3).
- [33] Z. S. Venter et al. “COVID-19 lockdowns cause global air pollution declines”. In: *Proc. Natl. Acad. Sci.* 117.32 (Aug. 2020), pp. 18984–18990. ISSN: 0027-8424. DOI: 10.1073/pnas.2006853117 (cit. on p. 3).
- [34] T. Doumbia et al. “Changes in global air pollutant emissions during the COVID-19 pandemic: a dataset for atmospheric modeling”. In: *Earth Syst. Sci. Data* 13.8 (Aug. 2021), pp. 4191–4206. ISSN: 1866-3516. DOI: 10.5194/essd-13-4191-2021 (cit. on p. 3).
- [35] B. Zheng et al. “Changes in China’s anthropogenic emissions and air quality during the COVID-19 pandemic in 2020”. In: *Earth Syst. Sci. Data* 13.6 (June 2021), pp. 2895–2907. ISSN: 1866-3516. DOI: 10.5194/essd-13-2895-2021 (cit. on p. 3).

- [36] J. C. von Fischer et al. “Rapid, Vehicle-Based Identification of Location and Magnitude of Urban Natural Gas Pipeline Leaks”. In: *Environ. Sci. Technol.* 51.7 (Apr. 2017), pp. 4091–4099. ISSN: 0013-936X. DOI: 10.1021/acs.est.6b06095 (cit. on p. 3).
- [37] A. Hoheisel et al. “An improved method for mobile characterisation of 13CH<sub>4</sub> source signatures and its application in Germany”. In: *Atmos. Meas. Tech.* 12.2 (Feb. 2019), pp. 1123–1139. ISSN: 1867-8548. DOI: 10.5194/amt-12-1123-2019 (cit. on p. 3).
- [38] P. Kumar et al. “Mobile atmospheric measurements and local-scale inverse estimation of the location and rates of brief CH<sub>4</sub> and CO<sub>2</sub> releases from point sources”. In: *Atmos. Meas. Tech.* 14.9 (Sept. 2021), pp. 5987–6003. ISSN: 1867-8548. DOI: 10.5194/amt-14-5987-2021 (cit. on p. 3).
- [39] K. Vinković et al. “Evaluating the use of an Unmanned Aerial Vehicle (UAV)-based active AirCore system to quantify methane emissions from dairy cows”. In: *Sci. Total Environ.* 831 (July 2022), p. 154898. ISSN: 00489697. DOI: 10.1016/j.scitotenv.2022.154898 (cit. on p. 3).
- [40] L. Tao et al. “Low-power, open-path mobile sensing platform for high-resolution measurements of greenhouse gases and air pollutants”. In: *Appl. Phys. B* 119.1 (Apr. 2015), pp. 153–164. ISSN: 0946-2171. DOI: 10.1007/s00340-015-6069-1 (cit. on p. 3).
- [41] P. M. Hundt et al. “Mid-IR spectrometer for mobile, real-time urban NO<sub>2</sub> measurements”. In: *Atmos. Meas. Tech.* 11.5 (May 2018), pp. 2669–2681. ISSN: 1867-8548. DOI: 10.5194/amt-11-2669-2018 (cit. on p. 3).
- [42] B. Tuzson et al. “A compact QCL spectrometer for mobile, high-precision methane sensing aboard drones”. In: *Atmos. Meas. Tech.* 13.9 (Sept. 2020), pp. 4715–4726. ISSN: 1867-8548. DOI: 10.5194/amt-13-4715-2020 (cit. on p. 3).
- [43] R. Tillmann et al. “Air quality observations onboard commercial and targeted Zeppelin flights in Germany – a platform for high-resolution trace-gas and aerosol measurements within the planetary boundary layer”. In: *Atmos. Meas. Tech.* 15.12 (June 2022), pp. 3827–3842. ISSN: 1867-8548. DOI: 10.5194/amt-15-3827-2022 (cit. on p. 3).
- [44] A. Luther et al. “Quantifying CH<sub>4</sub> emissions from hard coal mines using mobile sun-viewing Fourier transform spectrometry”. In: *Atmos. Meas. Tech.* 12.10 (Oct. 2019), pp. 5217–5230. ISSN: 1867-8548. DOI: 10.5194/amt-12-5217-2019 (cit. on p. 3).
- [45] F. Dietrich et al. “MUCCnet: Munich Urban Carbon Column network”. In: *Atmos. Meas. Tech.* 14.2 (Feb. 2021), pp. 1111–1126. ISSN: 1867-8548. DOI: 10.5194/amt-14-1111-2021 (cit. on p. 3).

- [46] R. L. Wagner et al. “Application of a mobile laboratory using a selected-ion flow-tube mass spectrometer (SIFT-MS) for characterisation of volatile organic compounds and atmospheric trace gases”. In: *Atmos. Meas. Tech.* 14.9 (Sept. 2021), pp. 6083–6100. ISSN: 1867-8548. DOI: 10.5194/amt-14-6083-2021 (cit. on p. 3).
- [47] F. M. Bréon et al. “An attempt at estimating Paris area CO<sub>2</sub> emissions from atmospheric concentration measurements”. In: *Atmos. Chem. Phys.* 15.4 (Feb. 2015), pp. 1707–1724. ISSN: 1680-7324. DOI: 10.5194/acp-15-1707-2015 (cit. on p. 3).
- [48] I. Xueref-Remy et al. “Diurnal, synoptic and seasonal variability of atmospheric CO<sub>2</sub> in the Paris megacity area”. In: *Atmos. Chem. Phys.* 18.5 (Mar. 2018), pp. 3335–3362. ISSN: 1680-7324. DOI: 10.5194/acp-18-3335-2018 (cit. on p. 3).
- [49] A. A. Shusterman et al. “The BERkeley Atmospheric CO<sub>2</sub> Observation Network: initial evaluation”. In: *Atmos. Chem. Phys.* 16.21 (Oct. 2016), pp. 13449–13463. ISSN: 1680-7324. DOI: 10.5194/acp-16-13449-2016 (cit. on p. 3).
- [50] J. Kim et al. “The BERkeley Atmospheric CO<sub>2</sub> Observation Network: field calibration and evaluation of low-cost air quality sensors”. In: *Atmos. Meas. Tech.* 11.4 (Apr. 2018), pp. 1937–1946. ISSN: 1867-8548. DOI: 10.5194/amt-11-1937-2018 (cit. on p. 3).
- [51] A. Elefante et al. “Dual-Gas Quartz-Enhanced Photoacoustic Sensor for Simultaneous Detection of Methane/Nitrous Oxide and Water Vapor”. In: *Anal. Chem.* 91.20 (Oct. 2019), pp. 12866–12873. ISSN: 0003-2700. DOI: 10.1021/acs.analchem.9b02709 (cit. on p. 3).
- [52] H. Xiao et al. “Ultra-sensitive ppb-level methane detection based on NIR all-optical photoacoustic spectroscopy by using differential fiber-optic microphones with gold-chromium composite nanomembrane”. In: *Photoacoustics* 26 (June 2022), p. 100353. ISSN: 22135979. DOI: 10.1016/j.pacs.2022.100353 (cit. on p. 3).
- [53] Z. Gong et al. “Ppb-level detection of methane based on an optimized T-type photoacoustic cell and a NIR diode laser”. In: *Photoacoustics* 21 (Mar. 2021), p. 100216. ISSN: 22135979. DOI: 10.1016/j.pacs.2020.100216 (cit. on p. 3).
- [54] M. Giglio et al. “Broadband detection of methane and nitrous oxide using a distributed-feedback quantum cascade laser array and quartz-enhanced photoacoustic sensing”. In: *Photoacoustics* 17 (Mar. 2020), p. 100159. ISSN: 22135979. DOI: 10.1016/j.pacs.2019.100159 (cit. on p. 3).
- [55] H. Zheng et al. “Sub-ppb-level CH<sub>4</sub> detection by exploiting a low-noise differential photoacoustic resonator with a room-temperature interband cascade laser”. In: *Opt. Express* 28.13 (June 2020), p. 19446. ISSN: 1094-4087. DOI: 10.1364/OE.391322 (cit. on p. 3).

- 
- [56] J. Peltola et al. “High sensitivity trace gas detection by cantilever-enhanced photoacoustic spectroscopy using a mid-infrared continuous-wave optical parametric oscillator”. In: *Optics Express* 21.8 (2013), p. 10240. ISSN: 1094-4087. DOI: 10.1364/OE.21.010240 (cit. on p. 3).



# Chapter 2

## Theory

## 2.1 Absorption spectroscopy

Spectroscopic measurement methods for gas analysis utilize the fundamental ability of molecules to absorb electromagnetic radiation, i.e. photon energy. According to Planck, the energy of a photon  $E_{\text{Ph}}$  is specified by its wavelength  $\lambda$ , respectively its frequency  $\nu_{\text{Ph}}$

$$E_{\text{Ph}} = \frac{h \cdot c_0}{\lambda} = h \cdot \nu_{\text{Ph}} \quad (2.1)$$

with  $h$  being the Planck's constant and  $c_0$  the speed of light in vacuum. A typical quantity in spectroscopy is the wavenumber  $\tilde{\nu}_{\text{Ph}}$  of the photon, which is calculated via

$$\tilde{\nu}_{\text{Ph}} = \frac{1}{\lambda} = \frac{\nu_{\text{Ph}}}{c_0} \quad (2.2)$$

When  $E_{\text{Ph}}$  corresponds to the difference of two molecular energy levels, there is a certain probability that the molecule absorbs the energy of the photon and is excited into a higher energy state. This can happen via electronic, rotational or vibrational transitions, as well as combinations of these. The absorption cross-section (ACS)  $\sigma(\tilde{\nu})$  provides a measure for the probability of photon absorption at the respective wavenumber  $\tilde{\nu}$ . Multiplying the ACS with the volume number density  $\rho_i$  of the absorbing molecules  $i$  yields the absorption coefficient (AC)  $\alpha(\tilde{\nu})$ .

$$\alpha(\tilde{\nu}) = \rho_i \cdot \sigma(\tilde{\nu}) = \underbrace{N_i \cdot \frac{N_A}{V_{\text{mol}}}}_{\rho_i} \cdot \sigma(\tilde{\nu}) \quad (2.3)$$

$N_i$  is the volume ratio of the absorbing molecules  $i$ ,  $N_A$  the Avogadro constant and  $V_{\text{mol}}$  is the molar volume of the sample gas, which depends on temperature  $T$  and pressure  $p$  of the gas\* and the gas constant  $R$ .

$$V_{\text{mol}} = \frac{RT}{p} \quad (2.4)$$

The spectral absorption lines are different for each molecule and thus represent a unique signature, resulting in excellent selectivity of spectroscopic measurement methods. The intensity of such absorption lines  $s_{kl}$  in [cm/molecule] for a transition from a lower energy state  $k$  to a upper state  $l$  is defined as [1]

$$s_{kl} = \frac{h\tilde{\nu}_{kl}}{c_0} \frac{\rho_k}{\rho_i} \left(1 - \frac{g_k \rho_l}{g_l \rho_k}\right) B_{kl} \quad (2.5)$$

in which  $B_{kl}$  in [ $\text{cm}^3/\text{erg s}^2$ ] is Einstein coefficient of induced absorption. The population densities of the respective energy states are denoted as  $\rho_k$  and  $\rho_l$  with their associated statistical weights  $g_k$  and  $g_l$  [2].  $B_{kl}$  depends on the weighted transition-moment squared  $\mathfrak{R}_{kl}$  in [Debye<sup>2</sup>]

$$B_{kl} = \mathfrak{R}_{kl} \frac{8\pi^3}{3h^2} \quad (2.6)$$

---

\*Assuming an ideal gas

Under the assumption of local thermodynamic equilibrium, the population density distribution of the energy states  $k$  and  $l$  is determined by Boltzmann statistics, see equations (2.7) and (2.8)

$$\frac{g_k \rho_l}{g_l \rho_k} = \exp\left(-\frac{hc_0 \tilde{\nu}_{kl}}{k_B T}\right) \quad (2.7)$$

$$\frac{\rho_k}{\rho_i} = \frac{g_k}{Q(T)} \exp\left(-\frac{hc_0 E_k}{k_B T}\right) \quad (2.8)$$

in which  $E_k$  in  $[\text{cm}^{-1}]$  is the energy of the lower state and  $Q(T)$  is the total internal partition function. Considering only state  $k$ ,  $Q_k(T)$  is given by the sum over the degenerate states of  $k$

$$Q_k(T) = \sum_k g_k \exp\left(-\frac{hc_0 E_k}{k_B T}\right) \quad (2.9)$$

Combining equations (2.7), (2.8), and (2.6) in equation (2.5), yields the final form of the line intensity [1]

$$\begin{aligned} s_{kl} &= \frac{h\tilde{\nu}_{kl}}{c_0} \underbrace{\frac{g_k}{Q(T)} \exp\left(-\frac{hc_0 E_k}{k_B T}\right)}_{\text{equation (2.8)}} \left[ \underbrace{1 - \exp\left(-\frac{hc_0 \tilde{\nu}_{kl}}{k_B T}\right)}_{\text{equation (2.7)}} \right] \underbrace{\mathfrak{R}_{kl} \frac{8\pi^3}{3h^2}}_{\text{equation (2.6)}} \\ &= \frac{8\pi^3}{3hc_0} \tilde{\nu}_{kl} \frac{g_k}{Q(T)} \exp\left(-\frac{hc_0 E_k}{k_B T}\right) \left[ 1 - \exp\left(-\frac{hc_0 \tilde{\nu}_{kl}}{k_B T}\right) \right] \mathfrak{R}_{kl} \end{aligned} \quad (2.10)$$

The temperature dependence of the methane and ethane absorption lines, simulated with the *HITRAN on the web* (**H**igh-resolution **T**RANsmision molecular absorption database) database is plotted in Figure 2.1 [3].

In the following chapters several broadening phenomena influencing the absorption characteristics (chapter 2.1.1), as well as some established spectral measurement methods for trace gas detection (chapter 2.1.2) will be discussed.

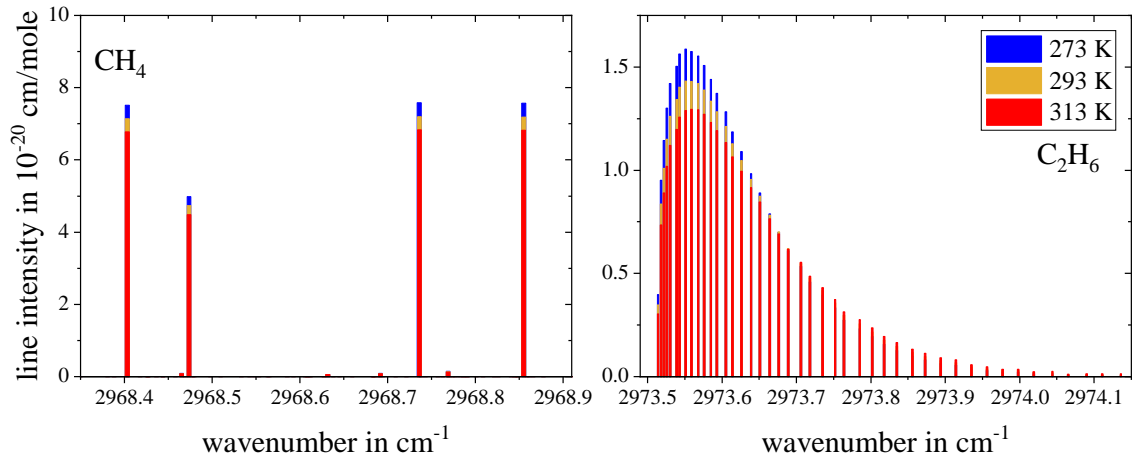


**Fig. 2.1.** Simulated line intensities of  $\text{CH}_4$  (left) and  $\text{C}_2\text{H}_6$  (right) for different temperatures in the spectral range investigated in this work.

### 2.1.1 Spectral broadening effects

Rather than discrete, monochromatic absorption lines, real spectra show absorption profiles with finite spectral width, as the absorption line is superimposed by a broadening function  $f_B$ . Multiplying the line intensity  $s$  with the broadening function yields the ACS  $\sigma$ .

$$\sigma(\tilde{\nu}) = s \cdot f_B(\tilde{\nu}) \quad (2.11)$$

The broadening function is usually normalized to unity, i.e.

$$\int_{-\infty}^{+\infty} f_B(\tilde{\nu}) d\tilde{\nu} = 1 \quad (2.12)$$

Accordingly, any given absorption line is characterized by its line strength  $s_{01}$ , which is independent of pressure. The ACS, however, is affected by the line shape function  $f_B$ , which shows the same analytical form for all transitions, but its exact shape depends on the respective line broadening mechanisms. The three most common forms of spectral broadening are

- natural broadening
- Doppler broadening
- collisional broadening

and will be briefly discussed in the following sections.

#### Natural broadening

Any excited state has a certain lifetime  $\tau_{sp}$  and its existence is therefore limited in time. According to the Heissenberg uncertainty principle, the energy of a state is subject to a certain inaccuracy  $\Delta E$  via [4, 5]

$$\tau_{sp} \Delta E \geq \frac{h}{2\pi} \quad (2.13)$$

With equations 2.1 and 2.2 the natural broadness  $\Delta\tilde{\nu}_{nat}$  is given by:

$$\Delta\tilde{\nu}_{nat} \geq \frac{1}{2\pi\tau_{sp}c_0} \quad (2.14)$$

As this effect is due to the fundamental quantum mechanic phenomenon,  $\Delta\tilde{\nu}_{nat}$  constitutes the minimal observable broadening of absorption spectra. For natural broadening the broadening function  $f_B$  shows Lorentzian distribution. Typical values for  $\Delta\tilde{\nu}_{nat}$  range from  $10^{-4} \text{ cm}^{-1}$  for electronic excited states, showing extremely short lifetimes, to  $10^{-9} \text{ cm}^{-1}$  for vibrational transitions and  $10^{-15} \text{ cm}^{-1}$  for long-living rotational states [5].

## Doppler broadening

According to kinetic gas theory the velocities of the molecules are distributed after Maxwell-Boltzmann velocity distribution [6, 7]

$$p(\vec{v}) = \left( \frac{M}{2\pi k_B T} \right)^{\frac{3}{2}} \cdot \exp\left( -\frac{M\vec{v}^2}{2k_B T} \right) \quad (2.15)$$

showing Brownian motion [8, 9]. Consequently, it will happen that the light beam, which passes the sample in a certain direction, encounters approaching and departing molecules. Thus, the transition wavelength is blue-shifted for approaching molecules

$$\lambda_b = [1 - \vec{v}c_0] \lambda \quad (2.16)$$

while for molecules moving in the same direction as the light beam the transition wavelength is red-shifted

$$\lambda_r = [1 + \vec{v}c_0] \lambda \quad (2.17)$$

The line broadening caused by the Doppler effect shows a Gaussian distribution around the absorption line center at  $\tilde{\nu}_0$  [10]

$$f_B(\tilde{\nu}) = \frac{2}{\Delta\tilde{\nu}_{\text{dop}}} \sqrt{\frac{\ln(2)}{\pi}} \exp\left[ -4\ln(2) \left( \frac{\tilde{\nu} - \tilde{\nu}_0}{\Delta\tilde{\nu}_{\text{dop}}} \right)^2 \right] \quad (2.18)$$

with a full halfwidth  $\Delta\tilde{\nu}_{\text{dop}}$  of [5]:

$$\Delta\tilde{\nu}_{\text{dop}} = \frac{2\tilde{\nu}_{01}}{c_0} \sqrt{\frac{2RT\ln(2)}{M}} \quad (2.19)$$

It is important to note, that  $\Delta\tilde{\nu}_{\text{dop}}$  increases linearly with the difference in wavenumber of the transition and depends on  $\sqrt{T/M}$ . Lighter molecules therefore show greater Doppler broadening, while decreasing the temperature of the sample decreases the broadening effects and thus increases the spectral resolution. Exciting methane ( $M = 16 \text{ g/mol}$ ) at  $T = 313 \text{ K}$  around  $\tilde{\nu} = 2968.4 \text{ cm}^{-1}$  the Doppler broadening can be approximated according to equation (2.19) as  $\Delta\tilde{\nu}_{\text{dop}} = 9.4 \cdot 10^{-4} \text{ cm}^{-1}$ .

## Collisional broadening

Due to Brownian motion collisions between molecules are inevitable. The collision rate  $Z$ , i.e. the reciprocal mean time between two consecutive collisions for a system containing only one species  $i$ , is given by [5]

$$Z = \bar{v}_{\text{rel}} \sigma_{\text{col}} \rho_i = \tau_{\text{col}}^{-1} \quad (2.20)$$

The mean relative velocity  $\bar{v}_{\text{rel}}$  of the molecules is

$$\bar{v}_{\text{rel}} = \sqrt{\frac{16RT}{\pi M_i}} = \sqrt{\frac{16k_B T}{\pi m_i}} \quad (2.21)$$

For a sample containing more than one species, e.g.  $(i, j)$ , the reduced mass  $\mu_{ij}$  has to be considered during collision [5]

$$\bar{v}_{\text{rel}} = \sqrt{\frac{8k_{\text{B}}T}{\pi\mu_{ij}}} = \sqrt{\frac{8k_{\text{B}}T(m_i + m_j)}{\pi m_i m_j}} \quad (2.22)$$

The collision cross-section of two molecules colliding is defined as [5]

$$\sigma_{\text{col},ij} = \pi(r_i + r_j)^2 \quad (2.23)$$

where  $r_i$  and  $r_j$  represent the molecular radii of the respective collision partner. For two colliding molecules of the same sort equation (2.23) simplifies to

$$\sigma_{\text{col},ii} = \pi 4r_i^2 \quad (2.24)$$

Considering a pure gas sample ( $N_i = 1$ ) and relation  $\rho_i = N_i N_{\text{A}} V_{\text{m}}^{-1}$  the collision rate thus can be finally written as

$$Z_i = \tau_{\text{col}}^{-1} = 16r_i^2 p \sqrt{\frac{\pi}{k_{\text{B}}T m_i}} \quad (2.25)$$

Assuming, that molecule collisions are necessary for a change in the molecular energy state, i.e. the deexcitation process, the collision rate can again be linked to Heisenbergs uncertainty principle and gives the expression for the width of collisional broadening.

$$\Delta\tilde{\nu}_{\text{col}} \approx \frac{1}{2\pi\tau_{\text{col}}c_0} \quad (2.26)$$

The boardening function for collisional broadening can be approximated by a Lorentzian curve [11].

$$f_{\text{B}}(\tilde{\nu}) = \frac{\Delta\tilde{\nu}_{\text{col}}}{\pi} \left[ \frac{1}{(\tilde{\nu} - \tilde{\nu}_0)^2 + \Delta\tilde{\nu}_{\text{col}}^2} \right] \quad (2.27)$$

Lower pressure results in a lower collision rate, i.e. more time between molecular collisions, which in return results in less collisional broadening.

In conclusion, the ACS is affected by environmental parameters, e.g. pressure, temperature and gas composition via different broadening effects. While *natural* broadening represents a fundamental limit, the effect of *Doppler* and *collisional* broadening can be minimize accordingly. High resolution spectra are thus often recorded at low temperature and more important low pressure, see equations (2.19) and (2.26). The effect of collisional broadening at pressures below atmospheric pressure plays a significant role in the results obtained and discussed in chapter 4.3 and 4.6 and is illustrated in Appendix A.5 - Figure (A3). Usually, Doppler and collsional broadening act simultaneously on the ACS, which is mathematically expressed by a convolution of the two broadening functions and yields the Voigt function  $f_{\text{V}}$  [4].

$$f_{\text{V}}(\tilde{\nu}) = (f_{\text{G}} * f_{\text{L}})(\tilde{\nu}) \quad (2.28)$$

## 2.1.2 Spectroscopic measurement techniques

Nowadays, spectroscopic measurement systems are the preferred choice for demanding measurement applications like greenhouse gas monitoring, because of their high sensitivity and selectivity. In this section the basic principles, as well as advantages and disadvantages of common spectroscopic measurement techniques that are relevant for this work, such as direct absorption spectroscopy (DAS - chapter 2.1.2), cavity ring-down spectroscopy (CRDS - chapter 2.1.2) and wavelength modulation spectroscopy (WMS - chapter 2.1.2) are discussed. Raman spectroscopy, fluorescence spectroscopy or nuclear magnetic resonance (NMR) spectroscopy are not addressed. A separate, more detailed chapter is dedicated to photoacoustic spectroscopy (PAS - chapter 2.2), which represents the main part of this work.

### Direct absorption spectroscopy

In direct absorption spectroscopy (DAS), a light source with a known emitted optical intensity  $I_0$  illuminates the sample. The transmitted intensity  $I_1$  is measured and used to calculate the volume number density  $\rho_i$  of the absorbing molecules via Beer-Lambert law [12].

$$I_1(\tilde{\nu}) = I_0(\tilde{\nu}) \cdot e^{(-\sigma_i(\tilde{\nu})\rho_i l_{\text{opt}})} \quad (2.29)$$

For DAS the optical detector must exhibit a high dynamic range in order to measure the high transmitted intensity, as well as a high resolution to detect the weak absorption in case of trace analyte concentrations\*. Both features are contrary and combining them is a challenging task. Another drawback of this technique becomes obvious from equation 2.29. For an increased absorption and thus better concentration resolution a longer optical path length  $l_{\text{opt}}$  of the system is required. With the aim of miniaturizing measurement devices, a trade-off between detection limit and system size must be found with the classical absorption method. So-called multi-pass cells offer a solution to this dilemma with the *White* [13] or *Herriott* [14] cells being the most popular design approaches. In these cells, the optical path is artificially extended by light reflection using optical mirrors, thus improving the detection limit, while maintaining reasonable small mechanical dimensions. Nowadays, more sophisticated optical arrangements, e.g. circular designs [15–18], are commonly used, due to their further increased compactness.

### Cavity ring-down spectroscopy

Similar to the *Herriott* cell, cavity ring-down spectroscopy (CRDS) uses two highly reflective mirrors (reflectivity  $R \geq 99.9\%$ ) that increase the optical path length up

---

\*To detect 1 ppbV methane at 313 K and atmospheric pressure with an ACS of  $\sigma_i = 4.3 \cdot 10^{-23} \text{ m}^2$  at an excitation wavenumber of  $\tilde{\nu} = 2968.4 \text{ cm}^{-1}$  with a commercial Herriott cell ( $l_{\text{opt}} = 31.2 \text{ m}$ ), the optical detector must be able to resolve 0.03 % of  $I_0$ .

to the kilometer range. At each reflection, a small fraction  $(1 - R)$  of the optical power is not reflected but decoupled and measured by a photodetector, see Figure 2.2. When the laser is switched on, the cavity fills with circulating laser light. As soon as the photodetector reaches a certain threshold the laser is abruptly switched off and the decay behavior of the optical power is measured. The decay time is defined as the time needed for the signal to reach  $1/e$ -th of the initial value. After  $n$  round trips the measured intensity  $I_n$  for a cavity of length  $L_c$  formed by mirrors with reflectivity  $R$  will be

$$I_n = I_0 R^{2n} \cdot e^{(-2n\sigma_i(\tilde{\nu})\rho_i L_c)} \quad (2.30)$$

The term  $R^{2n}$  can be expressed as  $e^{2n \cdot \ln(R)}$  [19]\*. For the highly reflective mirrors ( $R \approx 1$ ) one can approximate the term  $\ln(R) \approx (1 - R)$ . With this relation and  $n = t \cdot c_0 / (2L_c)$  equation (2.30) can be written as [19, 20]

$$I_n = I_0 \cdot e^{\left(-\frac{t \cdot c_0}{L_c} \cdot [(1 - R) + \sigma_i(\tilde{\nu})\rho_i L_c]\right)} \quad (2.31)$$

According to equation (2.31) more absorbing molecules inside the cavity yield a faster decay, compare (I) and (II) in Figure 2.2. The time dependent measured decay characteristic can be calculated via

$$I = I_0 \cdot e^{\left(-\frac{t}{\tau}\right)} \quad (2.32)$$

Combining equations (2.31) and (2.32), it becomes clear that the decay time  $\tau$  is proportional to the analyte volume number density  $\rho_i$  [21].

$$\tau = \frac{L_c}{c_0 [(1 - R) + (\sigma_i(\tilde{\nu})\rho_i L_c)]} \quad (2.33)$$

Due to its excellent sensitivity and its advantage of utilizing rather simple photodetectors compared to DAS, CRDS instruments are most widely used when it comes to continuous trace gas monitoring. Dube et al. developed a CRDS system for simultaneous atmospheric  $\text{NO}_3$  and  $\text{N}_2\text{O}_5$  monitoring, providing LoDs of 0.5 pptV and 1 pptV, respectively [22]. Regarding methane detection Tang et al. published an article reporting a limit of detection of 13 pptV with an averaging time of 10.4 s [23]. The US-american company Picarro Inc. is one of many companies, which sell multiple CRDS systems for various applications, including environmental monitoring. Those systems can be used for greenhouse gas monitoring, isotope analysis or detection of hazardous gases. For all applications the CRDS systems provide detection limits in the single digit ppbV, or even sup-ppbV range. The European scientific network *Integrated Carbon Observation System* (ICOS) aims to provide accurate, continuous and standardized measurements of greenhouse gases to the public. To achieve this, the Picarro G2301 CRDS systems are integrated in all 46 ICOS stations to monitor  $\text{CH}_4$  and  $\text{CO}_2$  [24]. In chapter 4.4 this device was used as a reference to be compared with the photoacoustic sensor developed in this work.

---

\*  $R^{2n} = e^{\ln(R^{2n})} = e^{2n \cdot \ln(R)}$

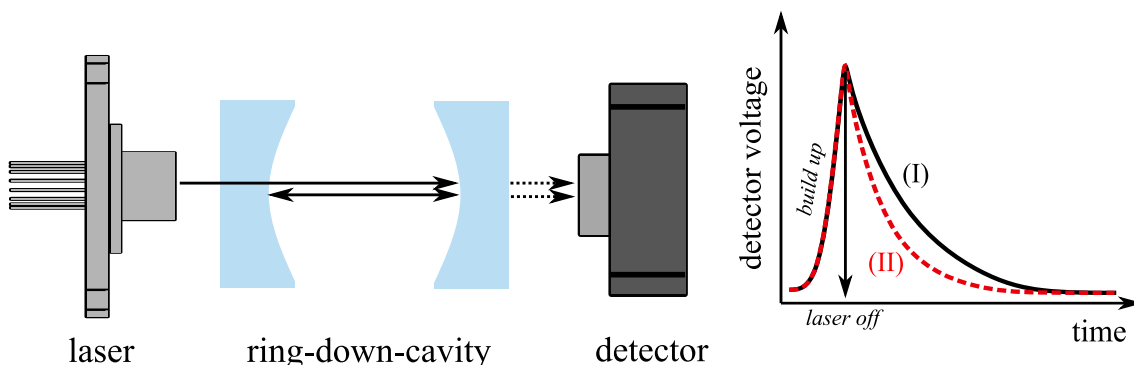


**Fig. 2.2.** Schematic representation of CRDS. The photodetector measures the transmitted optical power behind the cavity as a function of time. With more absorbing molecules inside the cavity (II - red dashed line) the decay time is faster, compared to an empty cell (I - black solid line)

The detection limit of CRDS systems is determined by the decay time of an empty cavity  $\tau_0$ , i.e. not containing any analyte

$$\tau_0 = \frac{L_c}{c_0(1 - R)} \quad (2.34)$$

and the minimal detectable time interval  $\Delta t_{\min}$  of the detector [19, 25].

The difference in decay time  $\Delta\tau$  of the empty cavity  $\tau_0$  and of an analyte containing sample gas must be equal or greater than  $\Delta t_{\min}$ . Using highly reflective mirrors  $R = 99.99\%$  in a cavity of length  $L_c = 25$  cm, which results in an effective optical path length of 11.5 km (23024 round trips\*) 1 ppbV methane, excited at  $\tilde{\nu} = 2968.4$   $\text{cm}^{-1}$  with an ACS of  $\sigma = 4.3 \cdot 10^{-23}$   $\text{m}^2$ , shows a decay time of  $\tau = 8.313$   $\mu\text{s}$ . For the empty cavity the decay time is  $\tau_0 = 8.333$   $\mu\text{s}$ . The photodetector must thus be able to resolve at least  $\Delta t_{\min} = 20$  ns. Figure 2.3 shows the differences in decay time  $\Delta\tau$  for an empty cavity and a cavity containing different analyt concentrations  $N_i$ , as well as for different reflectivities  $R$  (i) - (v) of the cavity mirrors. By increasing the reflectivity, the requirements for the photo detector, i.e. its time resolution, can be reduced. Figure 2.3 also highlights, that CRDS devices typically feature a high dynamic range [20].

In addition to the excellent detection limits and high dynamic range, a further significant advantage of CRDS is the independence of the signal from the emitted optical power, since the decay-time  $\tau$  is the measured quantity [26]. Fluctuations in the optical power may only affect the build up time inside the cavity, but not the measurement itself, see Figure 2.2.

While CRDS provides several advantages, it is not without limitations. The cavity is sensitive towards temperature fluctuations and mechanical vibrations, which may

\*For this number of round trips the optical power within the cavity has dropped below 1 % of its initial value.

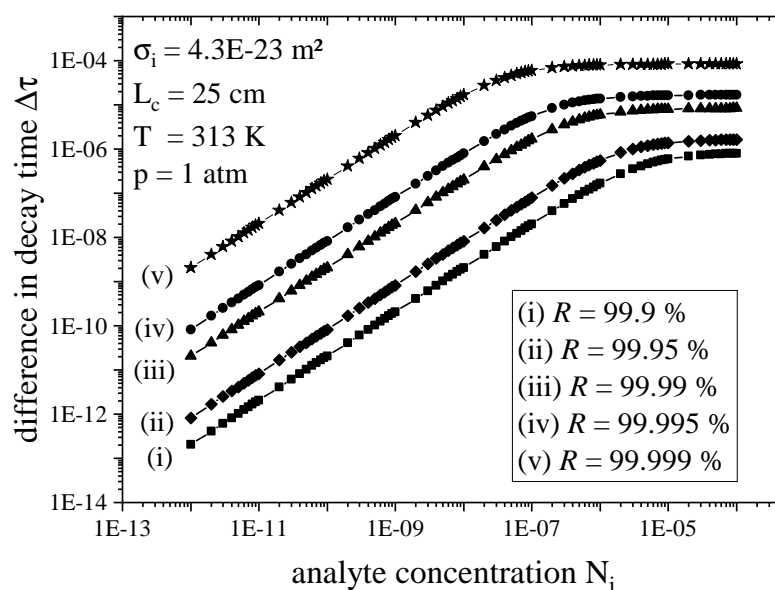


**Fig. 2.3.** Double logarithmic representation of the difference in decay time  $\Delta\tau$  for an empty and an analyt containing cavity. The calculations are performed for different reflectivities  $R$  of the cavity mirrors.

result in worse measurement precision. Additionally, the cavity must be precisely aligned and the employed optical components are often rather expensive.

### Wavelength modulation spectroscopy

Another common technique for gas analysis is wavelength modulation spectroscopy (WMS). Unlike in classical DAS, in which the light source is operated in continuous-wave (cw) mode, WMS utilizes the tunability of novel laser sources. The wavelength tunability is achieved by either current or temperature modulation of the laser. For laser modulation a small sinusoidal current  $I_{\text{mod}}$  with frequency  $f_{\text{mod}}$  is superimposed to the offset current  $I_{\text{offset}}$ . When scanning over an absorption feature the offset current is sawtooth modulated, with an frequency much slower than  $f_{\text{mod}}$ . The resulting signal consists of  $n$  harmonics of the sinusoidal frequency  $f_{\text{mod}}$ , which can be detected by a lock-in-amplifier (LIA)\*. In Figure 2.4 the scanning process over an Lorentzian absorption is illustrated in a simplified manner. The blue line shows the time dependend WMS signal at the detector prior to LIA data processing, while the red sine wave indicates the wavelength modulation. The offset current of the laser is increased from (a) to (d). When the offset current matches the maximum absorption of the peak (c) the dominant frequency of the WMS comes twice the modulation frequency. Assuming a wavenumber normalized Lorentzian shaped absorption profil  $G(x)$ , i.e. the center of absorption being at  $x_c = 0$

\*The principles of lock-in detection are discussed in Appendix A.3.

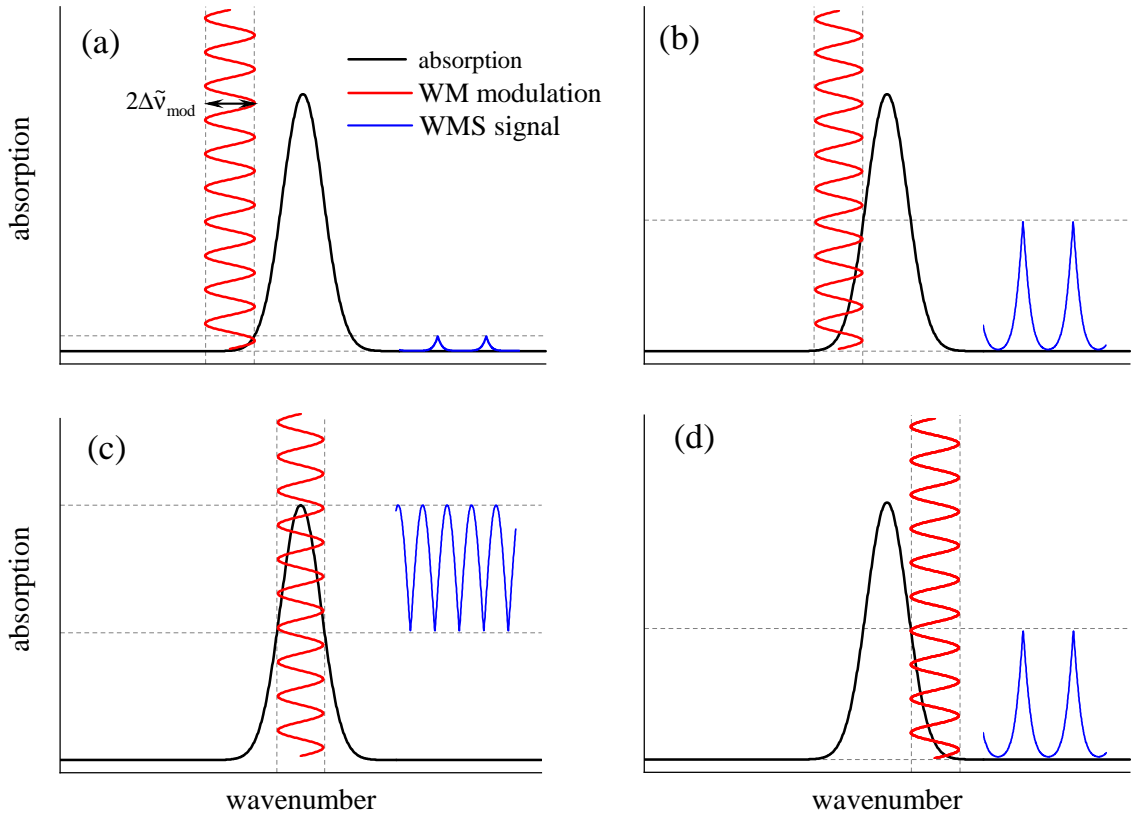


**Fig. 2.4.** Schematic representation of WMS technique. The laser offset current is increased from (a) to (d) scanning the absorption peak (black line), while the sinusoidal current (red line) causes the laser emission to slightly shift, resulting in the raw WMS signal at the detector (blue line).

$$G(x) = \frac{1}{1+x^2} \quad (2.35)$$

the Fourier transform  $g(y)$  of  $G(x)$  is given by equation (2.36) [27]

$$g(y) = \frac{1}{2\pi} \int_{-\infty}^{+\infty} \exp(-i \cdot x \cdot y) dx = \frac{1}{2} \exp(-|y|) \quad (2.36)$$

For sinusoidal modulation of the laser,  $x$  can be extended by  $x + m \cdot \cos(2\pi f_{\text{mod}}t)$ . The modulation index  $m$  is a function of the modulation width  $\Delta\tilde{\nu}$  and the half width at half maximum of the absorption feature  $\gamma$  [28]

$$m = \frac{\Delta\tilde{\nu}}{\gamma} = \frac{x}{\gamma} \quad (2.37)$$

The measured signal  $S(x)$  at the detector is defined as

$$S(x) = G(x + m \cdot \cos(2\pi f_{\text{mod}}t)) \quad (2.38)$$

with its Fourier transform

$$s(y) = g(y) \exp(i \cdot m \cdot y \cdot \cos(2\pi f_{\text{mod}}t)) \quad (2.39)$$

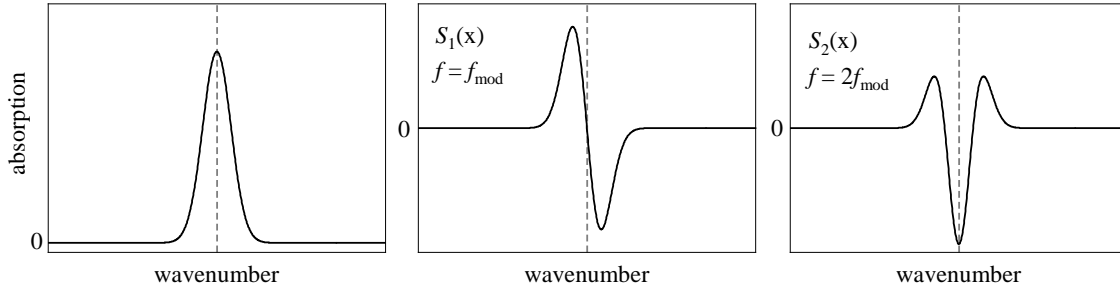


**Fig. 2.5.** Visualisation of the corresponding signal of WMS spectral scan, after LIA processing of  $S_1$  and the first harmonic  $S_2$  over an undistorted absorption peak (left graph).

Using the Jacobi-Anger formula [29] equation (2.39) can be expanded into a Fourier series [27]

$$s(y) = \sum_{n=0}^{\infty} i^n \varepsilon_n \cdot \cos(n \cdot 2\pi f_{\text{mod}} t) g(y) J_n(m \cdot y) \quad (2.40)$$

with  $\varepsilon = 1$  for  $n = 0$  and  $\varepsilon = 2$  for  $n \geq 2$  and  $J_n(m \cdot y)$  being the Bessel function of  $n$ -th order.

Performing the inverse transformation on equation (2.40) and subsequent integration, yields a mathematical description of the measured signal  $S_n(x)$  containing all  $n$  harmonics, when scanning over an Lorentzian shaped absorption peak with wavelength modulation

$$S_n(x) = \frac{1}{2m^n} \varepsilon_n i^n \cdot \frac{[\sqrt{(1-i \cdot x)^2 + m^2} - (1-i \cdot x)]^n}{\sqrt{(1-i \cdot x)^2 + m^2}} + \text{c.c.} \quad (2.41)$$

Schilt et al. provided an expression for the first two harmonics ( $n = 1$  and  $n = 2$ ) from equation (2.41) [30].

$$S_1(x) = \left[ \frac{\sqrt{2}}{m} \cdot \frac{-x\sqrt{r+M} + \text{sign}(x)\sqrt{r-M}}{r} \right] \quad (2.42)$$

$$S_2(x) = \left[ \frac{-4}{m^2} + \frac{\sqrt{2}}{m^2} \cdot \frac{(r+1-x^2)\sqrt{r+X} + 2|x|\sqrt{r-X}}{r} \right] \quad (2.43)$$

with  $M = (1 - x^2 + m^2)$  and  $r = \sqrt{M^2 + 4x^2}$ . The optimal modulation index for an ideal Lorentzian shaped absorption for the first harmonic signal becomes  $m_{1,\text{opt}} = 2$  and for the second harmonic  $m_{2,\text{opt}} = 2.197$  [27, 31, 32]. The detector output of  $S_1$  and  $S_2$  demodulated at  $f = f_{\text{mod}}$  and  $f = 2f_{\text{mod}}$ , respectively, is shown in Figure 2.5. While  $S_1$  shows a zero crossing at the maximum of the absorption peak (grey dotted line), the first harmonic  $S_2$  has a negative maximum.

Wavelength modulation spectroscopy provides several advantages over direct absorption spectroscopy, whose applicability is limited by overlapping absorption lines

and interference from non-target gases. WMS addresses these challenges by modulating the laser wavelength, allowing for better discrimination between the target gas absorption signal and interfering background signals [33]. The laser modulation introduces the possibility of phase-sensitive detection, e.g. via lock-in amplification, enabling the extraction of the specific absorption features with higher precision. This results in improved signal-to-noise ratio, which is beneficial for trace gas detection applications. Additionally, WMS provides effective background suppression, making it a suitable choice in harsh environments, where direct absorption spectroscopy may encounter limitations in distinguishing the analyte gases from interfering molecules. One major drawback of WMS is, however, the increased complexity of experimental setups and data analysis compared to direct absorption spectroscopy. The modulation parameters of the laser must be precisely monitored and controlled, demanding sophisticated devices. Moreover, in applications in which the modulation depth is limited the sensitivity of WMS may be reduced.

Chapter 4.6, discusses the influence and resulting limitations of overlapping absorption peaks as well as pressure broadening effects in case of WM PAS.

## References

- [1] L. Rothman et al. “THE HITRAN MOLECULAR SPECTROSCOPIC DATABASE AND HAWKS (HITRAN ATMOSPHERIC WORKSTATION): 1996 EDITION”. In: *J. Quant. Spectrosc. Radiat. Transf.* 60.5 (Nov. 1998), pp. 665–710. ISSN: 00224073. DOI: 10.1016/S0022-4073(98)00078-8 (cit. on pp. 12, 13).
- [2] M. Šimečková et al. “Einstein A-coefficients and statistical weights for molecular absorption transitions in the HITRAN database”. In: *Journal of Quantitative Spectroscopy and Radiative Transfer* 98.1 (Mar. 2006), pp. 130–155. ISSN: 00224073. DOI: 10.1016/j.jqsrt.2005.07.003 (cit. on p. 12).
- [3] L. Rothman et al. “The HITRAN 2004 molecular spectroscopic database”. In: *J. Quant. Spectrosc. Radiat. Transf.* 96.2 (Dec. 2005), pp. 139–204. ISSN: 00224073. DOI: 10.1016/j.jqsrt.2004.10.008 (cit. on p. 13).
- [4] W. Demtröder. *Laser Spectroscopy*. Berlin, Heidelberg: Springer Berlin Heidelberg, 2008. ISBN: 978-3-540-73415-4. DOI: 10.1007/978-3-540-73418-5 (cit. on pp. 14, 16).
- [5] P. W. Atkins and J. de Paula. *Physikalische Chemie*. 5th ed. Weinheim: WILEY-VCH, 2013. ISBN: 978-3-527-33247-2 (cit. on pp. 14–16).
- [6] J. C. Maxwell. “Illustrations of the dynamical theory of gases. Part II. On the process of diffusion of two or more kinds of moving particles among one another”. In: *The London, Edinburgh, and Dublin Philosophical Magazine and Journal of Science* 20.130 (July 1860), pp. 21–37. ISSN: 1941-5982. DOI: 10.1080/14786446008642902 (cit. on p. 15).

- [7] J. C. Maxwell. “Illustrations of the dynamical theory of gases. Part I. On the motions and collisions of perfectly elastic spheres”. In: *The London, Edinburgh, and Dublin Philosophical Magazine and Journal of Science* 19.124 (Jan. 1860), pp. 19–32. ISSN: 1941-5982. DOI: 10.1080/14786446008642818 (cit. on p. 15).
- [8] R. Brown. “XXVII. A brief account of microscopical observations made in the months of June, July and August 1827, on the particles contained in the pollen of plants; and on the general existence of active molecules in organic and inorganic bodies”. In: *The Philosophical Magazine* 4.21 (Sept. 1828), pp. 161–173. ISSN: 1941-5850. DOI: 10.1080/14786442808674769 (cit. on p. 15).
- [9] A. Einstein. “Über die von der molekularkinetischen Theorie der Wärme geforderte Bewegung von in ruhenden Flüssigkeiten suspendierten Teilchen”. In: *Annalen der Physik* 322.8 (1905), pp. 549–560. ISSN: 00033804. DOI: 10.1002/andp.19053220806 (cit. on p. 15).
- [10] B. Tuzson. “Symmetry Specific Study of Ozone Isotopomer Formation”. PhD thesis. University of Heidelberg, 2005. DOI: 10.11588/heidok.00005523 (cit. on p. 15).
- [11] J.-P. Besson. “Photoacoustic spectroscopy for multi-gas sensing using near infrared lasers”. PhD thesis. 2006 (cit. on p. 16).
- [12] A. Beer. “Bestimmung der Absorption des rothen Lichts in farbigen Flüssigkeiten”. In: *Annalen der Physik und Chemie* 162.5 (1852), pp. 78–88. ISSN: 00033804. DOI: 10.1002/andp.18521620505 (cit. on p. 17).
- [13] J. U. White. “Long Optical Paths of Large Aperture”. In: *J. Opt. Soc. Am.* 32.5 (May 1942), p. 285. ISSN: 0030-3941. DOI: 10.1364/JOSA.32.000285 (cit. on p. 17).
- [14] D. Herriott et al. “Off-Axis Paths in Spherical Mirror Interferometers”. In: *Appl. Opt.* 3.4 (Apr. 1964), p. 523. ISSN: 0003-6935. DOI: 10.1364/AO.3.000523 (cit. on p. 17).
- [15] B. Tuzson et al. “Compact multipass optical cell for laser spectroscopy”. In: *Opt. Lett.* 38.3 (Feb. 2013), p. 257. ISSN: 0146-9592. DOI: 10.1364/OL.38.000257 (cit. on p. 17).
- [16] M. Graf et al. “Compact, circular, and optically stable multipass cell for mobile laser absorption spectroscopy”. In: *Opt. Lett.* 43.11 (June 2018), p. 2434. ISSN: 0146-9592. DOI: 10.1364/OL.43.002434 (cit. on p. 17).
- [17] N. Rothbart et al. “A Compact Circular Multipass Cell for Millimeter-Wave/Terahertz Gas Spectroscopy”. In: *IEEE Trans. Terahertz Sci. Technol.* 10.1 (Jan. 2020), pp. 9–14. ISSN: 2156-342X. DOI: 10.1109/TTHZ.2019.2950123 (cit. on p. 17).
- [18] A. Manninen et al. “Versatile multipass cell for laser spectroscopic trace gas analysis”. In: *Appl. Phys. B* 109.3 (Nov. 2012), pp. 461–466. ISSN: 0946-2171. DOI: 10.1007/s00340-012-4964-2 (cit. on p. 17).

- [19] S. MAITHANI and M. PRADHAN. “Cavity ring-down spectroscopy and its applications to environmental, chemical and biomedical systems”. In: *J. Chem. Sci.* 132.1 (Dec. 2020), p. 114. ISSN: 0974-3626. DOI: 10.1007/s12039-020-01817-x (cit. on pp. 18, 19).
- [20] K. W. Busch and M. A. Busch. “Introduction to Cavity-Ringdown Spectroscopy”. In: Apr. 1999, pp. 7–19. DOI: 10.1021/bk-1999-0720.ch002 (cit. on pp. 18, 19).
- [21] J. P. Looney et al. “Quantitative Absorption Measurements Using Cavity-Ringdown Spectroscopy with Pulsed Lasers”. In: Apr. 1999, pp. 93–105. DOI: 10.1021/bk-1999-0720.ch007 (cit. on p. 18).
- [22] W. P. Dubé et al. “Aircraft instrument for simultaneous, in situ measurement of NO<sub>3</sub> and N<sub>2</sub>O<sub>5</sub> via pulsed cavity ring-down spectroscopy”. In: *Rev. Sci. Instrum.* 77.3 (Mar. 2006), p. 034101. ISSN: 0034-6748. DOI: 10.1063/1.2176058 (cit. on p. 18).
- [23] J. Tang et al. “High-precision measurements of nitrous oxide and methane in air with cavity ring-down spectroscopy at 7.6 μm”. In: *Atmos. Meas. Tech.* 12.5 (May 2019), pp. 2851–2861. ISSN: 1867-8548. DOI: 10.5194/amt-12-2851-2019 (cit. on p. 18).
- [24] ICOS RI. “ICOS Atmosphere Station Specifications V2.0 (editor: O. Laurent)”. In: 0.September (2020) (cit. on p. 18).
- [25] G. Berden and R. Engeln, eds. *Cavity Ring-Down Spectroscopy*. Wiley, Aug. 2009. ISBN: 9781405176880. DOI: 10.1002/9781444308259 (cit. on p. 19).
- [26] S. Shadman et al. “Open-path cavity ring-down spectroscopy sensor for atmospheric ammonia”. In: *Appl. Phys. B* 122.7 (July 2016), p. 194. ISSN: 0946-2171. DOI: 10.1007/s00340-016-6461-5 (cit. on p. 19).
- [27] R. Arndt. “Analytical Line Shapes for Lorentzian Signals Broadened by Modulation”. In: *J. Appl. Phys.* 36.8 (Aug. 1965), pp. 2522–2524. ISSN: 0021-8979. DOI: 10.1063/1.1714523 (cit. on pp. 21, 22).
- [28] Z. L. Wang et al. “Wavelength modulation technique-based photoacoustic spectroscopy for multipoint gas sensing”. In: *Appl. Opt.* 57.11 (Apr. 2018), p. 2909. ISSN: 1559-128X. DOI: 10.1364/AO.57.002909 (cit. on p. 21).
- [29] W. Magnus and F. Oberhettinger. *Formeln und Sätze für die Speziellen Funktionen der Mathematischen Physik*. Berlin, Heidelberg: Springer Berlin Heidelberg, 1943. ISBN: 978-3-662-41656-3. DOI: 10.1007/978-3-662-41791-1 (cit. on p. 22).
- [30] S. Schilt et al. “Wavelength Modulation Spectroscopy: Combined Frequency and Intensity Laser Modulation”. In: *Applied Optics* 42.33 (2003), p. 6728. ISSN: 0003-6935. DOI: 10.1364/AO.42.006728 (cit. on p. 22).
- [31] P. Kluczynski et al. “Wavelength modulation absorption spectrometry — an extensive scrutiny of the generation of signals”. In: *Spectrochim. Acta Part B At. Spectrosc.* 56.8 (Aug. 2001), pp. 1277–1354. ISSN: 05848547. DOI: 10.1016/S0584-8547(01)00248-8 (cit. on p. 22).

- [32] S. Schilt and L. Thévenaz. “Wavelength modulation photoacoustic spectroscopy: Theoretical description and experimental results”. In: *Infrared Phys. Technol.* 48.2 (June 2006), pp. 154–162. ISSN: 13504495. DOI: 10.1016/j.infrared.2005.09.001 (cit. on p. 22).
- [33] G. B. Rieker et al. “Calibration-free wavelength-modulation spectroscopy for measurements of gas temperature and concentration in harsh environments”. In: *Appl. Opt.* 48.29 (Oct. 2009), p. 5546. ISSN: 0003-6935. DOI: 10.1364/AO.48.005546 (cit. on p. 23).

## 2.2 Photoacoustic spectroscopy

When Alexander Graham Bell in 1880 periodically interrupted focused sunlight while illuminating a solid substance, he observed an audible sound, discovering the photoacoustic effect [1]. In photoacoustic spectroscopy (PAS) the effect of absorption of electromagnetic waves by molecules is used to generate an acoustic signal, which intensity is proportional to the number of absorbing molecules. Initially a modulated light source (amplitude – or wavelength modulation) electromagnetically excites the analyte of interest. Via collisions with surrounding molecules the additional energy of the excited analyte molecules may be converted into kinetic (translational) energy, see chapter 2.2.2. This energy transition from a vibrational to a translational energy state (VT relaxation) results in local heating of the sample gas. Due to the periodicity of the modulation, this heat input is also periodic. In case of amplitude modulation (AM) the PAS signal exhibits the same frequency as the laser modulation, while for wavelength modulation (WM) the signal at the first harmonic  $2f_{\text{mod}}$  is of interest. The heat input results in a periodic density fluctuation within the sample gas, i.e. periodic dilatation and contraction, which corresponds to an acoustic wave. The signal generation process is displayed as a flowchart in Figure 2.6. Compared to other spectral techniques, see equation (2.29) for DAS and equation (2.33) for CRDS the PA signal does not depend on the optical path length, increasing to potential for miniaturization without the need of complex optical mirror arrangements. As optical cavities or multipass cells are usually quite expensive, PA sensors additionally offer a significant cost advantage, while retaining ppbV or even sub-ppbV level sensitivity. These characteristics make PAS an attractive technique for highly demanding applications, such as medical diagnostics [3–6], environmental monitoring [7–10], isotope ratio analysis [11, 12] or hazardous and explosive compound detection [13–15].

The photoacoustically generated pressure  $p_a$  is converted into a voltage signal via an acoustic-electrical transducer. There is a variety of photoacoustic systems, which essentially differ in the choice of detector. Conventional PA systems use microphones as acoustic detectors, while in quartz enhanced PAS (QEPAS) the sharp resonance of quartz tuning forks (QTF) is exploited. Less common, but still relevant systems employ micromechanical cantilevers and detect the sound pressure induced cantilever deflection via optical readout [13, 16, 17], piezoresistive [18, 19], piezo-

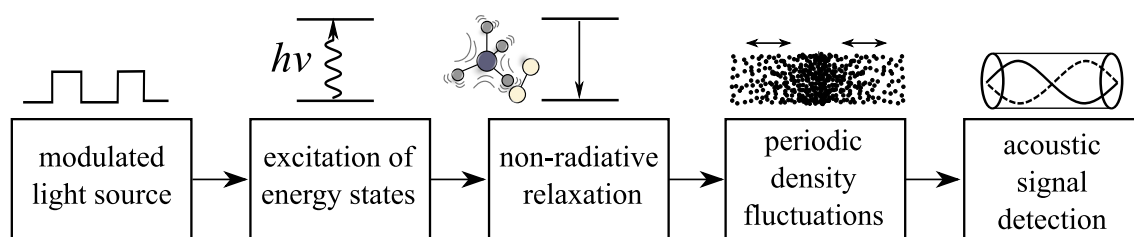


**Fig. 2.6.** Schematic representation of the signal generation process in PAS, adapted from [2].

electric [20, 21] or capacitive readout [22–24]. A comprehensive review regarding recent progress in cantilever enhanced PAS is provided by Yin et al. [25]. Since the photoacoustic measurements in this work were performed using microphone-based or quartz-enhanced PAS sensors, which are also the two most dominant techniques in PAS, cantilever-based sensors are not discussed further in the following.

To increase the signal to noise ratio (SNR) and thus improve the detection limit, both QEPAS and microphone PAS sensors often employ acoustic resonators [26]. As those systems utilize the resonance amplification of the resonators, this approach is called *resonant photoacoustic*. *Non-resonant photoacoustic* setups are also reported in literature [27–30], but not further discussed in this work. In case of resonant PAS, the modulation frequency is determined by the dimensions of the acoustic resonator, otherwise a mismatch in the modulation and the resonance frequency will cause signal losses. The resonator amplification properties are summarized in the quality  $Q$  factor, which is defined as the ratio of lost energy per oscillation with respect to the accumulated energy [31]. Higher  $Q$  factors yield better amplification of the acoustic wave and thus better SNR. Multiple resonator geometries have already been investigated in literature and summarized in [31]. The most common type is the so-called *H-type resonator* [32–35], i.e. an both sided open ended cylinder accompanied by two buffer volumes for acoustic noise suppression [36, 37]. Other geometries, like *Helmholtz resonators* [38–41] or *T-type resonators* [42–44] are also reported, but are less common and will not be discussed further. Cylindrical resonators exhibit three types of resonance modes, i.e. azimuthal, radial and longitudinal. The particle displacement for all three modes is shown schematically in Appendix A1. In further considerations, only the longitudinal resonance will be discussed, as the first longitudinal mode ( $n = 1$ ) was exploited in this work. For the first longitudinal mode, the maximum pressure oscillation is generated at half of the resonator length ( $L/2$ ). The resonance frequency of the longitudinal modes is given by [31]

$$f_{\text{res}} = n \frac{c_s}{2 \cdot L_{\text{res}}} \quad (2.44)$$

for  $n = 1, 2, \dots$  harmonics, with  $c_s$  being the speed of sound of the sample and  $L$  being the length of the cylinder. As  $c_s$  is a function of temperature  $T$  and gas composition  $\chi_i$  of the sample gas [45], so is  $f_{\text{res}}$ . Variations in the sample gas composition affect the speed of sound and thus shift the resonance frequency. If  $f_{\text{mod}}$  is not adjusted accordingly this will result in a signal loss and misinterpretation of the measurement data regarding the analyte concentration. In chapter 3.1.2 an integrated, real-time resonance monitoring system is presented to avoid such detuning. Regarding QEPAS systems, that additionally exploit acoustic resonators, the resonance amplification by the QTF exceeds the amplification by the resonators, thus the overall resonance frequency and accordingly the laser modulation frequency are determined by the QTF frequency  $f_{\text{QTF}}$ . Nevertheless, as the overall resonance amplification results from multiplication of the QTF and the acoustic resonator amplification, the optimal resonator length is defined by  $f_{\text{QTF}}$  to achieve maximum amplification. While  $f_{\text{QTF}}$  is constant, according to equation (2.44) the resonator frequency is a function of  $c_s$  and thus  $T$  and  $\chi_i$ . Therefore, changes in the sample composition, or temperature

may cause acoustic detuning by shifting the resonator amplification characteristics, but not of the QTF and, hence, yield non-negligible signal losses.

Although PA systems are independent of the optical path length, higher optical power within the measurement cell results in more excited molecules and thus a higher PA signal. Multipass approaches in PAS, e.g. employing *Herriott* cells, reported an improvement regarding the limit of detection by a factor of 12 [46] and 17.3 [47]. An improvement of the SNR by up to 640 using an optical cavity was reported in 2022 by Hayden et al. [48]. In 2013, Kachanov et al. were able to achieve pptV level sensitivity for  $\text{NH}_3$  detection by 181-fold optical power enhancement employing an external cavity [49]. Regarding  $\text{C}_2\text{H}_2$  detection an external cavity enhanced the photoacoustic signal by a factor of 100, thus achieving a detection limit in the double-digit pptV range [50].

Whether multipass cells, optical cavities or simple acoustic one-beam resonators are exploited, the excited analyte molecules must be able to release their vibrational energy in the form of translational energy within in one period of  $f_{\text{mod}}$  (VT relaxation) in order to generate a loss-free photoacoustic signal. However, VT relaxation is not the only process that can occur during molecule collisions of excited analyte molecules. For instance, the vibrational energy can be converted into rotational (VR relaxation), or again vibrational energy (VV relaxation) of a different state, whereas for further considerations VR relaxation is neglected. Whether VT or VV, every energy transfer process starting from an excited energy state might affect the overall relaxation cascade and, hence, the resulting PA signal. At least the rate of one of those transfer processes originating from a certain excited state has to be considerably faster than  $f_{\text{mod}}$ , otherwise a delay in relaxation occurs, yielding PA signal loss. The overall delay when considering the whole relaxation cascade is strongly dependent on environmental conditions, i.e. pressure  $p$ , temperature  $T$  and gas composition  $\chi_i$ . This complexity of mutually influencing and sometimes counteracting parameters makes relaxation one of the most challenging issues in photoacoustics, especially with respect to data reliability. In chapter 2.2.2 the relaxation process is theoretically discussed, and finally provides a brief summary of already reported relaxational effects for different analytes in PAS, highlighting the relevance of this issue. In chapter 4.2 an algorithm (CoNRad) is presented, which provides further insights to make relaxation more tangible and forms the basis of the obtained results in chapters 4.3, 4.4, and 4.5.

### 2.2.1 Signal generation

For understanding the heat generation process via relaxation a simplified two-level system is sufficient. To explain the effect of relaxation on the photoacoustic signal, the two-level system has to be extended considering all energy states participating in the relaxational cascade, see chapter 2.2.2. The amplification by employing acoustic resonators has already been extensively discussed in literature and will thus only be briefly summarized in this chapter.

## Heat production rate

Considering only two energy states, i.e. the ground state  $E_0$  and an excited state  $E_1$ , the analyte volume number density  $\rho$  can be expressed as the population densities of those two states  $\rho_0$  and  $\rho_1$ .

$$\rho = \rho_0 + \rho_1 \quad (2.45)$$

With the assumption, that significantly more molecules remain in the ground state ( $\rho_0 \gg \rho_1$ ) equation (2.45) can be approximated as  $\rho \approx \rho_0$ . The excited state gets populated by photon absorption with photon flux  $\Psi$  of the modulated light source

$$\Psi = \frac{P_0}{\underbrace{hc_0 \tilde{\nu}_{Ph} \pi \left(\frac{d_b}{2}\right)^2}_{\Psi_0}} (1 + e^{i\omega t}) \quad (2.46)$$

with the angular modulation frequency  $\omega = 2\pi f_{\text{mod}}$ ,  $P_0$  being the emitted optical power,  $d_b$  the diameter of the light beam and  $\Psi_0$  the flux without modulation in [ $\text{s} \cdot \text{m}^{-2}$ ].

The rate equation describing the time-dependent population of the excited energy state  $E_1$  is given by

$$\frac{d\rho_1}{dt} = \rho\sigma(\tilde{\nu}_{Ph})\Psi - \rho_1\sigma(\tilde{\nu}_{Ph})\Psi - \frac{\rho_1}{\tau_1} \quad (2.47)$$

The lifetime of  $E_1$  is considered by  $\tau_1$  and depends on the non-radiative  $\tau_{1,n}$  and the radiative  $\tau_{1,r}$  lifetimes

$$\tau_1^{-1} = \tau_{1,n}^{-1} + \tau_{1,r}^{-1} \quad (2.48)$$

For excitation in the infrared region the simplification  $\tau_1 \approx \tau_{1,n}$  can be applied as collision induced non-radiative relaxation processes dominate the deactivation of the excited state, i.e.  $\tau_{1,r} \gg \tau_{1,n}$  [51]. With this approximation equation (2.47) can be further simplified yielding

$$\frac{d\rho_1}{dt} = \rho\sigma(\tilde{\nu}_{Ph})\Psi - \frac{\rho_1}{\tau_1} = \rho\sigma(\tilde{\nu}_{Ph})\Psi_0 (1 + e^{i\omega t}) - \frac{\rho_1}{\tau_1} \quad (2.49)$$

The solution of this differential equation can be written as [52]

$$\rho_1(t) = \frac{\rho\sigma(\tilde{\nu}_{Ph})\tau_{1,n}\Psi_0}{\sqrt{1 + (\omega\tau_{1,n})^2}} \cdot e^{i(\omega t - \phi)} \quad (2.50)$$

in which  $\phi = \arctan(\omega\tau_{1,n})$  represents the phase lag between  $\rho_1$  of the excited state and the photon flux  $\Psi$ . The time-dependent heat production rate per volume  $\dot{H}(t)$  in [ $\text{Js}^{-1}\text{m}^{-3}$ ] is a function of  $\rho_1(t)$  [52]

$$\dot{H}(t) = \rho_1(t) \frac{hc_0 \tilde{\nu}_{Ph}}{\tau_{1,n}} = \dot{H}_0(t) \cdot e^{i(\omega t - \phi)} \quad (2.51)$$

with

$$\dot{H}_0 = \rho\sigma(\tilde{\nu}_{\text{Ph}})I_0 \underbrace{\frac{1}{\sqrt{1 + (\omega\tau_{1,n})^2}}}_{\epsilon_{\text{relax}}} \quad (2.52)$$

and  $I_0$  being the intensity of the light source. The quantity  $\epsilon_{\text{relax}}$  describes the overall efficiency of non-radiative relaxation. In chapters 2.2.2, 4.2, as well as Appendix A.4 the problem with relaxation times for complex relaxational systems, i.e. considering more than two energy states, is further addressed.

### Acoustic wave generation and resonance amplification

The theoretical considerations necessary to derivate a mathematical representation of the photoacoustically generated sound pressure  $p_a$  have been discussed many times in the literature [51–58] and will thus not be addressed in greater detail. Only a brief summary is given in this thesis and the reader is referred to the corresponding literature.

The damped wave equation of the photoacoustic pressure, which considers loss mechanisms induced by the viscosity of the medium, can be written as

$$\Delta p_a(\vec{r}, t) - \frac{1}{c_s^2} \left[ \frac{\delta^2}{\delta t^2} p_a(\vec{r}, t) - \underbrace{\gamma\mu_k \Delta \frac{\delta}{\delta t} p_a(\vec{r}, t)}_{\text{loss}} \right] = - \underbrace{\frac{\gamma - 1}{c_s^2} \frac{\delta}{\delta t} \dot{H}(\vec{r}, t)}_{\text{source}} \quad (2.53)$$

with  $\mu_k$  being the kinematic viscosity and  $\gamma$  the adiabatic exponent of the medium. Due to the loss term, equation (2.53) cannot be solved analytically. Thus, for initial approximations this loss term will be neglected, but later considered again by means of an excess term [52, 59]. Neglecting the loss term the undamped wave equation is described as

$$\Delta p_a(\vec{r}, t) - \frac{1}{c_s^2} \frac{\delta^2}{\delta t^2} p_a(\vec{r}, t) = - \frac{\gamma - 1}{c_s^2} \frac{\delta}{\delta t} \dot{H}(\vec{r}, t) \quad (2.54)$$

Performing a Fourier transform equation (2.54) can be solved [54, 57], resulting in

$$\left( \Delta + \frac{\omega^2}{c_s^2} \right) p_a(\vec{r}, \omega) = \left( \frac{\gamma - 1}{c_s^2} \right) i\omega \dot{H}(\vec{r}, \omega) \quad (2.55)$$

with

$$p_a(\vec{r}, t) = \int_{-\infty}^{\infty} p_a(\vec{r}, \omega) e^{i\omega t} d\omega \quad (2.56)$$

and

$$\dot{H}(\vec{r}, t) = \int_{-\infty}^{\infty} \dot{H}(\vec{r}, \omega) e^{i\omega t} d\omega \quad (2.57)$$

In resonant photoacoustics the generated pressure is amplified by exploiting the resonance condition of the acoustic resonator. There are several types of acoustic resonators, characterized by different geometries. The solution of equation (2.55) strongly depends on the resonator geometry. For a cylindrical resonator the acoustic

pressure  $p_a$  inside the PAC is defined as the sum over all possible acoustic modes  $p_j(\vec{r})$ , including azimuthal, radial and longitudinal, with their respective amplitude  $A_j(\omega)$  [52]

$$p_a(\vec{r}, \omega) = \sum_j A_j(\omega) p_j(\vec{r}) \quad (2.58)$$

The amplitude  $A_j(\omega)$  of the pressure wave inside a both-side open cylindrical resonator with volume  $V_{\text{res}}$  can be calculated via [54, 58]

$$A_j(\omega) = -\frac{i\omega}{\omega_j^2 \left(1 - \frac{\omega^2}{\omega_j^2}\right)} \frac{\gamma - 1}{V_{\text{res}}} \int p_j^*(\vec{r}) \dot{H}(\vec{r}, \omega) dV \quad (2.59)$$

with  $p_j^*(\vec{r})$  representing the complex conjugated normal mode. Since the loss term has been neglected so far, the amplitude of equation (2.59) would approach infinity, when the angular frequency  $\omega$  of the sound wave approaches the resonance frequency, i.e.  $A_j(\omega = \omega_j) \rightarrow \infty$ . Introducing the loss term  $[i\omega(\omega_j Q_j)^{-1}]$ , due to losses from fluid viscosity and heat conduction effects, equation (2.59) may be extend to [54]

$$A_j(\omega) = -\frac{i\omega}{\omega_j^2 \left(1 - \frac{\omega^2}{\omega_j^2} + i\frac{\omega}{\omega_j Q_j}\right)} \frac{\gamma - 1}{V_{\text{res}}} \int p_j^*(\vec{r}) \dot{H}(\vec{r}, \omega) dV \quad (2.60)$$

The quality factor of the  $j^{\text{th}}$  mode  $Q_j$  is a measure for the ratio of accumulated and dissipated energy of a wave during one period of oscillation [31].

$$Q_j = \frac{2\pi \cdot \text{accumulated energy}}{\text{energy lost during one oscillation period}} \quad (2.61)$$

The integral in equation (2.60) is the overlap integral and considers the coupling of the generated pressure mode  $p_j^*(\vec{r})$  and the spatial distribution of heat generation  $H(\vec{r})$ . The relationship between the heat production rate and the laser intensity from equation (2.51), allows to rewrite equation (2.60) [54]

$$A_j(\omega) = -\frac{i\omega}{\omega_j^2 \left(1 - \frac{\omega^2}{\omega_j^2} + i\frac{\omega}{\omega_j Q_j}\right)} \frac{(\gamma - 1) \cdot \rho_A \sigma(\tilde{\nu}_{\text{Ph}})}{V_{\text{res}}} \int p_j^*(\vec{r}) I_0(\vec{r}) dV \quad (2.62)$$

Expressing the light intensity as the product of the optical power  $P_0$  and the normalized spatial distribution function of the beam  $G(\vec{r})$

$$I_0(\vec{r}) = P_0 G(\vec{r}) \quad (2.63)$$

and assuming Gaussian intensity distribution of the laser beam, allows to solve the overlap integral [52]

$$\int p_j^*(\vec{r}) G(\vec{r}) dV = L_{\text{res}} p_j e^{-\mu_j} \quad (2.64)$$

with  $L_{\text{res}}$  being the length of the resonator,  $p_j$  the normalization coefficient and  $\mu_j$  the reciprocal light-to-sound coupling factor of the laser beam with the  $j$  acoustic

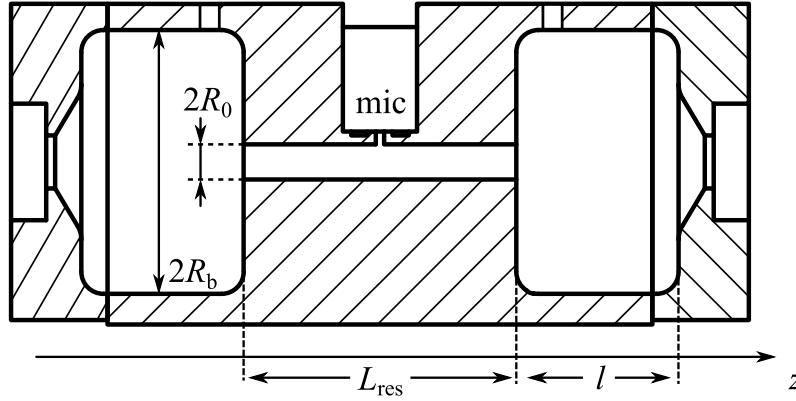


**Fig. 2.7.** Simplified cross-section of a typical *H* – *type* PAC, apated from [58].

mode [57]. Measuring in resonant mode, the amplitude of the PA pressure is defined as

$$A_j(\omega_j) = (\gamma - 1) \frac{Q_j}{\omega_j} \frac{1}{\pi R_0^2} p_j \epsilon_{\text{relax}} \rho_A \sigma(\tilde{\nu}_{\text{Ph}}) P_0 e^{-\mu_j} \quad (2.65)$$

with  $R_0^*$  being the resonator radius and  $\rho_A$  being the volume number density of the analyte. Considering optimal light-to-sound coupling, i.e. 100 % overlap of the illuminated area and the acoustic pressure mode ( $\mu_j = 0$ ), yields  $e^{-\mu_j} = 1$ . Combining equations (2.58) and (2.65) the photoacoustic pressure can be described as

$$p_a(\vec{r}, \omega_j) = (\gamma - 1) \underbrace{\frac{Q_j}{\omega_j} \frac{1}{\pi R_0^2} p_j \epsilon_{\text{relax}} \rho_A \sigma(\tilde{\nu}_{\text{Ph}}) P_0}_{A_j(\omega_j)} p_j(\vec{r}) \quad (2.66)$$

For the first longitudinal mode<sup>†</sup> (100) the pressure varies only in  $z$ -direction and the dimensionless normalization coefficient becomes  $p_{100} = \sqrt{2}$  [52]. The acoustic pressure wave  $p_{100}(\vec{r})$  may be regarded as a sinusoidale half-wave with the maximum located at the middle of the resonator  $p_{100}(\vec{r}_{\text{mic}}) = 1$  [35]. Accordingly, Figure 2.7 shows the cross-section of typical *H* – *type* PAC, with the microphone mounted at  $L_{\text{res}}/2$ .

Summarizing, the photoacoustic pressure for the first longitudinal mode of an open cylindrical resonator under the assumption of perfect light-to-sound coupling can be calculated via equation (2.67) [35, 52, 58].

$$p_a(\vec{r}_{\text{mic}}, \omega_{100}) = (\gamma - 1) \frac{Q_{100}}{\omega_{100}} \frac{1}{\pi R_0^2} \sqrt{2} \epsilon_{\text{relax}} \rho_A \sigma(\tilde{\nu}_{\text{Ph}}) P_0 \quad (2.67)$$

## 2.2.2 Non-radiative relaxation

The photoacoustic pressure is generated by periodic non-radiative relaxation, which means the conversion of vibrational energy into kinetic energy via molecular collisions.

\* $V_{\text{res}} = \pi R_0^2 L_{\text{res}}$

†This resonance mode was exploited in this thesis.

In this chapter the fundamental theory of non-radiative relaxation, as well as molecular collisions are discussed, while the two most relevant processes in photoacoustics, i.e. vibrational - translational transition and the vibrational - vibrational transfer are covered in greater detail. Concluding this section, a review of challenges regarding non-radiative relaxation characteristics for a variety of different analytes is given, which emphasizes the relevance of this topic.

## Molecular collisions

Molecules can gain or release vibrational energy by collisions with surrounding molecules. The theory of molecular collisions is therefore of great importance for understanding vibrational energy transitions. In this section, the theory of collisions is first developed for elastic interaction of inert, hard sphere molecules. The basic concepts derived for this simplified case will be extended in the next step for inelastic collisions between diatomic, vibrating molecules.

### Elastic collisions - inert gas molecules

The interaction of approaching molecules can be approximated by the Lennard-Jones potential [60]

$$V(r) = 4\varepsilon \left[ \underbrace{\left(\frac{\sigma}{r}\right)^{12}}_{\text{repulsive force}} - \underbrace{\left(\frac{\sigma}{r}\right)^6}_{\text{attractive force}} \right] \quad (2.68)$$

in which  $r$  describes the distance of the two molecules,  $\sigma$  the separation for which the potential energy becomes zero  $V(r = \sigma) = 0$  and  $\varepsilon$  the depth of the potential

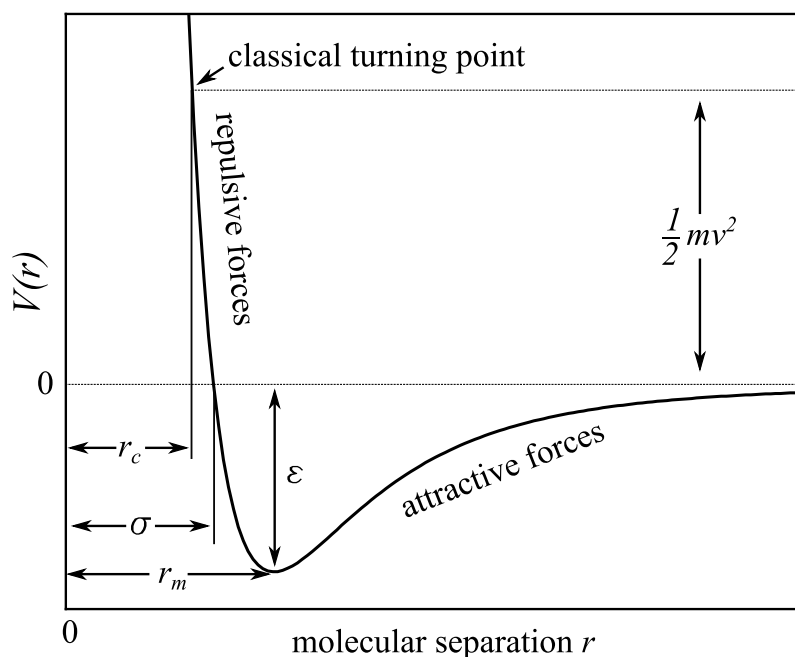
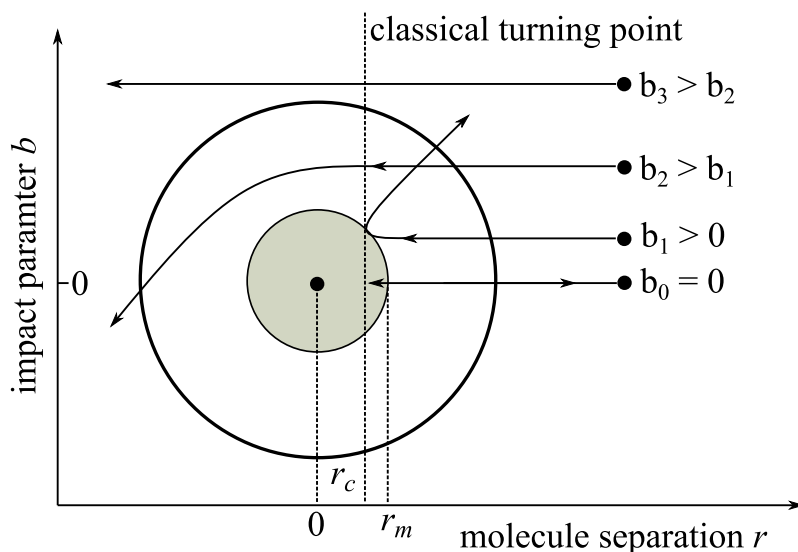


Fig. 2.8. Lennard-Jones potential, apated from [60].



**Fig. 2.9.** Simplified schematic of the trajectories of molecular collisions for different impact parameters  $b_{0-3}$ . Inside the inner, grey highlighted circle with radius  $r_m$  only repulsive forces act. The outer circle marks the distance, where the attractive forces start.

well, i.e. the molecular distance  $r_m$  at maximal attractive forces. The attractive forces consider the long-range interaction of the molecules, while the repulsive forces dominate at short distances and causes a steep increase of  $V(r)$ . For a head-on collision the approaching molecule, with kinetic energy  $\frac{1}{2}mv^2$ , will first accelerate as the attractive forces dominate, until it reaches the minimum of the potential  $V(r) = \varepsilon$ . For smaller distances the dominating repulsive forces cause the molecule to slow down, until it stops at  $r_c$  where  $V(r) = \frac{1}{2}mv^2$ . This marks the so called *classical turning point* from which the molecules begin to move away from each other [61]. A graphical representation of the Lennard-Jones potential is given in Figure 2.8.

Considering, that most collisions are not directly head-on, an impact parameter  $b$  has to be introduced. This impact parameter is defined as the closest distance of the molecular centers for the two approaching molecules [60]. In Figure 2.9 this effect is illustrated. A head-on collision is defined as  $b_0 = 0$ . In elastic collisions, the partners can exchange translational energy among each other. However, for an energy exchange to occur the condition  $b < r_m$  must be fulfilled, as for collisions with  $b > r_m$  (e.g.  $b_2$  in Figure 2.9), only attractive forces operate. The collision rate, i.e. the energy transfer rate whilst collision, finally results from kinetic gas theory, see equation (2.25).

## Vibration to translation (VT) energy transfer

### Inelastic collisions - diatomic molecules

Regarding vibrational energy transfer this hard sphere model must be extended. Assuming a collinear collision of molecule  $\mathbf{AB}$  with the vibrating molecule  $\mathbf{A}^*\mathbf{B}^*$ , which will be considered as a harmonic oscillator. In this case  $r$  is the separation of the respective center of mass of  $\mathbf{A}^*\mathbf{B}^*$  and  $\mathbf{AB}$ . The vibrational amplitude of  $\mathbf{A}^*\mathbf{B}^*$ , around its equilibrium distance  $d_0$  of  $\mathbf{A}^*$  and  $\mathbf{B}^*$ , will be denominated as  $\zeta$ . Since a collinear collision is assumed, the impact occurs only at  $\mathbf{B}^*$  and  $\mathbf{A}$ , see Figure 2.10. The time-dependend distance  $d$  of  $\mathbf{B}^*$  and  $\mathbf{A}$  is given by

$$d = r - d_0 - \zeta \quad (2.69)$$

The vibration of  $\mathbf{A}^*\mathbf{B}^*$  results in a time-dependend, periodic perturbation of  $V(r)$ , induced by the periodic vibrational amplitude  $\zeta$  [60]. According to Ehrenfest's adiabatic principle, an energy exchange, in this case a vibrational - translational transfer, can only take place if the changes of the force are large within a period of vibration [62, 63]. This implies that the vibrational period  $t_\nu$  of  $\mathbf{A}^*\mathbf{B}^*$  must be longer then the collision duration  $\tau_c^*$  for a vibrational - translational energy transfer to happen [60, 64]. The collision duration  $\tau_c$  can be assumed as the range  $s$  of the intermolecular forces for the mean relative velocity  $\bar{v}_{\text{rel}}$  of the colliding molecules.

$$\tau_c = \frac{s}{\bar{v}_{\text{rel}}} \quad (2.70)$$

The vibrational period of  $\mathbf{A}^*\mathbf{B}^*$  can be calculated by

$$t_\nu = \frac{1}{\nu_{\text{AB}}} = \frac{1}{c_0 \tilde{\nu}_{\text{AB}}} \quad (2.71)$$

For an energy transfer to happen the criterion  $\tau_c < t_\nu$  thus must be met.

Using equation (2.22) this condition can be rewritten to become [60]

$$\sqrt{\frac{8k_{\text{B}}T \cdot (m_{\text{AB}} + m_{\text{AB}})}{\pi \cdot m_{\text{AB}} \cdot m_{\text{AB}}}} > s \cdot \nu_{\text{AB}} \quad (2.72)$$

$\underbrace{\hspace{10em}}_{\bar{v}_{\text{rel}}}$

Equation (2.72) is satisfied for higher temperatures, low-weight collision partners, and low vibrational frequencies, but also for steeper intermolecular potentials, which correspond to smaller values of  $s$  [60]. Taking the example of traces of  $\text{CH}_4$  diluted in  $\text{N}_2$ , the relative mean velocity can be calculated to 806.7 m/s for a temperature of 40 °C. To satisfy the condition of equation (2.72) for VT relaxation of the excited methane vibrational mode at  $2968.4 \text{ cm}^{-1}$  with a vibrational period of  $1.12 \cdot 10^{-14} \text{ s}$  according to equation (2.71) the distance in the repulsive field for the approaching molecule must be less than 0.09 Å. For a lower vibrational energy of  $1000 \text{ cm}^{-1}$ , the maximum distance  $s$  increases to 0.27 Å, which corresponds to a higher VT probability per collision.

---

\* $\tau_c$  must not be mistaken for the average time between molecular collisions  $\tau_{\text{col}}$ , see equation (2.25).

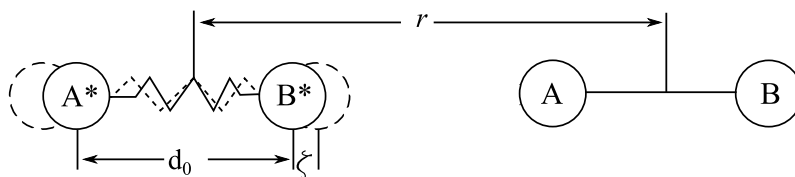


**Fig. 2.10.** Schematic of a collinear collision between a vibrating  $A^*B^*$  and a non-vibrating molecule  $AB$ . The collision impact occurs only at  $B^*$  and  $A$ .

### Landau-Teller theory

The fundamental theory of vibrational energy transfer was developed by Landau and Teller in 1936 [65]. Their model neglected the attractive forces of  $V(r)$ , as they assumed, that the energy transfer probability is only influenced by the steep repulsive part [60]. Using an exponential decay function  $V(r) = V_0 \exp(-\alpha \cdot r)$ , with  $\alpha$  being the steepness, to model the repulsive forces and exploiting classical time-dependent perturbation theory, the average probability of vibrational deactivation per collision as a function of temperature becomes [60]

$$P_{10} = \exp \left[ -3 \left( \frac{2\pi^4 \mu_{AB} \nu_{AB}^2}{\alpha^2 k_B T} \right)^{\frac{1}{3}} \right] \quad (2.73)$$

Generally speaking, the reciprocal average probability gives the average necessary collisions  $Z_{10} = P_{10}^{-1}$  required for the relaxation of a vibrational state. With this relation and considering equation (2.25) for the collision rate  $Z$  of the gas mixture, the relaxation time\*  $\tau_\nu$  for a certain vibrational mode  $\nu$  can be obtained, see equation (2.74).

$$\tau_\nu = \frac{Z_{10}}{Z} = \frac{1}{P_{10} \cdot Z} \quad (2.74)$$

### SSH theory

Schwartz, Slawsky and Herzfeld (SSH) provided an extension to the Landau-Teller theory [66, 67], which was further developed by Tanczos for polyatomic molecules [68]. The intermolecular potential in SSH theory differs from the exponential decay potential used in Landau-Teller theory

$$V(r) = U \exp(-\alpha \cdot r) - \varepsilon \quad (2.75)$$

The expression  $\exp(-\alpha \cdot r)$  still represents the repulsive forces and the attractive forces are no longer neglected, but considered with  $-\varepsilon$  [60]. Considering a molecular collision, in which one molecule shows a vibrational mode ( $\nu_a$ ) and the colliding partner shows a vibrational mode ( $\nu_b$ ). Both ( $\nu_a$ ) and ( $\nu_b$ ) can exist in different quantum states. The probability, that during the collision event ( $\nu_a$ ) changes its

\*Sometimes referred to as the lifetime.

quantum state from  $i$  to  $j$ , while  $(\nu_b)$  simultaneously changes its state from  $k$  to  $l$  can be obtained from SSH theory

$$P_{k \rightarrow l(\nu_b)}^{i \rightarrow j(\nu_a)} = S_0(\nu_a)S_0(\nu_b)[V^{ij}(\nu_a)]^2[V^{kl}(\nu_b)]^2 \cdot \left(\frac{4\mu}{k_B T}\right) \exp\left[\frac{-\epsilon}{k_B T}\right] \left(\frac{8\pi^3 \mu \Delta E}{h^2}\right)^2 \int_0^\infty f(\bar{u})d\bar{u} \quad (2.76)$$

in which

$$f(\bar{u}) = \frac{\bar{u}}{\alpha^4} \left(\frac{r_c}{\sigma}\right)^2 \exp\left[-\frac{\mu \bar{u}^2}{2k_B T}\right] \left\{ \frac{\exp[L - L']}{(1 - \exp[L - L'])^2} \right\} \quad (2.77)$$

and

$$L = \frac{4\pi^2 \mu}{\alpha} \bar{u} \quad (2.78)$$

$$L' = \frac{4\pi^2 \mu}{\alpha} \bar{v} \quad (2.79)$$

For superelastic collisions\* vibrational-translational (VT) energy exchange can occur, resulting in different relative velocities of the colliding molecules, with reduced mass  $\mu$ , before ( $\bar{u}$ ) and after ( $\bar{v}$ ) the collision. The energy difference  $\Delta E$  exchanged for any VT transition, while  $(\nu_b)$  remains in its original quantum state ( $k = l$ ), is given by

$$\Delta E = h\nu_a(i - j) = \frac{1}{2}\mu(\bar{v}^2 - \bar{u}^2) \quad (2.80)$$

The *vibrational factors*  $[V^{ij}(\nu_a)]^2$  and  $[V^{kl}(\nu_b)]^2$  in equation (2.76) consider the coupling of the initial and final quantum states of the perturbed oscillator, induced by the collision [60]. If no change in quantum state occurs, then vibrational factors are defined as unity. For changes in the quantum state of the vibration,  $[V^{ij}]^2$  becomes a function of the repulsive parameter  $\alpha$  of the potential, amplitude of the vibration ( $\bar{A}^2$ ), as well as its vibrational frequency  $\nu$ .

$$[V^{i \rightarrow i \pm 1}]^2 = \alpha^2 (\bar{A}^2) \frac{(i + 1)h}{8\pi^2 \nu} \quad (2.81)$$

For multiple quantum jumps, i.e. ( $i \rightarrow j \pm n$ ) with  $n \geq 2$  the vibrational factor decrease, thus a single quantum transition will always be the preferred process [60].

Real molecules, unlike idealized rigid spheres, are not necessarily spatially symmetric. This results in spatial orientations of the collision partners, for which an energy transfer is more efficient than for others. The *steric factor*  $S_0$  takes this effect into account. For diatomic molecules, as well as for longitudinal vibrations of linear molecules,  $S_0 = 1/3$  is applied. Non-linear molecules and bending modes are considered by  $S_0 = 2/3$  [60].

---

\*In superelastic collisions the internal (vibrational) energy is converted into kinetic energy.

Transitions which involve energy differences  $\Delta E > 200 \text{ cm}^{-1}$  the standard SSH theory must be slightly adapted to yield the Tanczos equation [68].

$$P_{k \rightarrow l(\nu_b)}^{i \rightarrow j(\nu_a)} = S_0(\nu_a)S_0(\nu_b) \left(\frac{r_c^*}{\sigma}\right)^2 [V^{ij}(\nu_a)]^2 [V^{kl}(\nu_b)]^2 8 \left(\frac{\pi}{3}\right)^{1/2} \cdot \left[\frac{8\pi^3 \mu \Delta E}{\alpha^{*2} h^2}\right] X^{1/2} \exp\left[-3X + \frac{\Delta E}{2k_B T} - \frac{\epsilon}{k_B T}\right] \quad (2.82)$$

with

$$X = \frac{\mu u^{*2}}{2k_B T} = \left(\frac{\Delta E^2 \mu \pi^2}{2\alpha^{*2} h^2 k_B T}\right)^{1/3} \quad (2.83)$$

As molecule velocities show Boltzmann distribution some approaching molecules show less probable vibrational energy transition, while others provide a greater transition probability [60]. The velocity showing the most effective vibrational energy transition is denoted as  $u^*$ . The *collisional cross-reference factor*  $(r_c^*/\sigma)^2$  in equation (2.82) is the ratio of the distance of closest approach  $r_c^*$  to the separation  $\sigma$  at  $V(r) = 0$  for  $u^*$ , see Figure 2.8 [68]. The intermolecular repulsive force constant  $\alpha^*$  also refers to  $u^*$ .

For polar molecules the SSH theory predicts lower transition probabilities, as the attractive potential of the approaching molecules is still inadequately assumed, see equation (2.75). To account for this discrepancy Shin introduced a Morse potential to substitute equation (2.75) [69]. Two further limitations of the present theory, which will only be briefly mentioned but not further discussed, is neglecting that molecules can possess several individual vibrational modes, which can relax independently from each other and neglecting the fact, that molecules change their shape during vibration.

### Vibration to vibration (VV) energy transfer

Compared to VT transitions in which the colliding partner remains in its initial quantum state, i.e.  $k = l$ , in VV transitions both molecules change their state, i.e.  $i \neq j$  and  $k \neq l$ . The exchanged energy for any VV transition is given by

$$\Delta E = h\nu_a(i - j) + h\nu_b(k - l) \quad (2.84)$$

If the vibrational energy after the collision is larger than prior to the collision, i.e.  $\Delta E > 0$  the surplus energy is withdrawn from the environment. As this effect causes the kinetic energy of the gas to decrease, this effect is called kinetic cooling [70, 71]. For the opposite scenario  $\Delta E < 0$ , the energy difference of the VV transition is released into the environment. Both scenarios are illustrated in Figure 2.11. It is important to note that both effects generate a photoacoustic signal, however, phase-shifted by  $180^\circ$ .

For resonant transitions  $\Delta E$  becomes zero, since the energy released by one collision partner is exactly equal to the energy absorbed by the other, i.e.  $h\nu_a(i - j) = h\nu_b(k - l)$ .

Resonant and near-resonant ( $|\Delta E| \leq 50 \text{ cm}^{-1}$ ) transfers are much faster, compared to processes involving a large energy gap and thus more likely [60].

While non-resonant VV transition probabilities can be calculated by equation (2.82) involving  $\Delta E$  from equation (2.84), the transition probability for resonant, or near-resonant transitions is slightly different compared to equation (2.82) [60, 68].

$$P_{k \rightarrow l(\nu_b)}^{i \rightarrow j(\nu_a)} = S_0(\nu_a)S_0(\nu_b)[V^{ij}(\nu_a)]^2[V^{kl}(\nu_b)]^2 \frac{64\pi^2 \mu k_B T}{\alpha^2 h^2} \exp\left[\frac{\epsilon}{k_B T}\right] \quad (2.85)$$

Figure 2.12 presents the VV probability for a simplified case, when the vibrating molecule  $\mathbf{A}^*\mathbf{B}^*$  collides with another molecule  $\mathbf{CD}$  in its vibrational ground state [72]. The highlighted grey areas (a) and (b) illustrate the collision event, in which the vibrational energy of  $\mathbf{A}^*\mathbf{B}^*$  ( $\nu_a$ ) (a) is transferred to  $\mathbf{C}^*\mathbf{D}^*$  ( $\nu_b$ ) (b). The energy difference  $\Delta E$ , see equation (2.84), is released into the surrounding environment. As expected, the transition probability exhibits a maximum for resonant or near-resonant transitions (highlighted grey area in the graph on the right side of Figure 2.12) and decreases with increasing  $\Delta E$ . Additionally, an increase of the gas temperature results in a higher transition probability.

### Non-radiative relaxation in photoacoustic spectroscopy

To emphasize the relevance of this issue in photoacoustic spectroscopy the following chapter provides an overview of non-relaxational effects for different analytes. The influence of the non-radiative relaxation behaviour on the photoacoustic signal is discussed in detail in chapter 4.2.

#### Carbon dioxide - $\text{CO}_2$

Carbon dioxide ( $\text{CO}_2$ ) is the most contributing greenhouse gas and thus an interesting analyte for photoacoustic sensors. In order to measure  $\text{CO}_2$  in the atmosphere the effect of variations in ambient humidity on the photoacoustic signal has to be

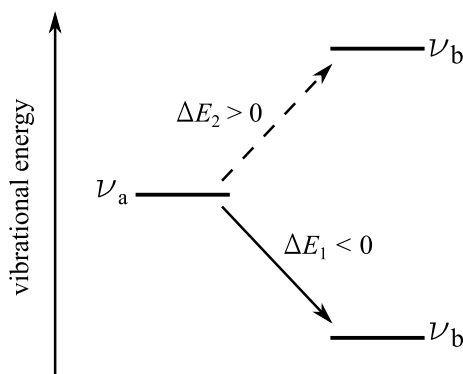


**Fig. 2.11.** VV transitions from  $\nu_a$  to  $\nu_b$  resulting in heating of the surrounding  $\Delta E_1$  and kinetic cooling  $\Delta E_2$ .

considered. In 2006 Wysocki et al. investigated this effect regarding  $\text{CO}_2$  detection at  $\lambda = 2 \mu\text{m}$  ( $5000 \text{ cm}^{-1}$ ) exploiting QEPAS ( $f = 32762 \text{ Hz}$ ) [73]. Compared to low  $\text{H}_2\text{O}$  concentrations ( $< 0.1 \text{ \%V}$ ), a sharp, exponential increase of the photoacoustic amplitude with rising humidity was measured. At about  $1.7 \text{ \%V}$ , the amplitude approached an amplification of about factor 6.7. This amplitude increase was accompanied by a pronounced phase shift of approximately  $60^\circ$ . In dry, or only very slightly humidified, conditions the relaxations process of  $\text{CO}_2$ ,  $\text{N}_2$  mixtures is dominated by the slow VT relaxation of  $\text{CO}_2$  to the ground state, as well as the fast VV energy exchange of  $\text{CO}_2$  with  $\text{N}_2$  at  $5000 \text{ cm}^{-1}$  with subsequent slow VT relaxation of  $\text{N}_2$ . For the rather high modulation frequency of  $32762 \text{ Hz}$ , this yields significant relaxational losses, i.e.  $\epsilon_{\text{relax}} < 1$ . By adding water the fast VV transfer from  $\text{CO}_2$ , as well as from  $\text{N}_2$  to  $\text{H}_2\text{O}$  at around  $5000 \text{ cm}^{-1}$  provides a fast relaxation path, increasing  $\epsilon_{\text{relax}}$  and thus the measured amplitude. Liu et al. supported these findings in 2022 [74]. With a significantly lower modulation frequency  $f = 28000 \text{ Hz}$  they measured a signal increase of about  $22.8 \text{ \%}$ , when increasing the humidity from  $0.27 \text{ \%V}$  to  $0.92 \text{ \%V}$ .

### Nitrogen dioxide - $\text{NO}_2$

Regarding ambient  $\text{NO}_2$  detection, relaxation cross-sensitivities towards oxygen and water are reported in literature [75–77]. Exciting  $\text{NO}_2$  at around  $445 \text{ nm}$  ( $22472 \text{ cm}^{-1}$ ) in a dry  $\text{N}_2$  mixture and increasing the oxygen concentration an amplitude drop of

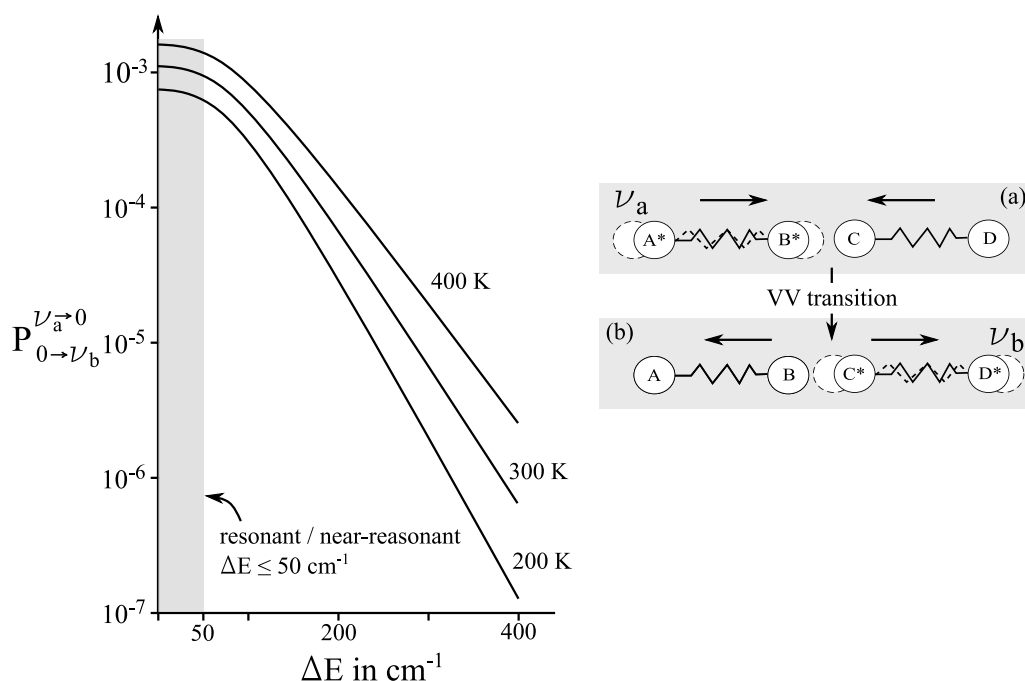


**Fig. 2.12.** Estimated VV probability of a collision between **AB** and **CD** as a function of  $\Delta E$  for a energy transition from  $\nu_a$  to  $\nu_b$  after [72]. The grey highlighted area on the right side (a) represents the approaching molecules before the collision, while (b) illustrates the departing molecules after the collision.

20 % for 20 %V O<sub>2</sub> at  $f \approx 5000$  Hz was measured. For higher O<sub>2</sub> concentrations the signal loss approached 25 % [77]. These results show good agreement with the reported 16 % relaxational loss at 20 %V O<sub>2</sub> for  $f_{\text{mod}} = 1688$  Hz by Kalkman et al. [75]. Both assumed a fast VT relaxation of NO<sub>2</sub> down to  $4\tilde{\nu}_{3,\text{NO}_2} = 6447$  cm<sup>-1</sup>, which contributes to the photoacoustic signal. As this energy state is close to the fourth harmonic of the oxygen vibrational state ( $4\tilde{\nu}_{\text{O}_2} = 6081$  cm<sup>-1</sup>) a fast VV energy exchange between NO<sub>2</sub> and O<sub>2</sub> is very likely to happen. Due to the rather slow relaxation characteristic of oxygen the vibrational energy accumulates in  $4\tilde{\nu}_{\text{O}_2}$ , i.e. being essentially lost regarding photoacoustic signal generation. Similar to the results for CO<sub>2</sub>, water also shows an accelerating effect on relaxation for NO<sub>2</sub>. For slow modulation frequencies, e.g.  $f = 1752$  Hz, already 0.3 %V H<sub>2</sub>O is sufficient to compensate for the relaxational loss caused by 20 %V O<sub>2</sub> [76]. With modulation frequencies in the range of 5000 Hz, about 1 %V humidity is required to approach complete relaxation [77].

### Carbon monoxide - CO

In the spectral region from 2060 - 2250 cm<sup>-1</sup> as well as from 6250 - 6410 cm<sup>-1</sup> carbon monoxide CO shows distinct absorption peaks, suitable for photoacoustic detection. At 2180 cm<sup>-1</sup> Hayden et al. and Sgobba et al. investigated the influence of water on photoacoustic CO detection. Both groups exploited a QEPAS sensor with a modulation frequency of 12.46 kHz [78, 79]. Their findings were explained by the following relaxation characteristics. In dry CO, N<sub>2</sub> mixtures the electromagnetically excited CO shows a fast intramolecular VV transition from 2180 cm<sup>-1</sup> to 2143 cm<sup>-1</sup>. From this state a rapid VV energy transfer to the N<sub>2</sub> vibrational state  $\tilde{\nu}_{\text{N}_2} = 2331$  cm<sup>-1</sup> occurs. As nitrogen is known for its slow relaxation properties, only the energy difference between the two states  $\Delta E_{\text{CO},\text{N}_2} = 188$  cm<sup>-1</sup> is converted into a photoacoustic signal. When adding water to the CO, N<sub>2</sub> mixture the photoacoustic amplitude decreases until reaching a minimum at approximately 0.19 %V of humidity and then starts to rise again. This effect can be attributed to two possible VV transitions from CO ( $\tilde{\nu}_{\text{CO}} = 2143$  cm<sup>-1</sup>) and N<sub>2</sub> ( $\tilde{\nu}_{\text{N}_2} = 2331$  cm<sup>-1</sup>), respectively, to water ( $\tilde{\nu}_{\text{H}_2\text{O}} = 1595$  cm<sup>-1</sup>). For both VV transitions the released energies, i.e.  $\Delta E_{\text{CO},\text{H}_2\text{O}} = -548$  cm<sup>-1</sup> and  $\Delta E_{\text{N}_2,\text{H}_2\text{O}} = -736$  cm<sup>-1</sup>, show an opposite sign compared to the VV transition from CO to N<sub>2</sub> ( $\Delta E_{\text{CO},\text{N}_2}$ ). At the turning point of the amplitude the VV transitions to H<sub>2</sub>O begin to dominate, resulting in a rising amplitude and a phase shift of the PA signal of 180 °. From there on the accelerating effect of H<sub>2</sub>O is observed, with a signal amplification of about factor 6 for 2 %V H<sub>2</sub>O compared to the dry nitrogen mixtures. Investigating the water influence for CO excitation at 6388 cm<sup>-1</sup> provides a different picture [80]. With rising water the photoacoustic amplitude rises in a linear manner, due to the accelerating effects of water, as no VV transition from CO to N<sub>2</sub> occurs. For the used QEPAS modul ( $f = 32755$  Hz) the signal was increased by a factor of 4 at 1.6 %V H<sub>2</sub>O compared to the dry mixture. Qiao et al. investigated the effect of SF<sub>6</sub>, another well known relaxation promoter, on CO detection at 6378 cm<sup>-1</sup>, using a microphone based sensor with resonance frequency of around 3000 Hz [81]. Without giving any details on the underlying

energy transitions of the relaxation processes they observed a signal increase of factor 2 for SF<sub>6</sub> concentration  $\geq 2$  %V.

### Nitric oxide - NO

Nitric oxide (NO) shows the strongest absorption at around 1900 cm<sup>-1</sup>. Using a QCL emitting at 5.26 μm (1901 cm<sup>-1</sup>) Dong et al. as well as Wu et al. developed photoacoustic NO sensors for environmental monitoring [82, 83]. Dong et al. used a QEPAS sensor operating at  $f = 32768$  Hz, while Wu et al. applied much lower modulation frequencies at around 1779 Hz for their microphone based sensor. Both measured the same qualitative characteristic when humidifying dry NO samples diluted in air. The PA amplitude increased exponentially with rising water due to the strongly accelerated VT relaxation of NO with H<sub>2</sub>O. For the microphone based sensor the amplitude reached a plateau at around 1.6 %V yielding a signal increase of factor 1.6 compared to the dry amplitude. This enhancement however was approximately 81 times weaker, than the measured data from [82]. For a rather low pressure of 280 mbar (210 Torr) inside the QEPAS sensor, Dong et al. reported an 130-fold signal increase for 2.5 %V H<sub>2</sub>O, which they approximated to rise until 146 and approach complete relaxation for a humidity of 5 %V. This significant discrepancy in the reported values can be linked to the much lower modulation frequency of [83] as well as the much lower applied pressure of [82], which result in initially major relaxational losses. The effect of reduced pressure on the relaxation efficiency is also addressed in chapter 4.3.

### Hydrogen chloride - HCl

Besson et al. developed a microphone based PA sensor with a resonance frequency of around 1000 Hz for gaseous HCl detection for the optical fibre manufacturing process, exploiting the absorption at  $2\tilde{\nu}_{\text{HCl}} = 5747$  cm<sup>-1</sup> [84, 85]. They investigated HCl diluted in pure helium (He) and added N<sub>2</sub> as well as O<sub>2</sub> to the mixture. The measured effects on the PA amplitude for N<sub>2</sub> and O<sub>2</sub> addition differed significantly. With increasing N<sub>2</sub>, the amplitude drops exponentially to about 50 % for 10 %V N<sub>2</sub> and to about 25 % of the initial value for 90 %V N<sub>2</sub>. The first step in the relaxation process is the relaxation from  $2\tilde{\nu}_{\text{HCl}}$  down to  $\tilde{\nu}_{\text{HCl}} = 2886$  cm<sup>-1</sup>. With both He as well as N<sub>2</sub> as collision partners this process is not fast enough to be fully completed within one periode of laser modulation, yielding relaxational losses. Proceeding from  $\tilde{\nu}_{\text{HCl}}$ , a fast VV transition to  $\tilde{\nu}_{\text{N}_2} = 2331$  cm<sup>-1</sup> occurs, according to [84]. Subsequent VT relaxation from N<sub>2</sub>, however, is very unlikely, which leads to further losses in terms of generated photoacoustic energy. A completely different result is obtained with the addition of O<sub>2</sub>. Up to about 30 %V O<sub>2</sub>, the amplitude increases by approximately 60 % and thereafter decreases continuously. The signal increase can be attributed to the accelerated process of  $2\tilde{\nu}_{\text{HCl}} \rightarrow \tilde{\nu}_{\text{HCl}}$  with O<sub>2</sub> as a collision partner, compared to He. Similar to N<sub>2</sub>, a fast VV transition from  $\tilde{\nu}_{\text{HCl}}$  to  $\tilde{\nu}_{\text{O}_2} = 1556$  cm<sup>-1</sup> occurs. The excited O<sub>2</sub> shows rather slow VT relaxation, which is however accelerated by collisions with He. Increasing the O<sub>2</sub> (> 30%V) concentration reduces the He content in the mixture, resulting in less VT relaxation from O<sub>2</sub>, i.e. less photoacoustic signal.

### Hydrogen sulfide - H<sub>2</sub>S

Using a QEPAS modul (ADM01, Thorlabs, Germany) with  $f = 12458$  Hz the relaxation characteristics of H<sub>2</sub>S regarding CH<sub>4</sub> and H<sub>2</sub>O were investigated by Olivieri et al. [86]. The absorption feature selected for H<sub>2</sub>S was located at  $3846\text{ cm}^{-1}$  exciting the vibrational triad consisting of the bending mode  $3\tilde{\nu}_{2,\text{H}_2\text{S}}$  and the two combination modes  $(\tilde{\nu}_{1,\text{H}_2\text{S}} + \tilde{\nu}_{2,\text{H}_2\text{S}})$  and  $(\tilde{\nu}_{2,\text{H}_2\text{S}} + \tilde{\nu}_{3,\text{H}_2\text{S}})$ . When adding CH<sub>4</sub> to a H<sub>2</sub>S, N<sub>2</sub> mixture an exponential signal drop of approximately 67 % for 5 %V of methane could be measured. The amplitude loss was attributed to a fast VV transfer from  $\tilde{\nu}_{2,\text{H}_2\text{S}}$  at  $1183\text{ cm}^{-1}$  to the  $\tilde{\nu}_{4,\text{CH}_4}$  bending mode at  $1306\text{ cm}^{-1}$ . As the subsequent VT relaxation of  $\tilde{\nu}_{4,\text{CH}_4}$  in dry N<sub>2</sub> mixtures is rather slow for higher modulation frequencies this VV transfer yields a relaxation induced signal loss. The applied Jablonsky diagram of [86] shows, that H<sub>2</sub>S and CH<sub>4</sub> exhibit similar vibrational modes at higher vibrational energies, i.e.  $2\tilde{\nu}_{4,\text{CH}_4} = 2612\text{ cm}^{-1}$ ,  $2\tilde{\nu}_{2,\text{H}_2\text{S}} = 2366\text{ cm}^{-1}$ ,  $\tilde{\nu}_{1,\text{H}_2\text{S}} = 2615\text{ cm}^{-1}$  and  $\tilde{\nu}_{1,\text{H}_2\text{S}} = 2626\text{ cm}^{-1}$ . Consequently, a VV transfer might also occur in this region. Comparing the amplitude for H<sub>2</sub>S diluted in N<sub>2</sub> with a mixture containing 20 %V O<sub>2</sub> and 1 %V H<sub>2</sub>O showed no difference, concluding no influence on the relaxational behaviour.

### Sulphur dioxide - SO<sub>2</sub>

The relaxation behavior of SO<sub>2</sub> resembles the previously presented results. Using a QEPAS sensor ( $f = 32768$  Hz), SO<sub>2</sub> was excited at  $1381\text{ cm}^{-1}$  and the N<sub>2</sub> measurement matrix was humidified [87]. With increasing water content, an exponential, albeit comparatively flat, increase in amplitude was measured for this analyte as well. The increase appeared to approach a plateau at higher humidities ( $>2\text{ %V}$ ), yielding a maximum amplification of factor 3.13 for a pressure of 175 mbar compared to the dry mixture. Once again, the reason behind this phenomenon is incomplete relaxation of SO<sub>2</sub> with only N<sub>2</sub> as a collision partner at low pressures for the fast modulation of QEPAS sensors. This loss is fully compensated by higher water concentrations, which accelerate the relaxation process.

### Further analytes

Literature provides much information regarding relaxation effects in photoacoustics for further analytes, e.g. ethylene (C<sub>2</sub>H<sub>4</sub>) [88], carbon disulfide (CS<sub>2</sub>) [89] and ozone (O<sub>3</sub>) [90, 91]. Another well known analyte prone towards relaxational effects is methane (CH<sub>4</sub>), which will be discussed in great detail in this work, see chapter 4.2 and 4.3.

Summarizing this section, for many applications of photoacoustic gas sensors the effect of non-radiative relaxation has to be considered. Since this effect is difficult to predict and usually non-linear, compensating for the influence on the photoacoustic signal is challenging. Calibration characteristics do not apply over a wide frequency range, i.e. the relaxational influence on QEPAS ( $f = 32768$  Hz) applications might not be the same for microphone-based sensors operating at much lower frequencies ( $< 10000$  Hz). Chapter 4.2 of this thesis introduces a novel approach for this problem,

which has proven to be applicable for different modulation frequencies and sensor designs, see chapter 4.5.

## References

- [1] A. G. Bell. “On the production and reproduction of sound by light”. In: *Am. J. Sci.* s3-20.118 (Oct. 1880), pp. 305–324. ISSN: 0002-9599. DOI: 10.2475/ajs.s3-20.118.305 (cit. on p. 27).
- [2] T. Rück. “Development, characterization and miniaturization of a trace gas detection system for NO<sub>2</sub> in air based on photoacoustic spectroscopy”. Ph. D. thesis. University of Regensburg, 2017 (cit. on p. 27).
- [3] M. Navas et al. “Human biomarkers in breath by photoacoustic spectroscopy”. In: *Clin. Chim. Acta* 413.15-16 (Aug. 2012), pp. 1171–1178. ISSN: 00098981. DOI: 10.1016/j.cca.2012.04.008 (cit. on p. 27).
- [4] T. Hibbard and A. J. Killard. “Breath ammonia levels in a normal human population study as determined by photoacoustic laser spectroscopy”. In: *J. Breath Res.* 5.3 (Sept. 2011), p. 037101. ISSN: 1752-7155. DOI: 10.1088/1752-7155/5/3/037101 (cit. on p. 27).
- [5] J. Pangerl et al. “A sub-ppbv-level Acetone and Ethanol Quantum Cascade Laser Based Photoacoustic Sensor – Characterization and Multi-Component Spectra Recording in Synthetic Breath”. In: *Photoacoustics* 30 (Apr. 2023), p. 100473. ISSN: 22135979. DOI: 10.1016/j.pacs.2023.100473 (cit. on p. 27).
- [6] N. Maurin et al. “First clinical evaluation of a quartz enhanced photo-acoustic CO sensor for human breath analysis”. In: *Sensors Actuators B Chem.* 319 (Sept. 2020), p. 128247. ISSN: 09254005. DOI: 10.1016/j.snb.2020.128247 (cit. on p. 27).
- [7] F. Sgobba et al. “Compact and portable quartz-enhanced photoacoustic spectroscopy sensor for carbon monoxide environmental monitoring in urban areas”. In: *Photoacoustics* 25 (Mar. 2022), p. 100318. ISSN: 22135979. DOI: 10.1016/j.pacs.2021.100318 (cit. on p. 27).
- [8] Y. Pan et al. “Compact and Highly Sensitive NO<sub>2</sub> Photoacoustic Sensor for Environmental Monitoring”. In: *Molecules* 25.5 (Mar. 2020), p. 1201. ISSN: 1420-3049. DOI: 10.3390/molecules25051201 (cit. on p. 27).
- [9] S. Schilt et al. “Ammonia monitoring at trace level using photoacoustic spectroscopy in industrial and environmental applications”. In: *Spectrochim. Acta Part A Mol. Biomol. Spectrosc.* 60.14 (Dec. 2004), pp. 3259–3268. ISSN: 13861425. DOI: 10.1016/j.saa.2003.11.032 (cit. on p. 27).
- [10] T. Rück et al. “Digital Twin of a photoacoustic trace gas sensor for monitoring methane in complex gas compositions”. In: *Sensors Actuators B Chem.* 378 (Mar. 2023), p. 133119. ISSN: 09254005. DOI: 10.1016/j.snb.2022.133119 (cit. on p. 27).

- [11] A. Loh and M. Wolff. “Multivariate Analysis of Photoacoustic Spectra for the Detection of Short-Chained Hydrocarbon Isotopologues”. In: *Molecules* 25.9 (May 2020), p. 2266. ISSN: 1420-3049. DOI: 10.3390/molecules25092266 (cit. on p. 27).
- [12] V. Spagnolo et al. “Modulation cancellation method for isotope  $^{18}\text{O}/^{16}\text{O}$  ratio measurements in water”. In: *Opt. Express* 20.4 (Feb. 2012), p. 3401. ISSN: 1094-4087. DOI: 10.1364/OE.20.003401 (cit. on p. 27).
- [13] T. Mikkonen et al. “Detection of gaseous nerve agent simulants with broadband photoacoustic spectroscopy”. In: *J. Hazard. Mater.* 440 (Oct. 2022), p. 129851. ISSN: 03043894. DOI: 10.1016/j.jhazmat.2022.129851 (cit. on p. 27).
- [14] C. K. Patel. “Laser photoacoustic spectroscopy helps fight terrorism: High sensitivity detection of chemical Warfare Agent and explosives”. In: *Eur. Phys. J. Spec. Top.* 153.1 (Jan. 2008), pp. 1–18. ISSN: 1951-6355. DOI: 10.1140/epjst/e2008-00383-x (cit. on p. 27).
- [15] Y. H. El-Sharkawy et al. “Instantaneous identification of hazardous explosive-related materials using laser induced photoacoustic spectroscopy”. In: *TrAC Trends Anal. Chem.* 106 (Sept. 2018), pp. 151–158. ISSN: 01659936. DOI: 10.1016/j.trac.2018.07.007 (cit. on p. 27).
- [16] J. Karhu et al. “LED-Based Photoacoustic  $\text{NO}_2$  Sensor with a Sub-ppb Detection Limit”. In: *ACS Sensors* 6.9 (Sept. 2021), pp. 3303–3307. ISSN: 2379-3694. DOI: 10.1021/acssensors.1c01073 (cit. on p. 27).
- [17] F. Ma et al. “Detection of trace  $\text{C}_2\text{H}_2$  in  $\text{N}_2$  buffer gas with cantilever-enhanced photoacoustic spectrometer”. In: *Optik (Stuttg.)* 232 (Apr. 2021), p. 166525. ISSN: 00304026. DOI: 10.1016/j.ijleo.2021.166525 (cit. on p. 27).
- [18] H. Lhermet et al. “Micro-Photoacoustic Cell with Integrated Microphone for Sub-Ppm Gas Sensing”. In: *2019 20th Int. Conf. Solid-State Sensors, Actuators Microsystems Eurosensors XXXIII (TRANSDUCERS EUROSENSORS XXXIII)*. IEEE, June 2019, pp. 68–71. ISBN: 978-1-5386-8104-6. DOI: 10.1109/TRANSDUCERS.2019.8808295 (cit. on p. 27).
- [19] A. Glière et al. “Downsizing and Silicon Integration of Photoacoustic Gas Cells”. In: *Int. J. Thermophys.* 41.2 (Feb. 2020), p. 16. ISSN: 0195-928X. DOI: 10.1007/s10765-019-2580-7 (cit. on p. 27).
- [20] K. Liu et al. “A novel photoacoustic spectroscopy gas sensor using a low cost polyvinylidene fluoride film”. In: *Sensors Actuators B Chem.* 277 (Dec. 2018), pp. 571–575. ISSN: 09254005. DOI: 10.1016/j.snb.2018.09.037 (cit. on p. 28).
- [21] H. Lv et al. “Application of piezoelectric transducers in photoacoustic spectroscopy for trace gas analysis”. In: *Microw. Opt. Technol. Lett.* 63.8 (Aug. 2021), pp. 2040–2051. ISSN: 0895-2477. DOI: 10.1002/mop.32830 (cit. on p. 28).
- [22] K. Chamassi et al. “Capacitive silicon micro-electromechanical resonator for enhanced photoacoustic spectroscopy”. In: *Appl. Phys. Lett.* 115.8 (Aug. 2019). ISSN: 0003-6951. DOI: 10.1063/1.5098140 (cit. on p. 28).

- [23] W. Trzpił et al. “Analytic Optimization of Cantilevers for Photoacoustic Gas Sensor with Capacitive Transduction”. In: *Sensors* 21.4 (Feb. 2021), p. 1489. ISSN: 1424-8220. DOI: 10.3390/s21041489 (cit. on p. 28).
- [24] W. Trzpił et al. “A silicon micromechanical resonator with capacitive transduction for enhanced photoacoustic spectroscopy”. In: *Sensors Actuators B Chem.* 353 (Feb. 2022), p. 131070. ISSN: 09254005. DOI: 10.1016/j.snb.2021.131070 (cit. on p. 28).
- [25] Y. Yin et al. “Cantilever-enhanced photoacoustic spectroscopy for gas sensing: A comparison of different displacement detection methods”. In: *Photoacoustics* 28 (Dec. 2022), p. 100423. ISSN: 22135979. DOI: 10.1016/j.pacs.2022.100423 (cit. on p. 28).
- [26] D. Hofstetter et al. “Photoacoustic spectroscopy with quantum cascade distributed-feedback lasers”. In: *Opt. Lett.* 26.12 (June 2001), p. 887. ISSN: 0146-9592. DOI: 10.1364/OL.26.000887 (cit. on p. 28).
- [27] V. Koskinen et al. “Extremely sensitive trace gas analysis with modern photoacoustic spectroscopy”. In: *Vib. Spectrosc.* 42.2 (Nov. 2006), pp. 239–242. ISSN: 09242031. DOI: 10.1016/j.vibspec.2006.05.018 (cit. on p. 28).
- [28] T. Mikkonen et al. “Sensitive multi-species photoacoustic gas detection based on mid-infrared supercontinuum source and miniature multipass cell”. In: *Phys. Chem. Chem. Phys.* 24.32 (2022), pp. 19481–19487. ISSN: 1463-9076. DOI: 10.1039/D2CP01731H (cit. on p. 28).
- [29] L. Fu et al. “Small-volume highly-sensitive all-optical gas sensor using non-resonant photoacoustic spectroscopy with dual silicon cantilever optical microphones”. In: *Photoacoustics* 27 (Sept. 2022), p. 100382. ISSN: 22135979. DOI: 10.1016/j.pacs.2022.100382 (cit. on p. 28).
- [30] M. Guo et al. “High-Sensitivity Silicon Cantilever-Enhanced Photoacoustic Spectroscopy Analyzer with Low Gas Consumption”. In: *Anal. Chem.* 94.2 (Jan. 2022), pp. 1151–1157. ISSN: 0003-2700. DOI: 10.1021/acs.analchem.1c04309 (cit. on p. 28).
- [31] A. Miklós et al. “Application of acoustic resonators in photoacoustic trace gas analysis and metrology”. In: *Rev. Sci. Instrum.* 72.4 (Apr. 2001), pp. 1937–1955. ISSN: 0034-6748. DOI: 10.1063/1.1353198 (cit. on pp. 28, 32).
- [32] O. E. Bonilla-Manrique et al. “Sub-ppm-Level Ammonia Detection Using Photoacoustic Spectroscopy with an Optical Microphone Based on a Phase Interferometer”. In: *Sensors* 19.13 (June 2019), p. 2890. ISSN: 1424-8220. DOI: 10.3390/s19132890 (cit. on p. 28).
- [33] S. Weigl et al. “Photoacoustic detection of acetone in N<sub>2</sub> and synthetic air using a high power UV LED”. In: *Sensors Actuators B Chem.* 316 (Aug. 2020), p. 128109. ISSN: 09254005. DOI: 10.1016/j.snb.2020.128109 (cit. on p. 28).
- [34] Y. Ma et al. “H-shaped acoustic micro-resonator-based quartz-enhanced photoacoustic spectroscopy”. In: *Opt. Lett.* 47.3 (Feb. 2022), p. 601. ISSN: 0146-9592. DOI: 10.1364/OL.449822 (cit. on p. 28).

- [35] J. Pangerl et al. “Characterizing a sensitive compact mid-infrared photoacoustic sensor for methane, ethane and acetylene detection considering changing ambient parameters and bulk composition (N<sub>2</sub>, O<sub>2</sub> and H<sub>2</sub>O)”. In: *Sensors Actuators B Chem.* 352 (Feb. 2022), p. 130962. ISSN: 09254005. DOI: 10.1016/j.snb.2021.130962 (cit. on pp. 28, 33).
- [36] F. G. C. Bijnen et al. “Intracavity CO laser photoacoustic trace gas detection: cyclic CH<sub>4</sub>, H<sub>2</sub>O and CO<sub>2</sub> emission by cockroaches and scarab beetles”. In: *Applied Optics* 35.27 (Sept. 1996), p. 5357. ISSN: 0003-6935. DOI: 10.1364/AO.35.005357 (cit. on p. 28).
- [37] F. J. Harren et al. “Photoacoustic Spectroscopy in Trace Gas Monitoring”. In: *Encyclopedia of Analytical Chemistry*. Chichester, UK: John Wiley & Sons, Ltd, Mar. 2012. DOI: 10.1002/9780470027318.a0718.pub2 (cit. on p. 28).
- [38] V. Zeninari et al. “Design and characteristics of a differential Helmholtz resonant photoacoustic cell for infrared gas detection”. In: *Infrared Phys. Technol.* 40.1 (Feb. 1999), pp. 1–23. ISSN: 13504495. DOI: 10.1016/S1350-4495(98)00038-3 (cit. on p. 28).
- [39] A. Grossel et al. “Photoacoustic detection of nitric oxide with a Helmholtz resonant quantum cascade laser sensor”. In: *Infrared Phys. Technol.* 51.2 (Oct. 2007), pp. 95–101. ISSN: 13504495. DOI: 10.1016/j.infrared.2006.11.004 (cit. on p. 28).
- [40] J. Rouxel et al. “Miniaturized differential Helmholtz resonators for photoacoustic trace gas detection”. In: *Sensors Actuators B Chem.* 236 (Nov. 2016), pp. 1104–1110. ISSN: 09254005. DOI: 10.1016/j.snb.2016.06.074 (cit. on p. 28).
- [41] S. Alahmari et al. “Diode laser photoacoustic spectroscopy of CO<sub>2</sub>, H<sub>2</sub>S and O<sub>2</sub> in a differential Helmholtz resonator for trace gas analysis in the biosciences and petrochemistry”. In: *Anal. Bioanal. Chem.* 411.17 (July 2019), pp. 3777–3787. ISSN: 1618-2642. DOI: 10.1007/s00216-019-01877-0 (cit. on p. 28).
- [42] Z. Gong et al. “Integration of T-type half-open photoacoustic cell and fiberoptic acoustic sensor for trace gas detection”. In: *Opt. Express* 27.13 (June 2019), p. 18222. ISSN: 1094-4087. DOI: 10.1364/OE.27.018222 (cit. on p. 28).
- [43] L. Liu et al. “Design and structural optimization of T-resonators for highly sensitive photoacoustic trace gas detection”. In: *Opt. Laser Technol.* 148 (Apr. 2022), p. 107695. ISSN: 00303992. DOI: 10.1016/j.optlastec.2021.107695 (cit. on p. 28).
- [44] L. Zhang et al. “T-type cell mediated photoacoustic spectroscopy for simultaneous detection of multi-component gases based on triple resonance modality”. In: *Photoacoustics* 31 (June 2023), p. 100492. ISSN: 22135979. DOI: 10.1016/j.pacs.2023.100492 (cit. on p. 28).
- [45] A. J. Zuckerwar. *Handbook of the Speed of Sound in Real Gases*. 2002. ISBN: 9780080545288 (cit. on p. 28).

- [46] T. Mikkonen et al. “Sensitive multi-species photoacoustic gas detection based on mid-infrared supercontinuum source and miniature multipass cell”. In: *Phys. Chem. Chem. Phys.* 24.32 (2022), pp. 19481–19487. ISSN: 1463-9076. DOI: 10.1039/D2CP01731H (cit. on p. 29).
- [47] M. Zhang et al. “Miniaturized multi-pass cell based photoacoustic gas sensor for parts-per-billion level acetylene detection”. In: *Sensors Actuators A Phys.* 308 (June 2020), p. 112013. ISSN: 09244247. DOI: 10.1016/j.sna.2020.112013 (cit. on p. 29).
- [48] J. Hayden et al. “Mid-infrared intracavity quartz-enhanced photoacoustic spectroscopy with pptv – Level sensitivity using a T-shaped custom tuning fork”. In: *Photoacoustics* 25 (Mar. 2022), p. 100330. ISSN: 22135979. DOI: 10.1016/j.pacs.2022.100330 (cit. on p. 29).
- [49] A. Kachanov et al. “Cavity-enhanced optical feedback-assisted photo-acoustic spectroscopy with a 10.4  $\mu\text{m}$  external cavity quantum cascade laser”. In: *Appl. Phys. B* 110.1 (Jan. 2013), pp. 47–56. ISSN: 0946-2171. DOI: 10.1007/s00340-012-5250-z (cit. on p. 29).
- [50] T. Tomberg et al. “Cavity-enhanced cantilever-enhanced photo-acoustic spectroscopy”. In: *The Analyst* 144.7 (2019), pp. 2291–2296. ISSN: 0003-2654. DOI: 10.1039/C9AN00058E (cit. on p. 29).
- [51] P. Hess. “Resonant photoacoustic spectroscopy”. In: 1983, pp. 1–32. DOI: 10.1007/3-540-12065-3\_1 (cit. on pp. 30, 31).
- [52] J.-P. Besson. “Photoacoustic spectroscopy for multi-gas sensing using near infrared lasers”. PhD thesis. 2006 (cit. on pp. 30–33).
- [53] C. Dewey. “Design of optoacoustic systems”. In: *Optoacoust. Spectrosc. Detect.* Academic, New York, 1977, pp. 47–77 (cit. on p. 31).
- [54] L. B. Kreuzer. “The Physics of Signal Generation and Detection”. In: *Optoacoust. Spectrosc. Detect.* 1977. ISBN: 9780323158817 (cit. on pp. 31, 32).
- [55] A. Miklós et al. “Application of acoustic resonators in photoacoustic trace gas analysis and metrology”. In: *Rev. Sci. Instrum.* 72.4 (Apr. 2001), pp. 1937–1955. ISSN: 0034-6748. DOI: 10.1063/1.1353198 (cit. on p. 31).
- [56] M. Mattiello. “Gas traces measurement by photoacoustic spectroscopy using Helmholtz resonator-based sensors”. PhD thesis. EPFL, 2008. DOI: <https://doi.org/10.5075/epfl-thesis-4002> (cit. on p. 31).
- [57] S. Weigl. “Development of a sensor system for human breath acetone analysis based on photoacoustic spectroscopy”. PhD thesis. University of Regensburg, 2020. DOI: 10.5283/epub.44776 (cit. on pp. 31, 33).
- [58] S. Weigl et al. “Scopes and Limits of Photoacoustic Spectroscopy in Modern Breath Analysis”. In: 2022, pp. 101–159. DOI: 10.1007/11663\_2022\_22 (cit. on pp. 31–33).
- [59] A. Rosencwaig. “Photoacoustic Spectroscopy”. In: *Annual Review of Biophysics and Bioengineering* 9.1 (1980), pp. 31–54. ISSN: 0084-6589. DOI: 10.1146/annurev.bb.09.060180.000335 (cit. on p. 31).

- [60] J. D. Lambert. *Vibrational and Rotational Relaxation in Gases*. Clarendon Press Oxford, 1977. ISBN: 978-0198556053 (cit. on pp. 34–40).
- [61] M. S. Child. *Molecular collision theory*. Courier Corporation, 1996 (cit. on p. 35).
- [62] P. Ehrenfest. “On adiabatic changes of a system in connection with the quantum theor”. In: *KNAW, Proc.* 19 (1917) (cit. on p. 36).
- [63] K. F. Herzfeld and T. A. Litovitz. *Absorption and Dispersion of Ultrasonic Waves*. 1959. ISBN: 9781483275703 (cit. on p. 36).
- [64] H. K. Shin. “Vibrational Energy Transfer”. In: *Dyn. Mol. Collisions*. Boston, MA: Springer US, 1976, pp. 131–210. DOI: 10.1007/978-1-4615-8867-2\_4 (cit. on p. 36).
- [65] L. Landau and E. Teller. “Theory of sound dispersion”. In: *Physik Zeitschrift der Sowjetunion* 10 (1936), pp. 34–38 (cit. on p. 37).
- [66] R. N. Schwartz et al. “Calculation of Vibrational Relaxation Times in Gases”. In: *The Journal of Chemical Physics* 20.10 (Oct. 1952), pp. 1591–1599. ISSN: 0021-9606. DOI: 10.1063/1.1700221 (cit. on p. 37).
- [67] R. N. Schwartz and K. F. Herzfeld. “Vibrational Relaxation Times in Gases (Three-Dimensional Treatment)”. In: *J. Chem. Phys.* 22.5 (May 1954), pp. 767–773. ISSN: 0021-9606. DOI: 10.1063/1.1740190 (cit. on p. 37).
- [68] F. I. Tanczos. “Calculation of Vibrational Relaxation Times of the Chloromethanes”. In: *The Journal of Chemical Physics* 25.3 (Sept. 1956), pp. 439–447. ISSN: 0021-9606. DOI: 10.1063/1.1742943 (cit. on pp. 37, 39, 40).
- [69] H. K. Shin. “Temperature dependence of intermolecular energy transfer in polar molecules”. In: *J. Am. Chem. Soc.* 90.12 (June 1968), pp. 3029–3039. ISSN: 0002-7863. DOI: 10.1021/ja01014a007 (cit. on p. 39).
- [70] R. A. Rooth et al. “Photoacoustic measurement of ammonia in the atmosphere: influence of water vapor and carbon dioxide”. In: *Applied Optics* 29.25 (Sept. 1990), p. 3643. ISSN: 0003-6935. DOI: 10.1364/AO.29.003643 (cit. on p. 39).
- [71] M. Hammerich et al. “Photoacoustic study of kinetic cooling”. In: *Chemical Physics* 163.2 (June 1992), pp. 173–178. ISSN: 03010104. DOI: 10.1016/0301-0104(92)87101-E (cit. on p. 39).
- [72] J. T. Yardley. *Introduction to Molecular Energy Transfer*. Elsevier, 1980. ISBN: 9780127685502. DOI: 10.1016/B978-0-12-768550-2.X5001-4 (cit. on pp. 40, 41).
- [73] G. Wysocki et al. “Influence of molecular relaxation dynamics on quartz-enhanced photoacoustic detection of CO<sub>2</sub> at  $\lambda = 2 \mu\text{m}$ ”. In: *Appl. Phys. B* 85.2-3 (Nov. 2006), pp. 301–306. ISSN: 0946-2171. DOI: 10.1007/s00340-006-2369-9 (cit. on p. 41).
- [74] Y. Liu et al. “Integrated near-infrared QEPAS sensor based on a 28 kHz quartz tuning fork for online monitoring of CO<sub>2</sub> in the greenhouse”. In: *Photoacoustics* 25 (Mar. 2022), p. 100332. ISSN: 22135979. DOI: 10.1016/j.pacs.2022.100332 (cit. on p. 41).

- [75] J. Kalkman and H. van Kesteren. “Relaxation effects and high sensitivity photoacoustic detection of NO<sub>2</sub> with a blue laser diode”. In: *Applied Physics B* 90.2 (Feb. 2008), pp. 197–200. ISSN: 0946-2171. DOI: 10.1007/s00340-007-2895-0 (cit. on pp. 41, 42).
- [76] X. Yin et al. “Highly sensitive SO<sub>2</sub> photoacoustic sensor for SF<sub>6</sub> decomposition detection using a compact mW-level diode-pumped solid-state laser emitting at 303 nm”. In: *Optics Express* 25.26 (Dec. 2017), p. 32581. ISSN: 1094-4087. DOI: 10.1364/OE.25.032581 (cit. on pp. 41, 42).
- [77] L. Escher et al. “3.3 - Digitaler Zwilling photoakustischer Spurengassensoren zur Prozessüberwachung”. In: *Vorträge*. AMA Service GmbH, Von-Münchhausen-Str. 49, 31515 Wunstorf, Germany, 2022, pp. 23–28. DOI: 10.5162/16dss2022/3.3 (cit. on pp. 41, 42).
- [78] J. Hayden et al. “Anomalous Humidity Dependence in Photoacoustic Spectroscopy of CO Explained by Kinetic Cooling”. In: *Appl. Sci.* 10.3 (Jan. 2020), p. 843. ISSN: 2076-3417. DOI: 10.3390/app10030843 (cit. on p. 42).
- [79] F. Sgobba et al. “Compact and portable quartz-enhanced photoacoustic spectroscopy sensor for carbon monoxide environmental monitoring in urban areas”. In: *Photoacoustics* 25 (Mar. 2022), p. 100318. ISSN: 22135979. DOI: 10.1016/j.pacs.2021.100318 (cit. on p. 42).
- [80] X. Yin et al. “Impact of Humidity on Quartz-Enhanced Photoacoustic Spectroscopy Based CO Detection Using a Near-IR Telecommunication Diode Laser”. In: *Sensors* 16.2 (Jan. 2016), p. 162. ISSN: 1424-8220. DOI: 10.3390/s16020162 (cit. on p. 42).
- [81] Y. Qiao et al. “Sensitivity enhanced NIR photoacoustic CO detection with SF<sub>6</sub> promoting vibrational to translational relaxation process”. In: *Photoacoustics* 25 (Mar. 2022), p. 100334. ISSN: 22135979. DOI: 10.1016/j.pacs.2022.100334 (cit. on p. 42).
- [82] L. Dong et al. “Ppb-level detection of nitric oxide using an external cavity quantum cascade laser based QEPAS sensor”. In: *Optics Express* 19.24 (2011), p. 24037. ISSN: 1094-4087. DOI: 10.1364/OE.19.024037 (cit. on p. 43).
- [83] H. Wu et al. “Ppb-level nitric oxide photoacoustic sensor based on a mid-IR quantum cascade laser operating at 52 °C”. In: *Sensors Actuators B Chem.* 290 (July 2019), pp. 426–433. ISSN: 09254005. DOI: 10.1016/j.snb.2019.04.007 (cit. on p. 43).
- [84] J.-P. Besson et al. “Molecular relaxation effects in hydrogen chloride photoacoustic detection”. In: *Appl. Phys. B* 90.2 (Feb. 2008), pp. 191–196. ISSN: 0946-2171. DOI: 10.1007/s00340-007-2821-5 (cit. on p. 43).
- [85] J.-P. Besson et al. “Multi-hydrogenated compounds monitoring in optical fibre manufacturing process by photoacoustic spectroscopy”. In: *Appl. Phys. B* 85.2-3 (Nov. 2006), pp. 343–348. ISSN: 0946-2171. DOI: 10.1007/s00340-006-2361-4 (cit. on p. 43).

- [86] M. Olivieri et al. “Characterization of H<sub>2</sub>S QEPAS detection in methane-based gas leaks dispersed into environment”. In: *Photoacoustics* 29 (Feb. 2023), p. 100438. ISSN: 22135979. DOI: 10.1016/j.pacs.2022.100438 (cit. on p. 44).
- [87] J. P. Waclawek et al. “Quartz-enhanced photoacoustic spectroscopy-based sensor system for sulfur dioxide detection using a CW DFB-QCL”. In: *Appl. Phys. B* 117.1 (Oct. 2014), pp. 113–120. ISSN: 0946-2171. DOI: 10.1007/s00340-014-5809-y (cit. on p. 44).
- [88] Z. Wang et al. “Quartz-Enhanced Photoacoustic Spectroscopy (QEPAS) Detection of the  $\nu$  7 Band of Ethylene at Low Pressure with CO 2 Interference Analysis”. In: *Appl. Spectrosc.* 71.8 (Aug. 2017), pp. 1834–1841. ISSN: 0003-7028. DOI: 10.1177/0003702817690406 (cit. on p. 44).
- [89] J. P. Waclawek et al. “Compact quantum cascade laser based quartz-enhanced photoacoustic spectroscopy sensor system for detection of carbon disulfide”. In: *Opt. Express* 24.6 (Mar. 2016), p. 6559. ISSN: 1094-4087. DOI: 10.1364/OE.24.006559 (cit. on p. 44).
- [90] M. I. Cotterell et al. “The impact of bath gas composition on the calibration of photoacoustic spectrometers with ozone at discrete visible wavelengths spanning the Chappuis band”. In: *Atmos. Meas. Tech.* 12.4 (Apr. 2019), pp. 2371–2385. ISSN: 1867-8548. DOI: 10.5194/amt-12-2371-2019 (cit. on p. 44).
- [91] M. I. Cotterell et al. “Photoacoustic studies of energy transfer from ozone photoproducts to bath gases following Chappuis band photoexcitation”. In: *Phys. Chem. Chem. Phys.* 23.1 (2021), pp. 536–553. ISSN: 1463-9076. DOI: 10.1039/D0CP05056C (cit. on p. 44).

# Chapter 3

## Experimental

## 3.1 Laboratory setup

In this chapter the gas mixing concept (section 3.1.1), the electronic setup of the photoacoustic experiments (section 3.1.2) as well as the characterization of the light sources (section 3.2) is reported. The results reported in chapters 4.2, 4.3, 4.7 and 4.6 were obtained with this laboratory setup. For the results in chapters 4.4 and 4.5, separate experimental setups were used, which are discussed in detail in the respective chapters.

### 3.1.1 Gas mixing concept

The basic gas mixing concept of the laboratory is visualised in Figure 3.1. Each gas tank is connected to a mass flow controller (MFC) of the type F-201CV-500-XXX (Bronkhorst, Karmen, Germany). All gas tanks have been supplied by Westfalen AG (Münster, Germany). The analyte gases used for laboratory measurements are 30 ppmV CH<sub>4</sub> and 30 ppmV C<sub>2</sub>H<sub>6</sub> diluted in nitrogen (5.0)\*. Both of these analyte gas tanks were specified with an accuracy of  $\pm 3\%$  ( $\pm 0.9$  ppmV). Further dilution of the analyte concentration can be achieved by mixing the analyte gas with the designated dilution gas (see Figure 3.1). The final (Cut-off) MFC sets the mass flow rate  $Q_{\text{vol}}$  of the probe gas. In case of humidification,  $Q_{\text{vol}}$  is split into a humidified  $Q_{\text{vol,(i)}}$  and a dry path  $Q_{\text{vol,(ii)}}$ , which can be manually controlled by two needle valves and thus allow adjustment of the humidification. For investigating the effect of lower pressures on the photoacoustic signal (see chapters 4.3 and 4.6) a pre-pressure controller (PPC) from Bronkhorst Instruments GmbH (P-720CV-6K0A-RAD-33-Z) was installed between the photoacoustic measurement cell and the vacuum pump of the type TRIVAC D 2.5 E (Leybold GmbH, Aschheim, Germany). With this setup pressures

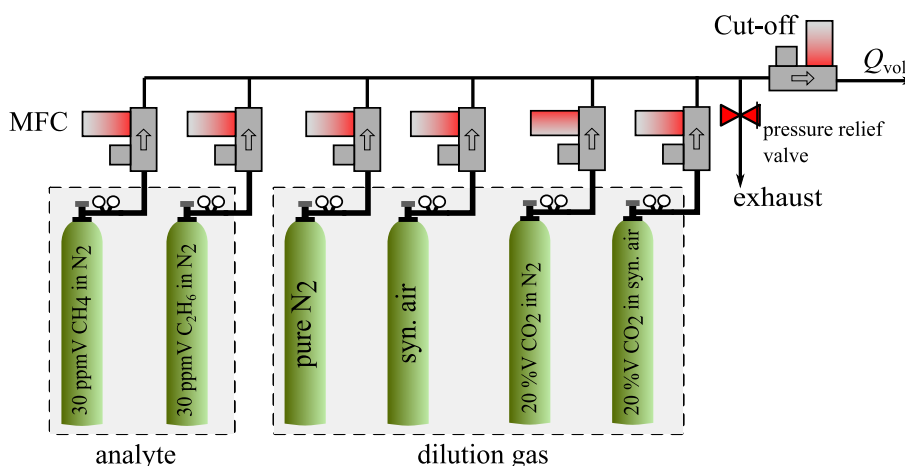


**Fig. 3.1.** Simplified schematic of the gas mixing concept used in chapters 4.2, 4.3, 4.7 and 4.6. **MFC** = mass flow controller.

\*A purity of 5.0 corresponds to 99.999 %.

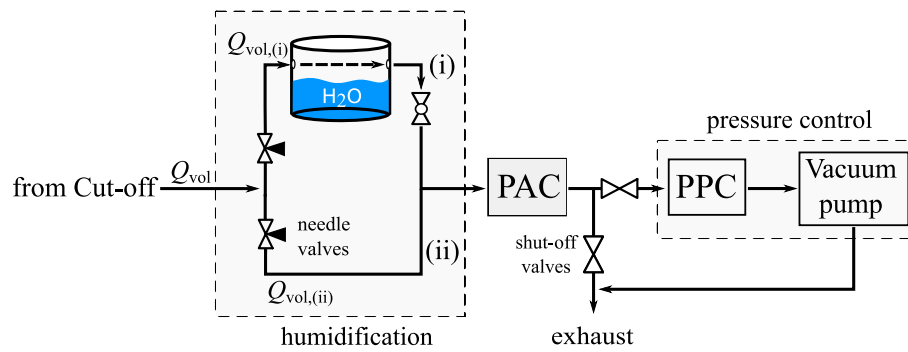


**Fig. 3.2.** Humidification and pressure control concept of the sample gas. **PAC** = photoacoustic measurement cell; **PPC** = pre-pressure controller.

down to 200 mbar are possible, limited by the gas tightness of the PAC. To monitor the temperature, pressure and humidity within the photoacoustic measurement cell a TpH sensor (BME280) from Bosch (Robert Bosch GmbH, Gerlingen, Germany) was integrated.

A LabVIEW based software tool allows to choose the desired analyte concentration, as well as the dilution gas matrix [1]. However, the minimal analyte concentration is limited by the minimum flow rate of the MFCs (20 ml/min). All results in chapters 4.2, 4.3, 4.7 and 4.6 were obtained with  $Q_{\text{vol}} = 500$  ml/min, if not specified otherwise. For the nominal concentrations of the analyte gas tanks of 30 ppmV the minimal achievable concentration of methane or ethane is 1.2 ppmV. The actual MFC flow rates can be monitored continuously, preventing faulty measurements due to incorrect flow conditions.

### 3.1.2 Electronic setup

This subsection discusses the electronic devices used within this thesis. The core of the electronic setup is a data acquisition and control unit (PC). This unit not only communicates with the individual devices, but also collects all necessary sensor data, which are then provided to a digital twin, which is described in chapter 4.3. The powermeter (PM) PM400 combined with an S401C (Thorlabs GmbH, Munich, Germany) sensor head, is used to monitor the optical power emitted by the light source, after passing the PAC. In order to characterize the emitting wavelength and peak width of the interband cascade lasers (ICL), a spectrum analyzer BRI-771B-MIR from Bristol Instruments, Inc. (Victor, US) was employed. Since the spectrum analyzer was only used for the initial light source characterization, it is not shown in Figure 3.3.

The temperature and current of the respective ICL are controlled by a laser driver (LD) from Newport Corporation (Irving, US) ILX Lightwave LDC 3726. A function generation (FG) of type 33500B (Keysight Technologies, Santa Rosa, US) sets the modulation frequency of the ICL current, and provides the reference frequency for

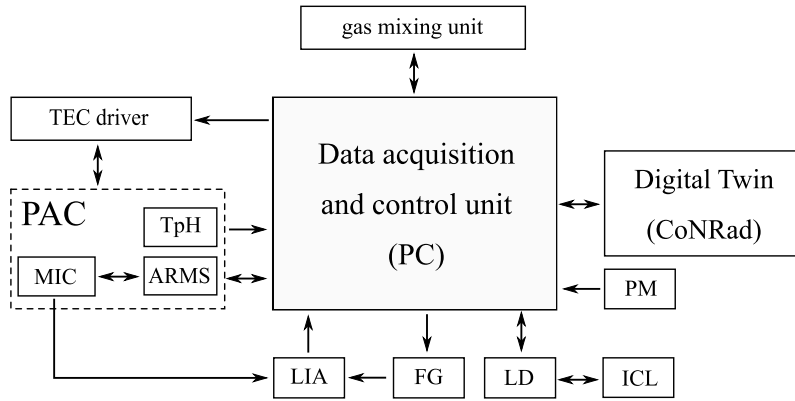


**Fig. 3.3.** Schematic of the basic electronic concept used in this work.

the lock-in-amplifier via its TTL output. The LIA 7270 DSP from Ametek, Inc. (Berwyn, US) is used to filter and process the microphone (MIC) signal. The results in chapters 4.2 and 4.3 were obtained with the microphone ICS-40720 from InvenSense (California, US). In chapters 4.4, 4.6, and 4.7 the newer model (ICS-40730), providing a better SNR\*, was employed. The microphone was powered with 3.3 V from a low noise voltage source HMP4040 from Rhode & Schwarz (Munich, Germany). While the humidification of the sample gas must be performed by manually adjusting the needle valves, the PC controls the MFCs and the PPC. To avoid condensation inside the measurement cell the PAC is temperature controlled by a dual-channel TEC-1122-SV from Meerstetter Engineering (Rubigen, Switzerland) to typically 35°C or 40°C.

To monitor the acoustic resonance characteristics of the PAC, i.e. frequency of resonance  $f_{\text{res}}$  and the  $Q$ -factor of amplification, an *acoustic resonance monitoring system* (ARMS) was integrated into the PAC and presented in [2]. A miniaturized speaker K 16 from Visaton (Germany) mounted into one buffer volume of the PAC gets excited by three 1 V pulses with a frequency near resonance, e.g. 5000 Hz. The microphone signal is processed by means of Fast Fourier Transform (FFT) analysis. Both, the speaker stimulation and the processing of the microphone signal during an ARMS cycle are performed by an ARM cortex A9+/ FPGA board (Red Pitaya, Slovenia). The magnitude of the FFT  $S_{\text{FFT}}$  is fitted with equation (3.1), provided by [3], to obtain  $f_{\text{res}}$  and the  $Q$ -factor.

$$S_{\text{FFT}} = \left| i \frac{f}{f^2 - f_{\text{res}}^2 + i f \frac{f_{\text{res}}}{Q}} \frac{1}{2\pi} A \right| \quad (3.1)$$

The FFT frequency is labeled  $f$  and the fitting parameters of equation (3.1)  $f_{\text{res}}$ ,  $Q$ , as well as the amplitude factor  $A$  are determined by Nelder-Mead convergence. Figure 3.4 shows the raw microphone signal after speaker excitation (left) and the resulting FFT magnitude (right) together with the results of the fit (red line). To reduce the noise of the data, this procedure is typically repeated ten times and

\*SNR<sub>ICS-40730</sub> = 74 dBA, SNR<sub>ICS-40720</sub> = 70 dBA

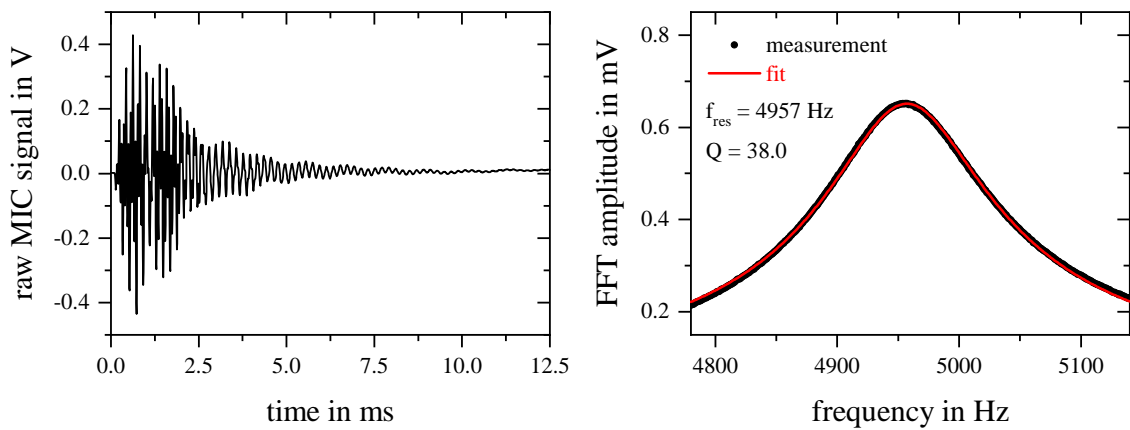


**Fig. 3.4.** Raw (left) and FFT (right) microphone voltage during ARMS. The black circles of the FFT signal depict the measured amplitude that is fitted according to [3] (red line). This figure is taken from the original publication [P2] (chapter 4.3).

then averaged. This yields an uncertainty in  $Q$  determination of  $3\sigma(Q) = 0.08$  and  $3\sigma(f_{\text{res}}) = 0.24$  Hz regarding frequency determination. To prevent a mismatch of modulation and resonance frequency and to monitor the  $Q$  factor, the ARMS routine should be performed before each photoacoustic measurement. Overall, this routine takes only a few seconds.

## 3.2 Light source characterization

This subsection presents the characterization of the two light sources used within this thesis. Generally this thesis presents two different approaches for photoacoustic measurements, i.e. wavelength modulation (WM) and amplitude modulation (AM). For both measurement modes an ICL was used. The results of the chapters 4.2, 4.3, 4.4, 4.5, and 4.6 were obtained in WM mode and AM was used only in chapter 4.7.

During his master thesis Jonas Pangerl performed an extensive characterization of the ICL used for the WM measurements [4]. The results regarding the spectral tunability are shown in Figure 3.5. The ICL chosen for this application was initially developed for fuel gas analysis, in which only traces of humidity and high analyte concentrations (in the %V-range) are expected (see chapter 4.6). The peak wavenumber of emission of an ICL can be controlled by either changing its temperature or current. On the left side of Figure 3.5 the emitted peak wavenumber in  $\text{cm}^{-1}$  for ICL temperatures ranging from 18 °C to 40 °C and currents from 75 mA up to 88 mA is presented. The preliminary spectral analysis for suitable ethane detection with the WM ICL was performed utilizing Molexplorer\* data, yielding the peak at  $2973.55 \text{ cm}^{-1}$ , which was also excited in this work. However, utilizing data from Harrison et al. [5], which was provided by HITRAN database revealed a significantly different ethane absorption

\*Molexplorer is based on theoretical calculations.

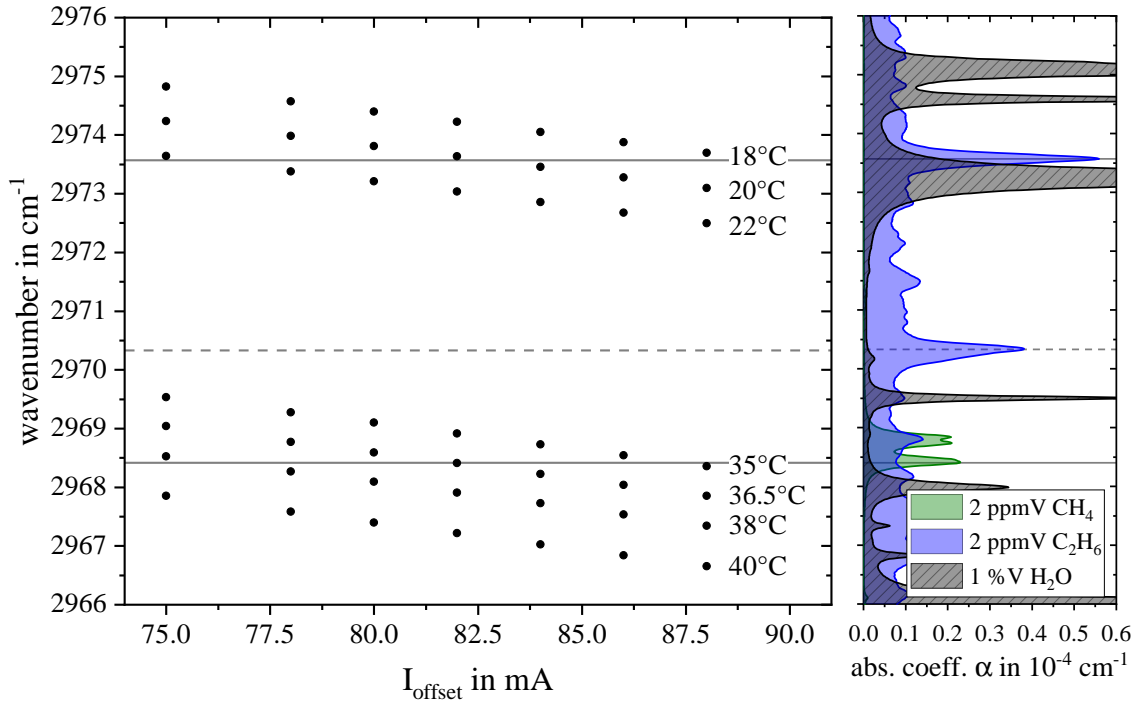


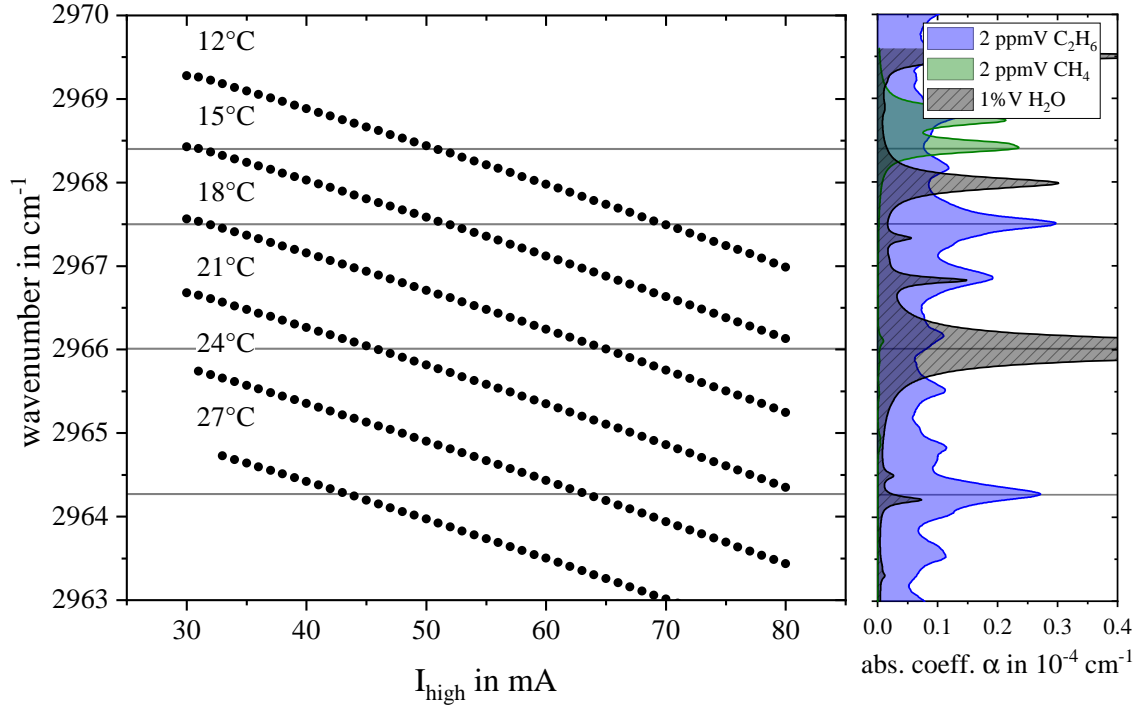
**Fig. 3.5.** Characterization of the ICL used for WM measurements. The left side shows the measured peak wavenumber of emission for different ICL temperatures and  $I_{\text{offset}}$ . The absorption coefficient of methane, ethane and water are displayed on the right side. The grey solid lines indicate the excited methane and ethane peaks. The dashed grey line marks the optimal ethane peak in this spectral range.

spectrum. According to this data the peak at around  $2970.33 \text{ cm}^{-1}$  is much more suitable, as it shows negelectable overlap with the water peak and thus less spectral influences on the PA signal are to be expected. The difference between HITRAN and Molexplorer database can be seen in Appendix (A.2) - Figure A2. Chapter 4.6 discusses the signal alterations due to spectral overlap in terms of WM photoacoustic. Thus, for subsequent research the peak at  $2970.33 \text{ cm}^{-1}$  should be utilized regarding ethane detection. The methane and water spectra were obtained from *HITRAN on the Web*. The ICL parameters, i.e. temperature  $T$ , offset current  $I_{\text{offset}}$ , the modulation current  $I_{\text{mod}}$ , and the optical power  $P_{\text{opt}}$  after the PAC for methane and ethane detection are listed in Table 3.1. The applied modulation currents  $I_{\text{mod}}$  for methane and ethane detection result in modulation depths of  $2\Delta\tilde{\nu}_{\text{WM}} = 0.352 \text{ cm}^{-1}$  ( $2968.44 \pm 0.176 \text{ cm}^{-1}$ ) and  $2\Delta\tilde{\nu}_{\text{WM}} = 0.348 \text{ cm}^{-1}$  ( $2973.55 \pm 0.174 \text{ cm}^{-1}$ ), respectively.

The characterization of the ICL for the AM measurements (chapter 4.7) was performed by the author. Again, the ICL temperature and current were used to control the emitted wavenumber, see Figure 3.6. Compared to the spectral range scanned with the WM ICL, the overlap of methane and ethane with water is significantly smaller. The ICL parameters, i.e. temperature  $T$ , high current  $I_{\text{high}}$  of the squarewave

**Tab. 3.1.** ICL parameters for WM methane and ethane detection.

analyte	$I_{\text{offset}}$ in mA	$I_{\text{mod}}$ in mA	$T_{\text{ICL}}$ in °C	$P_{\text{opt}}$ in mW
methane (CH <sub>4</sub> )	82.65	5.85	36.5	7.5
ethane (C <sub>2</sub> H <sub>6</sub> )	83.55	6.00	20.0	10.3

**Fig. 3.6.** Characterization of the ICL used for AM measurements. The left side shows the measured peak wavenumber of emission for different ICL temperatures and  $I_{\text{high}}$ . The absorption coefficient of methane, ethane and water are displayed on the right side.

modulation, and the optical power  $P_{\text{opt}}$  after the PAC for methane, ethane and water detection are listed in Table 3.2.

**Tab. 3.2.** ICL parameter for AM methane, ethane and water detection.

analyte	$I_{\text{high}}$ in mA	$T_{\text{ICL}}$ in °C	$P_{\text{opt}}$ in mW
methane (CH <sub>4</sub> )	52.0	12.0	3.0
ethane (C <sub>2</sub> H <sub>6</sub> )	71.5	12.0	4.9
water (H <sub>2</sub> O)	66.0	18.0	3.8

The light source used in chapter 4.5 was characterized by the group from Prof. Spagnolo in Bari, Italy and will not be further discussed.

## References

- [1] S. Weigl. “Development of a sensor system for human breath acetone analysis based on photoacoustic spectroscopy”. PhD thesis. University of Regensburg, 2020. DOI: 10.5283/epub.44776 (cit. on p. 55).
- [2] T. Rück et al. “Digital Twin of a photoacoustic trace gas sensor for monitoring methane in complex gas compositions”. In: *Sensors Actuators B Chem.* 378 (Mar. 2023), p. 133119. ISSN: 09254005. DOI: 10.1016/j.snb.2022.133119 (cit. on p. 56).
- [3] A. Miklós et al. “Application of acoustic resonators in photoacoustic trace gas analysis and metrology”. In: *Rev. Sci. Instrum.* 72.4 (Apr. 2001), pp. 1937–1955. ISSN: 0034-6748. DOI: 10.1063/1.1353198 (cit. on pp. 56, 57).
- [4] J. Pangerl. “Diagnostical evaluation of in oil dissolved C1-C2-hydrocarbons by photoacoustic spectroscopy”. Project thesis. Ostbayerische Technische Hochschule Regensburg, 2020 (cit. on p. 57).
- [5] J. J. Harrison et al. “Infrared absorption cross sections for ethane (C<sub>2</sub>H<sub>6</sub>) in the 3 $\mu$ m region”. In: *J. Quant. Spectrosc. Radiat. Transf.* 111.3 (Feb. 2010), pp. 357–363. ISSN: 00224073. DOI: 10.1016/j.jqsrt.2009.09.010 (cit. on p. 57).

# Chapter 4

## Results and discussion

## Synopsis

Chapter 4 is subdivided into six sections. Sections 4.2, 4.3 and 4.4 can be considered as a continuous research project whose results have already been published in peer-reviewed journals. In section 4.2, the algorithm CoNRad is introduced, which allows to compute the collision-based non-radiative relaxation behavior of a given gas matrix. The calculations of CoNRad were verified for photoacoustic methane measurements regarding cross-sensitivities towards nitrogen, oxygen and water. The concept of improving the confidence of photoacoustic sensors by implementing a digital twin (DT) is presented in section 4.3. Here, the influence of pressure, temperature and CO<sub>2</sub> was analyzed and successfully compensated by combining CoNRad with other methods, e.g. ARMS. Chapter 4.4 discusses the comparison of the developed photoacoustic methane sensor with a reference device at a meteorological observatory of the German Weather Service. In chapter 4.5, the DT from chapter 4.3 is compared with an well-established statistical method, i.e. *partial least squares regression* (PLSR) with respect to the capability of compensating for cross-influences on the photoacoustic signal. While in sections 4.2 to 4.4 relaxational as well as acoustic effects showed the greatest influence on the measured signal, in section 4.6 spectral effects concerning WM photoacoustics were investigated. Finally, in section 4.7, the potential for multicomponent photoacoustic detection with AM is briefly demonstrated.

To avoid repetitions in the following chapters, especially concerning relaxational effects and experimental setups, the chapters 4.2, 4.3 and 4.4 were partially adapted regarding the original publications [P1], [P2] and [P3].

## 4.1 General information

For all methane measurements dealing with relaxational effects the Jablonsky diagram from Figure 4.1 was applied. The reaction rates  $k$  of the respective energy transitions are listed in Table 4.1. Further parameter, i.e. molecular mass  $M$ , radii at infinite temperature  $r|_{T \rightarrow \infty}$  and Sutherland constant  $T_V$  for different molecules are listed in Table 4.2. Table 4.3 shows the energies of vibrational states used for the calculations.

### 4.1.1 Jablonsky diagramm

For the methane measurements performed by the author the excitation wavenumber was  $2968.4 \text{ cm}^{-1}$ . In chapter 4.5 the laser emitting wavenumber was with  $2989.5 \text{ cm}^{-1}$  slightly different, which however resulted in the same Jablonsky diagramm of non-radiative relaxation, see Figure 4.1.

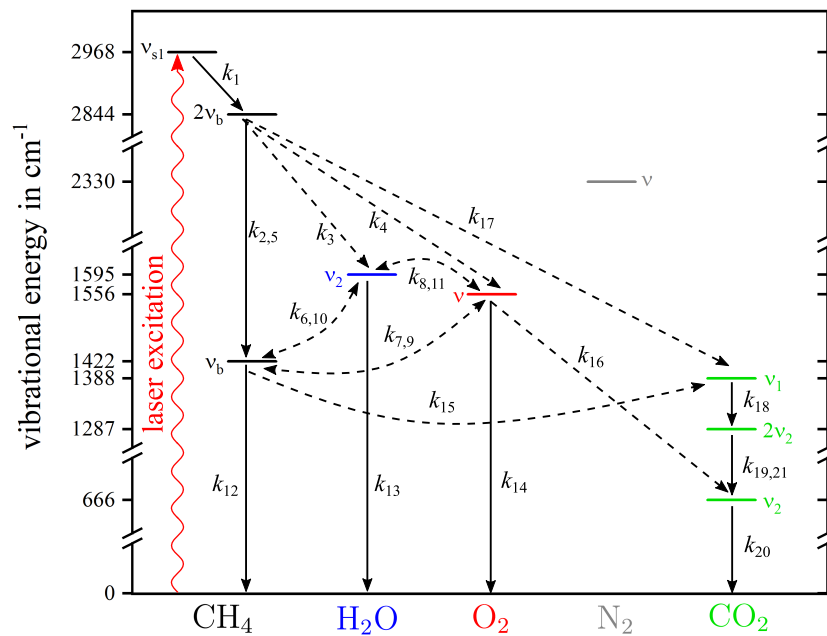


**Fig. 4.1.** Jablonsky diagram of mid-IR laser excitation of methane, followed by collision-based non-radiative relaxation processes with methane, water, oxygen, nitrogen and carbon dioxide. Intramolecular energy transitions or VT-transitions are indicated as solid arrows. Dashed arrows represent intermolecular transitions.

### 4.1.2 Energy transitions

**Tab. 4.1.** Summary of all 50 collision-based energy transitions (reactions) that have been considered for computing relaxational effects in mixtures containing CH<sub>4</sub>, N<sub>2</sub>, O<sub>2</sub>, H<sub>2</sub>O and CO<sub>2</sub>. Every reaction is assigned to the Jablonsky diagram in Figure 4.1 and includes the energy difference  $\Delta E$  of products minus reactants (exergonic reactions are indicated by  $\Delta E < 0$ ) as well as the reaction rates  $k$ . These rates were fine-tuned or estimated by means of least square method, depending on whether literature values could have been found or not. The table is continued on the next page.

	Reaction	$\Delta E$ in cm <sup>-1</sup>	Reaction rate $k$ in s <sup>-1</sup> used	literature
			$k_1^{\text{CH}_4} = 2.1 \cdot 10^8$	$2.1 \cdot 10^8$ [1]
			$k_1^{\text{N}_2} = 4.6 \cdot 10^8$	$4.6 \cdot 10^8$ [2]
(1)	$\text{CH}_4(\nu_{s,1}) + M \xrightarrow{k_1^M} \text{CH}_4(2\nu_b) + M$	-124	$k_1^{\text{H}_2\text{O}} = 1 \cdot 10^8$	-
			$k_1^{\text{O}_2} = 4.6 \cdot 10^8$	$4.6 \cdot 10^8$ [2]
			$k_1^{\text{N}_2} = 4.6 \cdot 10^8$	-
(2)	$\text{CH}_4(2\nu_b) + \text{CH}_4 \xrightarrow{k_2} \text{CH}_4(\nu_b) + \text{CH}_4(\nu_b)$	0	$k_2 = 5 \cdot 10^8$	$5.5 \cdot 10^8$ [3]
(3)	$\text{CH}_4(2\nu_b) + \text{H}_2\text{O} \xrightarrow{k_3} \text{CH}_4(\nu_b) + \text{H}_2\text{O}(\nu_2)$	173	$k_3 = 1 \cdot 10^8$	-
(4)	$\text{CH}_4(2\nu_b) + \text{O}_2 \xrightarrow{k_4} \text{CH}_4(\nu_b) + \text{O}_2(\nu)$	134	$k_4 = 1 \cdot 10^7$	$6.6 \cdot 10^6$ [3]
			$k_5^{\text{CH}_4} = 1.6 \cdot 10^6$	$1.6 \cdot 10^6$ [4]
			$k_5^{\text{N}_2} = 2 \cdot 10^5$	$1.6 \cdot 10^5$ [4]
(5)	$\text{CH}_4(2\nu_b) + M \xrightarrow{k_5^M} \text{CH}_4(\nu_b) + M$	-1422	$k_5^{\text{H}_2\text{O}} = 2.4 \cdot 10^5$	-
			$k_5^{\text{O}_2} = 2.6 \cdot 10^5$	-
			$k_5^{\text{CO}_2} = 2 \cdot 10^5$	-
(6)	$\text{CH}_4(\nu_b) + \text{H}_2\text{O} \xrightarrow{k_6} \text{CH}_4 + \text{H}_2\text{O}(\nu_2)$	173	$k_6 = 7 \cdot 10^7$	-
(7)	$\text{CH}_4(\nu_b) + \text{O}_2 \xrightarrow{k_7} \text{CH}_4 + \text{O}_2(\nu)$	134	$k_7 = 2 \cdot 10^6$	$3.3 \cdot 10^6$ [3]
(8)	$\text{O}_2(\nu) + \text{H}_2\text{O} \xrightarrow{k_8} \text{O}_2 + \text{H}_2\text{O}(\nu_2)$	39	$k_8 = 2.2 \cdot 10^7$	$1.3 \cdot 10^7$ [5]
(9)	$\text{O}_2(\nu) + \text{CH}_4 \xrightarrow{k_9} \text{O}_2 + \text{CH}_4(\nu_b)$	-134	$k_9 = 3.3 \cdot 10^7$	$3.3 \cdot 10^7$ [3]
(10)	$\text{H}_2\text{O}(\nu_2) + \text{CH}_4 \xrightarrow{k_{10}} \text{H}_2\text{O} + \text{CH}_4(\nu_b)$	-173	$k_{10} = 2 \cdot 10^7$	-
(11)	$\text{H}_2\text{O}(\nu_2) + \text{O}_2 \xrightarrow{k_{11}} \text{H}_2\text{O} + \text{O}_2(\nu)$	-39	$k_{11} = 2 \cdot 10^7$	$3.8 \cdot 10^7$ [6]

*Continued on next page*

Table 4.1 – *Continued from previous page*

Reaction		$\Delta E$ in $\text{cm}^{-1}$	Reaction rate $k$ in $\text{s}^{-1}$	
			used	literature
(12)	$\text{CH}_4(\nu_b) + M \xrightarrow{k_{12}^M} \text{CH}_4 + M$	-1422	$k_{12}^{\text{CH}_4} = 8 \cdot 10^5$	$8 \cdot 10^5$ [3]
			$k_{12}^{\text{N}_2} = 4.5 \cdot 10^4$	$8 \cdot 10^4$ [4]
			$k_{12}^{\text{H}_2\text{O}} = 1.2 \cdot 10^5$	-
			$k_{12}^{\text{O}_2} = 7 \cdot 10^4$	$1.4 \cdot 10^5$ [3]
			$k_{12}^{\text{CO}_2} = 1 \cdot 10^5$	-
(13)	$\text{H}_2\text{O}(\nu_2) + M \xrightarrow{k_{13}^M} \text{H}_2\text{O} + M$	-1595	$k_{13}^{\text{CH}_4} = 1 \cdot 10^6$	-
			$k_{13}^{\text{N}_2} = 1 \cdot 10^7$	$1 \cdot 10^6$ [7]
			$k_{13}^{\text{H}_2\text{O}} = 1.2 \cdot 10^9$	$1.2 \cdot 10^9$ [5]
			$k_{13}^{\text{O}_2} = 1 \cdot 10^6$	$1 \cdot 10^6$ [7]
			$k_{13}^{\text{CO}_2} = 2.5 \cdot 10^6$	-
(14)	$\text{O}_2(\nu) + M \xrightarrow{k_{14}^M} \text{O}_2 + M$	-1556	$k_{14}^{\text{CH}_4} = 1 \cdot 10^6$	$1 \cdot 10^6$ [8]
			$k_{14}^{\text{N}_2} = 18$	18 [9]
			$k_{14}^{\text{H}_2\text{O}} = 1.1 \cdot 10^6$	$8 \cdot 10^5$ [7]
			$k_{14}^{\text{O}_2} = 81$	81 [5]
			$k_{14}^{\text{CO}_2} = 0.6$	0.6 [9]
(15)	$\text{CH}_4(\nu_b) + \text{CO}_2 \xrightarrow{k_{15}} \text{CH}_4 + \text{CO}_2(\nu_1)$	34	$k_{15} = 2.65 \cdot 10^6$	-
(16)	$\text{O}_2(\nu) + \text{CO}_2 \xrightarrow{k_{16}} \text{O}_2 + \text{CO}_2(\nu_2)$	901	$k_{16} = 2.35 \cdot 10^5$	$1.6 \cdot 10^5$ [10]
(17)	$\text{CH}_4(2\nu_b) + \text{CO}_2 \xrightarrow{k_{17}} \text{CH}_4(\nu_b) + \text{CO}_2(\nu_1)$	34	$k_{17} = 5.3 \cdot 10^6$	-
(18)	$\text{CO}_2(\nu_1) + M \xrightarrow{k_{18}^M} \text{CO}_2(2\nu_2) + M$	-101	$k_{18}^{\text{N}_2} = 3.7 \cdot 10^8$	$3.7 \cdot 10^8$ [9]
			$k_{18}^{\text{H}_2\text{O}} = 3.7 \cdot 10^8$	$3.7 \cdot 10^8$ [9]
			$k_{18}^{\text{O}_2} = 3.7 \cdot 10^8$	$3.7 \cdot 10^8$ [9]
			$k_{18}^{\text{CO}_2} = 3.7 \cdot 10^8$	$3.7 \cdot 10^8$ [9]
(19)	$\text{CO}_2(2\nu_2) + M \xrightarrow{k_{19}^M} \text{CO}_2(\nu_2) + M$	-632	$k_{19}^{\text{N}_2} = 3 \cdot 10^5$	$2.9 \cdot 10^5$ [11]
			$k_{19}^{\text{H}_2\text{O}} = 8.7 \cdot 10^8$	-
			$k_{19}^{\text{O}_2} = 3 \cdot 10^5$	$3.9 \cdot 10^5$ [11]
			$k_{19}^{\text{CO}_2} = 3.2 \cdot 10^5$	-
(20)	$\text{CO}_2(\nu_2) + M \xrightarrow{k_{20}^M} \text{CO}_2 + M$	-655	$k_{20}^{\text{H}_2\text{O}} = 4.4 \cdot 10^8$	$4.4 \cdot 10^8$ [11]

*Continued on next page*

Table 4.1 – *Continued from previous page*

Reaction		$\Delta E$ in $\text{cm}^{-1}$	Reaction rate $k$ in $\text{s}^{-1}$	
			used	literature
			$k_{20}^{\text{O}_2} = 1.3 \cdot 10^5$	$1.3 \cdot 10^5$ [11]
			$k_{20}^{\text{CO}_2} = 1.6 \cdot 10^5$	$1.6 \cdot 10^5$ [11]
(21)	$\text{CO}_2(2\nu_2) + \text{CO}_2 \xrightarrow{k_{21}} \text{CO}_2(\nu_2) + \text{CO}_2(\nu_2)$	23	$k_{21} = 5.9 \cdot 10^8$	$5.9 \cdot 10^8$ [11]

### 4.1.3 Molecule parameters

**Tab. 4.2.** Listing of the molecular parameters mass  $M$ , radii at infinite temperature  $r|_{T \rightarrow \infty}$  and Sutherland constants  $T_V$  [12]

Molecule	$M$ in g/mol	$r _{T \rightarrow \infty}$ in Å	$T_V$ in K
N <sub>2</sub>	28	1.6	112
O <sub>2</sub>	32	1.48	132
H <sub>2</sub> O	18	1.34	600
CO <sub>2</sub>	44	1.73	273
CH <sub>4</sub>	16	1.66	164

**Tab. 4.3.** Listing of the molecules' vibration details notation, energy  $\Delta E$  and degeneracy  $n$ .

Molecule	notation of vibration	$\Delta E$ in cm <sup>-1</sup>	$n$
N <sub>2</sub>	$\nu$	2330	1
O <sub>2</sub>	$\nu$	1556	1
H <sub>2</sub> O	$\nu_2$	1595	1
CO <sub>2</sub>	$\nu_2$	655	2
	$2\nu_2$	1287	2
CH <sub>4</sub>	$\nu_1$	1388	1
	$\nu_b$	1422	5
	$2\nu_b$	2844	5
	$\nu_{s,1}$	2968	4

## References

- [1] P. Hess et al. “Vibration→vibration energy transfer in methane”. In: *J. Chem. Phys.* 72.10 (May 1980), pp. 5525–5531. ISSN: 0021-9606. DOI: 10.1063/1.438970 (cit. on p. 64).
- [2] L. Doyennette et al. “Vibrational Energy Transfer in Methane Excited to  $2\nu_3$  in CH<sub>4</sub>-N<sub>2</sub>/O<sub>2</sub> Mixtures from Laser-Induced Fluorescence Measurements”. In: *J. Phys. Chem. A* 102.22 (May 1998), pp. 3849–3855. ISSN: 1089-5639. DOI: 10.1021/jp9806462 (cit. on p. 64).
- [3] C. Boursier et al. “Vibrational Relaxation of Methane by Oxygen Collisions: Measurements of the Near-Resonant Energy Transfer between CH<sub>4</sub> and O<sub>2</sub> at Low Temperature”. In: *J. Phys. Chem. A* 111.30 (Aug. 2007), pp. 7022–7030. ISSN: 1089-5639. DOI: 10.1021/jp072377y (cit. on pp. 64, 65).
- [4] C. Boursier et al. “Rovibrational Relaxation of Methane in CH<sub>4</sub>-N<sub>2</sub> Mixtures: Time-Resolved IR-IR Double-Resonance Measurements at 193 K and Kinetic Modeling”. In: *J. Phys. Chem. A* 107.27 (July 2003), pp. 5280–5290. ISSN: 1089-5639. DOI: 10.1021/jp034265m (cit. on pp. 64, 65).
- [5] D. L. Huestis. “Vibrational Energy Transfer and Relaxation in O<sub>2</sub> and H<sub>2</sub>O”. In: *J. Phys. Chem. A* 110.21 (June 2006), pp. 6638–6642. ISSN: 1089-5639. DOI: 10.1021/jp054889n (cit. on pp. 64, 65).
- [6] J. N. Bass. “Translation to vibration energy transfer in O + NH<sub>3</sub> and O + CO<sub>2</sub> collisions”. In: *J. Chem. Phys.* 60.7 (Apr. 1974), pp. 2913–2921. ISSN: 0021-9606. DOI: 10.1063/1.1681461 (cit. on p. 64).
- [7] H. E. Bass et al. “Vibrational and rotational relaxation in mixtures of water vapor and oxygen”. In: *J. Acoust. Soc. Am.* 60.1 (July 1976), pp. 74–77. ISSN: 0001-4966. DOI: 10.1121/1.381050 (cit. on p. 65).
- [8] D. R. White. “Vibrational Relaxation of Oxygen by Methane, Acetylene, and Ethylene”. In: *J. Chem. Phys.* 42.6 (Mar. 1965), pp. 2028–2032. ISSN: 0021-9606. DOI: 10.1063/1.1696241 (cit. on p. 65).
- [9] H. E. Bass. “Absorption of sound by air: High temperature predictions”. In: *J. Acoust. Soc. Am.* 69.1 (Jan. 1981), pp. 124–138. ISSN: 0001-4966. DOI: 10.1121/1.385356 (cit. on p. 65).
- [10] H. E. Bass and H.-J. Bauer. “Kinetic Model for Thermal Blooming in the Atmosphere”. In: *Applied Optics* 12.7 (July 1973), p. 1506. ISSN: 0003-6935. DOI: 10.1364/AO.12.001506 (cit. on p. 65).
- [11] M. García-Comas et al. “Errors in Sounding of the Atmosphere using Broadband Emission Radiometry (SABER) kinetic temperature caused by non-local-thermodynamic-equilibrium model parameters”. In: *J. Geophys. Res.* 113.D24 (Dec. 2008), p. D24106. ISSN: 0148-0227. DOI: 10.1029/2008JD010105 (cit. on pp. 65, 66).

- 
- [12] G. Wiegleb. “Physikalische Eigenschaften von Gasen”. In: *Gasmesstechnik Theor. und Prax.* Wiesbaden: Springer Fachmedien Wiesbaden, 2016, pp. 7–118. DOI: 10.1007/978-3-658-10687-4\_2 (cit. on p. 67).

## 4.2 [P1] - An algorithmic approach to compute the effect of non-radiative relaxation processes in photoacoustic spectroscopy

This chapter has already been published in *Photoacoustics*, vol. 26, no. June 2022, p. 100371, June 2022, <https://doi.org/10.1016/j.pacs.2022.100371>.

In the last 20 years, scientific and commercial interest in photoacoustic (PA) gas sensors has increased immensely. In previous works, the focus was often solely on the advantages of photoacoustic gas sensors, e.g. high spectral selectivity, high sensitivity and the great potential for miniaturization, in order to demonstrate the capability for mobile trace gas analysis. As a result, miniaturized and low-cost PA sensor systems with remarkable limits of detection (LoD) in the parts per billion (ppbV) or even parts per trillion (pptV) range have been published [1–18]. However, in recent years the major disadvantage of photoacoustics, namely the PA-signal dependency on a changing bulk composition due to relaxation-based energy dissipation has been increasingly addressed and analyzed by the scientific community [2, 7, 11, 12, 19–24]. The photoacoustic signal results from molecular collisions converting internal energy states into kinetic energy of translation. By studying recent literature dealing with the importance of molecular relaxation in photoacoustics, it becomes noticeable that a wealth of the published work is prone to inadequacies in the assumptions made. The cascade of relaxation processes is often oversimplified, e.g. by hypothesizing two-level systems, which can only be applied if the initially excited state is the lowest one, i.e. no species of the composition exhibits an intermediate state between the excited one and ground state [25], and by disregarding vibrational-vibrational (VV) energy transfer processes. However, to be able to develop photoacoustic sensors that provide reliable analyte readings even in complex, frequently altering bulk mixtures, a comprehensive understanding of the phenomenon of molecular collisional relaxation is inevitable. Hunter et al. [25] already presented a universal relaxation model based on reaction kinetics in 1974 to calculate the population densities of all energy states of every molecule involved in PA-signal generation as well as the complex heat production rates of the separate relaxation paths finally yielding the overall heat production and photoacoustic phase lag. In a previous work we implemented the underlying mathematical correlations of Hunter et al. into a MATLAB script by predefining the route of relaxation in terms of mid-infrared methane excitation in a gas matrix containing nitrogen, oxygen and water and compared the simulations with our measurement results [7]. However, due to restrictions in the measurement setup in [7], we were incapable of measuring the water-induced signal increase in detail, since the smallest adjustable water concentration already resulted in 100% accelerated relaxation. For this reason, we modified our gas mixing system by integrating a simple self-designed humidity generator (see chapter 3.1.1, Figure 3.2). This setup enables humidification of the sample gas in much smaller increments, which allows for a more detailed investigation of amplitude and phase characteristics. The development of CoNRad was based on the fundamental physical understanding of

relaxation processes. CoNRad autonomously identifies the entire relaxation cascade of a given system. Based on this, the overall relaxation efficiency considering mutually competing energy transitions is calculated, yielding a completely theoretically derived photoacoustic signal. Thus, potential influences on the PA signal resulting from relaxation phenomena can be determined not only qualitatively but also quantitatively. As a result, our approach prevents erroneous conclusions that might otherwise be drawn due to a lack of distinction between various physical effects.

## 4.2.1 Methods

### Photoacoustic signal generation

The first step in order to describe the photoacoustic signal mathematically is to establish a formula for the time dependent heat production rate per volume  $\dot{H}(t)$  with unit  $[\text{Js}^{-1}\text{m}^{-3}]$ .

$$\dot{H}(t) = [\nu_A](t) \frac{(hc_0 \tilde{\nu}_{\text{Ph}})}{\tau_A} = \dot{H}_0 e^{i(\omega t - \phi_A)} \quad (4.1)$$

$$\dot{H}_0 = \frac{(\rho_A \sigma_A \tilde{\nu}_{\text{Ph}})}{\pi r_b^2} \cdot \frac{1}{\sqrt{1 + (\omega \tau_A)^2}} \quad (4.2)$$

Therein  $\rho_A$  is the volume number density of the analyte A,  $[\nu_A](t)$  is the time dependent population density of the excited analyte state,  $h$  is the Planck constant,  $c_0$  the speed of light in vacuum,  $\sigma_A(\tilde{\nu}_{\text{Ph}})$  the absorption cross section in  $\text{m}^2$  at the emitted wavenumber  $\tilde{\nu}_{\text{Ph}}$  and  $\tau_A$  is the non-radiative relaxation lifetime of the excited state of the analyte. The phase lag  $\phi_A = \arctan(\omega \tau_A)$  represents the time that is needed for PA signal generation, i.e. the duration from photon absorption to local heat input. The laser beam radius is designated to  $r_b$  and its optical power  $P_0$  is modulated with an angular frequency  $\omega = 2\pi f$ . In terms of photoacoustic spectroscopy (PAS), the combined solution of the Navier-Stokes equation, the thermal diffusion equation and the mass-density continuity equation yields a dampened wave equation for the photoacoustic sound pressure  $p_a$  [3, 7, 26]. This wave equation provides the correlation between heat input and acoustic pressure. Regardless of the photoacoustic measurement setup, the photoacoustic pressure  $p_a$  can generally be defined as a function of the relaxation induced heat production rate  $\dot{H}(t)$  (refer to equations 4.1 and 4.2)

$$p_a \propto \frac{(\rho_A \sigma_A \tilde{\nu}_{\text{Ph}})}{\pi r_b^2} \cdot \frac{1}{\underbrace{\sqrt{1 + (\omega \tau_A)^2}}_{|\vec{\epsilon}_{\text{relax}}|}} \quad (4.3)$$

with  $|\vec{\epsilon}_{\text{relax}}|$  representing the efficiency of total non-radiative relaxation. If, for instance, the lowest energy state  $\nu_{1,A}$  of a molecule A, with its time dependent popu-

lation density written as  $[\nu_{1,A}](t)$ , is excited by laser radiation that may exclusively relax to the vibronic ground state, equation can be written as,

$$\dot{H}_{\nu_{1,A}}(t) = [\nu_{1,A}](t) \cdot \frac{hc_0 \tilde{\nu}_{1,A}}{\tau_{\nu_{1,A}}} = [\nu_{1,A}](t) \cdot (k_{\nu_{1,A}} \cdot hc_0 \tilde{\nu}_{1,A}) \quad (4.4)$$

where the relaxation time is substituted with its inverse relaxation rate  $k_{\nu_{1,A}} = 1/\tau_{\nu_{1,A}}$ . However, equation 4.4 only accounts for the simplest scenario of exclusive vibrational-translational (VT) relaxation of the initially excited energy level to the ground state  $\nu_0$ . Inter – or intramolecular energy transitions (VV relaxation), in which some of the vibronic energy is not released as translational energy are neglected. Barreiro et al. as well as our group demonstrated in previous works, that these simplifications cannot be applied to many real applications [7, 23, 24]. Hunter et al. modified equation 4.4 for arbitrarily complex relaxation systems [25]. A brief derivation of the formula established by Hunter et al. is provided in the appendix A.4. For a more in-depth explanation refer to [25]. Hence, the population densities of the individual energy states not only depend on the quantity of initially excited analyte molecules, but also on the entire relaxation process [25]. Each energy transition contributes an individual phase and amplitude to the overall photoacoustic signal vector. Real-life applications of photoacoustic sensors are often subject to complex and varying gas compositions (e.g. relative humidity in ambient air or carbon dioxide (CO<sub>2</sub>) in exhaled breath), which significantly increases the number of collision reactions to be considered compared to simple gas matrices containing only the analyte diluted in nitrogen. However, it is impractical to manually compute the entire relaxation cascade, considering a multitude of mutually influencing energy transitions. Therefore, we developed an algorithm (CoNRad) that provides an elegant solution to this problem.

### The algorithm (CoNRad)

CoNRad, an algorithm to compute the collision based non-radiative efficiency and phase lag of energy relaxation on a molecular level, implemented in Python programming language, requires all energy states and all possible vibronic energy transfer reactions of the system for cascade computation, which often demands elaborate literature research. Those reactions are tabulated and linked to a relaxation rate, which must also be searched for in literature. The main difference between our approach and Hunter's et al. is that we take into account the heat released for each single reaction, while Hunter et al. consider the cumulative heat production of all reactions that contribute to one specific change of states [25]. Therefore, CoNRad can be described as a reaction-based approach, whereas Hunter's et al. calculations are rather based on changes in density of states. Figure 4.2 illustrates a simplified programming flowchart of CoNRad. As a prerequisite for cascade calculation, the initially laser-excited analyte state  $i_0$  must be predefined. Further start conditions are  $\vec{\epsilon}_{\text{relax}} = 0$  and weighting  $w = 1$  specifying the complex efficiency of overall relaxation and a weighting factor, respectively. After computation, the absolute value  $|\vec{\epsilon}_{\text{relax}}|$  of



relaxation rate  $k_j$  and the volume ratio of the collision partner  $N_j$  summarized over all reactions  $m$ , which reveals their competitive nature. To quantify heat production, the term  $dE/E_0$  considers the energy of product states minus reactant states  $dE$  as well as the energy of the initially laser-excited state  $E_0$ . Whilst iterative execution, every reaction  $j$  is checked to see whether both collision products have reached the ground state already. If not, the excited product states are used as input value to recursively trigger the algorithm from the start, i.e. looking up all reactions  $m$  that manate from state  $i$ . If, on the other hand, both collisional products have reached the ground state and both *For*-loops iterating energy states and reactions have run through, the calculation is completed. The resulting relaxation efficiency  $\vec{\epsilon}_{\text{relax}}$  is multiplied with the cell constant  $C_{\text{cell}}$ , containing the quality factor  $Q$ , the resonance frequency  $\omega_{\text{res}}$ , the ratio of acoustical resonator length and volume  $L_r/V_r$  and the decremented adiabatic exponent of the measurement gas  $(\gamma - 1)$ . Further, the optical power  $P_0$ , the microphone sensitivity in  $\mu\text{V mbar}^{-1}$  and a refinement factor  $C_{\text{corr}}$  are also considered. This factor was found to be 0.865 and kept constant for every data point and every measurement series. The purpose of  $C_{\text{corr}}$  is to transfer the simulated data from CoNRad to the measured photoacoustic voltage, by accounting for a multitude of potential non-ideal conditions in the measurement setup, e.g. non-ideal ( $< 100\%$ ) light to sound coupling.

It should be noted that only the general function principle of the algorithm is discussed within this context. More sophisticated routines had to be developed to account for reactions which depend on each other or even form circular references (refer to Figure 4.3). Particularly, methane, oxygen and water form such circular transitions (see Figure 4.1,  $k_{6-11}$ ), which are discussed in detail in chapter 4.2.2.

## Experimental setup

The experimental setup used for this work was already described in chapter 3.1 and is almost identical to [7]. The complete gas mixing system is illustrated in Figures 3.1 and 3.2. The commercially available humidity generator used in our previous work [7] was substituted by a simple self-designed humidity generator, which consists of a temperature-controlled aluminum tank filled with water, see Figure 3.2. The measurement gas can be directed into the photoacoustic measurement cell (PAC) via

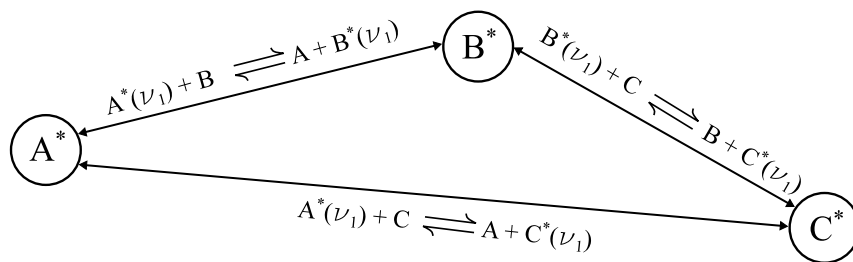


**Fig. 4.3.** Example of three excited states  $A^*(\nu_1)$ ,  $B^*(\nu_1)$  and  $C^*(\nu_1)$  forming a circular reference.

a tee fitting connected to the humidified gas path (Figure 3.2,  $F_{(i)}$ ) and the dry path (Figure 3.2,  $F_{(ii)}$ ). It should be mentioned that the process gas is humidified only by the gas phase inside the aluminum tank, as it does not pass through the liquid water. The fraction of the process gas that is humidified can be adjusted manually, using two needle valves. The final humidity content present in the PAC cell is measured by a BME280 (Bosch, Germany). When bypassing gas path  $F_{(i)}$  the dry gas mixture enters the PAC directly.

Analogous to [7], we use the same interband cascade laser (ICL) diode mounted into a TO66 package, emitting at 3368.8 nm ( $2968.4 \text{ cm}^{-1}$ ) for methane ( $\sigma_{\text{CH}_4} = 4.9 \cdot 10^{-19} \text{ cm}^2 \text{ mole}^{-1}$  at ambient pressure and  $40^\circ \text{C}$ ) detection.

## 4.2.2 Results and discussion

To emphasize the relevance of VV transitions when interpreting photoacoustic measurements, in chapter 4.2.2. the simplest possible theoretical Jablonsky diagram of a ternary system is discussed. In this theoretical relaxation scenario the analyte molecule A can only relax via VT transitions. Molecule C is successively added to the measurement matrix by increments of 0.1 %V and up to a maximum volume ratio of  $N_C = 4.9 \text{ %V}$ . The analyte volume ratio remains constant with  $N_A = 15 \text{ ppmV}$  for each gas composition. Hence, the volume ratio of molecule B is  $N_B = 1 - N_A - N_C$ . The following chapters deal with the different effects of oxygen (chapter 4.2.2), water (chapter 4.2.2) and the combined effect of oxygen and water (chapter 4.2.2) on the mid-IR ( $2968 \text{ cm}^{-1}$ ) photoacoustic detection of methane, to verify CoNRad for real-life scenarios. Chapter 4.2.2 compares the data provided by Hayden et al. [19] with those obtained from CoNRad for the mid-IR ( $2180 \text{ cm}^{-1}$ ) detection of carbon monoxide, with regards to water induced relaxational phenomena.

### Vibrational-translational relaxation

The theoretical Jablonski diagram shown in Figure 4.4 describes the simplest case of non-radiative relaxation of a ternary system. The y-axis represents the energy of the respective vibrational states in  $\text{cm}^{-1}$ , the x-axis subdivides the participating molecules A, B and C. Although C shows an energetically comparable vibrational state ( $\nu_{1,C}$ ) to the initially excited state  $\nu_{1,A}$ , in this example  $\nu_{1,A}$  can only relax directly to the ground state via classical VT relaxation. Molecule B shows no relevant vibrational state in the displayed region.

The rates of ( $R_1$ ) and ( $R_2$ ) were kept constant in this example, since the influence of molecule C on the VT relaxation is of particular interest. For this purpose, five scenarios (Figure 4.5) were simulated starting with a comparatively slow VT energy transition  $k_3 = 1 \cdot 10^2$  of A with C, logarithmically increasing up to  $k_3 = 1 \cdot 10^6$ .

**Tab. 4.4.** Individual reactions and their reaction ratios  $k_{1,2,3}$  for the discussed Jablonski diagram (Figure 4.4).

	Reaction	$k$ in $\text{s}^{-1}\text{atm}^{-1}$
(R <sub>1</sub> )	$A^*(\nu_1) + A \xrightarrow{k_1} A + A; dE = -E_{\nu_1,A}$	$1 \cdot 10^6$
(R <sub>1</sub> )	$A^*(\nu_1) + B \xrightarrow{k_1} A + B; dE = -E_{\nu_1,A}$	$5 \cdot 10^3$
		$1 \cdot 10^2$
		$1 \cdot 10^3$
(R <sub>1</sub> )	$A^*(\nu_1) + C \xrightarrow{k_1} A + C; dE = -E_{\nu_1,A}$	$1 \cdot 10^4$
		$1 \cdot 10^5$
		$1 \cdot 10^6$

As this scenario is purely hypothetical, for the purpose of simplicity the resonance frequency was kept constant at  $\omega_{\text{res}} = 2\pi \cdot 1000$  Hz. In real applications, gas composition induced resonance frequency variations must be accounted for, too. However, the influence of frequency shifts usually affects the photoacoustic signal only in a minor way compared to the influence of relaxation rates. Furthermore, in this subchapter the additional calculations mentioned in chapter 4.2.1, i.e. considering  $C_{\text{cell}}$ ,  $S_{\text{mic}}$  and  $C_{\text{corr}}$  are omitted.

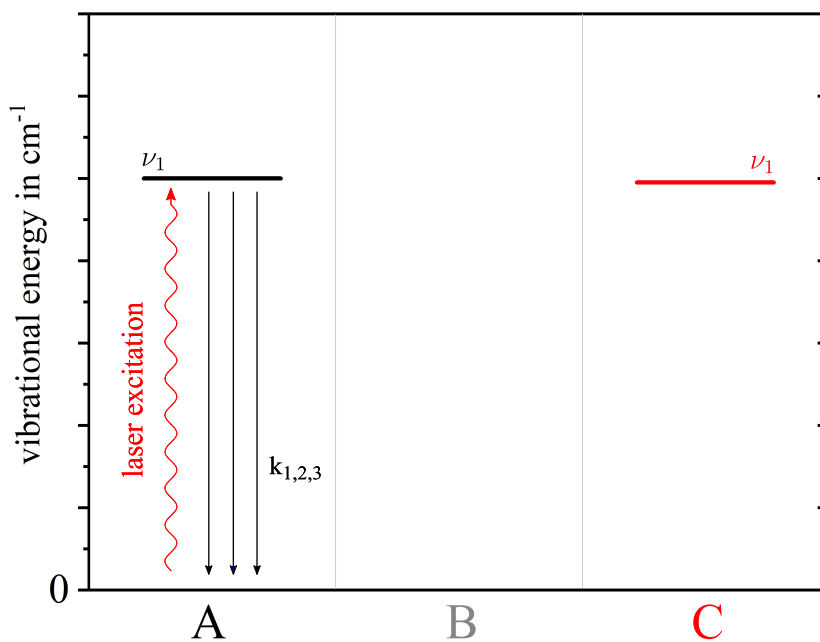


**Fig. 4.4.** Theoretical Jablonski diagram for non-radiative relaxation, only considering VT transitions.

In Figure 4.5 the upper graph displays the overall efficiency of relaxation  $\epsilon_{\text{relax}}$ , being equivalent to the relaxation dependent photoacoustic magnitude. In addition, the graph below represents the corresponding relative phase lag  $\phi$  with reference to the photoacoustic phase of the first simulation point. A relative photoacoustic signal amplitude of  $\epsilon_{\text{relax}} = 1$  would be equivalent to 100 % relaxation of all states actively involved in the cascade, yielding no relaxation losses. In this particular two-level scenario (see Figure 4.4)  $\epsilon_{\text{relax}} = 1$  would correspond to 100 % relaxation of  $\nu_{1,A}$ . Referring to Figure 4.5, the first amplitude value is  $\epsilon_{\text{relax}} = 0.62$ . This implies that  $N_A = 15$  ppmV being only diluted with molecules of type B, i.e. no C is present, and with the relaxation rates given in Table 4.4, 38 % of the initially excited analyte molecules A are not able to relax in time, thus not releasing any extra kinetic energy into the system. Regarding photoacoustic signal generation, this percentage is lost. By successively adding C to the composition, five different amplitude and phase characteristics are obtained for the respective relaxation rate  $k_3$ . The most distinct effect, both in amplitude and phase, can be observed for very rapid VT relaxation of A colliding with C ( $k_3 = 1 \cdot 10^6$ ), represented by the orange downward pointing

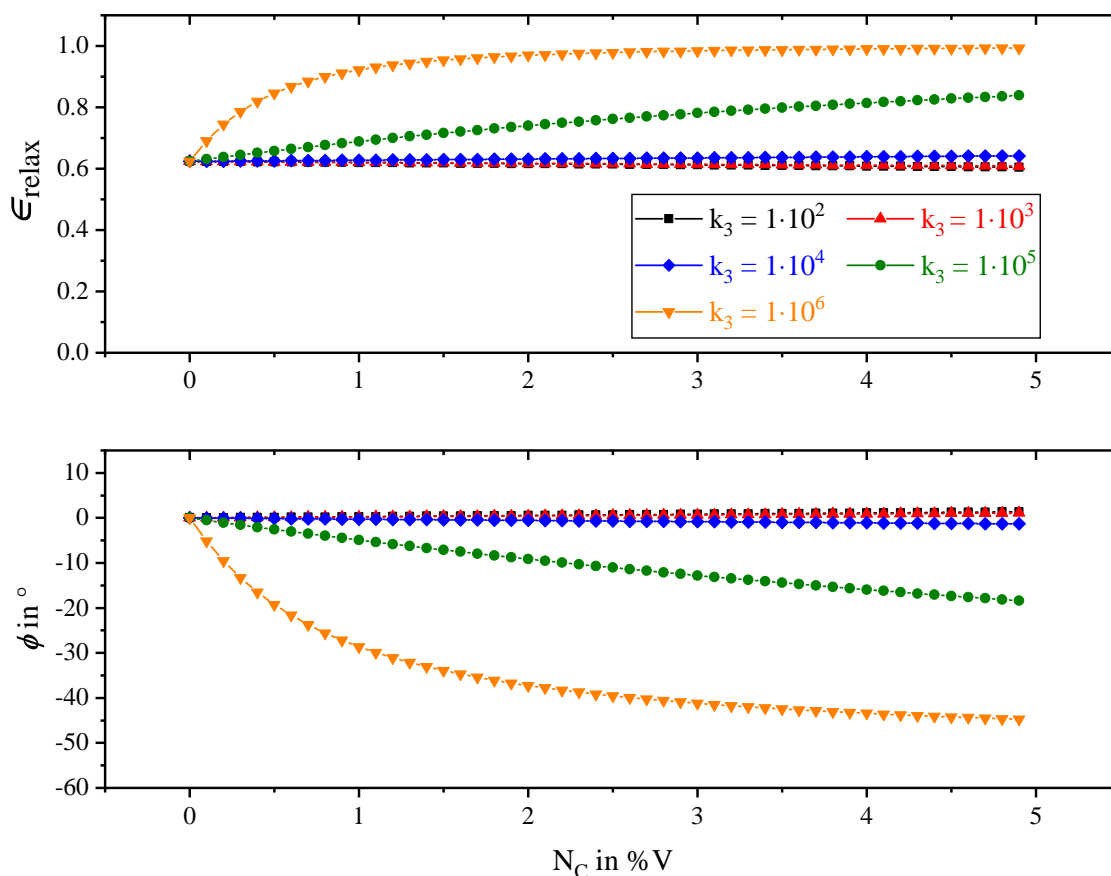


**Fig. 4.5.** Simulated relative photoacoustic signal amplitudes (upper graphs) and corresponding phase lags (lower graphs) for the theoretical relaxation cascade shown in Figure 4.4. The reaction rate of VT relaxation of A colliding with C (Table 4.4,  $R_3$ ) is varied from  $1 \cdot 10^2$  to  $1 \cdot 10^6$  in logarithmic steps.

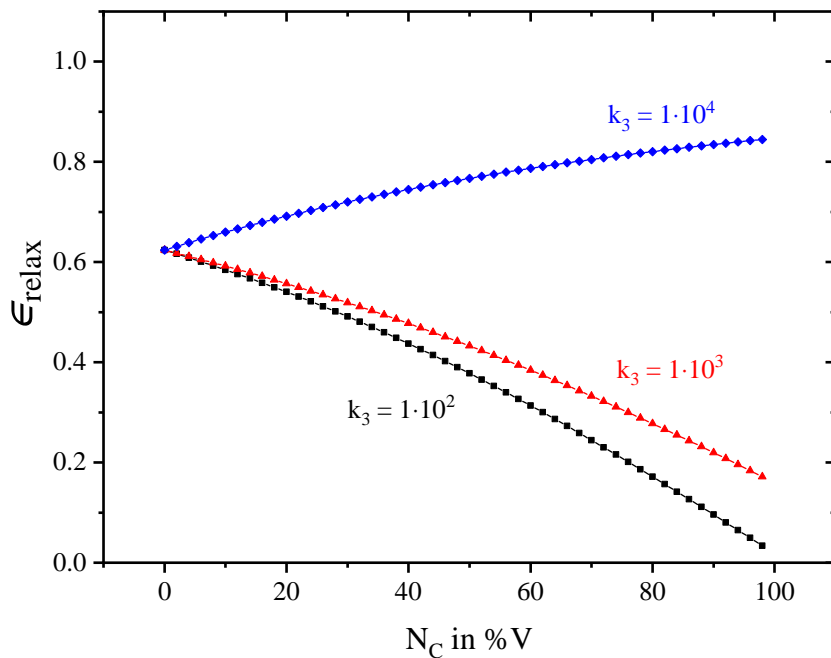


**Fig. 4.6.** Relative photoacoustic signal amplitude for higher C concentrations ( $N_{C,\max} = 99\%V$ ) simulated for  $k_3 = 1 \cdot 10^4$  (blue rhombus),  $k_3 = 1 \cdot 10^3$  (red triangles) and  $k_3 = 1 \cdot 10^2$  (black squares).

triangles in Figure 4.5. At the maximum simulated volume ratio of  $N_C = 4.9\%V$ , the relative photoacoustic amplitude corresponds to  $\epsilon_{\text{relax}} = 0.99$ . Conversely, the relaxation-related signal loss is only around 1%. The exponential signal increase for  $k_3 = 1 \cdot 10^6$  is accompanied by a significant phase shift  $\Delta\phi(N_C = 4.9\%V) = -44.7^\circ$ . However, once the VT relaxation of A with C is only decreased by a factor of 10 ( $k_3 = 1 \cdot 10^5$ ), this exponential effect in amplitude and phase becomes an almost linear characteristic (green circle data points in Figure 4.5). Even slower relaxation rates hardly show any significant influence on the photoacoustic signal anymore.

By simulating higher concentrations of C up to almost 100 %V, it becomes clear that moderately fast VT transitions of A with C ( $k_3 = 1 \cdot 10^4$ ) still result in an increasing amplitude, albeit with a modest slope (see Figure 4.6). On the contrary, the decelerating effect of the improbable VT relaxation ( $k_3 \leq 1 \cdot 10^3$ ) of A with C dominates for higher C concentrations, even yielding a further amplitude decrease due to relaxation losses. Figure 4.5 and Figure 4.6 demonstrate that assuming exclusively VT relaxation of the analyte, decelerating relaxation processes fail to explain exponential amplitude losses. Those amplitude characteristics are, however, published in literature [7, 27] and addressed in detail in chapter 4.2.2.

### The effect of oxygen on the photoacoustic detection of methane

This chapter addresses the interpretations of empirically data obtained by photoacoustic detection of traces of methane in mixtures of nitrogen and oxygen. Figure

4.1 provides the complete Jablonsky diagram of the laser excitation of methane and subsequent collisional relaxation processes that can occur in such mixtures, further including water, which influence is addresses in chapter 4.2.2 and 4.2.2. Analogous to [7] some vibrational modes of methane are summarized for simplicity. Mode  $\nu_b = 1422 \text{ cm}^{-1}$  (dyad) includes the  $\nu_2$  and  $\nu_4$  bending modes, the harmonics of the bending modes  $2\nu_2$ ,  $2\nu_4$  and  $\nu_4 + \nu_2$  are combined into  $2\nu_b = 2844 \text{ cm}^{-1}$  and  $\nu_{s_1} = 2968 \text{ cm}^{-1}$  represents the two stretching modes  $\nu_1$  and  $\nu_3$ . Figure 4.1 illustrates the purely passive role of nitrogen in the complete relaxation process of methane, i.e. no involvement in any VV transitions. As soon as oxygen is added to a mixture of methane and nitrogen, an exponential magnitude decrease accompanied by a pronounced phase shift can be observed. At the maximum added  $\text{O}_2$  concentration of 19.03 %V, the PA amplitude drops to 7.8 % of its initial value. At the same time, a phase shift of approximately  $14.4^\circ$  is observed. The results calculated by CoNRad are plotted as solid lines in Figure 4.7, showing excellent agreement with the measurement. A list with all relevant energy transitions can be found in Table 4.1. The relaxation characteristics for this scenario can be explained as follows. The ICL excites  $\nu_{s_1}$  at  $2968 \text{ cm}^{-1}$ , which relaxes with  $k_1$  quite fast to the  $2\nu_b$  state. From this state, several energy transitions are possible. Via  $k_2$  and  $k_5$  intramolecular energy

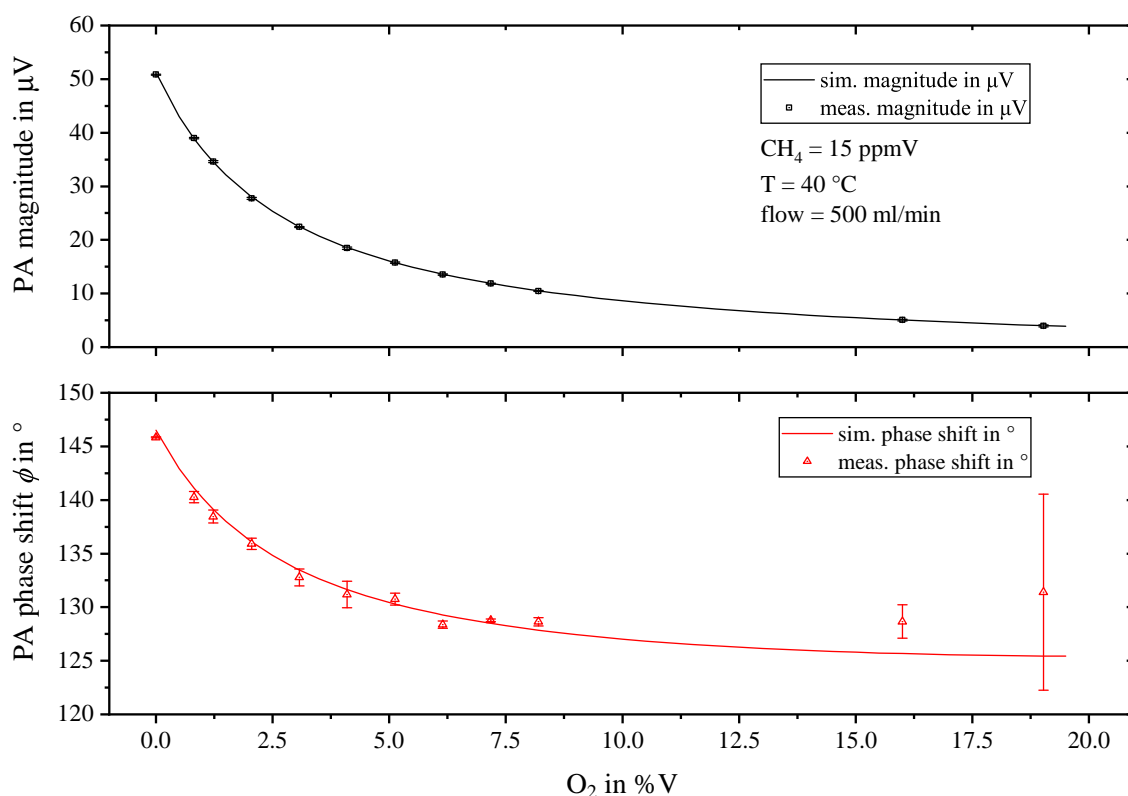


**Fig. 4.7.** Measured photoacoustic magnitude (black squares, upper graph) and phase shift  $\phi$  (red triangles, lower graph) for 15 ppmV methane diluted in dry nitrogen with rising oxygen content. The calculation results obtained from CoNRad with the energy transitions and reaction rates listed in Table 4.1.

transitions resulting in  $\nu_{1,b}$  occur. With reaction 4 ( $k_4$ ), part of the vibronic energy is transferred to the vibrational state of oxygen  $O_2(\nu)$ . This state can also be excited via reaction 7 ( $k_7$ ), which is in direct competition with the classical VT relaxation processes ( $k_{12}$ ) of the  $\nu_{1,b}$  state. Since the intermolecular (VV) energy transitions ( $k_4, k_7$ ) are comparatively fast ( $> 1 \cdot 10^6 \text{ s}^{-1} \text{ atm}^{-1}$ ), see Table 4.1, they dominate the relaxational behavior of  $CH_4$  even at low  $O_2$  concentrations. Due to the rather slow relaxation process originating from  $O_2(\nu)$  ( $k_{14}$ ), a majority of the initially absorbed laser energy accumulates in  $O_2(\nu)$  and can no longer contribute to photoacoustic signal generation, yielding a magnitude decrease.

All measurements are based on raw data that was averaged over one minute, with a data acquisition rate of 5 Hz and a lock-in time constant of 5 s. The error bars indicate  $\pm 3$  times the standard deviation of raw data.

### The effect of water on the photoacoustic detection of methane

To further investigate the signal characteristics resulting from water-induced relaxation changes, we integrated a setup that allows trace humidification of the sample

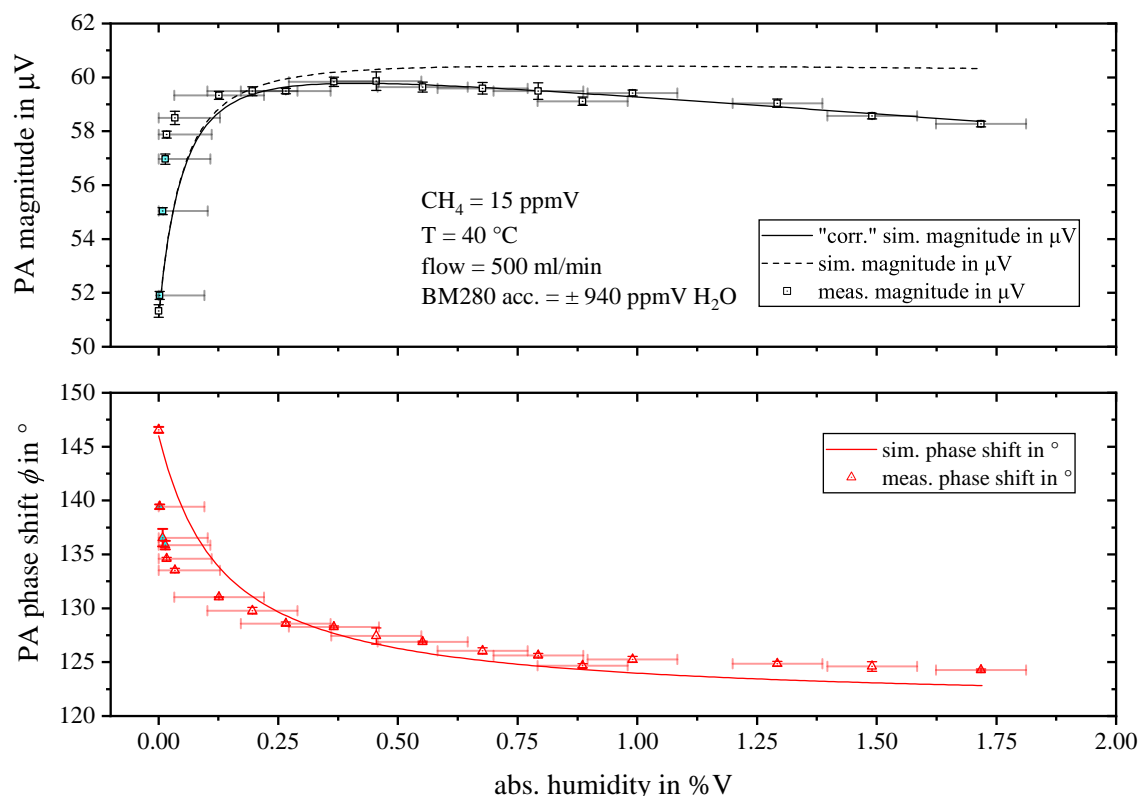


**Fig. 4.8.** Measured photoacoustic magnitude (black squares, upper graph) and phase shift  $\phi$  (red triangles, lower graph) for 15 ppmV methane diluted in nitrogen with rising humidity content. The calculation results obtained from CoNRad are represent by solid lines.

(refer to Figure 3.2). As the BME280 is not able to monitor traces of water, the first three water concentrations (light blue filled measurement points in Figure 4.8) were approximated linearly to the respective measured PA magnitude and to the BME reading of the fourth measuring point. According to the datasheet, the measurement accuracy of the BME280 is specified as  $\pm 3\%$  relative humidity at  $25\text{ }^\circ\text{C}$ . This corresponds to approximately  $\pm 940\text{ ppmV H}_2\text{O}$ . By adding water to the measurement matrix, the exact opposite is achieved compared to adding  $\text{O}_2$ . While oxygen inhibits PA signal generation due to extremely slow VT relaxation rates ( $k_{14}$ ),  $\text{H}_2\text{O}$  causes a significant increase in magnitude ( $+16.6\%$  at  $0.45\%$   $\text{H}_2\text{O}$ , compared to the dry nitrogen). Again, this magnitude change is accompanied by a distinct phase shift, of  $-22.3^\circ$  for  $1.72\%$   $\text{H}_2\text{O}$ . This implies, that methane cannot relax completely in pure nitrogen at an acoustic frequency of  $f_{\text{res}} = 5205\text{ Hz}$ . Due to the two very fast VV transitions ( $k_3, k_6$ ) from methane to water, the transitions from  $2\nu_b$  and  $\nu_b$  to  $\text{H}_2\text{O}(\nu_2)$  dominate the relaxation of methane. Since excited  $\text{H}_2\text{O}(\nu_2)$  itself rapidly relaxes to the ground state via reaction 13 ( $k_{13}$ ), the entire absorbed energy is transferred into kinetic energy contributing to PA signal generation and resulting in a pronounced signal increase by adding small amounts of water. By further adding water, Figure 4.8 reveals the photoacoustic magnitude to linearly decrease with  $-1.9\%$ / $\%V_{\text{H}_2\text{O}}$ . This decay was included as an empirical value in CoNRad as it is assumed to be no relaxation effect. The original simulation without this empirical quantity is displayed as a dashed line in Figure 4.8. We confirmed our assumption of a non-relaxation dependent decay of the PA magnitude due to water by repeating this measurement series using amplitude modulation (AM) of the ICL instead of

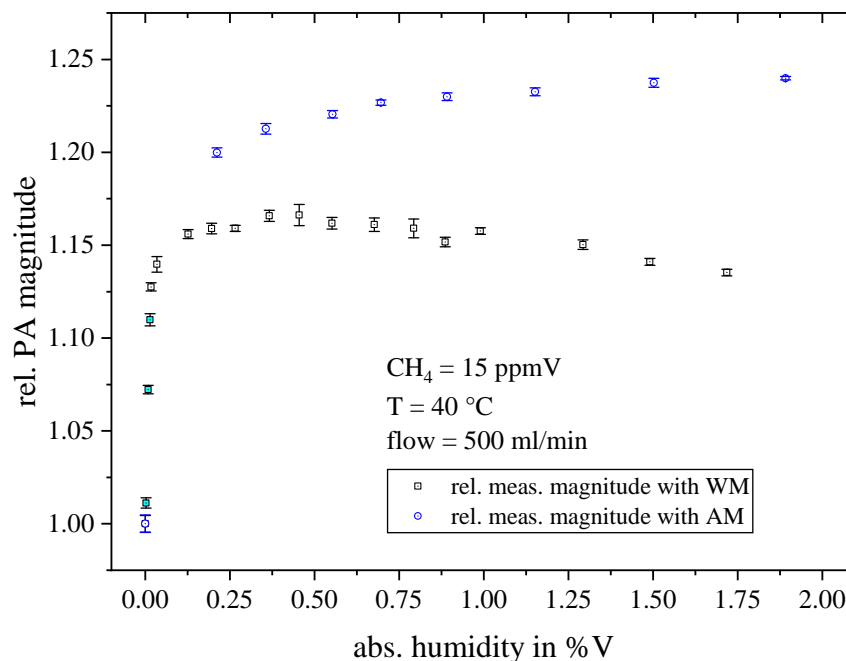


**Fig. 4.9.** Comparison of the measured relative magnitudes resulting from amplitude modulated (AM, blue circles) and wavelength modulated (WM, black squares) methane detection, normalized to the magnitude measured for dry conditions.

wavelength modulation (WM) (see Figure 4.9). Since Figure 4.9 reveals this signal decay to only occur when applying WM, we rather assume peak deformations caused by pressure or collisional broadening effects to be responsible.

### The combined effect of oxygen and water on the photoacoustic detection of methane

Starting with a gas matrix of 15 ppmV CH<sub>4</sub> diluted in a nitrogen (89.75 %V), oxygen (10.25 %V) mixture and continuously adding water using the setup from Figure 3.2 allowed us to investigate the PA signal characteristics in much more detail compared to [7]. As displayed in the upper graph of Figure 4.10, the magnitude loss induced by O<sub>2</sub> is completely compensated by adding water (refer to Table 4.1, reactions 3,6,8 and 13). In total, 29 individual energy transitions were considered by CoNRad for the calculations of this relaxation scenario. The linear magnitude decrease by adding water was observed again and implemented in the calculations (solid line, upper graph in Figure 4.10). For very low moisture levels the phase exhibits a sharp shift of

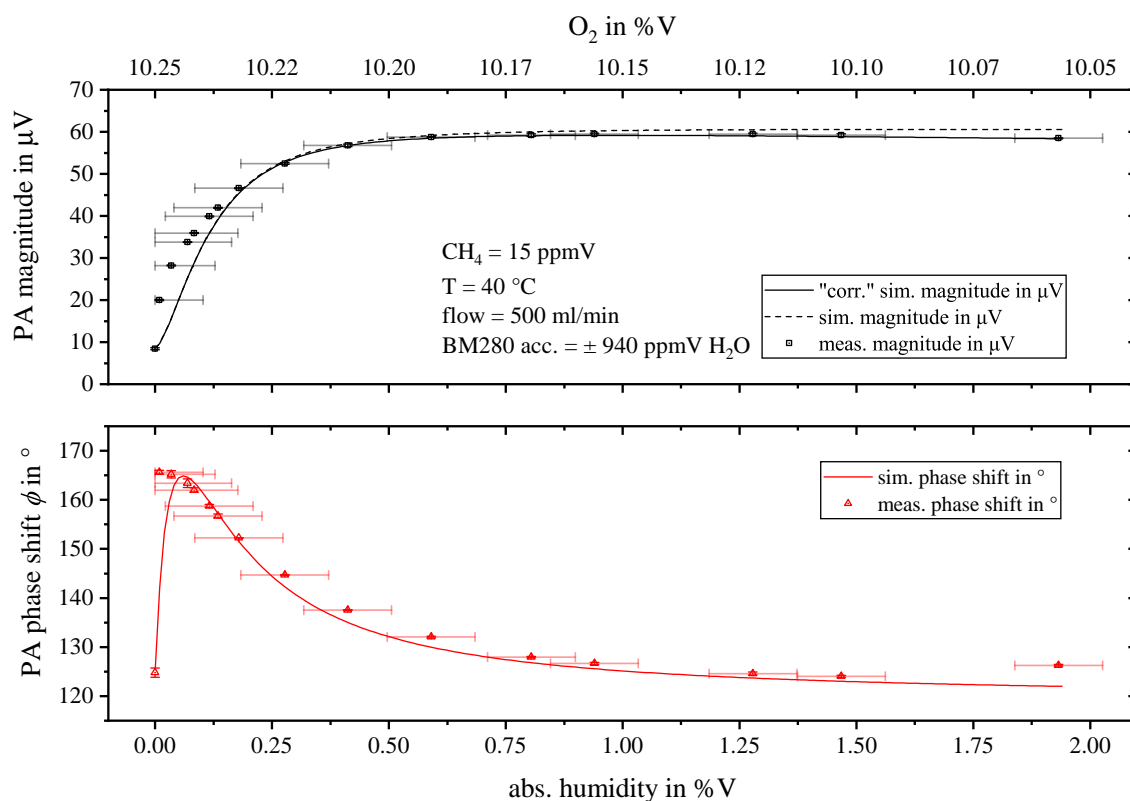


**Fig. 4.10.** Measured photoacoustic magnitude (black squares, upper graph) and phase shift  $\phi$  (red triangles, lower graph) for 15 ppmV methane diluted in a nitrogen, oxygen mixture with rising humidity content. The calculation results obtained from CoNRad are represented by solid lines.

about  $40.9^\circ$ . As soon as the slope of the PA magnitude weakens, the phase decreases again and remains almost constant for higher humidity values ( $> 1\%V$ .)

### Applying CoNRad to other setups

CoNRad allows to quantify relaxation-induced signal changes for arbitrary complex systems. Besides relaxation phenomena, other parameters such as  $Q$ -factor, speed of sound or heat capacity ratio might also significantly affect the PA signal. However, as these parameters, in turn, are influenced in a complex way by environmental conditions, i.e. temperature, pressure and gas composition, those correlations as well as their effect on PA signal generation are discussed in a separate work, see chapter 4.3.

Relaxational and non-relaxational effects on the photoacoustic signal are often mixed when interpreting cross-sensitivities which can lead to misinterpretations. Recently, Wu et al. and Elefante et al. developed compact quartz enhanced photoacoustic

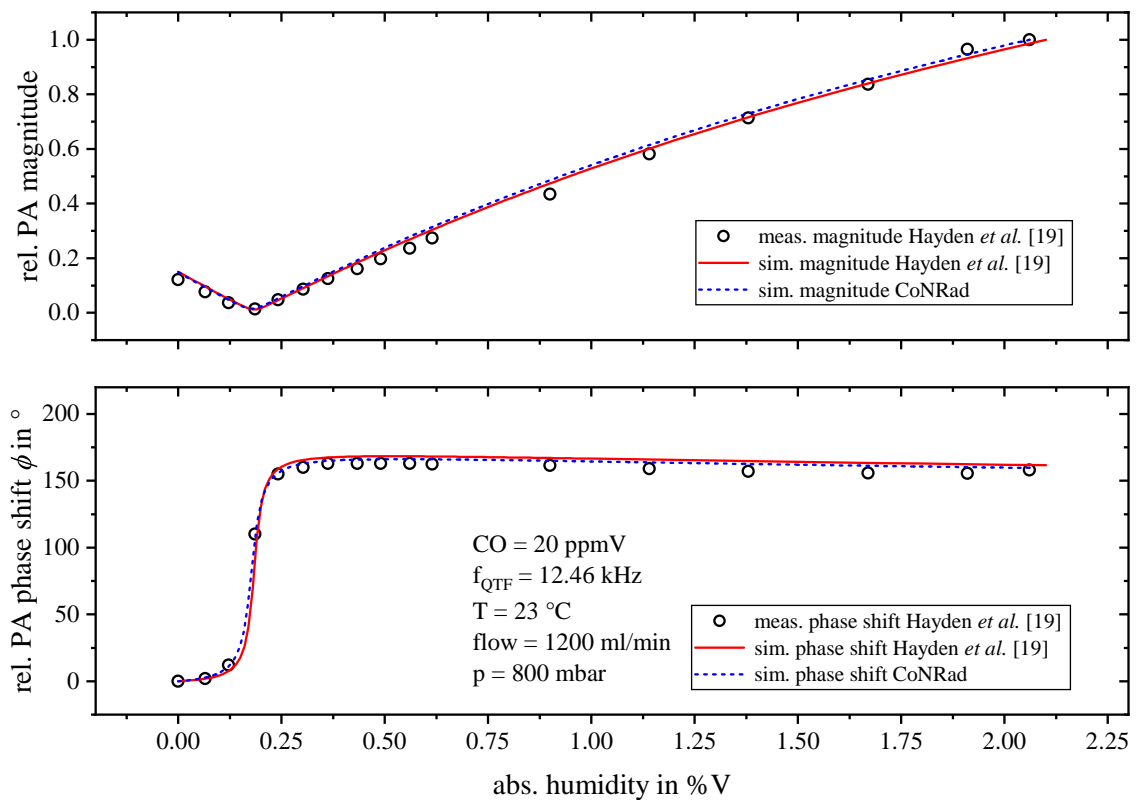


**Fig. 4.11.** Direct comparison of the relative measured photoacoustic data (black circles) from [19] (upper graphs: magnitude, lower graphs: phase shift) with the simulation results from [19] (red solid lines) and the algorithm (CoNRad) presented in this work (blue dashed lines). The data was measured by Hayden et al. by means of QEPAS based carbon monoxide (CO) detection diluted in nitrogen ( $N_2$ ) with varying humidity content.

spectroscopy (QEPAS) sensors for the detection of  $\text{CH}_4$  in humid environments with resonance frequencies of 17.741 kHz and 12.456 kHz, respectively [2, 28]. They were able to achieve parts per billion level LoDs, i.e. 50 ppbV ( $1\sigma$ ) with 1 s integration time [2] and 180 ppbV ( $1\sigma$ ) with 0.2 s integration time [28]. Wu et al. and Elefante et al. employed an interband cascade laser (ICL) emitting at  $3038.5\text{ cm}^{-1}$  and  $2988.8\text{ cm}^{-1}$ , respectively. However, they describe a linear increase of the PA amplitude by continuously adding water within a humidity range from approximately 0.38 %V up to 1.6 %V to a mixture of traces of  $\text{CH}_4$  diluted in  $\text{N}_2$  or laboratory air, respectively. In both publications, this linear correlation was assumed to result from a water-induced acceleration of the VT relaxation behavior of  $\text{CH}_4$ . Simulating these systems with CoNRad reveals a sharp amplitude gain due to water induced acceleration of relaxation, which, however, is already completed for water concentrations of about 0.4 %V. Further adding water does not cause any further relaxation-induced increase in PA amplitude. Therefore, we assume this linear signal increase in [2, 28] rather to be attributed to acoustic detuning. As already reported earlier, double-resonant QEPAS systems are known to be prone to acoustic detuning, as the acoustic resonance depends on the speed of sound within the resonator tube, which in turn depends on temperature and composition of the sample, while the resonance frequency of the QTF is hardly affected by temperature and composition [6, 29].

For the photoacoustic detection of carbon monoxide (CO), by means of QEPAS, in air-like gas matrices, Hayden et al. [19] and Sgobba et al. [12] both developed a theoretical rate equation model describing the complete non-radiative relaxation process of CO in humid nitrogen and humid air. Their theoretical calculations showed excellent agreement with their measurement results. Based on the relaxation rates listed in [19] and [12], we were also able to reproduce the amplitude and phase characteristics of the photoacoustic measurement data reported in [19] (see Figure 4.11). This emphasizes the versatile application possibilities of CoNRad.

### 4.2.3 Conclusion

In this work we have demonstrated the relevance of correctly modelling the relaxation cascade in view of photoacoustic signal generation. Simplified two-level systems and not accounting for intermolecular energy transitions often fail to adequately describe relaxation-induced signal changes. We presented an autonomous algorithm that is capable of modelling any relaxation cascade, regardless of its complexity, thus providing the basis for calculating photoacoustic signals. This algorithm only requires the individual reactions with their corresponding reaction rates and the energies of the vibrational states as input data. Since literature regarding the reaction rates is often not available, this poses the biggest restriction of the algorithm. However, using this approach, we provide a solid basis for calculating different relaxation effects for any analyte, in different applications. Combining CoNRad with spectral measurements, e.g. performing spectral scans as conducted by Menduni et al., would significantly improve the resilience of photoacoustic sensors towards potential cross-sensitivities,

even in complex measurement conditions [30]. This enables the successful transfer of photoacoustic sensor systems from academia to industry.

## References

- [1] H. Zheng et al. “Sub-ppb-level CH<sub>4</sub> detection by exploiting a low-noise differential photoacoustic resonator with a room-temperature interband cascade laser”. In: *Opt. Express* 28.13 (June 2020), p. 19446. ISSN: 1094-4087. DOI: 10.1364/OE.391322 (cit. on p. 70).
- [2] H. Wu et al. “Atmospheric CH<sub>4</sub> measurement near a landfill using an ICL-based QEPAS sensor with V-T relaxation self-calibration”. In: *Sensors Actuators B Chem.* 297 (Oct. 2019), p. 126753. ISSN: 09254005. DOI: 10.1016/j.snb.2019.126753 (cit. on pp. 70, 84).
- [3] T. Rück et al. “NO<sub>2</sub> trace gas monitoring in air using off-beam quartz enhanced photoacoustic spectroscopy (QEPAS) and interference studies towards CO<sub>2</sub>, H<sub>2</sub>O and acoustic noise”. In: *Sensors and Actuators B: Chemical* 255 (Feb. 2017), pp. 2462–2471. ISSN: 09254005. DOI: 10.1016/j.snb.2017.09.039 (cit. on pp. 70, 71).
- [4] P. Breitegger et al. “Towards low-cost QEPAS sensors for nitrogen dioxide detection”. In: *Photoacoustics* 18 (June 2020), p. 100169. ISSN: 22135979. DOI: 10.1016/j.pacs.2020.100169 (cit. on p. 70).
- [5] X. Yang et al. “A Miniaturized QEPAS Trace Gas Sensor with a 3D-Printed Acoustic Detection Module”. In: *Sensors* 17.8 (July 2017), p. 1750. ISSN: 1424-8220. DOI: 10.3390/s17081750 (cit. on p. 70).
- [6] T. Rück et al. “NO<sub>2</sub> trace gas monitoring in air using off-beam quartz enhanced photoacoustic spectroscopy (QEPAS) and interference studies towards CO<sub>2</sub>, H<sub>2</sub>O and acoustic noise”. In: *Sensors and Actuators, B: Chemical* 255.2 (2018), pp. 2462–2471. ISSN: 09254005. DOI: 10.1016/j.snb.2017.09.039 (cit. on pp. 70, 84).
- [7] J. Pangerl et al. “Characterizing a sensitive compact mid-infrared photoacoustic sensor for methane, ethane and acetylene detection considering changing ambient parameters and bulk composition (N<sub>2</sub>, O<sub>2</sub> and H<sub>2</sub>O)”. In: *Sensors Actuators B Chem.* 352 (Feb. 2022), p. 130962. ISSN: 09254005. DOI: 10.1016/j.snb.2021.130962 (cit. on pp. 70–72, 74, 75, 78, 79, 82).
- [8] S. Weigl et al. “Photoacoustic detection of acetone in N<sub>2</sub> and synthetic air using a high power UV LED”. In: *Sensors Actuators B Chem.* 316 (Aug. 2020), p. 128109. ISSN: 09254005. DOI: 10.1016/j.snb.2020.128109 (cit. on p. 70).
- [9] T. Milde et al. “QEPAS sensor in a butterfly package and its application”. In: *Appl. Opt.* 60.15 (May 2021), p. C55. ISSN: 1559-128X. DOI: 10.1364/AO.415236 (cit. on p. 70).

- [10] M. El-Safoury et al. “On-Board Monitoring of SO<sub>2</sub> Ship Emissions Using Resonant Photoacoustic Gas Detection in the UV Range”. In: *Sensors* 21.13 (June 2021), p. 4468. ISSN: 1424-8220. DOI: 10.3390/s21134468 (cit. on p. 70).
- [11] J. B. Christensen et al. “Calibration of Quartz-Enhanced Photoacoustic Sensors for Real-Life Adaptation”. In: *Molecules* 26.3 (Jan. 2021), p. 609. ISSN: 1420-3049. DOI: 10.3390/molecules26030609 (cit. on p. 70).
- [12] F. Sgobba et al. “Compact and portable quartz-enhanced photoacoustic spectroscopy sensor for carbon monoxide environmental monitoring in urban areas”. In: *Photoacoustics* 25 (Mar. 2022), p. 100318. ISSN: 22135979. DOI: 10.1016/j.pacs.2021.100318 (cit. on pp. 70, 84).
- [13] X. Yin et al. “Compact QEPAS humidity sensor in SF<sub>6</sub> buffer gas for high-voltage gas power systems”. In: *Photoacoustics* 25 (Mar. 2022), p. 100319. ISSN: 22135979. DOI: 10.1016/j.pacs.2021.100319 (cit. on p. 70).
- [14] J. Hayden et al. “Mid-infrared intracavity quartz-enhanced photoacoustic spectroscopy with pptv – Level sensitivity using a T-shaped custom tuning fork”. In: *Photoacoustics* 25 (Mar. 2022), p. 100330. ISSN: 22135979. DOI: 10.1016/j.pacs.2022.100330 (cit. on p. 70).
- [15] H. Lin et al. “Ppb-level gas detection using on-beam quartz-enhanced photoacoustic spectroscopy based on a 28 kHz tuning fork”. In: *Photoacoustics* 25 (Mar. 2022), p. 100321. ISSN: 22135979. DOI: 10.1016/j.pacs.2021.100321 (cit. on p. 70).
- [16] L. Liu et al. “Highly sensitive broadband differential infrared photoacoustic spectroscopy with wavelet denoising algorithm for trace gas detection”. In: *Photoacoustics* 21 (Mar. 2021), p. 100228. ISSN: 22135979. DOI: 10.1016/j.pacs.2020.100228 (cit. on p. 70).
- [17] L. Liu et al. “Design and structural optimization of T-resonators for highly sensitive photoacoustic trace gas detection”. In: *Opt. Laser Technol.* 148 (Apr. 2022), p. 107695. ISSN: 00303992. DOI: 10.1016/j.optlastec.2021.107695 (cit. on p. 70).
- [18] S. Weigl et al. “Effects of ambient parameters and cross-sensitivities from O<sub>2</sub>, CO<sub>2</sub> and H<sub>2</sub>O on the photoacoustic detection of acetone in the UV region”. In: *Sensors Actuators B Chem.* 328 (Feb. 2021), p. 129001. ISSN: 09254005. DOI: 10.1016/j.snb.2020.129001 (cit. on p. 70).
- [19] J. Hayden et al. “Anomalous Humidity Dependence in Photoacoustic Spectroscopy of CO Explained by Kinetic Cooling”. In: *Appl. Sci.* 10.3 (Jan. 2020), p. 843. ISSN: 2076-3417. DOI: 10.3390/app10030843 (cit. on pp. 70, 75, 83, 84).
- [20] S. Dello Russo et al. “Quartz-enhanced photoacoustic spectroscopy exploiting low-frequency tuning forks as a tool to measure the vibrational relaxation rate in gas species”. In: *Photoacoustics* 21 (Mar. 2021), p. 100227. ISSN: 22135979. DOI: 10.1016/j.pacs.2020.100227 (cit. on p. 70).

- [21] B. Lang et al. “Molecular relaxation effects on vibrational water vapor photoacoustic spectroscopy in air”. In: *Applied Physics B* 126.4 (Apr. 2020), p. 64. ISSN: 0946-2171. DOI: 10.1007/s00340-020-7409-3 (cit. on p. 70).
- [22] A. A. Kosterev et al. “QEPAS methane sensor performance for humidified gases”. In: *Applied Physics B: Lasers and Optics* 92.1 (2008), pp. 103–109. ISSN: 09462171. DOI: 10.1007/s00340-008-3056-9 (cit. on p. 70).
- [23] N. Barreiro et al. “Influence of oxygen on the resonant photoacoustic signal from methane excited at the  $\nu$  3 mode”. In: *Appl. Phys. B* 104.4 (Sept. 2011), pp. 983–987. ISSN: 0946-2171. DOI: 10.1007/s00340-011-4546-8 (cit. on pp. 70, 72).
- [24] N. Barreiro et al. “Water-based enhancement of the resonant photoacoustic signal from methane–air samples excited at 3.3  $\mu\text{m}$ ”. In: *Appl. Phys. B* 108.2 (Aug. 2012), pp. 369–375. ISSN: 0946-2171. DOI: 10.1007/s00340-012-5018-5 (cit. on pp. 70, 72).
- [25] T. F. Hunter et al. “Photophysical processes in the vapour-phase measured by the optic-acoustic effect. Part 1.—The model and apparatus for the study of radiationless processes”. In: *J. Chem. Soc., Faraday Trans. 2* 70 (1974), pp. 1010–1021. ISSN: 0300-9238. DOI: 10.1039/F29747001010 (cit. on pp. 70, 72).
- [26] J.-P. Besson. “Photoacoustic spectroscopy for multi-gas sensing using near infrared lasers”. Ph. D. thesis. University of Lausanne, 2006 (cit. on p. 71).
- [27] S. Schilt et al. “Methane monitoring by near infrared photoacoustic spectroscopy: The importance of relaxation phenomena”. In: *J. Phys. IV* 125 (June 2005), pp. 7–10. ISSN: 1155-4339. DOI: 10.1051/jp4:2005125002 (cit. on p. 78).
- [28] A. Elefante et al. “Environmental Monitoring of Methane with Quartz-Enhanced Photoacoustic Spectroscopy Exploiting an Electronic Hygrometer to Compensate the H<sub>2</sub>O Influence on the Sensor Signal”. In: *Sensors* 20.10 (May 2020), p. 2935. ISSN: 1424-8220. DOI: 10.3390/s20102935 (cit. on p. 84).
- [29] L. Dong et al. “QEPAS spectrophones: design, optimization, and performance”. In: *Appl. Phys. B* 100.3 (Sept. 2010), pp. 627–635. ISSN: 0946-2171. DOI: 10.1007/s00340-010-4072-0 (cit. on p. 84).
- [30] G. Menduni et al. “High-concentration methane and ethane QEPAS detection employing partial least squares regression to filter out energy relaxation dependence on gas matrix composition”. In: *Photoacoustics* 26 (June 2022), p. 100349. ISSN: 22135979. DOI: 10.1016/j.pacs.2022.100349 (cit. on p. 85).

### 4.3 [P2] - Digital Twin of a photoacoustic trace gas sensor for monitoring methane in complex gas compositions

This chapter has already been published in *Sensors and Actuators, B: Chemical*, vol. 378, no. March 2023, p. 133119, March 2023, <https://doi.org/10.1016/j.snb.2022.133119>.

The term Industry 4.0 was established in the context of a research agenda and a recommendation to further digitalize industrial processes by the German Federal Ministry of Education and Research in 2013 [1]. Today, the term is used worldwide for a future project that focuses on building smart factories to optimize energy and resource efficiency, to avoid supply shortage and, to flexibly adapt processes to market demands [2]. To achieve these goals, novel concepts such as Internet-of-Things (IoT), Predictive Maintenance (PdM) and Digital Twins (DT) have been developed or adapted from other research areas. PdM for example aims to plan maintenance as accurately as possible in advance in order to avoid unexpected equipment failures. The challenge of this concept is the necessity of descriptive process-dependent data, which on the one hand must be generated and on the other hand must be processed. Both challenges can be met by equipping factories with smart sensor systems that are capable of edge computing, i.e. decentralized data preprocessing. Pech et al. provide a comprehensive review of current literature concerning the occurrences of the terms “smart factory”, “predictive maintenance” and “smart sensors”, respectively [3]. Even though the number of publications containing any of these keywords increased sharply since 2000, they found the latter one to stand out, pointing out that the application of smart sensors is mandatory to make the project Industry 4.0 a success. However, many process parameters such as substance-specific quantities in chemical production plants cannot yet be monitored because suitable sensors are simply not available. In order to remedy this lack of availability, several funding initiatives are launched aiming to support the technology transfer from lab to industry. A promising technology in view of this transfer is photoacoustic (PA) spectroscopy as it allows for developing highly sensitive, small-sized and low-cost inline sensors for trace gas monitoring [4–12]. However, due to the complex nature of PA signal generation by molecular collisions [13] as well as miscellaneous signal dependencies on ambient parameters [14, 15], PA sensors are prone to changes in bulk composition, temperature and pressure, thus requiring sophisticated multi-dimensional calibration. To obviate elaborate calibration and to ensure sensor accuracy, we are the first to introduce a Digital Twin of a photoacoustic sensor system by taking a holistic approach. In this work, we present the implementation and evaluation of that model of a Digital Twin to an application for monitoring traces of CH<sub>4</sub> in complex and varying gas compositions of N<sub>2</sub>, O<sub>2</sub>, H<sub>2</sub>O and CO<sub>2</sub> at different temperatures and pressures. The concentration readings of the sensor after DT compensation are compared to those of a standard calibration in nitrogen and the improvement due to DT application is quantified.

### 4.3.1 Theoretical correlations and Digital Twin representation

Even though there is a consensus that the concept of Digital Twins plays an important role in the context of Industry 4.0, there are numerous different definitions of what experts actually understand by the term Digital Twin [16, 17]. Our interpretation of a DT of a sensor system follows the original definition by NASA, which describes a DT as “an integrated multi-physics, multi-scale, probabilistic simulation of a [...] system that uses the best available physical models, sensor updates [...] to mirror the life of its [...] twin” [18]. In terms of a photoacoustic sensor system, this means to monitor all parameters in real-time, which can affect the PA signal, and which may change in a real-world application, i.e. temperature  $T$ , pressure  $p$  and bulk composition  $\sum \chi_i$ . These primary parameters affect different system parameters (see Figure 4.12) in different ways, which in turn influence the photoacoustic signal. Therefore, the correlation of primary parameters and photoacoustic signal generation either must be understood and simulated in real time or the system parameters, in turn, must be determined empirically. The knowledge about all these correlations and mechanisms of influence is combined into a holistic algorithmic approach to analytically predict the PA signal. A single-point calibration, which can be done in any bulk composition, is used to extract the so-called refinement factor, i.e. a setup-specific constant (refer to 4.3.1). With this refinement factor, the DT algorithm and the single-point calibration, the predicted PA signal can be related to the current analyte concentration within the sample.

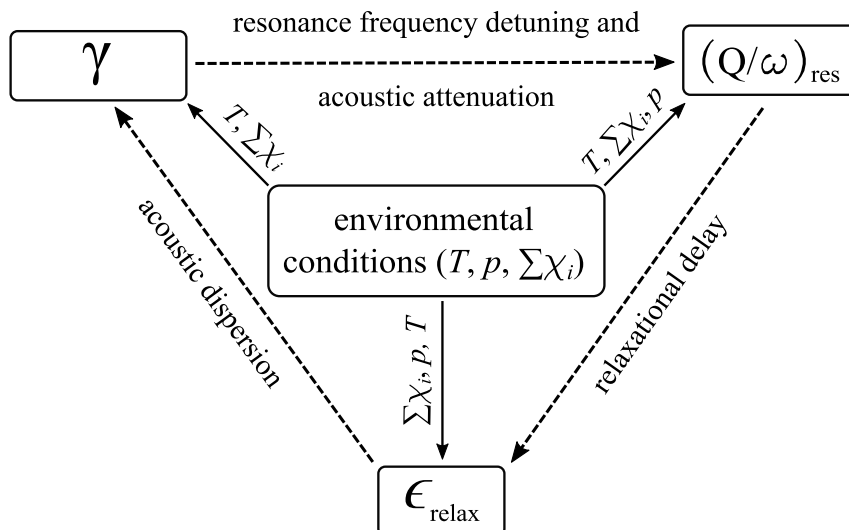


**Fig. 4.12.** Schematic representation of the circular dependencies of different environmental parameters, i.e., temperature  $T$ , pressure  $p$ , and gas composition  $\sum \chi_i$  on certain PA parameters. The environmental influences are arranged in descending order of influence. This figure is taken from [19].

## Photoacoustic signal dependencies

Equation 4.5 describes the PA signal voltage after lock-in amplification  $U_{LIA}$ , i.e. the root mean square of the sinusoidal microphone signal  $U_{mic}$  generated by the photoacoustic effect. The microphone is mounted at half-length on top of an open-ended cylindrical resonator to record the acoustic pressure amplitude. The tube is illuminated by a modulated light source, while the frequency of modulation is adjusted to excite the first longitudinal mode of acoustic resonance, i.e. the formation of one acoustic pressure antinode at half-length of the tube. A general derivation of the photoacoustic signal has already been described in detail in [14].

$$\begin{aligned} U_{LIA} &= \frac{1}{\sqrt{2}} U_{mic} \\ &= C_{corr} B_{mic} (\gamma - 1) \frac{Q}{\omega_{res}} \frac{1}{2\pi^2 r^2} \frac{N_A}{V_{mol}} N_i \sigma_i(\lambda) P_0 \epsilon_{relax} \end{aligned} \quad (4.5)$$

The average optical power of illumination\*  $P_0$  and the quality factor  $Q$  together with the frequency  $\omega_{res}$  of acoustic resonance are determined separately for each photoacoustic measuring point using a thermal power meter and an integrated speaker (see section 3.1.2), respectively. The radius of the resonator tube  $r$ , the microphone sensitivity  $B_{mic}$  and a refinement factor  $C_{corr}$  are set constant as they were empirically validated to not depend on temperature, pressure, or bulk composition. The refinement factor was introduced to quantitatively converge the virtual space of the Digital Twin to the physical space, as it factors in

- a constant deviation of the optical power that is monitored after illuminating the PAC, e.g. due to light absorption by the exit window,
- a PAC specific constant, e.g. considering the efficiency of sound coupling from the resonator tube to the microphone,
- the actual efficiency of light-to-sound coupling, which for the sake of simplicity is usually approximated to be 100 % when deriving the PA signal.

$N_i$  is the dimensionless volume ratio of the analyte,  $N_A$  the Avogadro constant and  $V_{mol}$  the molar volume of the sample, which depends directly on temperature and pressure via  $V_{mol} = RTp^{-1}$ , where  $R$  is the gas constant. The absorption cross-section of the analyte  $\sigma_i$  at the wavelength  $\lambda$  of illumination is simulated using the HITRAN API (HAPI). Since this work is based on wavelength modulation (WM), we used the differential cross-section while sweeping the laser emission over the absorption peak of  $CH_4$  at 3368.8 nm.<sup>†</sup>

\*In the context of this work, all PA measurements are based on wavelength modulation. In case of amplitude modulation,  $P_0$  is specified as the average of high-level minus low-level power, thus  $P_0$  measured by a thermal power meter must be adjusted once the low-level power is greater than zero.

<sup>†</sup>Especially when applying amplitude modulation, it must be ensured that no other species than the analyte absorbs at the wavelength that is used for excitation.

The coefficient  $\epsilon_{\text{relax}}$  describes the efficiency of energy conversion of photonic excitation into heat production by molecular collisions, which is referred to as vibrational-translational (VT) relaxation. This collision based **non-radiative** efficiency represents the real part of the complex efficiency of overall relaxation, which is calculated by means of a novel algorithm (**CoNRad**) that is presented in [13]. The heat capacity ratio  $\gamma$  results from the number of molecular degrees of freedom that can store and release energy following the frequency of modulation, thus contributing to sound propagation (see section 4.3.1).

As already addressed above, the overall concept of the Digital Twin is to monitor the primary parameters temperature, pressure and the concentration of species that may vary in a real-world application, e.g.  $\text{H}_2\text{O}$  and  $\text{CO}_2$ . As these primary parameters affect system parameters in different ways, those must either be measured as well, or they must be simulated with respect to the particular physical mechanism of influence. Figure 4.12 visualizes how ambient parameters and bulk composition may affect photoacoustic signal generation as well as how these effects are considered in the representation of the Digital Twin. Especially the arrows in Figure 4.12 indicate the complexity of how primary parameters affect the PA signal. The efficiency of energy conversion  $\epsilon_{\text{relax}}$  accordingly not only depends directly on  $\sum \chi_i, p$  and  $T$ , but also on the resonance frequency  $\omega_{\text{res}}$  which, in turn, depends on temperature and composition as well. These mechanisms of influence become even more complex with respect to  $\gamma$ , which further depends on  $\epsilon_{\text{relax}}$  while inversely affecting  $Q$  and  $\omega_{\text{res}}$  at the same time. These interrelationships underline the difficulty of standard calibration of a PA sensor system. While the physical mechanisms *relaxational delay* and *acoustic dispersion* address the phenomena of energy dissipation in view of PA signal generation and sound propagation, respectively,  $\gamma$  is visualized to affect standing acoustic wave formation due to *detuning* and *acoustic attenuation*. Both phenomena of energy dissipation generally result from fast modulation and are further discussed in more detail hereinafter. While the effects of  $\sum \chi_i, p$  and  $T$  on  $\epsilon_{\text{relax}}$ ,  $\gamma$  and  $\sigma_i$  are computed, it is easier to determine their effects on acoustic resonance amplification, i.e.  $(Q/\omega_{\text{res}})$ , empirically (see section 3.1.2), as theoretical quantification requires profound knowledge about the underlying bulk- and surface thermodynamics. However, irrespective of whether calculated or directly measured, those complex PA signal dependencies on primary parameters can be compensated by the Digital Twin.

### The effect of ambient parameters on the efficiency of relaxation

As already stated in Section 4.3.1, PA signal generation results from the transformation of laser-excited vibronic energy into translational energy due to superelastic\* molecular collisions. This energy conversion is referred to as VT relaxation. The overall process of relaxation depends on a variety of collision reactions (refer to Table 4.1) either transferring all of the vibrational energy into kinetic energy or causing

---

\*Superelastic collisions are a special case of inelastic collisions, where kinetic energy is not converted to internal energy but vice versa.

vibrational excitation of the collision partner (VV relaxation), thus only releasing the energy difference of collision products minus reactants. Those reactions, that must be searched in literature, are specified by a certain rate of relaxation  $k$  in units  $\text{s}^{-1}$ . Besides the rate of relaxation, the frequency  $f$  of the photoacoustic signal indirectly affects its magnitude and phase, too, since relaxation must be completed prior to de novo laser excitation, otherwise causing a loss in PA signal generation due to relaxational delay. The percentage of a single collision reaction  $j$  contributing to PA signal generation, i.e. its efficiency of relaxation  $\epsilon_j$ , is calculated via

$$\epsilon_j = \frac{1}{\sqrt{1 + \left(\frac{2\pi f}{k_j}\right)^2}} \quad (4.6)$$

However, the rate of a relaxation reaction  $j$  is not a constant but depends on ambient parameters. While the effect of pressure on the efficiency of relaxation already has been described in literature earlier [20–23], we rather consider the overall collision frequency  $Z$  to affect  $\epsilon_j$ , thus adding the influence of temperature. The following equations demonstrate how to adjust relaxation rates, which are specified for a given temperature  $T_0$  and pressure  $p_0$  in literature, to the currently prevailing ambient conditions  $T$  and  $p$ .

$$k(p, T) = k_0(p_0, T_0) \cdot \frac{Z(p, T)}{Z_0(p_0, T_0)} \quad (4.7)$$

with

$$Z(p, T) = \tilde{\rho} \langle \nu \rangle \sigma_c \quad (4.8)$$

Herein,  $\tilde{\rho} \langle \nu \rangle$  and  $\sigma_c$  denominate the volumetric mass density of the sample, the mean speed of the collision partners A and B and the reaction cross section, respectively, which are defined as

$$\tilde{\rho} = \frac{N_A p}{RT} \quad (4.9)$$

$$\langle \nu \rangle = \sqrt{\frac{8k_B T}{\pi \mu}} \quad (4.10)$$

$$\sigma_c = \pi (r_A + r_B)^2 \quad (4.11)$$

Herein,  $r_A$  and  $r_B$  are the radii of the collision partners,  $k_B$  is the Boltzmann constant, and  $\mu$  represents the reduced mass whilst collision. Further considering the temperature dependency of the molecules' radii by using the Sutherland constant  $T_V$  and the molecules' radii at infinite temperature  $r|_{T \rightarrow \infty}$ ,

$$r(T) = r|_{T \rightarrow \infty} \sqrt{\frac{T_V}{T} + 1} \quad (4.12)$$

the relaxation rate can be adjusted to the currently prevailing ambient parameters according to

$$k(p, T) = k_0 \frac{p}{p_0} \sqrt{\frac{T_0}{T}} \frac{(r_A + r_B)^2}{(r_{A0} + r_{B0})^2} \quad (4.13)$$

The accordingly adjusted rates of collision reactions are finally used to compute the overall efficiency of relaxation  $\epsilon_{\text{relax}}$  by means of the novel and autonomous algorithm CoNRad that is published in [13].

## Sound propagation and acoustic dispersion

Another quantity that must be known in order to create the Digital Twin of a PA sensor system according to equation (4.5) is the heat capacity ratio  $\gamma$ . Within the ideal gas model,  $\gamma$  is simplified to  $\gamma = 1 + \frac{2}{d}$ , where  $d$  is the number of degrees of freedom for a given species. The total number of degrees of freedom, in turn, sums up the translational ( $d_{\text{trans}} = 3$ ), the vibrational  $d_{\text{vib}}$  and the rotational ones, i.e.  $d_{\text{rot}} = 2$  and  $d_{\text{rot}} = 3$  in case of linear and non-linear molecules, respectively. The number of vibrational degrees of freedom  $d_{\text{vib}}$  hence are calculated to  $(3N-5)$  and  $(3N-6)$ , respectively, where  $N$  accounts for the number of atoms, which the molecule consists of. However, to accurately calculate  $\gamma$  with regard to acoustic phenomena, only those degrees of freedom may be considered that contribute to sound propagation, i.e. thermally excited degrees of freedom  $d_{\text{therm}}$ . While  $d_{\text{trans}}$  and  $d_{\text{rot}}$  are assumed to be fully excited even at moderate temperatures, the quota of vibrational ones is calculated according to

$$d_{\text{vib}}(T) = 2n \left( \frac{\Theta_{\text{vib}}}{T} \right)^2 \left( \frac{\exp\left(-\frac{\Theta_{\text{vib}}}{2T}\right)}{1 - \exp\left(-\frac{\Theta_{\text{vib}}}{T}\right)} \right)^2 \quad (4.14)$$

where  $n$  is the degeneracy and  $\Theta_{\text{vib}}$  is the temperature of the vibration. The latter depends on the wavenumber of vibration  $\tilde{\nu}$ , further including the speed of light  $c_0$  and the Planck constant  $h$ .

$$\Theta_{\text{vib}} = \frac{hc_0\tilde{\nu}}{k_b} \quad (4.15)$$

Thus, the temperature-dependent heat capacity ratio  $\gamma(T)$  is calculated after

$$\begin{aligned} \gamma(T) &= 1 + \frac{2}{d_{\text{therm}}} \\ &= 1 + \frac{2}{d_{\text{trans}} + d_{\text{rot}} + \sum_{j=1}^m + \sum_{i=1}^n d_{\text{vib},i}(T)} \end{aligned} \quad (4.16)$$

where  $\sum_{j=1}^m + \sum_{i=1}^n d_{\text{vib},i}(T)$  sums up all vibrational states  $i$  of every species  $j$ , which the gas sample is composed of. However, apart from its temperature dependency, the effect of acoustic frequency on  $\gamma$  must be considered as well. Analogous to Equation 4.6, at a high sound frequency, which equals the frequency of laser modulation in terms of AM and twice the modulation frequency in terms of WM, respectively, the molecular vibrations may not be able to follow repetitive compression followed by dilatation whilst sound propagation anymore, termed acoustic dispersion. Since the fundamental algorithm this DT is based on (refer to [13]) allows for computing relaxational processes, it can be used to quantify acoustic dispersion as well. However, unlike PA signal simulation, calculating acoustic dispersion needs the algorithm to be rerun, summing up the efficiency of relaxation of every vibrational state  $i$  of every species  $j$  of the gas sample, yielding extended  $\gamma(T, f)$  calculation.

$$\gamma(T, f) = 1 + \frac{2}{d_{\text{trans}} + d_{\text{rot}} + \sum_{j=1}^m + \sum_{i=1}^n (d_{\text{vib},i}(T)\epsilon_{\text{relax},i})} \quad (4.17)$$

Concluding these theoretical correlations, we created a Digital Twin of a PA sensor system for monitoring traces of methane, to which current temperature, pressure, optical power, humidity, bulk composition as well as frequency and quality factor of acoustic resonance amplification are provided in real-time. With these primary input parameters, the DT allows an analytical description of all physical mechanisms of influence (refer to Figure 4.12) and ultimately to infer the current methane concentration based on the complex PA signal delivered by the lock-in amplifier.

### 4.3.2 Experimental section

The experimental setup is already excessively discussed in previous chapters, hence only the important parts are mentioned in this section.

A power meter and a lock-in amplifier are used to monitor optical power and to preprocess the microphone signal, respectively, and provide this data to the Digital Twin, too. By integrating a speaker (model K 16, Visaton, Germany) into the buffer volume of the PAC, a new hardware feature, termed Acoustic Resonance Monitoring System, was realized to acquire the prevailing characteristics of acoustic resonance amplification in real-time (refer to section 3.1.2). Considering all these input parameters together with the theoretical correlations described in Section 4.3.1, relaxation cascade computing by means of CoNRad [13], and real-time calculation of the absorption cross-section of the sample using HITRAN API, the methane concentration reading after DT compensation  $(\text{CH}_4)_{\text{sim}}$  can be compared with the methane concentration reading after standard calibration in nitrogen  $(\text{CH}_4)_{\text{meas}}$ . The parameters that were used for DT computation, i.e. molecular masses, Sutherland constants, molecular radii at infinite temperature, as well as the wavenumbers and degeneracies of molecular vibrations are listed in Table 4.2 and 4.3. Furthermore, all 50 different collision reactions together with the associated reaction rates  $k$  with units  $\text{s}^{-1}$  that were considered for simulating relaxation effects on the basis of CoNRad are given in Table 4.1 and visualized in Figure 4.1. According to its datasheet, the microphone sensitivity (ICS-40720, InvenSense Inc., US) is specified to be  $-32$  dBV, i.e.  $25.1$  mV/Pa, and the refinement factor of the setup was experimentally determined to 0.865.

### 4.3.3 Results and discussion

This Digital Twin of a photoacoustic trace gas sensor for methane detection was evaluated within a temperature and a pressure range from  $28$  °C to  $40$  °C and from  $350$  mbar to  $1050$  mbar, respectively. Besides, starting from pure nitrogen, the effects of varying bulk compositions containing up to  $19$  %V oxygen,  $9$  %V carbon dioxide and  $1.9$  %V water vapor on the photoacoustic signal have been investigated. While Section 4.3.3 highlights the importance to reproduce how primary parameters affect different system parameters using the example of carbon dioxide addition, Section 4.3.3 metrologically quantifies the improvement of DT implementation by

comparing the  $\text{CH}_4$  concentration readings of the sensor after standard calibration in dry nitrogen with the concentration readings of the sensor after utilizing DT compensation. Section 4.3.3 finally outlines the performance of the sensor system, i.e. accuracy, precision, sensor drift and reproducibility.

### Contrary effects of $\text{CO}_2$ addition on different system parameters

Figure 4.13 compares the measured photoacoustic magnitude (black squares) and phase shift (black triangles) with the magnitude (blue half-filled diamonds) and phase shift (blue half-filled circles) that was computed based on the Digital Twin, when successively adding  $\text{CO}_2$  to a mixture of 15 ppmV  $\text{CH}_4$  diluted in  $\text{N}_2$ . While

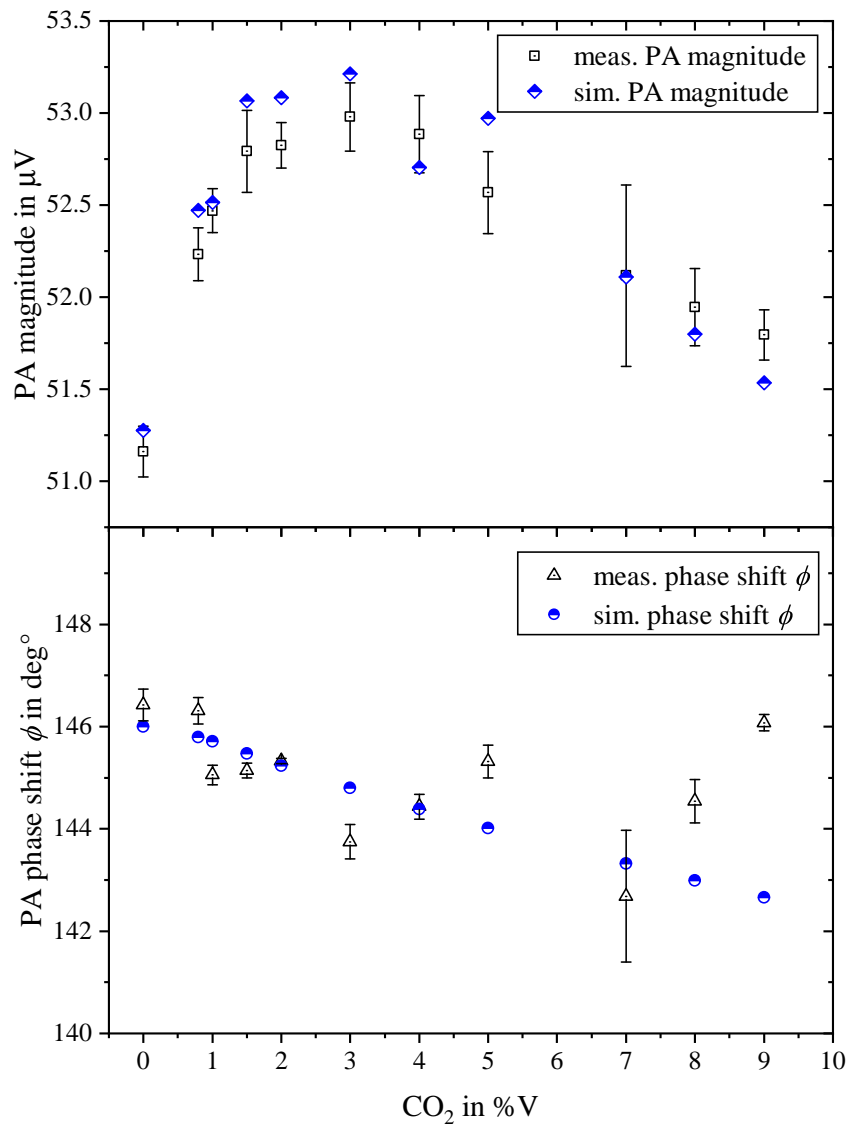


**Fig. 4.13.** Comparison of experimental and Digital Twin data when successively adding  $\text{CO}_2$  to a constant analyte concentration of 15 ppmV  $\text{CH}_4$  diluted in  $\text{N}_2$ .

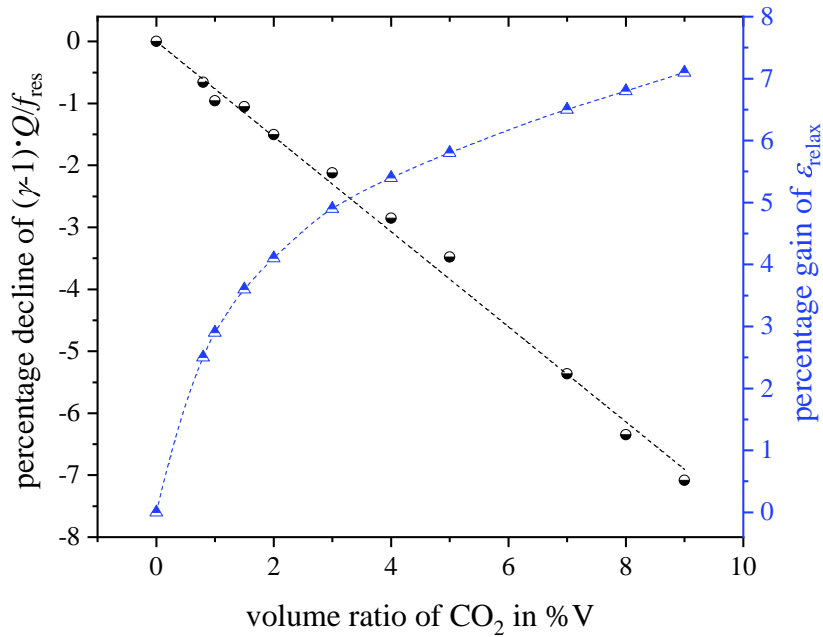


**Fig. 4.14.** Illustration of how CO<sub>2</sub> addition contrarily affects different system parameters. The excess weight of the gradients of relaxation gain (blue triangles) versus acoustic losses (black circles) determines the characteristics of the PA magnitude (upper graph in Figure 4.13).

the error bars of empirical data indicate  $\pm 3$  times the standard deviation of raw data that was sampled over one minute with a rate of 5 Hz and a lock-in time constant of 5 s, the maximum uncertainty of DT magnitudes can be generally approximated to  $\pm 1\%$ , mainly resulting from optical power and acoustic quality factor determination. The measuring conditions were set to 40 °C PAC temperature and ambient pressure. By adding up to 9 %V CO<sub>2</sub>,  $\epsilon_{\text{relax}}$  non-linearly increases from 0.84 to 0.91 (see Figure 4.14), which is accompanied by a phase shift of about 3.5 °. Nevertheless, accelerated relaxation only yields an increase in PA magnitude up to a CO<sub>2</sub> volume ratio of about 3 %V but starts to decrease afterwards, as acoustic losses start to dominate. Figure 4.14 illustrates how adding CO<sub>2</sub> contrarily affects different system parameters and, hence, the PA magnitude. Since heat capacity ratio, quality factor and frequency of acoustic resonance as well as efficiency of relaxation influence the photoacoustic magnitude differently and in opposite ways, it becomes clear how important it is to compute  $\epsilon_{\text{relax}}$  and  $\gamma$  through CoNRad, but also to determine  $Q$  and  $f_{\text{res}}$  via ARMS, which was introduced in section 3.1.2

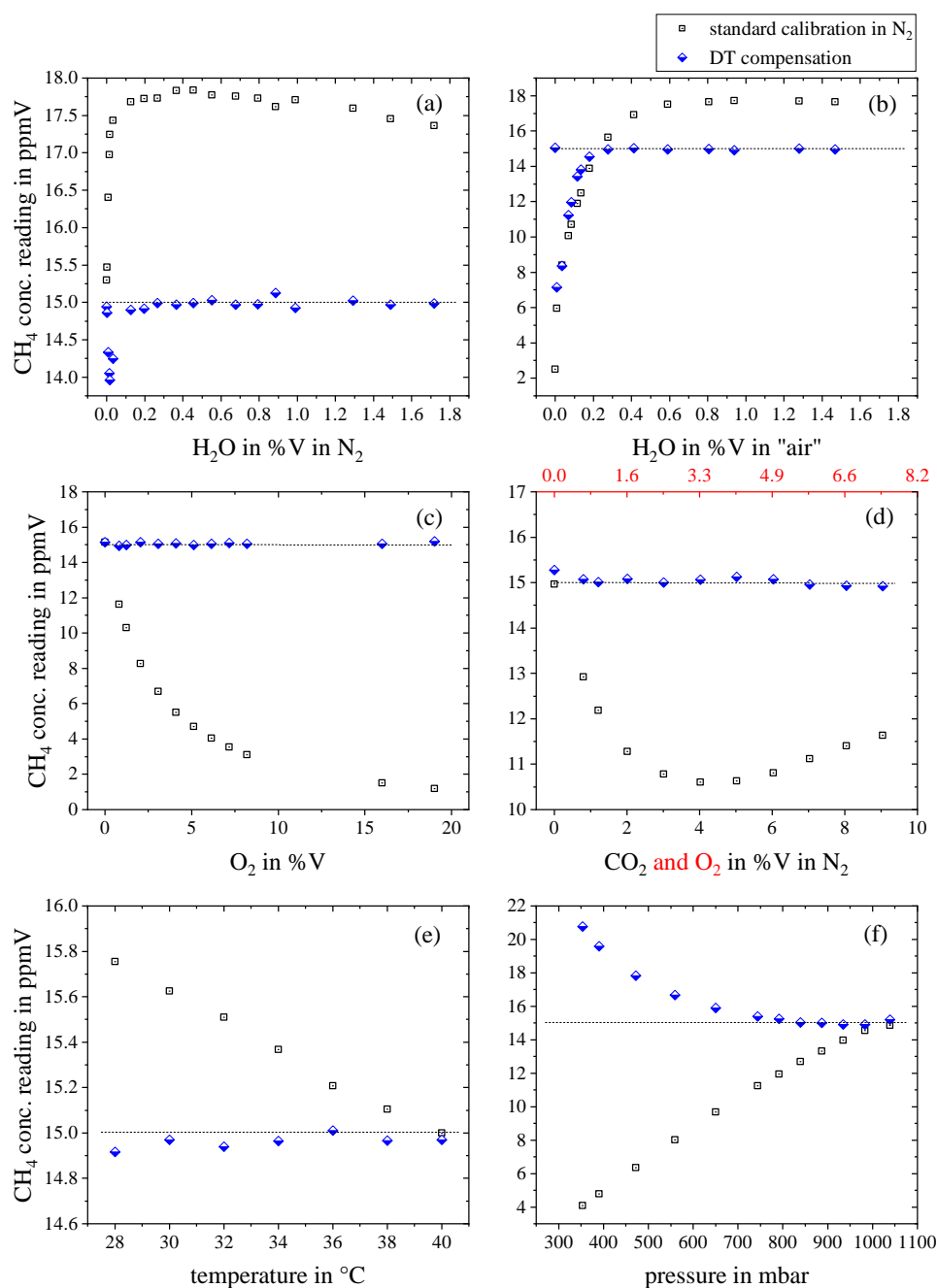
### Metrological quantification of DT based sensor reading improvements

Figure 4.15 graphically represents a metrological comparison of the CH<sub>4</sub> concentration readings of the PA sensor based on standard calibration in dry nitrogen (black squares) and Digital Twin compensation (blue half-filled diamonds), respectively. The analyte

concentration was kept constant at 15 ppmV methane (illustrated by the black dashed lines), while bulk composition and environmental conditions have been varied. The graphs in Figure 4.15(a) and (b) depict the sensor readings when adding water to methane diluted in pure nitrogen and diluted in nitrogen with a concentration of 10 %V oxygen\*, respectively. Although the DT clearly yields a reduction of the measurement error compared to standard N<sub>2</sub> calibration, the DT compensated sensor readings still deviate from 15 ppmV CH<sub>4</sub> in case of low H<sub>2</sub>O concentrations, mainly due to minor inaccuracies of the humidity sensor. While Figure 4.15(c) shows that the DT can handle delayed relaxation due to oxygen, Figure 4.15(d) illustrates an even more complex case as O<sub>2</sub> and CO<sub>2</sub> are added to the system simultaneously. While the isolated effect of oxygen has already been discussed in [13] in detail, simultaneously adding O<sub>2</sub> and CO<sub>2</sub> causes the photoacoustic magnitude to diminish by 29 % before it slightly starts to rise again. Similar to, albeit more pronounced than solely adding CO<sub>2</sub>, the addition of oxygen and carbon dioxide up to 7.4 %V and 9 %V, respectively, consistently causes the heat capacity ratio as well as the quality factor and the frequency of acoustic resonance to decrease. However, the efficiency of relaxation decreases from 0.84 to 0.61, but then again increases to 0.69, also causing the PA magnitude to slightly rise again. These complex PA signal dependencies, inter alia, result from a variety of competing relaxational processes, while at some point, it is hardly possible to assign certain observations to specific energy transfer processes anymore. For this reason, standard sensor calibration methods that are usually applied in case of varying bulk compositions quickly reach their limits in terms of photoacoustic spectroscopy. However, this limitation can be circumvented by utilizing a Digital Twin. Besides changes in the bulk composition, Figure 4.15(e) and (f) illustrate that the photoacoustic magnitude is also sensitive to variations in temperature and pressure. In view of calculating the mean absolute percentage error to quantify the prediction accuracy of the Digital Twin, variations of ambient pressure in the range from 744 mbar to 1040 mbar have been considered. With decreasing pressure this accuracy deteriorates which is assumed to mainly result from the emergence of absorption peak separation (refer to Appendix A.5 - Figure A3), which may be included in the next version of the system model. Further excluding the sensor readings at very low humidity, i.e. less than 1000 ppmV H<sub>2</sub>O which approximately corresponds to 35 % relative humidity at -10°C, the mean absolute percentage error in view of the measurements depicted in Figure 4.15 was identified to 24 % in case of N<sub>2</sub> sensor calibration and 0.8 % in case of Digital Twin compensation, respectively.

---

\*In fact, humidification of the sample causes minor deviation of the oxygen concentration, which, however, was verified to not affect the PA signal if water is present.



**Fig. 4.15.** Metrological comparison of the CH<sub>4</sub> concentration readings of the PA sensor based on standard calibration in dry nitrogen (black squares) and Digital Twin compensation (blue half-filled diamonds). The analyte concentration was kept constant at 15 ppmV methane (illustrated by the black dashed lines), while bulk composition and environmental conditions have been varied. In this regard, we investigated the effect of a) adding H<sub>2</sub>O to N<sub>2</sub>, b) adding H<sub>2</sub>O to 10 %V to O<sub>2</sub> in N<sub>2</sub>, c) adding O<sub>2</sub> to N<sub>2</sub>, d) adding CO<sub>2</sub> and O<sub>2</sub> to N<sub>2</sub>, e) temperature and f) pressure.

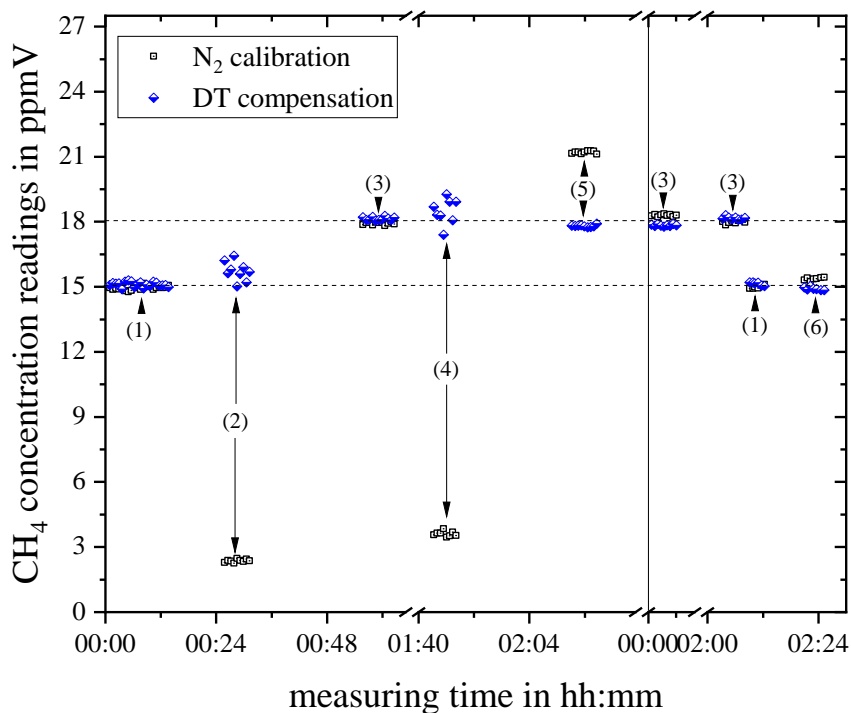
### Performance of the sensor system

Figure 4.16 shows a series of measurements that have been carried out to evaluate the accuracy, precision, sensor drift and reproducibility of the presented photoacoustic monitoring system. For this purpose, the composition and temperature of the sample have been varied according to Table 4.5, while the concentration readings based on standard calibration in  $N_2$  (black squares) as well as after Digital Twin compensation (blue half-filled diamonds) have been monitored. The sensor system was re-initialized several times and the measurements were carried out on two days with a break of 18 days to evaluate its reproducibility. While the solid vertical line in Figure 4.16 represents this break, the two dashed horizontal lines indicate the actual pre-set methane concentrations of 15 ppmV and 18 ppmV. Figure 4.16 identifies no sensor-

**Tab. 4.5.** Measuring conditions for the experiment shown in Figure 4.16.

	CH <sub>4</sub> in ppmV	O <sub>2</sub> in %V	H <sub>2</sub> O in %V	T in °C
(1)	15	-	-	40
(2)	15	10.25	-	40
(3)	18	-	-	40
(4)	18	8.2	-	40
(5)	18	8.2	1.3	40
(6)	15	-	-	35

drift as well as a good reproducibility regardless of whether calibration in nitrogen or Digital Twin compensation is applied. As expected, the figure shows good accuracy for both methods as long as the sample gas consists of analyte and nitrogen only, and the temperature is the same as the temperature set during calibration. The corresponding measuring conditions are labeled as (1) and (3) in Figure 4.16. By decreasing the temperature from 40 °C to 35 °C the concentration readings based on standard  $N_2$  calibration show slightly deteriorated accuracy (6), although frequency detuning was already considered by adjusting the frequency of modulation. This slight deviation can be attributed to a change in the particle density and a change in the quality of acoustic resonance amplification. However, the figure clearly illustrates the significant decline in accuracy of the sensor reading based on  $N_2$  calibration as soon as the composition of the sample changes. Those experiments are labeled as (2), (4) and (5). In detail, the inaccuracies in case of measurements (2), (4) and to some extent (5) in terms of standard calibration mainly result from incomplete relaxation due to VV energy transfer reactions to oxygen (refer to  $k_3$  and  $k_7$  in Table 4.1), which are partially compensated by water in case of (5) (refer to  $k_8$  and  $k_{14}^{H_2O}$  in Table 4.1). The Digital Twin can compensate for this, even though accompanied with lower precision in the case of experiments (2) and (4), since compensation of PA signal losses due to ambient conditions may yield increased standard deviation in absolute terms.



**Fig. 4.16.** Comparison of concentration readings after N<sub>2</sub> calibration (black squares) and DT compensation (half-filled blue diamonds) for analyte concentrations of 15 ppmV and 18 ppmV CH<sub>4</sub> at different measuring conditions (see Table 4.5), respectively. The dashed horizontal lines indicate the pre-set methane concentrations, while the solid vertical line indicates a break of 18 days between the measurements.

#### 4.3.4 Conclusion

In this paper, we discussed the creation and metrological validation of a Digital Twin of a photoacoustic trace gas sensor for methane that builds on a previously published algorithm for relaxation cascade computing [13]. In addition, the DT requires knowledge about the acoustic properties of the system. For this reason, we have developed an acoustic resonance monitoring system to determine the quality factor and frequency in real-time. We elaborated the great relevance of such a DT, as standard calibration often fails in terms of photoacoustic-based sensors because of the multitude and complex nature of how measurement conditions might affect the PA signal. The DT was examined towards changes in composition (CH<sub>4</sub>, N<sub>2</sub>, O<sub>2</sub>, CO<sub>2</sub>, H<sub>2</sub>O), temperature and pressure. With a mean absolute percentage error of 0.8 % compared to 24 % we have demonstrated the improvement in accuracy compared to that of standard calibration and, thus, paved the way to transfer the advantageous photoacoustic technique from academia to application, e.g. industrial processes. However, the DT requires the input data of relevant changes in temperature, pressure and bulk composition for reliable prediction of the analyte

concentration. Furthermore, all energy transfer reactions that are effectively involved in signal generation must be known, which also includes the reactions rate constants. Knowing these parameters and physical processes, the concept of the DT can be adapted to any microphone based photoacoustic sensor for monitoring any analyte species.

## References

- [1] H. Kagermann et al. “Umsetzungsempfehlungen für das Zukunftsprojekt”. In: *Plattf. Ind. 4.0* April (2013), pp. 1–116 (cit. on p. 88).
- [2] A. Reitze et al. “Roadmap for a Smart Factory: A Modular, Intelligent Concept for the Production of Specialty Chemicals”. In: *Angew. Chemie Int. Ed.* 57.16 (Apr. 2018), pp. 4242–4247. ISSN: 14337851. DOI: 10.1002/anie.201711571 (cit. on p. 88).
- [3] M. Pech et al. “Predictive Maintenance and Intelligent Sensors in Smart Factory: Review”. In: *Sensors* 21.4 (Feb. 2021), p. 1470. ISSN: 1424-8220. DOI: 10.3390/s21041470 (cit. on p. 88).
- [4] T. Rück et al. “Low-cost photoacoustic NO<sub>2</sub> trace gas monitoring at the pptV-level”. In: *Sensors and Actuators A: Physical* 263.2 (2017), pp. 501–509. ISSN: 09244247. DOI: 10.1016/j.sna.2017.06.036 (cit. on p. 88).
- [5] K. Chen et al. “Highly Sensitive Photoacoustic Microcavity Gas Sensor for Leak Detection”. In: *Sensors* 20.4 (Feb. 2020), p. 1164. ISSN: 1424-8220. DOI: 10.3390/s20041164 (cit. on p. 88).
- [6] T. Milde et al. “QEPAS sensor in a butterfly package and its application”. In: *Appl. Opt.* 60.15 (May 2021), p. C55. ISSN: 1559-128X. DOI: 10.1364/AO.415236 (cit. on p. 88).
- [7] P. Breitegger et al. “Towards low-cost QEPAS sensors for nitrogen dioxide detection”. In: *Photoacoustics* 18 (June 2020), p. 100169. ISSN: 22135979. DOI: 10.1016/j.pacs.2020.100169 (cit. on p. 88).
- [8] T. Milde et al. “QEPAS sensor for breath analysis: a behavior of pressure”. In: *Appl. Opt.* 57.10 (Apr. 2018), p. C120. ISSN: 1559-128X. DOI: 10.1364/AO.57.00C120 (cit. on p. 88).
- [9] X. Yang et al. “A Miniaturized QEPAS Trace Gas Sensor with a 3D-Printed Acoustic Detection Module”. In: *Sensors* 17.8 (July 2017), p. 1750. ISSN: 1424-8220. DOI: 10.3390/s17081750 (cit. on p. 88).
- [10] A. Glière et al. “Downsizing and Silicon Integration of Photoacoustic Gas Cells”. In: *Int. J. Thermophys.* 41.2 (Feb. 2020), p. 16. ISSN: 0195-928X. DOI: 10.1007/s10765-019-2580-7 (cit. on p. 88).
- [11] Infineon Technologies. “XENSIV™ PAS CO<sub>2</sub> Measure what matters”. In: (2020) (cit. on p. 88).

- [12] E. Parliament et al. “Press release Press release”. In: 20120523 (2011), pp. 32–33 (cit. on p. 88).
- [13] M. Müller et al. “An Algorithmic Approach to Compute the Effect of Non-Radiative Relaxation Processes in Photoacoustic Spectroscopy”. In: *Photoacoustics* 26 (June 2022), p. 100371. ISSN: 22135979. DOI: 10.1016/j.pacs.2022.100371 (cit. on pp. 88, 91–94, 97, 100).
- [14] J. Pangerl et al. “Characterizing a sensitive compact mid-infrared photoacoustic sensor for methane, ethane and acetylene detection considering changing ambient parameters and bulk composition (N<sub>2</sub>, O<sub>2</sub> and H<sub>2</sub>O)”. In: *Sensors Actuators B Chem.* 352 (Feb. 2022), p. 130962. ISSN: 09254005. DOI: 10.1016/j.snb.2021.130962 (cit. on pp. 88, 90).
- [15] S. Weigl et al. “Effects of ambient parameters and cross-sensitivities from O<sub>2</sub>, CO<sub>2</sub> and H<sub>2</sub>O on the photoacoustic detection of acetone in the UV region”. In: *Sensors Actuators B Chem.* 328 (Feb. 2021), p. 129001. ISSN: 09254005. DOI: 10.1016/j.snb.2020.129001 (cit. on p. 88).
- [16] L. F. C. S. Durão et al. “Digital Twin Requirements in the Context of Industry 4.0”. In: 2018, pp. 204–214. DOI: 10.1007/978-3-030-01614-2\_19 (cit. on p. 89).
- [17] E. Negri et al. “A Review of the Roles of Digital Twin in CPS-based Production Systems”. In: *Procedia Manuf.* 11 (2017), pp. 939–948. ISSN: 23519789. DOI: 10.1016/j.promfg.2017.07.198 (cit. on p. 89).
- [18] M. Shafto et al. “DRAFT Modelling, simulation, information technology & processing roadmap - technology area 11”. In: *Natl. Aeronaut. Sp. Adm.* November (2010), p. 27 (cit. on p. 89).
- [19] S. Weigl et al. “Scopes and Limits of Photoacoustic Spectroscopy in Modern Breath Analysis”. In: 2022, pp. 101–159. DOI: 10.1007/11663\_2022\_22 (cit. on p. 89).
- [20] H. Wu et al. “Atmospheric CH<sub>4</sub> measurement near a landfill using an ICL-based QEPAS sensor with V-T relaxation self-calibration”. In: *Sensors Actuators B Chem.* 297 (Oct. 2019), p. 126753. ISSN: 09254005. DOI: 10.1016/j.snb.2019.126753 (cit. on p. 92).
- [21] S. Dello Russo et al. “Quartz-enhanced photoacoustic spectroscopy exploiting low-frequency tuning forks as a tool to measure the vibrational relaxation rate in gas species”. In: *Photoacoustics* 21 (Mar. 2021), p. 100227. ISSN: 22135979. DOI: 10.1016/j.pacs.2020.100227 (cit. on p. 92).
- [22] X. Yin et al. “Impact of Humidity on Quartz-Enhanced Photoacoustic Spectroscopy Based CO Detection Using a Near-IR Telecommunication Diode Laser”. In: *Sensors* 16.2 (Jan. 2016), p. 162. ISSN: 1424-8220. DOI: 10.3390/s16020162 (cit. on p. 92).
- [23] H. Zheng et al. “Sub-ppb-level CH<sub>4</sub> detection by exploiting a low-noise differential photoacoustic resonator with a room-temperature interband cascade laser”. In: *Opt. Express* 28.13 (June 2020), p. 19446. ISSN: 1094-4087. DOI: 10.1364/OE.391322 (cit. on p. 92).

## 4.4 [P3] - Comparison of photoacoustic spectroscopy and cavity ring-down spectroscopy for ambient methane monitoring at Hohenpeißenberg

This chapter has already been published in *Atmospheric Measurement Techniques*, vol. 16, no. September 2023, p. 4263-4270, <https://amt.copernicus.org/articles/16/4263/2023/>.

In the European network Integrated Carbon Observation System (ICOS), 16 different nations united to measure greenhouse gas (GHG) concentrations continuously in the atmosphere and in a standardized way. In order to ensure data comparability of the 46 atmosphere monitoring stations, the required accuracies of the devices were defined in the ICOS program. For CH<sub>4</sub>, this was specified to be less than  $\pm 2$  ppbV, emphasizing the high standards set internationally for reliable atmospheric GHG monitoring [1]. For this purpose a state-of-the-art cavity ring-down spectrometer (CRDS) G2301 (Picarro, Inc., USA) was selected by the ICOS program for both CH<sub>4</sub> and CO<sub>2</sub> quantification, which provides a  $3\sigma$  precision for CH<sub>4</sub> less than 1.5 ppbV and less than 210 ppbV for CO<sub>2</sub> at an averaging time of 5 seconds. For leakage detection of gas pipelines or identification of various methane sources, measurement instruments with slightly lower precision may also be appropriate. In 2021, Defratyka et al. installed a cavity ring-down system (G2201-i, Picarro, Inc., USA) on a car and identified several methane sources in Paris which increased the CH<sub>4</sub> concentration up to 2.7 parts per million (ppmV,  $10^{-6}$ ) [2]. Elevations of CH<sub>4</sub> levels up to 88.6 ppmV were measured in Washington, DC, USA, in 2014 by [3]. This work reported a total of 5893 pipeline leaks over a distance of 2414 km (1500 road miles), from which 1122 leaks increased the ambient CH<sub>4</sub> concentration to more than 5 ppmV and 67 leaks even over 25 ppmV. The threshold for leakage identification was proposed by von Fischer et al., who defined a 10% increase over the normal background concentration as a leakage [4]. For a typical background concentration of about 2 ppmV, this corresponds to 200 ppbV. As an alternative to elaborate measurements in cities, low-cost devices with suitable CH<sub>4</sub> resolution ( $< 200$  ppbV) could be installed at multiple locations and combined with a sensor network, which allows continuous remote leakage detection or emission monitoring. Photoacoustic (PA) gas sensors could meet these requirements of low-cost devices while retaining low enough detection limits. In PA sensors the signal originates from converting vibrational energy of molecules into kinetic energy. A modulated light source electromagnetically excites the analyte of interest, which subsequently can release its additional vibrational energy as kinetic (translational) energy into the sample gas by colliding with surrounding molecules. This process is called vibrational-translational (VT) relaxation. The VT energy transfer increases the kinetic energy of the sample gas, causing the temperature to rise above its equilibrium value. Due to the modulation of the light source, the heat input induced by VT relaxation is also periodic, resulting in periodic density fluctuations, which per definition corresponds to a sound wave. By designing the optical path as an acoustic resonator, e.g. a cylindrical resonator, the photoacoustic

sound wave can be amplified and filtered. The sound pressure linearly depends on the analyte concentration and may be detected by an acoustoelectric transducer (e.g. a microphone), quartz tuning fork (QTF), or a cantilever. Generally, the photoacoustically generated sound pressure amplitude,  $p_{\text{PA}}$ , for cylindrical resonators, excited in their first longitudinal mode, can be described as follows [5, 6]:

$$p_{\text{PA}} = (\gamma - 1) \frac{Q}{f_{\text{res}}} \frac{1}{2\pi^2 r^2} \frac{N_{\text{A}}}{V_{\text{mol}}} N_{\text{i}} \sigma_{\text{i}}(\lambda) P_0 \epsilon_{\text{relax}} \quad (4.18)$$

The heat capacity ratio  $\gamma$  contains the number of all degrees of freedom (rotational, vibrational, translational) of the sample gas actively participating in sound propagation. Acoustic cross-sensitivities of the PA signal can be described by the ratio of the quality factor  $Q$  and the frequency  $f_{\text{res}}$  of acoustic resonance amplification. In the equation  $r$  represents the radius of the resonator tube,  $N_{\text{A}}$  is the Avogadro constant,  $V_{\text{mol}}$  is the molar volume of the sample gas, and  $N_{\text{i}}$  is the dimensionless volume fraction of the analyte with an absorption cross-section  $\sigma_{\text{i}}$  at the emitted wavelength  $\lambda$ . The optical power of the light source inside the photoacoustic measurement cell is designated as  $P_0$ . The efficiency of non-radiative relaxation is denoted as  $\epsilon_{\text{relax}}$ , which is a quantity between 0 and 1. This quantity depends on the efficiency of all involved energy transitions of the gas mixture [7]. Chapter 2.2.2 discusses the effect of non-radiative relaxation on the photoacoustic signal.

Regarding photoacoustic methane detection, recent literature provides several publications reporting ppbV - level limit of detection using infrared laser sources [8–13]. In this work we present the results of a five day  $\text{CH}_4$  measurement campaign in ambient air at the meteorological observatory of the German Weather Service (DWD) at Hohenpeißenberg with a photoacoustic sensor using a G2301 cavity ring-down spectrometer as a reference. The photoacoustic sensor used in this work provides a limit of detection of 6.8 ppbV. The mountain Hohenpeißenberg (47.48° N, 11.01° E) is located southwest of Munich at around 985 meters above sea level. Due to the naturally occurring fluctuations in ambient humidity during the measurement series, the relaxation behavior was significantly affected. Without including the algorithm CoNRad (see chapter 4.4.1) for data evaluation, no reasonable conclusions about the  $\text{CH}_4$  concentration would be possible by the PA sensor. The intention of this paper is to demonstrate that the developed PA sensor in combination with the applied signal corrections provides an appropriate choice for reliable and ppbV-level-precise GHG monitoring. During the measuring campaign, the PA sensor does not show any trends in sensitivity (see Table 4.6); however, it is evident that it is advisable to calibrate the PA sensor frequently in order to maintain the accuracy of the sensor. The G2301, on the other hand, does not show any significant fluctuations in its methane calibration values.

#### 4.4.1 Non-radiative relaxation in photoacoustic spectroscopy

The effect of variations in the non-radiative relaxation process is omnipresent in photoacoustic spectroscopy and has already been discussed for several analytes in

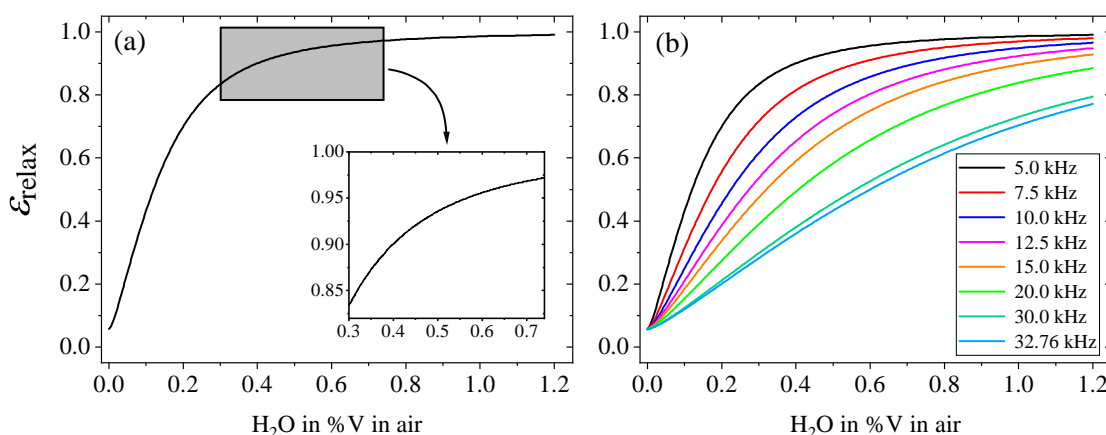


**Fig. 4.17.** Overall efficiency of non-radiative relaxation  $\epsilon_{\text{relax}}$  at 5055 Hz laser modulation for CH<sub>4</sub> in air with rising humidity content (a). The highlighted grey area in (a) indicates the observed humidity during the measurement period. Panel (b) displays how humidification of the sample affects  $\epsilon_{\text{relax}}$  at different acoustic frequencies up to 32.76 kHz, which is a typical modulation frequency utilized in quartz-enhanced PA sensor (QEPAS) systems.

chapter 2.2.2. To compensate for signal losses due to incomplete relaxation we introduced an algorithm to compute the *collision-based non-radiative* efficiency of energy relaxation (CoNRad), which is presented in chapter 4.2. For an accurate description of the overall relaxation cascade in case of mid-infrared (MIR) - 2968.4 cm<sup>-1</sup> methane monitoring in ambient air, i.e. mainly containing N<sub>2</sub>, O<sub>2</sub> and H<sub>2</sub>O, a total of 29 individual collision reactions have to be considered, according to [14].

In Figure 4.17(a) the overall relaxation efficiency  $\epsilon_{\text{relax}}$  at an acoustic frequency of 5055 Hz for methane diluted in air is plotted against continuous humidification of the sample. The data shown in Figure 4.17 was obtained via CoNRad. A detailed discussion of relaxational behaviour for methane in humid air, considering the individual energy transitions has been presented in chapter 4.2. The graphs demonstrate that with rising acoustic frequencies the relaxation losses become much more pronounced, yielding lower PA signals and thus worse detection limits.

## 4.4.2 Experimental

### Photoacoustic data evaluation

A description of the complete photoacoustic measurement system used to obtain these results is given in chapter 3.1.2. The interband cascade laser (ICL) parameters are listed in Table 3.1 and the PAC was temperature controlled to 40 °C.

Together with the simulated non-radiative relaxation efficiency  $\epsilon_{\text{relax}}$ ,  $P_0$ , the measured  $Q$  - factor and resonance frequency  $f_{\text{res}}$  (ARMS) and the calculated heat capacity

ratio  $\gamma$  the raw photoacoustic signal  $U_{\text{PA, raw}}$  in  $\mu\text{V}$  is compensated after equation (4.19), yielding the final methane concentration output of the PA sensor  $\text{CH}_{4,\text{PA}}$ .

$$\text{CH}_{4,\text{PA}} = \frac{U_{\text{PA, raw}}}{S_{\text{cali}}} \cdot \frac{\epsilon_{\text{relax, cali}}}{\epsilon_{\text{relax}}} \cdot \frac{Q_{\text{cali}}}{Q} \cdot \frac{f_{\text{res}}}{f_{\text{res, cali}}} \cdot \frac{(\gamma_{\text{cali}} - 1)}{(\gamma - 1)} \cdot \frac{P_{0,\text{cali}}}{P_0} \quad (4.19)$$

The quantities labeled with *cali* in the index were obtained during the respective calibration measurements, with the calibration sensitivity  $S_{\text{cali}}$  in  $(\mu\text{V ppmV}^{-1})$ . For comparison purposes the sensitivity  $S$  in Table 4.6 is normalized to a humidity of 0.3 %V.

### Measurement setup

The measurement setup is visualized in Figure 4.18. Ambient air was sampled by means of a pump from outside the laboratory. A three-way valve was used to automatically switch between reference gas and ambient air. Dry natural air was chosen as the reference gas, which consists mostly of  $\text{N}_2$  and  $\text{O}_2$  but also includes noble gases as well as trace gases ( $\text{CH}_4$ ,  $\text{CO}_2$ ,  $\text{N}_2\text{O}$ ,  $\text{CO}$ ). The reference gas tank was filled and calibrated by the ICOS Flask and Calibration Laboratory (FCL) and is linked to the WMO X2004A scale, which provides 2020 ppbV  $\text{CH}_4$  with an uncertainty below 0.5 ppbV [15]. During the measurement campaign, the reference gas was used a total of seven times for 30 minutes per interval to avoid and detect potential sensor drifts; see Table 4.6. As the difference between the theoretical calculations of CoNRad and the measured data is highest for only slightly humidified measuring environments ( $\text{H}_2\text{O} < 0.25$  %V), see Figure 4.10 from chapter 4.2, an additional humidification of the sample gases of about 0.3 %V was chosen to avoid this issue. This was realized by a humidity generator installed upstream of the PA sensor. A lock-in-amplifier (LIA) time constant of  $\tau_{\text{LIA}} = 20$  s was chosen to reduce the effect of white noise on the PA data. Every 10 minutes, the PA sensor recorded three single-point measurements (SPMs) each for 20 s with a data acquisition rate of 5 Hz. The three SPMs themselves were further averaged, as well as the individual standard deviations, yielding the final values. The ARMS routine (see section 3.1.2) was performed to determine  $Q$  and  $f_{\text{res}}$  each time before the three SPMs were recorded. Based on the ARMS, the modulation frequency of the laser was automatically adjusted, while the PA ICL was switched off between the measurements. According to equation (4.19), the raw photoacoustic signal was corrected for variations in  $\epsilon_{\text{relax}}$ ,  $\gamma$ ,  $Q$ ,  $f_{\text{res}}$ , and  $P_0$ . As shown in Figure 4.18, the G2301, operated with a data acquisition rate of 0.2 Hz and an averaging time of 5 s, was installed in the gas setup parallel to the PA sensor, ensuring that both devices received the same sample gas, providing comparability of the sensor readings.

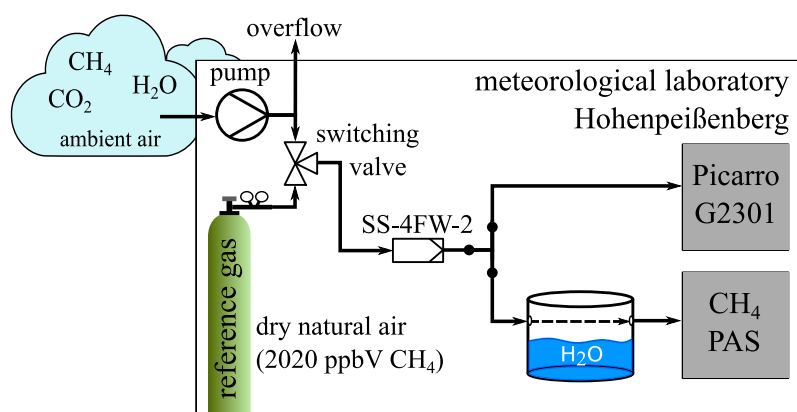


**Fig. 4.18.** Schematic of the experimental setup for the measurement campaign. The pump delivers ambient air from outside the laboratory. A three-way valve is used to switch between ambient air and reference gas. The reference gas consists of 2020 ppbV of methane in dry natural air. Before the respective sample gas is fed into the two measurement instruments, it passes through a stainless-steel filter (SS-4FW-2) to avoid particle contamination.

### 4.4.3 Results and discussion

The data of the PA sensor during reference gas measurements are summarized in Table 4.6. The sensitivity of the PA sensor varies only slightly (maximum -2.61 % from the average value), which demonstrates the stability of the photoacoustic system, but still shows the necessity for frequent calibration to ensure high accuracy. While the mean CH<sub>4</sub> precision ( $3\sigma_{\text{PAS}} = 6.75$  ppbV) is worse than the observed precision of the reference ( $3\sigma_{\text{G2301}} = 1.16$  ppbV), the PA sensor is nevertheless sufficiently precise to reliably detect the atmospheric CH<sub>4</sub> fluctuations, refer to Figure 4.19(a). Figure 4.19 illustrates the CH<sub>4</sub> readings (in ppbV) (a) obtained by the PA sensor, including the previously mentioned signal corrections (black) and the G2301 data (red), respectively. The dashed grey lines indicate a new day. It is obvious, that the CH<sub>4</sub> concentration characteristics monitored with both devices agree quite well with each other. However, more significant discrepancies up to  $> \pm 80$  ppbV are also evident. As of now, no clear explanation could be identified for these deviations. It is unlikely that these errors are induced by differences in the sample gas of the two systems since the humidity readings of the BME280 integrated into the PA sensor match very well with the readings of the G2301, as shown in Figure 4.19(c). By evaluating the data acquisition system (DAS), cavity, and etalon temperature of the Picarro G2301 temporal anomalies regarding CH<sub>4</sub> discrepancies could be identified (see Appendix A.7 - Figure A5).

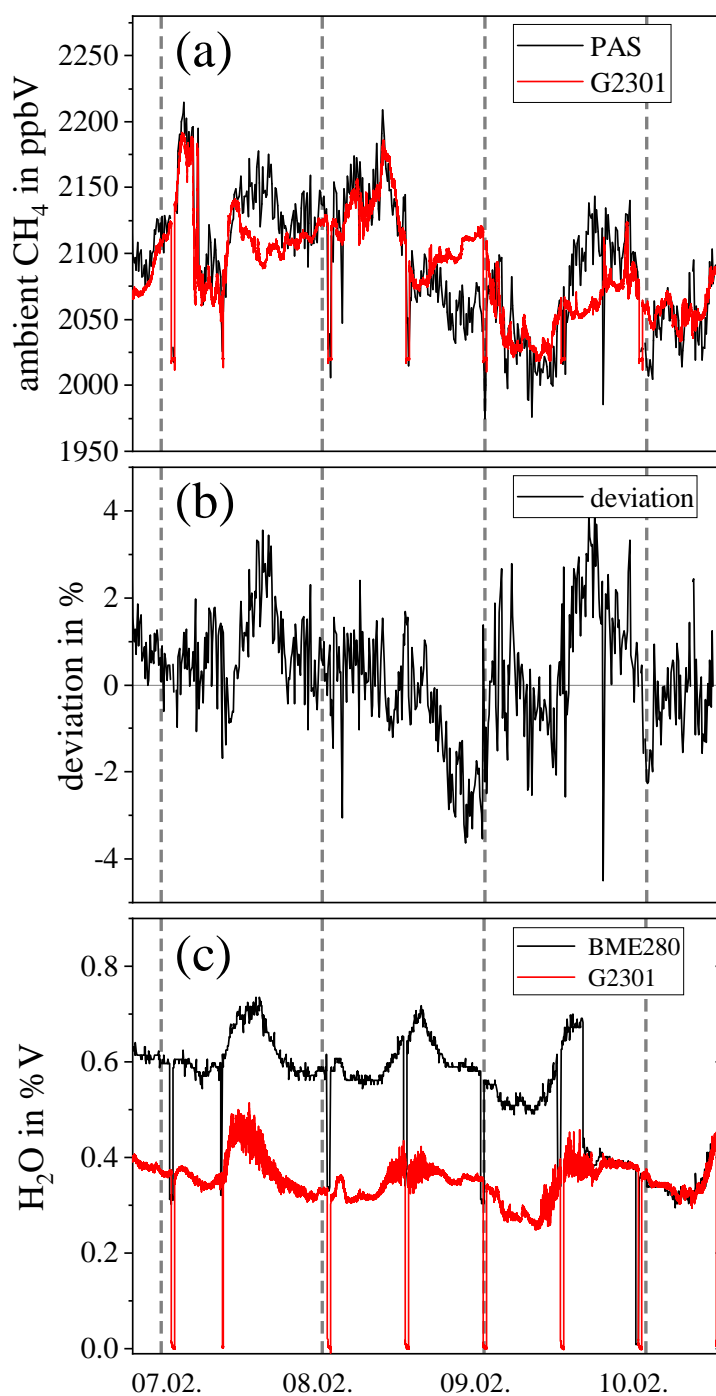


**Fig. 4.19.** Direct comparison of the methane concentration readings (a), the deviation of the PA sensor compared to the Picarro G2301 (in %) (b) and the water readings (c). The humidity offset induced by the measurement setup is clearly visible. During 9 February, the humidity tank became empty, resulting in no additional humidification.

Since the temperature spikes are probably caused by direct sunlight on the G2301, it is recommended to avoid this for similar experiments. Still, the average percentage deviation of the PA sensor and the G2301 reference of 1.11 % is rather moderate; see Figure 4.19(b). Over the entire period of the measurement campaign, the water

**Tab. 4.6.** Sensitivity of the PA sensor over the five day measurement period. An average deviation of 0.98 % and a maximum deviation of -2.61 % from the mean of the observed sensitivities show the stability of the PA sensor. The long-term accuracy and the precision of the G2301 are listed in the two right columns. The campaign started on 6 February 2023 (afternoon) and ended on 10 February 2023 (morning).

calibra- tion	PAS sensitivity $S$ in $\mu\text{V ppmV}^{-1}$	$3\sigma$ precision in nV	$3\sigma$ precision in ppbV	G2301 in ppbV	$3\sigma$ G2301 in ppbV
#1	2.08	14.14	6.80	2019.99	0.96
#2	2.12	22.50	10.61	2020.13	0.72
#3	2.13	7.18	3.37	2019.70	0.92
#4	2.16	8.59	3.98	2019.88	0.86
#5	2.14	17.91	8.37	2020.07	2.04
#6	2.16	14.93	6.91	2019.67	1.52
#7	2.15	15.56	7.24	2019.61	1.04

content in the PA sample gas varied from about 0.30 %V to about 0.73 %V (see Figure 4.19(c)), causing the raw PA sensor readings to alter by about 13.5 % due to relaxation effects (refer to Figure 4.17(a)), which makes standard calibration unfeasible. For this reason, algorithmic compensation methods like CoNRad are essential. The  $Q$ -factor quantification,  $f_{\text{res}}$ , and  $P_0$  remained virtually constant during the measurement period. Also, the variation of  $\gamma$  induced by fluctuating humidity was negligible compared to the relaxation effect. Figure 4.20 illustrates the impact of CoNRad on the reliability of the PA sensor readings. The y axis represents the difference between the CH<sub>4</sub> concentration readings of the PA sensor and that of the G2301 (in ppbV). The dashed grey lines again indicate a new day. The black curve in Figure 4.20(a) shows the deviation when CoNRad is implemented ( $\Delta\text{CH}_4(\text{PA}_{\text{CoNRad}} - \text{G2301})$ ) in the data evaluation, and the red curve illustrates the deviation based on the raw PA data ( $\Delta\text{CH}_4(\text{PA}_{\text{raw}} - \text{G2301})$ ). This red curve illustrates that, due to the exponential effect of relaxation processes, the offset between raw data and the reference measurement is not constant. The data highlighted in grey in Figure 4.20 show the results for dry PA reference gas operation, with the empty humidity tank during 9<sup>th</sup> of February. Without CoNRad dry calibration leads to

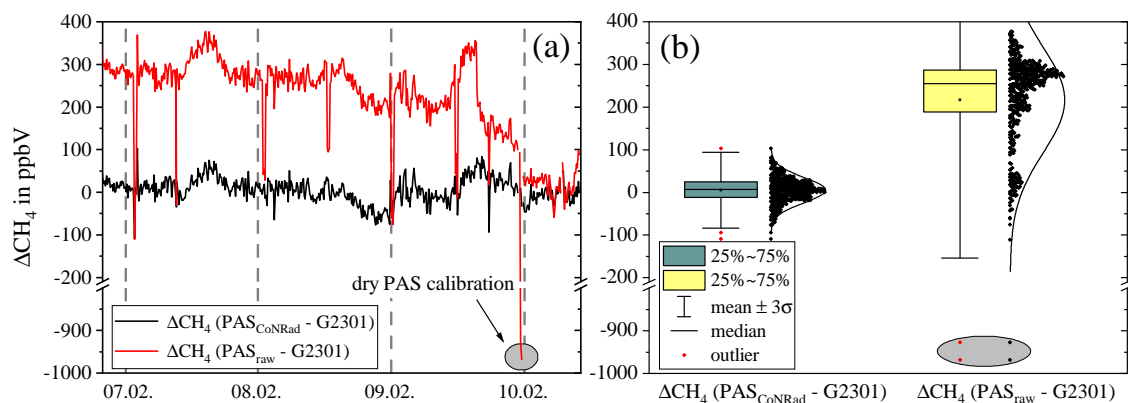


**Fig. 4.20.** Absolute difference of  $\text{CH}_4$  in ppbV (a) based on raw PA data (red) and after CoNRad compensation (black) with regard to the G2301 reference methane readings. Panel (b) displays the boxplots and histograms of the deviations with CoNRad compensation (green) and without (yellow). The data highlighted in grey indicate dry PAS calibration without CoNRad compensation.

considerable misinterpretations of the PA data. Thus ambient  $\text{CH}_4$  PAS monitoring is not possible without the algorithmic compensation approaches. Figure 4.20(b) shows a statistical evaluation of the absolute differences with CoNRad compensation (green boxplot) and without (yellow boxplot). It indicates that with CoNRad the variance of the measured deviation with respect to the reference decreases significantly. In addition, the compensated values show a normal distribution around 5.26 ppbV, indicating no long-term drift. The raw values (yellow boxplot), however, are not normally distributed and show a substantially higher variance. The large deviation of about 1000 ppbV  $\text{CH}_4$  of the raw PA data (highlighted grey area) can be attributed to the dry reference gas mode, in which pronounced relaxation losses occur, see Figure 4.17.

#### 4.4.4 Conclusion

We compared our PA methane gas sensor with an established and calibrated cavity ring-down spectrometer (G2301) used for global GHG monitoring. Over a period of five days, ambient air has been monitored at the meteorological observatory Hohenpeißenberg of the DWD by both systems. The obtained results demonstrate that the PA sensor ( $3\sigma$  precision = 6.75 ppbV) is able to detect even small natural methane fluctuations in ambient air, thus providing an alternative to established devices. Further applications of the sensor would cover natural-gas leakage detection, identification of new methane sources, and emissions monitoring from agriculture or landfills. Generally, photoacoustic systems provide low detection limits and a high potential for miniaturization; however, relaxation-induced signal alterations pose a major drawback of this technique. The counteracting water- and oxygen-induced relaxation effects play an important role in ambient photoacoustic methane

detection, as highlighted in this work. Only in environments with a clearly defined and constant measurement matrix, e.g. contamination measurement of high-purity gases, can the effect of relaxation on the photoacoustic signal be neglected. For measurement applications with varying gas composition, e.g. fluctuating ambient humidity, PA devices essentially require the implementation of algorithmic models, such as CoNRad, in order to compensate for signal losses due to delayed relaxation that otherwise might cause significant errors in PA sensor data. The combination of CoNRad to simulate the non-radiative relaxation cascade and ARMS for real-time monitoring of  $Q$  and  $f_{\text{res}}$  allows for reliable analyte concentration readings with photoacoustic sensors.

## References

- [1] ICOS RI. “ICOS Atmosphere Station Specifications V2.0 (editor: O. Laurent)”. In: 0.September (2020) (cit. on p. 103).
- [2] S. M. Defratyka et al. “Mapping Urban Methane Sources in Paris, France”. In: *Environ. Sci. Technol.* 55.13 (July 2021), pp. 8583–8591. ISSN: 0013-936X. DOI: 10.1021/acs.est.1c00859 (cit. on p. 103).
- [3] R. B. Jackson et al. “Natural Gas Pipeline Leaks Across Washington, DC”. In: *Environ. Sci. Technol.* 48.3 (Feb. 2014), pp. 2051–2058. ISSN: 0013-936X. DOI: 10.1021/es404474x (cit. on p. 103).
- [4] J. C. von Fischer et al. “Rapid, Vehicle-Based Identification of Location and Magnitude of Urban Natural Gas Pipeline Leaks”. In: *Environ. Sci. Technol.* 51.7 (Apr. 2017), pp. 4091–4099. ISSN: 0013-936X. DOI: 10.1021/acs.est.6b06095 (cit. on p. 103).
- [5] A. Miklós et al. “Application of acoustic resonators in photoacoustic trace gas analysis and metrology”. In: *Rev. Sci. Instrum.* 72.4 (Apr. 2001), pp. 1937–1955. ISSN: 0034-6748. DOI: 10.1063/1.1353198 (cit. on p. 104).
- [6] T. Rück et al. “Digital Twin of a photoacoustic trace gas sensor for monitoring methane in complex gas compositions”. In: *Sensors Actuators B Chem.* 378 (Mar. 2023), p. 133119. ISSN: 09254005. DOI: 10.1016/j.snb.2022.133119 (cit. on p. 104).
- [7] T. F. Hunter et al. “Photophysical processes in the vapour-phase measured by the optic-acoustic effect. Part 1.—The model and apparatus for the study of radiationless processes”. In: *J. Chem. Soc., Faraday Trans. 2* 70 (1974), pp. 1010–1021. ISSN: 0300-9238. DOI: 10.1039/F29747001010 (cit. on p. 104).
- [8] A. Elefante et al. “Dual-Gas Quartz-Enhanced Photoacoustic Sensor for Simultaneous Detection of Methane/Nitrous Oxide and Water Vapor”. In: *Anal. Chem.* 91.20 (Oct. 2019), pp. 12866–12873. ISSN: 0003-2700. DOI: 10.1021/acs.analchem.9b02709 (cit. on p. 104).

- [9] A. Elefante et al. “Environmental Monitoring of Methane with Quartz-Enhanced Photoacoustic Spectroscopy Exploiting an Electronic Hygrometer to Compensate the H<sub>2</sub>O Influence on the Sensor Signal”. In: *Sensors* 20.10 (May 2020), p. 2935. ISSN: 1424-8220. DOI: 10.3390/s20102935 (cit. on p. 104).
- [10] M. Giglio et al. “Broadband detection of methane and nitrous oxide using a distributed-feedback quantum cascade laser array and quartz-enhanced photoacoustic sensing”. In: *Photoacoustics* 17 (Mar. 2020), p. 100159. ISSN: 22135979. DOI: 10.1016/j.pacs.2019.100159 (cit. on p. 104).
- [11] Z. Gong et al. “Ppb-level detection of methane based on an optimized T-type photoacoustic cell and a NIR diode laser”. In: *Photoacoustics* 21 (Mar. 2021), p. 100216. ISSN: 22135979. DOI: 10.1016/j.pacs.2020.100216 (cit. on p. 104).
- [12] Z. Li et al. “Design of a high-sensitivity differential Helmholtz photoacoustic cell and its application in methane detection”. In: *Opt. Express* 30.16 (Aug. 2022), p. 28984. ISSN: 1094-4087. DOI: 10.1364/OE.465161 (cit. on p. 104).
- [13] H. Xiao et al. “Ultra-sensitive ppb-level methane detection based on NIR all-optical photoacoustic spectroscopy by using differential fiber-optic microphones with gold-chromium composite nanomembrane”. In: *Photoacoustics* 26 (June 2022), p. 100353. ISSN: 22135979. DOI: 10.1016/j.pacs.2022.100353 (cit. on p. 104).
- [14] M. Müller et al. “An Algorithmic Approach to Compute the Effect of Non-Radiative Relaxation Processes in Photoacoustic Spectroscopy”. In: *Photoacoustics* 26 (June 2022), p. 100371. ISSN: 22135979. DOI: 10.1016/j.pacs.2022.100371 (cit. on p. 105).
- [15] J. Armin and M. Schumacher. “Quality Control Report 2021”. In: March (2021), pp. 26–28 (cit. on p. 106).

## 4.5 Multivariate analysis and digital twin modeling: alternative approaches to molecular relaxation in photoacoustic spectroscopy

The results in this chapter have already been published in *Photoacoustics*, vol. 33, no. October 2023, p. 100564, October 2023, <https://doi.org/10.1016/j.pacs.2023.100564>.

The original manuscript was written for the most part by Andrea Zifarrelì and the author of this thesis. The data acquisition was carried out by Aldo Cantatore in the course of his PhD thesis. Andrea Zifarrelì and Angelo Sampaolo performed the PLSR analysis, while the Digital Twin analysis was realized by the author of this thesis. Thomas Rück from the OTH Regensburg, Christine Hölzl and Huber Rossmadl from Thorlabs GmbH (Bergkirchen, Germany), and Pietro Patimisco and Vincenzo Spagnolo from the Polytechnic University of Bari, Italy were involved in supervision, validation, reviewing and editing of the original manuscript.

This chapter was adapted compared to the original publication.

### 4.5.1 Introduction

While in traditional PAS systems a microphone is used for detecting the photoacoustic sound pressure, quartz-enhanced photoacoustic spectroscopy (QEPAS). QEPAS was introduced in 2002 as an alternative to conventional PAS sensors, providing a smaller footprint of the acoustic detection part, as well as higher  $Q$ -factors [1]. QEPAS sensors have been used for trace gas sensing in many different applications, e.g. atmospheric monitoring [2, 3], air pollutant detection [4] or breath analysis [5], in recent years. However, as the effect of non-radiative relaxation fundamentally determines the photoacoustic signal generation, not only traditional PAS sensors, but also QEPAS sensors are affected. As described in chapter 4.2, the efficiency of non-radiative relaxation  $\epsilon_{\text{relax}}$  is a value between 0 and 1 and strongly depends on the composition of the gas matrix, the possible energy transitions, and the modulation frequency of the laser. Since the modulation frequency for QEPAS sensors is typically higher than for microphone-based setups the relaxation effects are more pronounced, see Figure 4.17. To minimize the effect of incomplete relaxation, literature proposed intentional humidification of the sample gas, as water is known to promote the non-radiative relaxation for many analytes [6–8]. For field measurements, a sensor must be able to provide reliable data even under fluctuating environmental conditions, e.g. ambient humidity. Thus the implementation of sophisticated data analysis techniques to compensate for relaxational effects or other cross-sensitivities is necessary.

In chapter 4.3 a digital twin (DT) of a traditional microphone-based photoacoustic sensor was presented for the first time and evaluated in field measurements in chapter 4.4. This approach significantly increased the accuracy of the microphone-based sensor, resulting in high agreement of the compensated PAS data with a reference

device. Regarding QEPAS sensors, a statistical compensation method based on *Partial Least Squares Regression* (PLSR) was published recently [9]. Both approaches attempt to improve the accuracy of photoacoustic sensors via different procedures. While the DT is based on theoretical calculations of the relaxation behavior, as well as on the empirical quantification of the resonance characteristics (see chapter 4.3) and aims to mimic the real sensor as closely as possible, the PLSR intends to statistically model the cross-correlations of gas matrix effects on the QEPAS signal without sophisticated knowledge of causal relationships.

In this chapter, the DT is applied to a QEPAS sensor and compared to a PLSR approach, regarding cross-sensitivities mid-infrared methane detection in humidified air.

### 4.5.2 Experimental setup for QEPAS detection

The QEPAS sensor was integrated into a 50x50x20 cm aluminum box. To prevent misalignment of the laser source the optical components, as well as the acoustic detection module (ADM) were mounted into a separate stainless-steel box (sensor head) placed within the aluminum box. This stainless-steel box contains an ICL (Thorlabs ID3345HHLH-A), emitting at around  $2989\text{ cm}^{-1}$ , a hygrometer (iST HYT 939) to monitor the humidity inside the ADM, as well as a reference cell (RC) and a photodiode (PD) to monitor the emitted optical power. The reference cell, which is filled with 0.5 %V methane diluted in  $\text{N}_2$ , is placed between ADM and photodiode and thus allows to monitor the laser emission wavenumber. The sensor element of the ADM (Thorlabs ADM01) consists of a custom T-shaped quartz tuning fork (QTF), with a resonance frequency of 12458 Hz and two acoustic resonator tubes enclosing the QTF perpendicular to the bending plane of its prongs for additional signal amplification. This sensor design is called *on-beam QEPAS* [10]. A  $\text{CaF}_2$  lens with 2-5  $\mu\text{m}$  anti-reflective coating mounted in front of the ADM is used to focus the laser

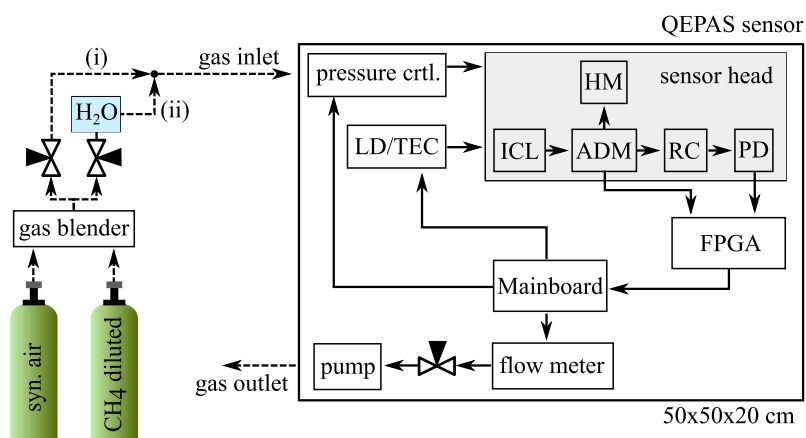


**Fig. 4.21.** Simplified schematic of the experimental setup. The dashed arrows indicate gas flow, the solid arrows indicate electronic signals.

beam between the QTF prongs. The measurement gas is fed into the ADM via the gas inlet. For signal evaluation a LIA was implemented on an FGPA, which acquires both the QEPAS voltage and the photodiode signal to compensate for potential power fluctuations of the laser emission [11]. Inside the aluminum box a laser driver (LD), as well as a thermoelectric cooler (TEC) are used to control the laser current and temperature, respectively. Additionally, to control the pressure inside the ADM and monitor the gas flow rate a pressure controller (ALICAT EPC-15PSIAP01-BM0P), flow meter (ALICAT BC-C1000), needle valve, and a diaphragm pump (Thomas 1420VR 24V) were embedded inside the aluminum box. The FPGA is connected to a dedicated mainboard, which also controls and monitors the LD, TEC, flow meter, and the pressure controller. The data, including the lock-in-amplifier voltage is fed to a PC and acquired by a LabVIEW-based software tool. Figure 4.21 shows a simplified block diagram of the experimental setup. Two methane concentration ranges from 25 ppmV to 200 ppmV, hereafter labeled as *low*  $CH_4$  and from 0.11 %V to 1.1 %V, hereafter labeled as *high*  $CH_4$  were investigated. The humidity for each methane concentration was varied between 0.25 %V and 2.0 %V. The gas samples were generated by mixing 500 ppmV and 2.177 %V  $CH_4$ , respectively, diluted in synthetic air (80 %V  $N_2$ , 20 %V  $O_2$ ) with a gas cylinder containing pure synthetic air. The gas cylinders containing methane provided an uncertainty of 1 % regarding the nominal concentration, i.e.  $500 \pm 5$  ppmV and  $2.177 \pm 0.02$  %V. The humidification of the sample gas is realized by splitting the gas flow into a dry and a humidified path, which is connected to a humidifier (PermSelect PDMSXA-1000). Two needle valves control the flow through each path, thus allowing to set the  $H_2O$  content by varying the flow ratio of the dry (i) and humidified path (ii). The QEPAS measurements were performed utilizing 2f-wavelength modulation (2f-WM). While the PLSR evaluation utilizes the QEPAS spectral scans, the digital twin (DT) only needs on-peak scanning. For both measurement modes a pressure of 533 mbar (400 Torr), a gas flow of 50 ml/min, and a LIA time constant of 125 ms were chosen.

### 4.5.3 Target features selection

#### On-peak measurements - DT analysis

The ICL covers the spectral range from  $2987.3 \text{ cm}^{-1}$  to  $2989.3 \text{ cm}^{-1}$ . At  $2988.79 \text{ cm}^{-1}$   $CH_4$  exhibits the strongest absorption with an absorption cross-section (ACS) of  $8.67 \cdot 10^{-19} \text{ cm}^2/\text{molecule}$ . However, since  $H_2O$  shows fairly strong absorption at  $2988.62 \text{ cm}^{-1}$ , the peak at  $2988.93 \text{ cm}^{-1}$  with an ACS of  $6.36 \cdot 10^{-19} \text{ cm}^2/\text{molecule}$  was chosen for photoacoustic on-peak excitation, in order to minimize spectral cross-influences. To avoid non-linear calibration characteristics due to Beer-Lambert losses and since the employed lock-in amplifier has a limited voltage input, the strong absorption at  $2988.93 \text{ cm}^{-1}$  could not be exploited for  $CH_4$  measurement in the higher concentration range (0.11 %V to 1.10 %V). Therefore, for the higher  $CH_4$  concentration range, the weaker absorption at  $2987.88 \text{ cm}^{-1}$  was used with an ACS of only  $9.33 \cdot 10^{-21} \text{ cm}^2/\text{molecule}$ . Figure 4.22 shows the absorption characteristics of methane and water in the analyzed region simulated with the *HITRAN on the*

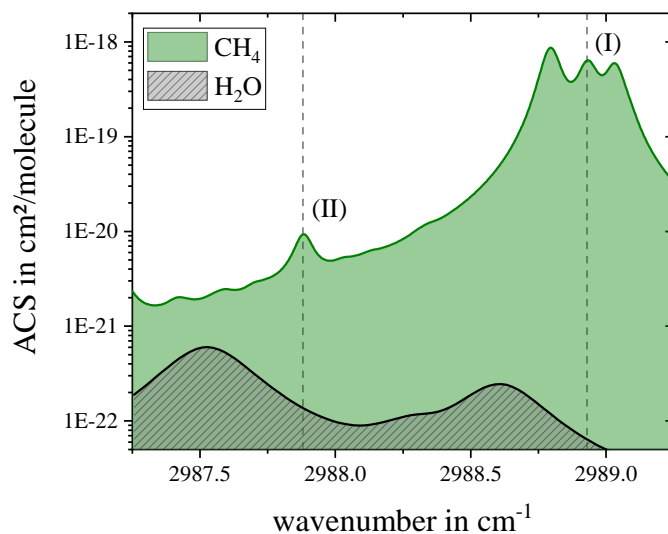


**Fig. 4.22.** Absorption cross-section of  $\text{CH}_4$  and  $\text{H}_2\text{O}$  in the spectral range from  $2987.25 \text{ cm}^{-1}$  to  $2989.25 \text{ cm}^{-1}$  at 533 mbar (400 Torr) and 301 K.

*web* database [12]. The dashed grey lines in Figure 4.22 indicate the targeted peaks for the on-peak measurements in the low (I) and the high  $\text{CH}_4$  concentration range (II). For each on-peak measurement the QEPAS data was acquired for 200 seconds. The averaged value was subsequently considered in the DT analysis.

#### QEPAS spectral scans - PLSR analysis

Contrary to the DT analysis, the PLSR analysis is based on spectral scans. In the low  $\text{CH}_4$  concentration range the QEPAS sensors performs a spectral scan from  $2987.3 \text{ cm}^{-1}$  to  $2989.3 \text{ cm}^{-1}$  by increasing the offset current of the ICL from 115 mA to 142 mA. Each spectrum consists of 537 data points, resulting in a spectral resolution of approximately  $0.0036 \text{ cm}^{-1}$  and takes about 240 seconds to acquire. As for the high  $\text{CH}_4$  concentrations the measured spectral region is smaller ( $2987.3 \text{ cm}^{-1}$  to  $2988.2 \text{ cm}^{-1}$ ) only 237 data points with a total acquisition time of 120 seconds are necessary. Figure 4.23 shows the acquired QEPAS spectra for the low (a) and the high (b)  $\text{CH}_4$  concentration range. The highlighted grey areas indicate the water peak and the dashed grey lines indicate the targeted peaks for the on-peak measurements. Referring to Figure 4.23 (b), it can be seen that for both methane concentration ranges the water peaks are well distinguished from the methane peak and only neglectable spectral interference is expected.

#### 4.5.4 Partial Least Squares Regression

*Partial Least Squares Regression* (PLSR) combines the properties of *Multiple Linear Regression* (MLR) and *Principal Component Analysis* (PCA), with the goal of

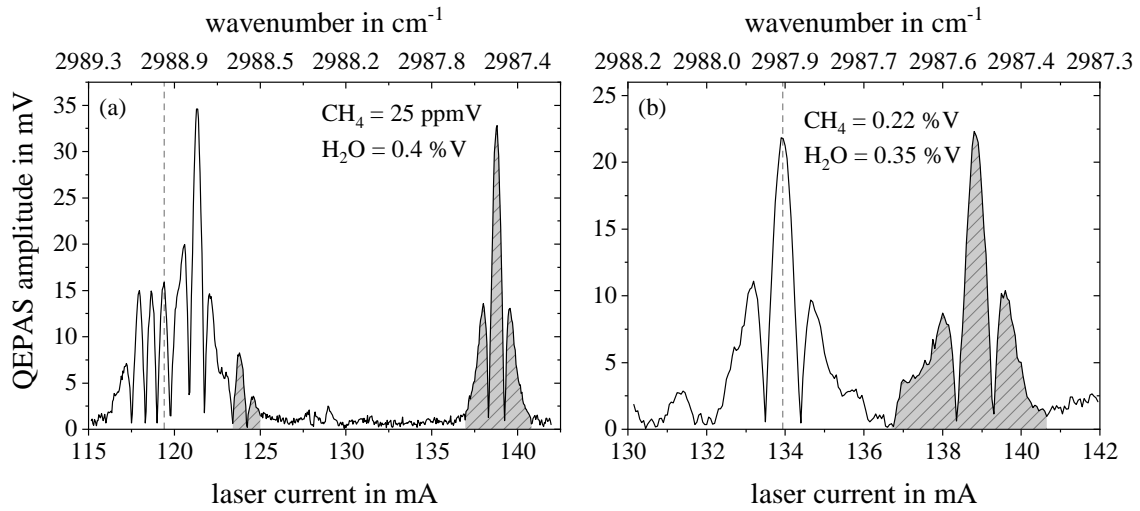


**Fig. 4.23.** Measured QEPAS spectra for the low (a) and the high (b)  $\text{CH}_4$  concentration range. The dashed grey lines indicate the selected on-peak  $\text{CH}_4$  peaks, the highlighted grey areas result from the water absorption.

predicting one or more dependent variables, e.g.  $\text{CH}_4$  concentration, from independent measured variables, e.g. QEPAS spectra [13]. The value  $\mathbf{Y}$  is to be predicted from the measured data  $\mathbf{X}$  with the regression coefficients  $\mathbf{B}$  and the residuals  $\mathbf{E}$ . In matrix form this can be expressed as equation (4.20), while  $n$  is the number of samples and  $m$  the number of independent variables [14].

$$\underbrace{\begin{pmatrix} Y_1 \\ Y_2 \\ Y_3 \\ \vdots \\ Y_n \end{pmatrix}}_{\mathbf{Y}} = \underbrace{\begin{pmatrix} X_{11} & X_{12} & X_{13} & \dots & X_{1m} \\ X_{21} & X_{22} & X_{23} & \dots & X_{2m} \\ X_{31} & X_{32} & X_{33} & \dots & X_{3m} \\ \vdots & \vdots & \vdots & \ddots & \vdots \\ X_{n1} & \dots & \dots & \dots & X_{nm} \end{pmatrix}}_{\mathbf{X}} \cdot \underbrace{\begin{pmatrix} B_1 \\ B_2 \\ B_3 \\ \vdots \\ B_m \end{pmatrix}}_{\mathbf{B}} + \underbrace{\begin{pmatrix} E_1 \\ E_2 \\ E_3 \\ \vdots \\ E_n \end{pmatrix}}_{\mathbf{E}} \quad (4.20)$$

The PLSR searches for a set of components (latent variables - LVs) that allows a simultaneous decomposition of  $\mathbf{X}$  and  $\mathbf{Y}$  with the requirement that these components explain a maximum amount of covariance between  $\mathbf{X}$  and  $\mathbf{Y}$  [14, 15]. It is assumed that only these LVs influence the investigated system and thus allow to predict  $\mathbf{Y}$ , e.g. the methane concentration. To avoid under- or overfitting in case of non-linear relations, when more than one LV is necessary, the number of used LVs must be carefully evaluated [14, 16]. Since PLSR does not require detailed knowledge about the system to be analyzed, e.g. regarding cross influences on the measurement signal, but offers high versatility and prediction power this approach is a popular evaluation method in chemometrics [15]. In recent years PLSR has also produced promising results in photoacoustic applications especially when dealing with complex gas matrices showing highly overlapping spectra [17, 18] or strong relaxation phenomena [9].

### PLSR algorithm optimization

The spectral QEPAS scans (see Figure 4.23) form the  $\mathbf{X}$  matrix, and the methane concentrations represent  $\mathbf{Y}$ . To account for photoacoustic phase shifts induced by rising humidity (see Figure 4.10), the in-phase as well as the quadrature QEPAS spectra, from which amplitude and phase can be calculated\* were used in the PLSR analysis. The measurement data were divided into a calibration set and a test set. To determine the optimal number of LVs for both concentration ranges a 10-fold cross-validation (CV) was performed before analyzing the test set. The aim is to minimize the CV error, expressed as root-mean-square error (RMSECV), while avoiding overfitting due to an excessive number of LVs used. For the low  $\text{CH}_4$  concentration range, the calibration data revealed an optimal number of LVs of five, correlating with an RMSECV of about 6 ppmV. Further increasing the LVs does not show a considerable improvement of the RMSECV. The optimal number of LVs for the high concentration range, with an RMSECV of 250 ppmV, was found to be six.

While it is not possible to directly attribute the individual LVs to specific physical parameters, or phenomena, the increase from five to six may potentially be assigned to the effect of self-relaxation, which is negligible at low  $\text{CH}_4$  concentrations. This could however, not be verified so far.

### 4.5.5 Results and disussion

The PLSR approach and DT were compared with respect to their methane concentration prediction accuracy. As the investigated methane concentrations cover a wide range (25 ppmV - 200 ppmV and 0.11 %V - 1.1 %V) the *mean absolute percentage error* (MAPE) is used as a comparison parameter. The MAPE can be calculated by equation (4.21).

$$\text{MAPE} = \frac{1}{n} \sum_{i=1}^n \left| \frac{[\text{CH}_4]_{i,\text{true}} - [\text{CH}_4]_{i,\text{pred}}}{[\text{CH}_4]_{i,\text{true}}} \right| \quad (4.21)$$

In which  $[\text{CH}_4]_{i,\text{true}}$  is the actual (*true*) methane concentration,  $[\text{CH}_4]_{i,\text{pred}}$  is the predicted value and  $n$  is the number of samples. The performance of the two approaches was evaluated separately for the low and high concentration ranges. Table 4.7 summarizes the results. For the trace concentration range, the DT shows a lower MAPE (3.8 %) and thus higher accuracy with respect to the actual value compared to the PLSR (4.6 %). In the high concentration range, however, the MAPE of the DT doubles up to 7.6 %, while the PLSR with 4.9 % shows only slightly worse results compared to the low range.

From Figure 4.24 it is evident that the DT shows the highest deviations to the measured data particularly at the lowest concentrations, i.e. 25 ppmV and 0.11 %V. However, comparing the QEPAS measurement data (black squares) it can also be

---

\*See Appendix A.3

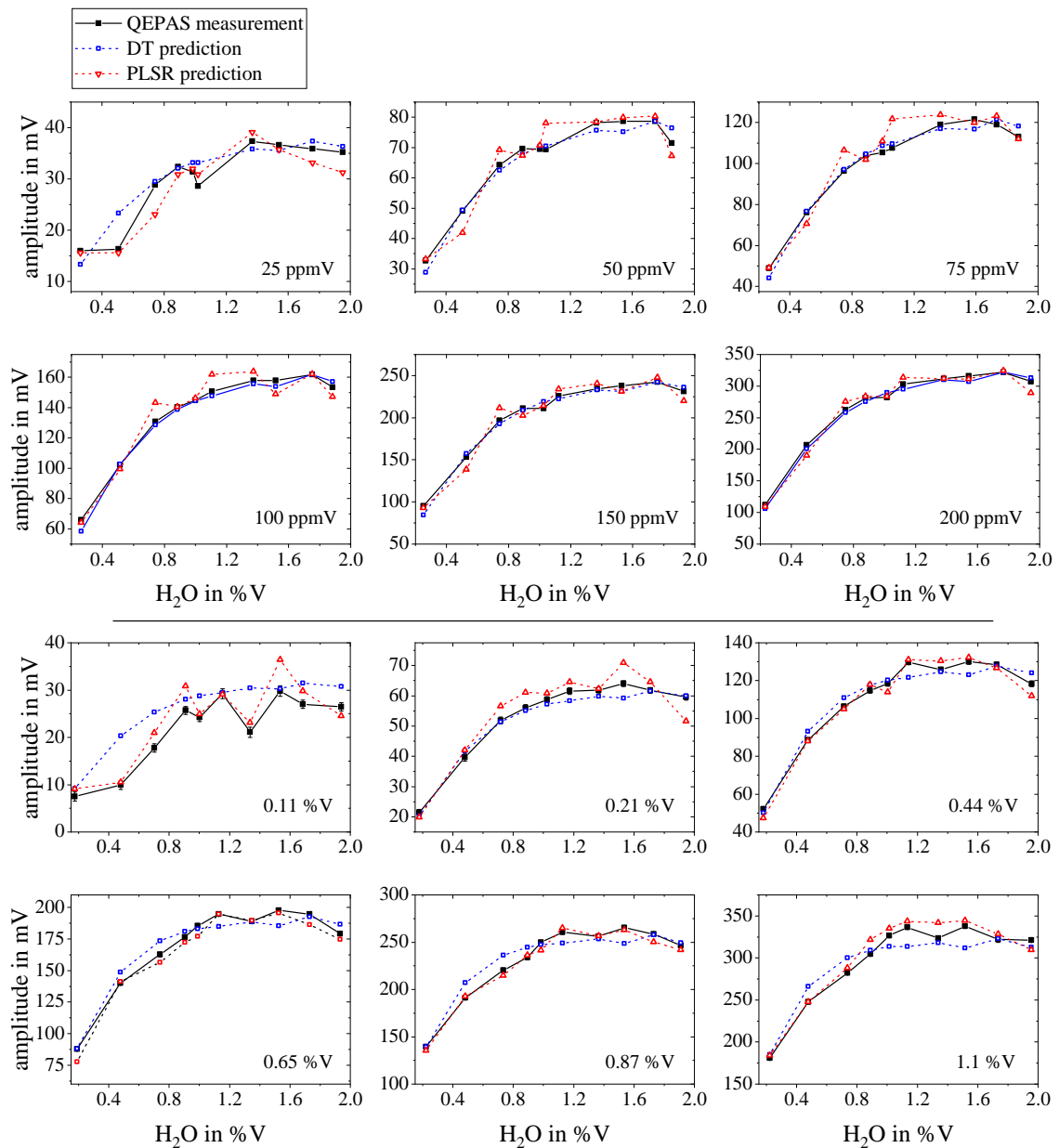


**Fig. 4.24.** Direct comparison of the QEPAS measurements (black squares), the DT (blue open squares) and the PLSR predictions (red open triangles).

observed that the 25 ppmV and the 0.11 %V curves deviate significantly from the others and hardly show any functional correlation. The reason for this is not yet completely clear. As these irregularities only occurred at the lowest methane concentrations of the respective concentration range, it might be suspected that they were induced by the gas mixing system operating at the lower limit. The PLSR is nevertheless able to reproduce these irregularities quite well, which is confirmed by a lower MAPE. Since modelling experimental artifacts will negatively affect the predictions in the field applications, the PLSR analysis must be evaluated regarding this issue. Omitting the 25 ppmV and 0.11 %V measurements from the data analysis,

**Tab. 4.7.** MAPE for the DT and PLSR analysis for the low and the high CH<sub>4</sub> concentrations.

	DT MAPE in %	PLSR MAPE in %
low CH <sub>4</sub>	3.8	4.6
high CH <sub>4</sub>	7.6	4.9

the MAPE of the DT improves to 2.9 %, and 3.5 %, respectively. Likewise, the PLSR MAPE can be reduced to 4.2 %, and 3.5 %, respectively. As a result, the DT shows the same accuracy as the PLSR predictions even in the high concentration range. Figure 4.25 presents the accuracy of the predictions in percentage deviation from the set CH<sub>4</sub> concentration as violin plots. In this representation, the effect of omitting the lowest concentrations, i.e. 25 ppmV and 0.11 %V, becomes very apparent, especially for the DT analysis. For humidities exceeding > 1.5 %V the measured QEPAS signal decreases, as shown in Figure 4.24. This effect cannot be explained by the relaxation behavior, since the relaxation efficiency  $\epsilon_{\text{relax}}$  increases continuously with more humidity towards 100 %, see Figure 4.17. The slight signal drop can be attributed to the  $Q$ -factor of the quartz tuning fork (QTF). By exciting the QTF electrically with an external function generator, the frequency response of the QTF can be measured, see Figure 4.26 (a). From this, the resonance frequency  $f_{\text{res}}$  and  $Q$ -factor of the QTF can be determined. While  $f_{\text{res}}$  remained constant over the entire humidity range, the  $Q$ -factor for humidities > 0.6 %V showed a steady decay\*, see Figure 4.26 (b). Summarizing, both approaches show a linear trend of the predicted CH<sub>4</sub> concentration versus the actual for both concentration ranges, see Figure 4.27. Table 4.8 summarizes the results of the best respective

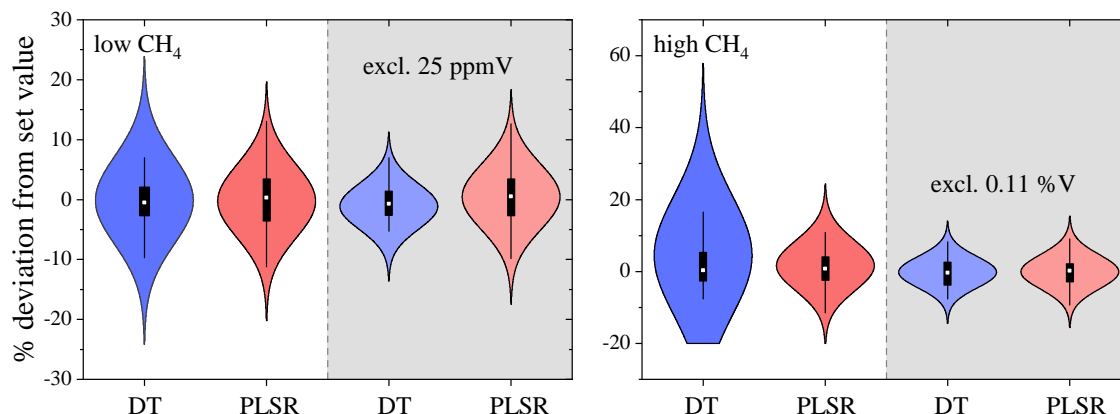


**Fig. 4.25.** Violin plots of the percentage prediction deviation obtained with the DT (blue) and with the PLSR (red). The shaded grey areas show the results, when excluding the lowest concentrations, i.e. 25 ppmV and 0.11 %V.

\*Except at H<sub>2</sub>O = 1.7 %V

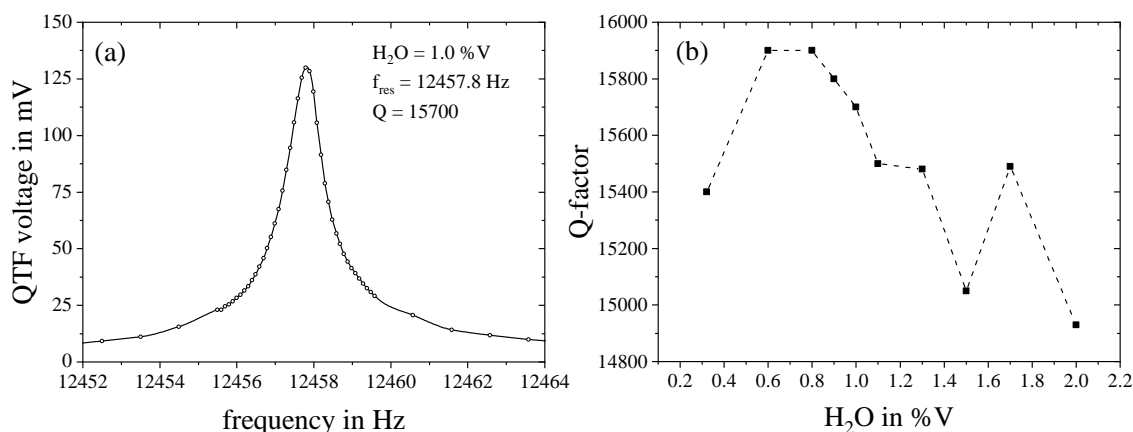


**Fig. 4.26.** Measured QTF frequency response for electrical stimulation (a). The Q-factors for different humidities are plotted on the right side (b).

linear fits, i.e. coefficient of determination  $R^2$  and slope, including the 25 ppmV and 0.11 %V measurements. While both approaches show a high  $R^2$  of  $\geq 0.990$ , the slopes calculated from the PLSR analysis are closer to the ideal case (slope = 1.000) compared to the DT analysis. Neglecting the lowest concentrations, the slope of the DT analysis improves to 0.986 ( $\pm 0.011$ ) for the low  $CH_4$  range and to 1.002 ( $\pm 0.015$ ) for the high range. For the PLSR analysis, this results in slightly worse slopes of 0.983 ( $\pm 0.015$ ) and 1.013 ( $\pm 0.011$ ), respectively. The  $R^2$  value deteriorates only very slightly for both approaches. Generally, it can be assumed that if the relaxation behavior, i.e. all energy transitions with the corresponding reaction rates, of the measurement matrix is fully known, the DT allows a more accurate prediction compared to the PLSR. If these conditions are met, the DT approach can be applied to any photoacoustic systems without much effort, as demonstrated in this chapter. The main limitation of DT is the uncertainty of the relaxation behavior. Current literature offers only little help in this context, since for most reaction rates no values are reported. The advantage of PLSR is that the fundamental principle can be easily applied to other analytes without the need for detailed knowledge of the physical behavior, e.g. non-radiative relaxation rates. However, PLSR cannot be applied to other photoacoustic systems without considerable effort, as the model is not generally

**Tab. 4.8.** Results of the best linear fits regarding the predicted  $CH_4$  concentrations, including 25 ppmV and 0.11 %V.

	low $CH_4$		high $CH_4$	
	$R^2$	slope	$R^2$	slope
DT	0.995	0.981 ( $\pm 0.009$ )	0.990	0.983 ( $\pm 0.013$ )
PLSR	0.992	0.992 ( $\pm 0.012$ )	0.996	1.001 ( $\pm 0.009$ )

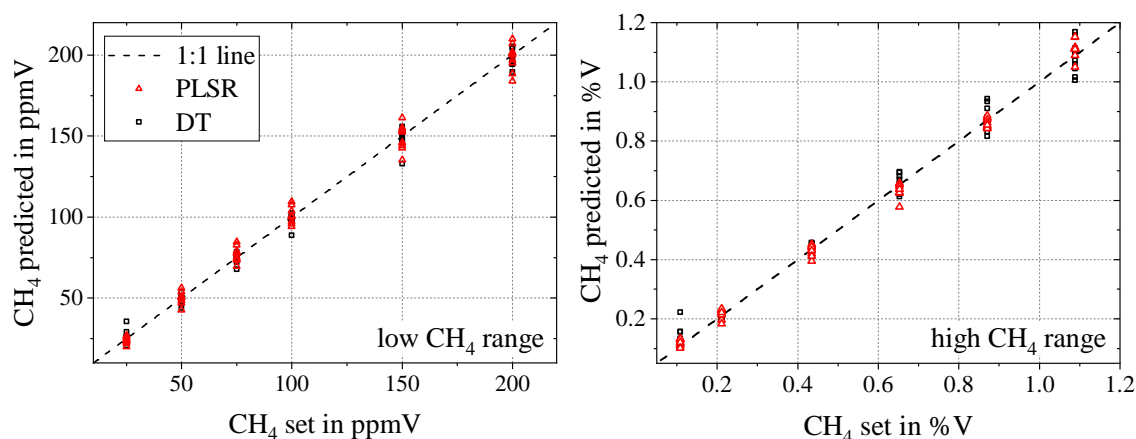


**Fig. 4.27.** Comparison of the DT (black open squares) and PLSR (red open triangles) predictions for the low and the high concentration range. The dashed grey lines indicate perfect linear behavior.

valid. Furthermore, the acquisition of training and test datasets is always necessary and time-consuming, while the effect of overfitting must be considered and avoided.

#### 4.5.6 Conclusion

In this chapter, a comparative analysis of two methods was presented with the aim of reducing the susceptibility of QEPAS sensors towards relaxation effects. While the first method (PLSR) is an established statistical technique, the second approach (DT) was first published in 2023 (see chapter 4.3). For the experimental setup, a compact QEPAS system was utilized which, in addition to the commercially available photoacoustic sensor, also contains electronics for signal generation and evaluation, as well as control and communication electronics. Two methane concentration ranges from 25 ppmV - 200 ppmV and 0.11 %V - 1.1 %V diluted in synthetic air excited with an ICL at around 3.345  $\mu\text{m}$  were investigated while increasing the humidity (0.25 %V - 2.0 %V). Despite the humidification strongly affecting the measured signal due to relaxation effects, both approaches were able to compensate for this quite well, showing an average concentration prediction accuracy of about 95 %. Subsequent research will focus on further improving the accuracy of both approaches. In order to be able to make a definitive statement about the performance in field measurements, PLSR and DT must be evaluated against a reference device, e.g. a Picarro G2301 cavity ring-down analyzer.

## References

- [1] A. A. Kosterev et al. “Quartz-enhanced photoacoustic spectroscopy”. In: *Opt. Lett.* 27.21 (Nov. 2002), p. 1902. ISSN: 0146-9592. DOI: 10.1364/OL.27.001902 (cit. on p. 113).
- [2] Y. Liu et al. “Integrated near-infrared QEPAS sensor based on a 28 kHz quartz tuning fork for online monitoring of CO<sub>2</sub> in the greenhouse”. In: *Photoacoustics* 25 (Mar. 2022), p. 100332. ISSN: 22135979. DOI: 10.1016/j.pacs.2022.100332 (cit. on p. 113).
- [3] G. Menduni et al. “Measurement of methane, nitrous oxide and ammonia in atmosphere with a compact quartz-enhanced photoacoustic sensor”. In: *Sensors Actuators B Chem.* 375 (Jan. 2023), p. 132953. ISSN: 09254005. DOI: 10.1016/j.snb.2022.132953 (cit. on p. 113).
- [4] B. Li et al. “Quartz-enhanced photoacoustic spectroscopy (QEPAS) and Beat Frequency-QEPAS techniques for air pollutants detection: A comparison in terms of sensitivity and acquisition time”. In: *Photoacoustics* 31 (June 2023), p. 100479. ISSN: 22135979. DOI: 10.1016/j.pacs.2023.100479 (cit. on p. 113).
- [5] R. De Palo et al. “Quartz-Enhanced Photoacoustic Sensors for Detection of Eight Air Pollutants”. In: *Adv. Photonics Res.* 4.6 (June 2023). ISSN: 2699-9293. DOI: 10.1002/adpr.202200353 (cit. on p. 113).
- [6] A. Kosterev et al. “QEPAS methane sensor performance for humidified gases”. In: *Applied Physics B* 92.1 (July 2008), pp. 103–109. ISSN: 0946-2171. DOI: 10.1007/s00340-008-3056-9 (cit. on p. 113).
- [7] L. Dong et al. “Compact QEPAS sensor for trace methane and ammonia detection in impure hydrogen”. In: *Applied Physics B: Lasers and Optics* 107.2 (2012), pp. 459–467. ISSN: 09462171. DOI: 10.1007/s00340-012-4908-x (cit. on p. 113).
- [8] Y. Ma et al. “Sensitive Detection of CO and N<sub>2</sub>O using a High Power CW 4.61  $\mu$ m DFB-QCL Based QEPAS Sensor”. In: *Optics Express* 21.1 (2013), pp. 1008–19. DOI: 10.1364/CLEO\_AT.2013.JW2A.80 (cit. on p. 113).
- [9] G. Menduni et al. “High-concentration methane and ethane QEPAS detection employing partial least squares regression to filter out energy relaxation dependence on gas matrix composition”. In: *Photoacoustics* 26 (June 2022), p. 100349. ISSN: 22135979. DOI: 10.1016/j.pacs.2022.100349 (cit. on pp. 114, 117).
- [10] A. A. Kosterev et al. “Quartz-enhanced photoacoustic spectroscopy”. In: *Opt. Lett.* 27.21 (Nov. 2002), p. 1902. ISSN: 0146-9592. DOI: 10.1364/OL.27.001902 (cit. on p. 114).
- [11] Q. Wang et al. “Wavelength-stabilization-based photoacoustic spectroscopy for methane detection”. In: *Meas. Sci. Technol.* 28.6 (June 2017), p. 065102. ISSN: 0957-0233. DOI: 10.1088/1361-6501/aa6a08 (cit. on p. 115).

- [12] I. Gordon et al. “The HITRAN2020 molecular spectroscopic database”. In: *J. Quant. Spectrosc. Radiat. Transf.* 277 (Jan. 2022), p. 107949. ISSN: 00224073. DOI: 10.1016/j.jqsrt.2021.107949 (cit. on p. 116).
- [13] H. Abdi. “Partial least squares regression and projection on latent structure regression (PLS Regression)”. In: *WIREs Comput. Stat.* 2.1 (Jan. 2010), pp. 97–106. ISSN: 1939-5108. DOI: 10.1002/wics.51 (cit. on p. 117).
- [14] P. Geladi and B. R. Kowalski. “Partial least-squares regression: a tutorial”. In: *Anal. Chim. Acta* 185 (1986), pp. 1–17. ISSN: 00032670. DOI: 10.1016/0003-2670(86)80028-9 (cit. on p. 117).
- [15] S. Wold et al. “PLS-regression: a basic tool of chemometrics”. In: *Chemom. Intell. Lab. Syst.* 58.2 (Oct. 2001), pp. 109–130. ISSN: 01697439. DOI: 10.1016/S0169-7439(01)00155-1 (cit. on p. 117).
- [16] M. Gómez-Carracedo et al. “Selecting the optimum number of partial least squares components for the calibration of attenuated total reflectance-mid-infrared spectra of undesigned kerosene samples”. In: *Anal. Chim. Acta* 585.2 (Mar. 2007), pp. 253–265. ISSN: 00032670. DOI: 10.1016/j.aca.2006.12.036 (cit. on p. 117).
- [17] A. Loh and M. Wolff. “Multivariate Analysis of Photoacoustic Spectra for the Detection of Short-Chain Hydrocarbon Isotopologues”. In: *Molecules* 25.9 (May 2020), p. 2266. ISSN: 1420-3049. DOI: 10.3390/molecules25092266 (cit. on p. 117).
- [18] A. Zifarelli et al. “Partial Least-Squares Regression as a Tool to Retrieve Gas Concentrations in Mixtures Detected Using Quartz-Enhanced Photoacoustic Spectroscopy”. In: *Anal. Chem.* 92.16 (Aug. 2020), pp. 11035–11043. ISSN: 0003-2700. DOI: 10.1021/acs.analchem.0c00075 (cit. on p. 117).

## 4.6 Spectral influences on WM-2f photoacoustic detection

As shown in sections 4.2, 4.3 and 4.4 the ICL emitting at around  $2968.4\text{ cm}^{-1}$  can be utilized for detecting traces of methane in ambient air. However, the initial purpose of this ICL was to simultaneously quantify the first three alkanes, namely methane, ethane and propane in fuel gas. Table 4.9 lists the expected concentration ranges of the analytes the potential interfering components, provided by Messko GmbH (Oberursel, Germany).

**Tab. 4.9.** List of the target analytes (**bold**) methane, ethane and propane for fuel gas analysis, including the expected concentration ranges. The potential interfering components are marked in *italics*.

	expected conc. range
<b>CH<sub>4</sub></b>	5 - 100 %V
<b>C<sub>2</sub>H<sub>6</sub></b>	0.1 - 20 %V
<b>C<sub>3</sub>H<sub>8</sub></b>	500 ppmV - 20 %V
<i>CO<sub>2</sub></i>	10 ppmV - 15 %V
<i>CO</i>	1 ppmV - 2 %V
<i>H<sub>2</sub>O</i>	1 - 500 ppmV
<i>H<sub>2</sub>S</i>	0.1 ppmV - 0.5 %V

In order to measure these analytes using a single laser source, a spectroscopic analysis was performed a priori. This analysis yielded the spectral range from  $2967\text{ cm}^{-1}$  to  $2975\text{ cm}^{-1}$  to be the most promising, see Figure 4.28. The three analytes dominate this spectral region and show individual distinct peaks. All possible interfering components listed in Table 4.9 show either no relevant absorption at all ( $\text{CO}_2$ ,  $\text{CO}$ ) or several orders of magnitude less absorption ( $\text{H}_2\text{O}$ ,  $\text{H}_2\text{S}$ ). Since in this present work the focus was not on fuel gas analysis, but methane detection in the environment, see chapter 4.4 it was necessary to evaluate the spectral range regarding environmental monitoring. For a typical ambient methane concentration of around 2 ppmV the spectral overlap with water in the %V - range is only modest, see Figure 4.29. Regarding ethane, from 1999 to 2015, a yearly periodic concentration oscillation from about 500 to 2500 ppbV was measured at the Hohenpeißenberg meteorological observatory, with a slight increase starting at 2010 of about 22 pptV per year [1]. Newer data from January 2015 to December 2018 at the Greenland Environmental Observatory at Summit station revealed a decrease in concentration of 58.4 pptV per year. Measurements after 2019 indicate however, that the decrease in concentration might have only been temporary and will rise again [2]. For this concentration range the selected spectral region is not suitable, as the ethane peak would be dominated

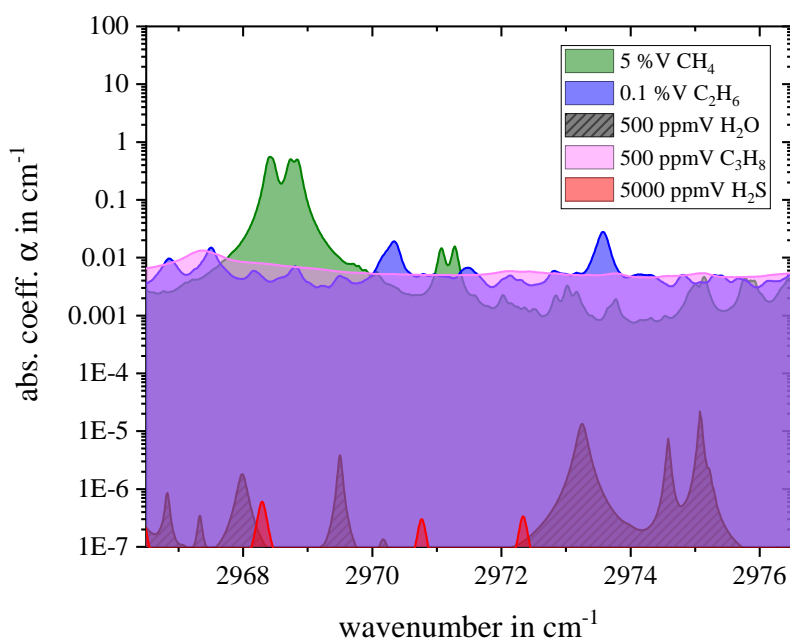


**Fig. 4.28.** Logarithmic representation of the absorption coefficients  $\alpha$  for typical fuel gas analysis in the spectral range from 2966.65 to 2975.25  $\text{cm}^{-1}$ .

by water absorption. Considering that, in case of gas leakage detection for example, the ethane concentration rises up to the lower ppmV range [3], this absorption peak might still be of interest. Natural gas has a specific methane/ethane ratio, thus simultaneous monitoring of both analytes could drastically increase the confidence of gas leak classification. For this purpose, the photoacoustic signal emanating from the ethane peak at  $2973.55 \text{ cm}^{-1}$  was examined for spectral and non-spectral influences due to  $\text{O}_2$  and  $\text{H}_2\text{O}$ , which are the most abundant species in air besides  $\text{N}_2$ . Besides affecting the resonance frequency of the PA sensor, oxygen was found to have no significant influence on the photoacoustic ethane signal. Increasing the humidity inside the measurement cell yielded a significant decrease in PA amplitude while not affecting the signal phase. The measured amplitude decrease was found to be strongly dependent on the analyte concentration, i.e. more pronounced decrease for lower ethane concentrations. The relative effect on the photoacoustic amplitude induced by changes in the relaxation cascade is known to not depend on the analyte concentration in terms of trace gas analysis, e.g.  $<1 \text{ \%V}$ . This indicates that the measured signal decrease in chapter 4.6.2 is not caused by relaxational, but rather by spectral effects. For this reason a Python based simulation tool was developed, which allows for quantification of the expected WM-2f PAS amplitude and phase with regard to peak deformation caused by either spectral overlap (see chapter 4.6.2) or pressure deformation (see chapter 4.6.3).

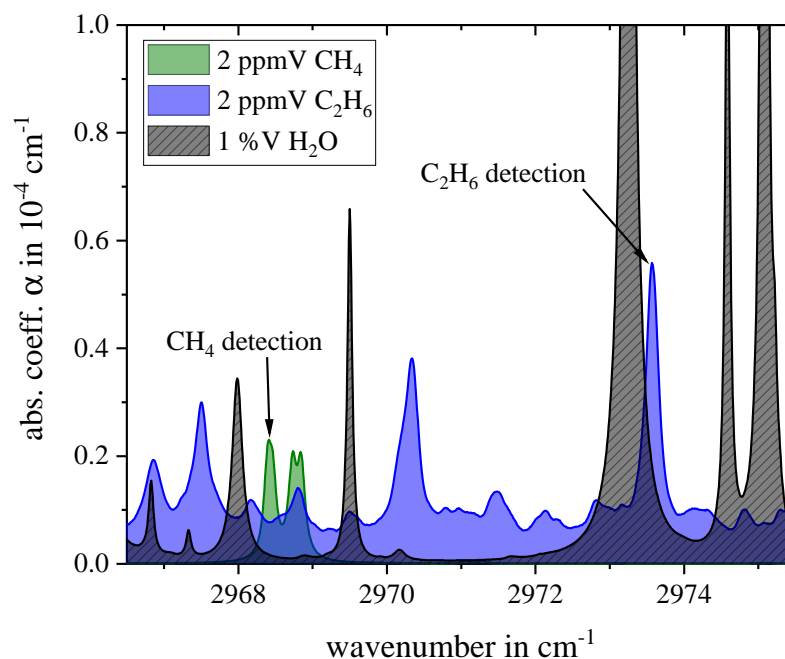


**Fig. 4.29.** Absorption coefficient of ambient methane (2 ppmV) and water (1 %V) concentration, as well as 2 ppmV ethane.

#### 4.6.1 Alternative representation of WM-2f PAS signal

The theory behind WM spectroscopy was introduced in chapter 2.1.2. The consequences of this modulation technique on the photoacoustic signal will be discussed in the subsequent sections. In order to evaluate spectral influences, such as spectral overlap or peak deformation, on the WM-2f PAS signal, the signal generation process was simplified and simulated, see Figure 4.30. First the absorption spectrum of the individual components (A, B) were added to yield the sum spectrum (A+B) (1). The sum spectrum was then superimposed with the sinusoidal modulation of the laser (2). This results in a time periodic PA pressure, due to the differences in the absorption coefficient during laser modulation (3). The PA pressure is then analyzed via FFT in order to determine the signals frequency components (4). The amplitude of the characteristic peak at twice the laser modulation frequency  $2f_{\text{mod}}$  is a metric for the measured photoacoustic signal, as typically in WM-2f PAS only the first harmonic of the modulation frequency is evaluated. This type of analysis therefore allows to predict spectral influences on the photoacoustically measured WM-2f signal.

Another equivalent approach would be simulating the second derivative of the sum spectrum. The amplitude of the derivation at the on-peak wavelength is similarly a measure of the photoacoustic signal. While the applied laser modulation depth  $\Delta\tilde{\nu}$  is an important input for the FFT-based analysis, see Figure 4.30 (2), the instrument function  $B(\tilde{\nu})$  of the laser is essential for the derivative analysis.  $B(\tilde{\nu})$  accounts for non-ideal characteristics of the laser emission profil. An ideal line emitter would have no instrument function, i.e. only emitting at one wavenumber  $\tilde{\nu}$ , and could

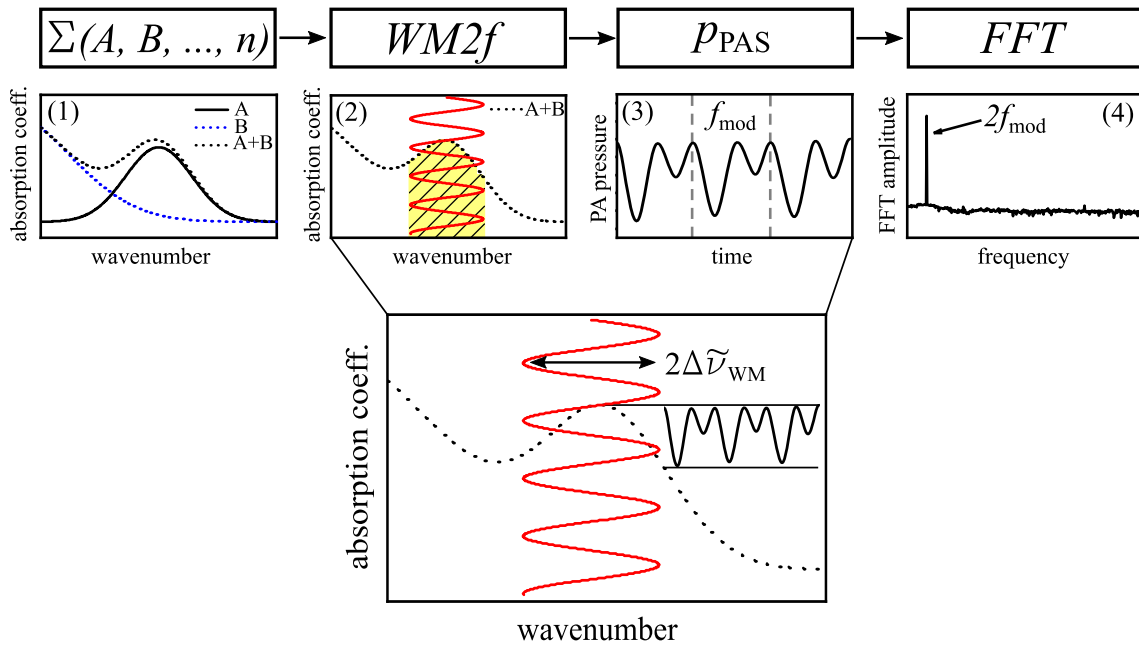


**Fig. 4.30.** Schematic of the FFT-based simulation process to quantify PAS signal alteration due to peak deformation.

perfectly scan and replicate the absorption spectrum. Real laser sources show mostly gaussian distributed emissions profiles, which must be convoluted over the absorption spectrum  $F(\tilde{\nu})$  to yield the measured spectrum  $F'(\tilde{\nu})$ , see Figure 4.31. The spectral full width at half-maximum (FWHM) in units [ $\text{cm}^{-1}$ ] of  $B(\tilde{\nu})$  is hereafter labeled as IF [4, 5].

$$(F * B)(\tilde{\nu}) = F'(\tilde{\nu}) = \int_{-\infty}^{\infty} B(\tilde{\nu} - \tilde{\nu}')F(\tilde{\nu}')d\tilde{\nu}' \quad (4.22)$$

With the normalized instrument function [4]

$$B(\tilde{\nu}) = \sqrt{\frac{\ln(2)}{\pi}} \exp\left(-\ln(2) \left(\frac{\tilde{\nu} - \tilde{\nu}'}{\text{IF}}\right)^2\right) \quad (4.23)$$

By comparing the left side (a) and right side (b) of Figure 4.31, it becomes clear why IF is an important parameter when applying second derivative analysis that must not be neglected. A smaller IF results in higher resolution in terms of absorption spectra replication. When scanning over an absorption profile applying WM, the modulation depth dominates the spectral overlap of laser emission with molecule absorption. Accordingly,  $\tilde{\nu}_{WM}$  corresponds to the spectral width of the instrument function.

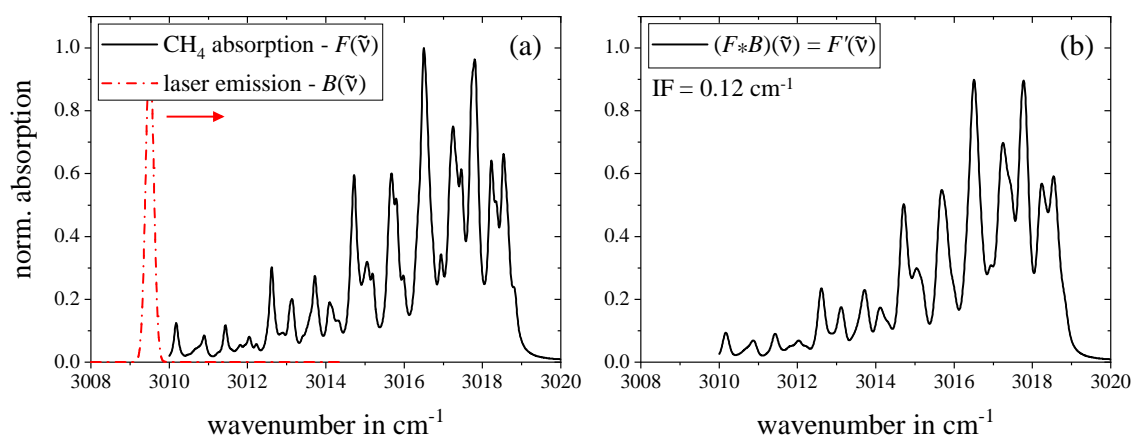


**Fig. 4.31.** Representation of the effect of non-ideal light sources on the measured absorption spectrum. Both graphs are normalized to the maximal absorption. The left side (a) displays the *HITRAN on the Web* simulated  $\text{CH}_4$  absorption from 3010 - 3020  $\text{cm}^{-1}$ , without any applied instrument function. The red dashed-dotted line in (a) shows a gaussian distributed laser emission scanning over  $F(\tilde{\nu})$ , according to equation 4.23. As a result, the right side (b) illustrates the effect of  $B(\tilde{\nu})$  with a spectral width of  $\text{IF} = 0.12 \text{ cm}^{-1}$  on the measured spectrum  $F'(\tilde{\nu})$ .

#### 4.6.2 Spectral overlap of water with ethane

As shown in Figure 4.29 the ethane peak at  $2973.57 \text{ cm}^{-1}$  shows strong overlap with the neighboring  $\text{H}_2\text{O}$  absorption at  $2973.25 \text{ cm}^{-1}$ . The effect of water on the  $\text{C}_2\text{H}_6$  detection was investigated for humidities ranging from 0 %V to 2.25 %V (40.5 %r.H. at  $35^\circ\text{C}$ ) and for ethane concentrations from 1.2 ppmV up to 15.1 ppmV. A modulation depth of  $\Delta\tilde{\nu}_{\text{WM}} = 0.174 \text{ cm}^{-1} \hat{=} I_{\text{mod}} = 6 \text{ mA}$  was applied for all measurements and for the WM-2f FFT analysis. The complete procedure of the FFT analysis for measured data is shown in Appendix A6 - Figure A6. Figure 4.32 (a) - (e) shows the normalized measured PAS amplitudes (black circles), as well as the simulation results (red solid lines). For all investigated ethane concentrations the measured amplitude characteristics decline with rising humidity starting with dry sample gas. The slope of this decrease in amplitude, however, was found to be strongly dependent on the  $\text{C}_2\text{H}_6$  concentration, as indicated by (f) in Figure 4.32. This effect on the slope was not linear, but is more pronounced towards lower  $\text{C}_2\text{H}_6$  concentrations. The WM-2f FFT calculation was able to simulate these characteristics, showing good agreement with the measurement data for all investigated compositions. For the lowest ethane concentration, i.e.  $\text{C}_2\text{H}_6 = 1.2 \text{ ppmV}$ , the PAS amplitude reached a minimum at  $\text{H}_2\text{O} = 0.83 \text{ %V}$  and started to rise again for higher humidities accompanied by a phase shift of  $180^\circ$  as indicated by the dotted grey line in Figure 4.32 (e). Relaxational or acoustic ( $Q$ -factor, resonance frequency shifts) effects could be excluded as the cause for these measurement results. Both the decline in amplitude for all ethane concentrations, as well as the phase shift of  $180^\circ$  for the lowest ethane concentration, can be explained by the WM-2f absorption spectrum. As described in chapter 2.1.2 the WM-2f spectrum is equivalent to the second derivative of the absorption spectrum.

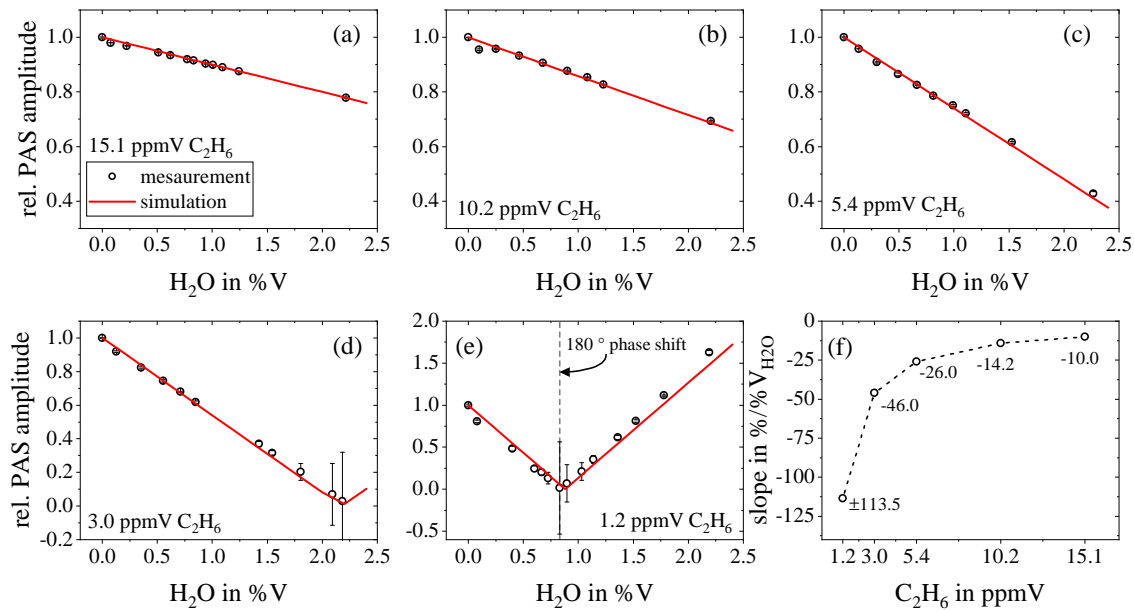


**Fig. 4.32.** Effect of rising humidity on the photoacoustic  $C_2H_6$  detection at  $2973.57 \text{ cm}^{-1}$  with a modulation depth of  $\Delta\tilde{\nu}_{WM} = 0.174 \text{ cm}^{-1}$  for different  $C_2H_6$  concentrations. The lower right graph (f) summarizes the relative slopes of the amplitude decrease.

A Gaussian or Lorentzian shaped absorption peak yields the characteristic shape of the WM-2f spectrum, i.e. zero crossings at the turning points, the maximum at the absorption peak and negative minima at the steepest point of the rising and falling edges, see Figure 4.33 - black dashed lines (I). Due to the spectral overlap of the edge of the water absorption with the ethane peak, the inflection points of the total absorption are distorted, and the ethane absorption maximum is covered. This strongly influences the resulting WM-2f spectrum, see Figure 4.33. With rising water the amplitude at the actual ethane peak maximum, which is indicated by the vertical dashed grey line in Figure 4.33, decreases until it reaches zero for a mixture containing 1.2 ppmV ethane and 0.83 %V H<sub>2</sub>O, see the green curve (III). This corresponds to the exact water concentration, for which both the measured and the simulated PA amplitude is zero (Figure 4.32 - (e)). Even further humidification (IV) yields negative values in the second derivative of the absorption spectrum at the ethane on-peak detection wavenumber. As typically in PAS a lock-in amplifier is employed for signal evaluation, and the measured amplitude  $\hat{u}_s$  of the complex PA signal is calculated via equation (9). From this relation it is evident, that no negative values for  $\hat{u}_s$  can occur. If both the in-phase  $\hat{U}_i$  and quadrature  $\hat{U}_q$  LIA output are negative, this will result in a positive amplitude, but with the phase shifted by 180°. Accordingly, at the transition from positive to negative values, and vice versa, in the 2f spectrum, the LIA would measure a phase jump, while retaining a positive amplitude, see Figure 4.34.

The FFT analysis calculates the amplitude  $R$  from the real  $X$  and imaginary  $Y$  part of the signal via  $R = \sqrt{X^2 + Y^2}$  and the phase accordingly  $\Phi = \arctan(Y/X)$ , resulting

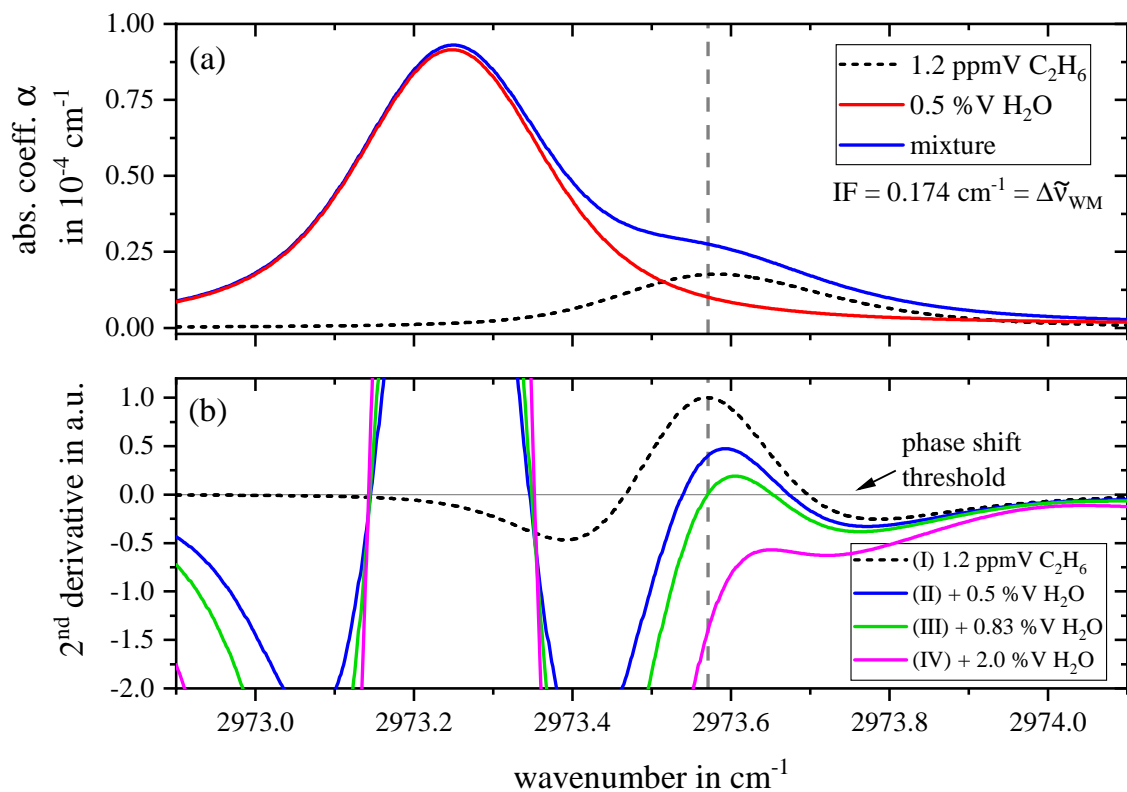


**Fig. 4.33.** Absorption spectra (a) of 1.2 ppmV  $\text{C}_2\text{H}_6$ , 0.5 %V  $\text{H}_2\text{O}$  and the mixture with an applied IF of  $0.174 \text{ cm}^{-1}$ . The data was generated with Molexplorer database. The bottom graphs (b) show the resulting second derivatives of different mixtures containing increasingly more water. The vertical grey dashed line indicates the ethane on-peak detection wavenumber.

in the same output as the LIA. For higher ethane concentrations, the spectral overlap with water is smaller, which means that the influence of peak distortion on the WM-2f PA signal is much smaller, but still significant for the investigated conditions.

In order to examine the influence of peak distortion for the lowest concentration of 1.2 ppmV ethane in detail, the laser modulation depth was varied from  $0.065 \text{ cm}^{-1}$  to  $0.18 \text{ cm}^{-1}$  and measured for six different humidities, see Figure 4.35. The measured data (black dots) were again compared with the WM-2f FFT simulation (red line) and showed quite good agreement. For all measurements the amplitude steadily increased up to a certain modulation depth, reached a maximum and declined thereafter. As soon as a minimum is reached, the amplitude starts to rise again. For low modulation depths, the Gaussian shape of the ethane peak dominates, resulting in a strong 2f frequency component. At the turning point, the laser modulation reaches too far in the edge of the water absorption, distorting the sum spectrum, yielding a lower amplitude at the ethane on-peak wavenumber in the second derivative spectrum, see Figure 4.33. Even further increasing the modulation depth results in negative values in the WM-2f spectrum, which would be displayed by the lock-in-amplifier and the FFT analysis as positive amplitudes accompanied by a phase shift of  $180^\circ$ .

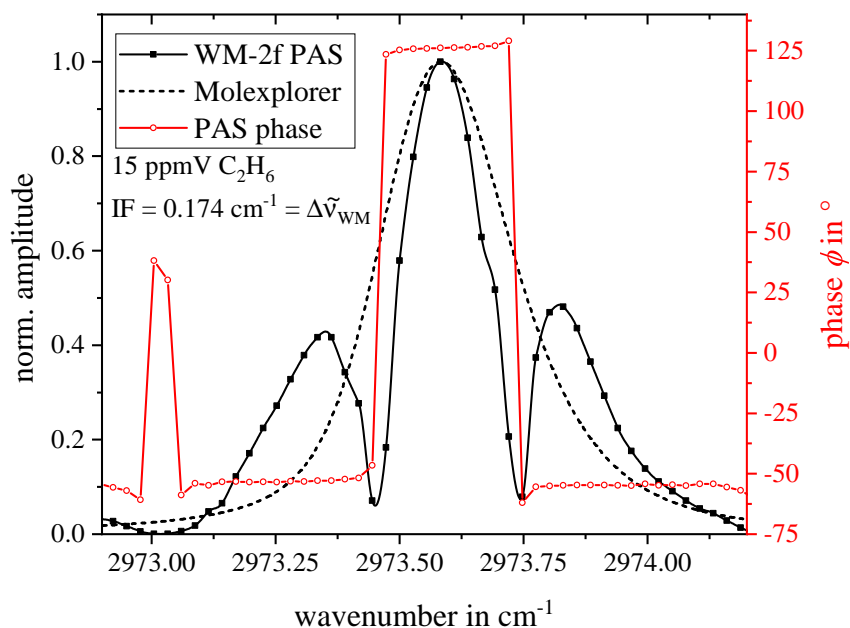


**Fig. 4.34.** Measured WM-2f spectrum of 15 ppmV  $C_2H_6$  diluted in  $N_2$ . The PAS amplitude is marked as black, the phase information in red and the dashed line indicates absorption peak simulated with  $IF = 0.174 \text{ cm}^{-1}$ .

Although with the presented method the water influence can be predicted well for different ethane concentrations, see Figure 4.32, for reliable ethane detection a spectral region with less overlap should be selected nevertheless. Chapter 4.7 discusses a slightly different spectral region for ppbV level ethane detection, providing promising results.

### 4.6.3 Methane absorption pressure deformation

In chapter 4.3 the results of the DT for a variety of different environmental conditions, e.g. different pressures regarding methane detection was presented. While for higher pressures the predicted methane concentration of the DT was very close to the set concentration, for lower pressures ( $< 650 \text{ mbar}$ ) the prediction became gradually worse, see Figure 4.15 (f). The DT considers the effect of relaxation, the  $Q$ -factor, resonance frequency shifts and the adiabatic exponent to their full extend. However, in the current version of the DT, the ACS is only considered in a very simplified manner by calculating the peak-to-baseline difference of absorption coefficient for the WM modulation. Reducing the pressure inside the photoacoustic measurement cell from 1035 mbar to 354 mbar induces the  $Q$ -factor to drop from 39.5 to 24.0, as well as a shift in resonance frequency by 34.3 Hz, mainly due to node shifting effects [6]. While the probability of VV or VT relaxation processes per molecule collision does not depend on the pressure, the collision rate does. This decrease in collision rate for lower pressures causes the overall relaxation efficiency to drop from 84.4 % at 1035 mbar to 55.5 % at 354 mbar. The discrepancies in DT prediction

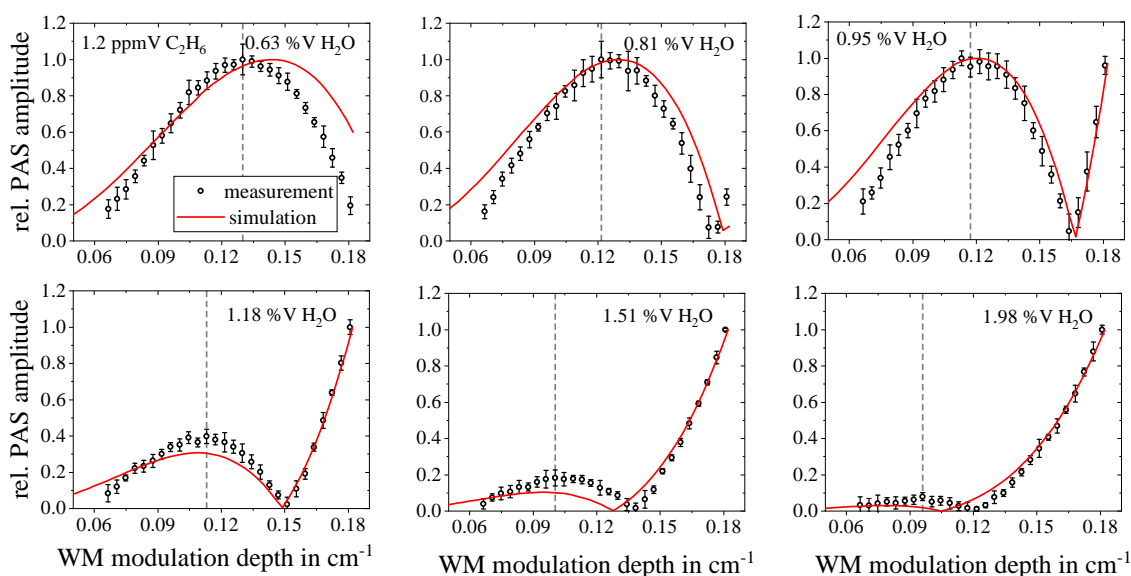


**Fig. 4.35.** Variation of applied laser modulation depth for 1.2 ppmV ethane and different humidities. The measured data are indicated by the black circles, the simulation results by the red solid line. The grey dotted lines indicate the optimal modulation depth for ethane detection, according to the measurements.

to the set value for low pressures could thus be linked to the simplified absorption coefficient consideration, as the modulated methane peak gets significantly distorted, see Figure 4.36\*. While for the WM-2f simulations ethane and water spectra from Molexplorer database were used, for the investigated pressure deformation of methane self-acquired photoacoustic spectra were found to yield the best simulation results. This is mainly due to two reasons. Comparing the results of Molexplorer and *HITRAN on the web* simulations for the pressure dependency of the methane absorption from  $2968.1\text{ cm}^{-1}$  to  $2968.8\text{ cm}^{-1}$  significant discrepancies between the databases became obvious see Appendix A.5 - Figure A3. The Molexplorer simulation revealed a much greater pressure separation of the two absorption lines located at  $2968.4\text{ cm}^{-1}$  and  $2968.48\text{ cm}^{-1}$  compared to the *HITRAN on the web* calculations. Although the *HITRAN on the web* database utilizes more recent data, the differences to the Molexplorer data were so significant that it was decided to measure the spectra for different pressures in-house. This was done by amplitude modulating a separate ICL, which allowed spectral tunability in AM mode from  $2968\text{ cm}^{-1}$  to  $2969\text{ cm}^{-1}$ . Unlike in WM mode, AM PAS shows a background signal (BGS) mostly induced by periodic light absorption of the windows or other parts of the measurement cell [7–9]. This BGS depends also on the acoustic properties of the PAC, i.e.  $Q$ -factor and resonance frequency, and must thus be recorded for every pressure, as both the  $Q$ -factor and the resonance frequency show a non-linear pressure dependency. After recording the BGS the methane spectrum was recorded and subtracted by the BGS yielding the final spectrum. Further correction of the PA signal was performed by normalizing the spectra to the measured optical power. As seen in Appendix A.5 - Figure A3 the

\*The complete set of measured spectra can be found in Appendix A.6 - Figure A4.

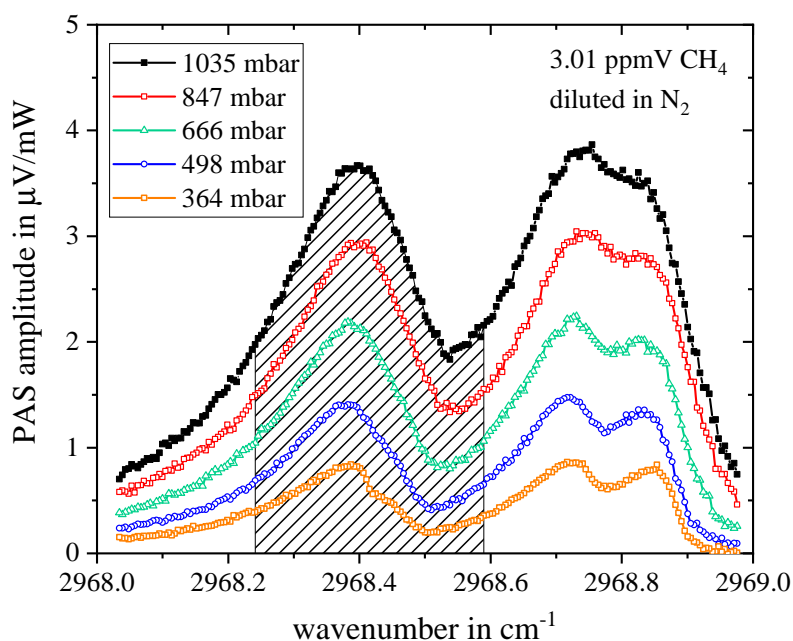


**Fig. 4.36.** Measured PA spectra of 3.01 ppmV CH<sub>4</sub> for selected pressures ranging from 1035 mbar to 364 mbar. For the sake of visual clarity, the measured spectra for the intermediate pressures have not been plotted. The shaded grey area indicates the WM scanning range.

absorption peak centered at 2968.4 cm<sup>-1</sup> deteriorates with lower pressure compared to pure Voigt shape. At ambient pressure the two separate absorption lines located at 2968.4 cm<sup>-1</sup> and 2968.47 cm<sup>-1</sup> form, due to pressure broadening, a single peak. Decreasing the pressure reveals the two separate absorption peaks, see Appendix A.5 - Figure A3 upper graphs. In the measured data (Figure 4.36) this separation is not clearly visible, even for the lowest pressure of 364 mbar, due to the instrument function of the used ICL. The finite spectral width of the ICL yields a worse resolution of the absorption spectra  $F_i(\nu)$ , which can also be seen in the simulated spectra in the lower graphs of Appendix A.5 - Figure A3.

Supplementing the DT with the presented WM-2f FFT simulation tool, the error in methane prediction could drastically be reduced from previous 5.6 ppmV (39.5 %) at the lowest investigated pressure of 354 mbar down to -1.3 ppmV (8.9 %), see Figure 4.37.

#### 4.6.4 Conclusion

WM in photoacoustic spectroscopy offers several advantages, mainly the absence of background signal [10, 11], yet some issues have to be taken into account. Peak deformations, whether due to spectral overlap or pressure broadening, also have an influence on the WM signal [11, 12]. While the influence of peak deformations in AM spectroscopy is additive and thus rather easy to deal with (refer to chapter 4.7),

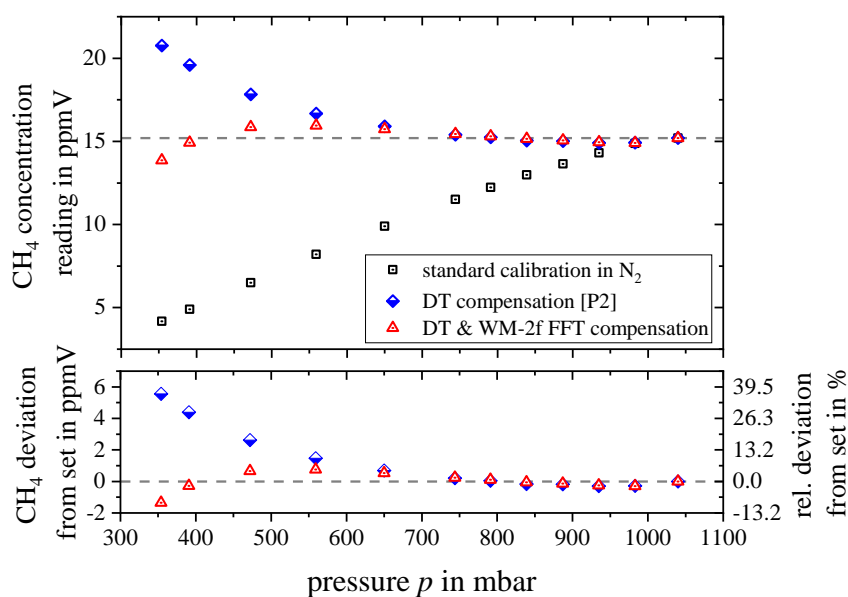


**Fig. 4.37.** Predicted  $\text{CH}_4$  concentration in ppmV based on standard calibration in dry nitrogen (black squares), DT compensation (blue half-filled diamonds) and combination of DT and WM-2f FFT analysis (red triangle). The lower graph shows the improvement in deviation (in ppmV - left y-axis and in % - right y-axis) from the set value for the DT calculations compared to the combined analysis.

it is more complex in terms of WM. Instead of signal increase due to additional absorption (spectral overlap), for example, the measured signal decreases, if the modulation of the laser reaches into the edge of the overlapping absorption feature. However, with the presented WM-2f FFT method such effects can be calculated. Thus, the WM method can also be applied in regions which are not completely free of spectral overlaps caused by interfering components. Combining this method with the DT (chapter 4.3), one obtains a very versatile tool, which is able to compute relaxational, acoustic and spectral effects on the photoacoustic signal and thus significantly increases the reliability of photoacoustic measurement data.

## References

- [1] D. Helmig et al. “Reversal of global atmospheric ethane and propane trends largely due to US oil and natural gas production”. In: *Nat. Geosci.* 9.7 (July 2016), pp. 490–495. ISSN: 1752-0894. DOI: 10.1038/ngeo2721 (cit. on p. 125).
- [2] H. Angot et al. “Temporary pause in the growth of atmospheric ethane and propane in 2015–2018”. In: *Atmos. Chem. Phys.* 21.19 (Oct. 2021), pp. 15153–15170. ISSN: 1680-7324. DOI: 10.5194/acp-21-15153-2021 (cit. on p. 125).

- [3] R. B. Jackson et al. “Natural Gas Pipeline Leaks Across Washington, DC”. In: *Environ. Sci. Technol.* 48.3 (Feb. 2014), pp. 2051–2058. ISSN: 0013-936X. DOI: 10.1021/es404474x (cit. on p. 126).
- [4] F. Schreier. “The Voigt and complex error function: A comparison of computational methods”. In: *J. Quant. Spectrosc. Radiat. Transf.* 48.5-6 (Nov. 1992), pp. 743–762. ISSN: 00224073. DOI: 10.1016/0022-4073(92)90139-U (cit. on p. 128).
- [5] L. Rothman et al. “The HITRAN 2004 molecular spectroscopic database”. In: *J. Quant. Spectrosc. Radiat. Transf.* 96.2 (Dec. 2005), pp. 139–204. ISSN: 00224073. DOI: 10.1016/j.jqsrt.2004.10.008 (cit. on p. 128).
- [6] A. Miklós et al. “Application of acoustic resonators in photoacoustic trace gas analysis and metrology”. In: *Rev. Sci. Instrum.* 72.4 (Apr. 2001), pp. 1937–1955. ISSN: 0034-6748. DOI: 10.1063/1.1353198 (cit. on p. 132).
- [7] M. Nägele and M. Sigrist. “Mobile laser spectrometer with novel resonant multipass photoacoustic cell for trace-gas sensing”. In: *Applied Physics B* 70.6 (June 2000), pp. 895–901. ISSN: 0946-2171. DOI: 10.1007/PL00021151 (cit. on p. 133).
- [8] S. Borri et al. “Intracavity quartz-enhanced photoacoustic sensor”. In: *Appl. Phys. Lett.* 104.9 (Mar. 2014). ISSN: 0003-6951. DOI: 10.1063/1.4867268 (cit. on p. 133).
- [9] Z. Wang et al. “Doubly resonant sub-ppt photoacoustic gas detection with eight decades dynamic range”. In: *Photoacoustics* 27 (Sept. 2022), p. 100387. ISSN: 22135979. DOI: 10.1016/j.pacs.2022.100387 (cit. on p. 133).
- [10] S. Schilt and L. Thévenaz. “Wavelength modulation photoacoustic spectroscopy: Theoretical description and experimental results”. In: *Infrared Phys. Technol.* 48.2 (June 2006), pp. 154–162. ISSN: 13504495. DOI: 10.1016/j.infrared.2005.09.001 (cit. on p. 134).
- [11] G. B. Rieker et al. “Calibration-free wavelength-modulation spectroscopy for measurements of gas temperature and concentration in harsh environments”. In: *Appl. Opt.* 48.29 (Oct. 2009), p. 5546. ISSN: 0003-6935. DOI: 10.1364/AO.48.005546 (cit. on p. 134).
- [12] G. Rieker et al. “Measurements of near-IR water vapor absorption at high pressure and temperature”. In: *Appl. Phys. B* 87.1 (Mar. 2007), pp. 169–178. ISSN: 0946-2171. DOI: 10.1007/s00340-006-2523-4 (cit. on p. 134).

## 4.7 Photoacoustic AM measurements

To further investigate the influence of overlapping absorption peaks in photoacoustic spectroscopy, amplitude modulated (AM) PAS was applied. The characterization of the ICL employed for this purpose is depicted in Figure (3.6). The examined spectral range covers from  $2963.5 \text{ cm}^{-1}$  to  $2969.5 \text{ cm}^{-1}$ , wherein methane, ethane and water show well distinct absorption peaks. The photoacoustically recorded spectra in Figure 4.38(a) show good agreement with the theoretical data from Molexplorer ( $\text{CH}_4$  and  $\text{H}_2\text{O}$ ) and the measured data ( $\text{C}_2\text{H}_6$ ) from Harrison et al. [1], provided by HITRAN database. However, more pronounced deviations can be observed at lower wavenumbers. In terms of AM PAS the measured peak is consistently broader towards the lower wavenumbers. Considering the emission profile of the ICL for current-controlled amplitude modulation this effect can be explained, as illustrated in Figure 4.39. At higher wavenumbers, the emission spectrum deviates significantly from a Gaussian distribution function (shaded grey curve). As the

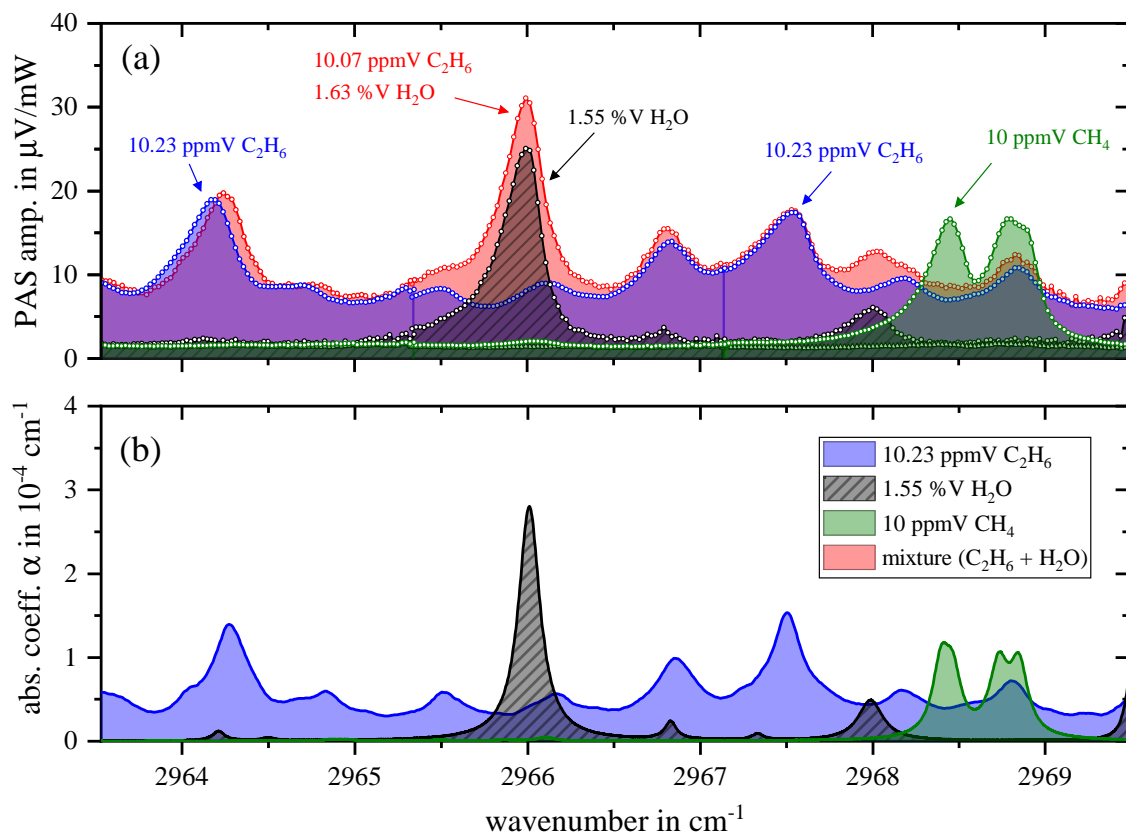


**Fig. 4.38.** Measured absorption spectra (a) normalized for the emitted optical power of ethane, water and methane using AM photoacoustic spectroscopy. The black triangles in (a) indicate the background signal, induced by light absorption of the windows. The Molexplorer simulations ( $\text{CH}_4$  and  $\text{H}_2\text{O}$ ) as well as the measured HITRAN ( $\text{C}_2\text{H}_6$ ) data of the corresponding absorption coefficients  $\alpha$  are shown in the lower graphs (b).

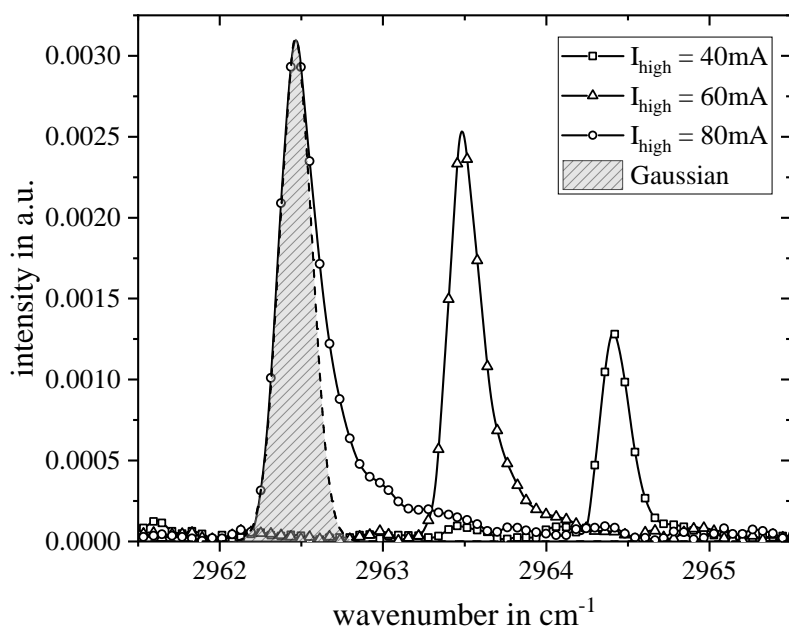


**Fig. 4.39.** Measured emission spectra of the ICL temperature controlled to 27 °C for different high currents. The shaded grey curve shows Gaussian distributed emission.

measured absorption spectrum results from a convolution of the laser emission and the theoretical absorption this deteriorated instrument function of the ICL yields the observed deviation, according to equation (4.22). Increasing the ICL current shifts the emission peak wavenumber to lower values, consequently the effect is measured for the absorption edge at lower wavenumbers. Using a mechanical chopper instead of current modulation could mitigate this effect [2].

In order to evaluate the performance of the AM PAS setup with regard to trace gas detection, the limit of detection (LoD) of the sensor for the different analytes was determined. For this purpose, concentration measurements were performed in pure nitrogen, from which the LoD was calculated as the ratio of the  $3\sigma$  noise in [ $\mu\text{V}$ ] and the sensitivity  $S$  in [ $\mu\text{V ppmV}^{-1}$ ] of the sensor.

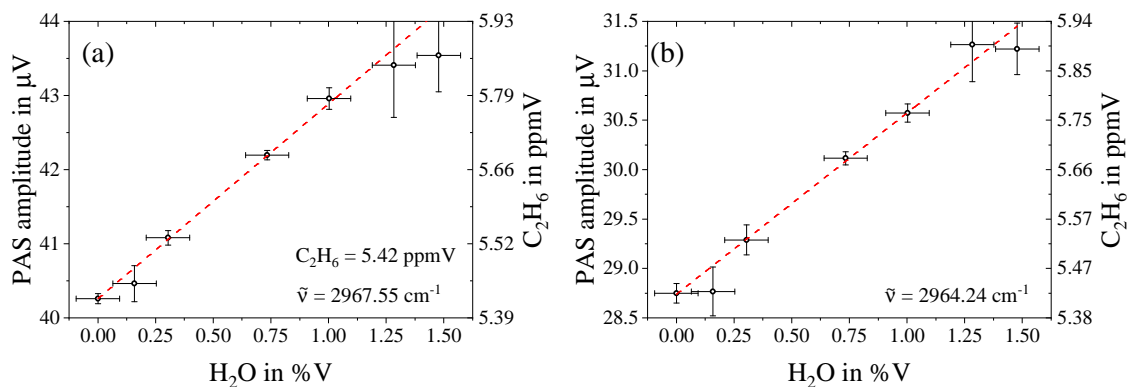
$$LoD = \frac{3\sigma}{S} \quad (4.24)$$

Adjustments were made to the measured sensitivity for methane due to delayed relaxation in pure nitrogen, as discussed in chapter 4.2. Neither water nor ethane showed relaxation-related effects towards humidity or oxygen, justifying the assumption that both analytes fully relax at the applied modulation frequencies. Table 4.10 lists the obtained calibration characteristics of photoacoustic sensor in AM mode with a LIA time constant of 5 s. Despite the similar strength of the absorption coefficients of the selected ethane peaks at 2964.24 cm<sup>-1</sup> and 2967.55 cm<sup>-1</sup> (see Figure 4.38(b)), the sensitivity of the PAS sensor at the higher wavenumber is about 43 % better. This discrepancy can be attributed to the 53 % higher emitted optical power at 2967.55 cm<sup>-1</sup>, due to the higher applied ICL current (see Figure 3.6).

**Tab. 4.10.** Calibration characteristics for ethane, methane and water in the spectral range shown in Figure 4.38.

analyte	sensitivity $S$ in $\mu\text{V ppmV}^{-1}$	LoD ( $3\sigma$ ) in ppbV	wavenumber in $\text{cm}^{-1}$	$P_{\text{opt}}$ in mW
$\text{C}_2\text{H}_6$	7.7	5.4	2967.55	4.9
$\text{C}_2\text{H}_6$	5.4	22.5	2964.24	3.2
$\text{CH}_4$	3.9	20.6	2968.45	3.0
$\text{H}_2\text{O}$	$5.6 \cdot 10^{-3}$	$28.6 \cdot 10^3$	2966.01	3.8

Returning to the investigation of the influence of spectral overlap in AM PAS, the sample humidity was progressively increased for a constant ethane concentration of 5.42 ppmV. Due to the additive nature of the individual spectra and the, albeit only minor, overlap, the water increase showed a linear influence on the ethane detection, see Figure 4.40. Since the PAS phase remained constant, it can be concluded that this effect is not relaxation related. The water-induced signal increase for ethane detection corresponds to  $2.63 \mu\text{V}/\%V_{\text{H}_2\text{O}}$  ( $0.34 \text{ ppmV}_{\text{C}_2\text{H}_6}/\%V_{\text{H}_2\text{O}}$ ) at  $2967.55 \text{ cm}^{-1}$  and  $1.83 \mu\text{V}/\%V_{\text{H}_2\text{O}}$  ( $0.33 \text{ ppmV}_{\text{C}_2\text{H}_6}/\%V_{\text{H}_2\text{O}}$ ) at  $2964.24 \text{ cm}^{-1}$ , respectively. The x-axis errorbars in Figure 4.40 correspond to the  $\pm 940 \text{ ppmV H}_2\text{O}$  BME280 specified accuracy. The broad absorption characteristics of ethane in the investigated spectral region will result in similar challenges for methane and water detection, making reliable multicomponent analysis (MCA) complex. Expressing the measured photoacoustic signal  $U_{\text{PA},j}$  of any sample gas consisting of  $n$  species  $A_i$  at the emitted peak wavenumber  $\tilde{\nu}_j$  equation (4.25) is obtained [3, 4]. To solve this equation, the photoacoustic signal must be measured at a minimum of  $j \geq n$  wavenumbers. Thereby it is recommended to target the individual absorption peaks of the respective analytes.

**Fig. 4.40.** Water-induced signal increase regarding ethane detection at  $2967.55 \text{ cm}^{-1}$  (a) and  $2964.24 \text{ cm}^{-1}$  (b), including linear fits (dashed red line). The water concentration was determined by the BME280 humidity sensor.

$$U_{\text{PA},j,n} = \begin{pmatrix} \sum_{i=1}^n S_{1,i}(\tilde{\nu}_1)A_i \\ \sum_{i=1}^n S_{2,i}(\tilde{\nu}_2)A_i \\ \dots \\ \dots \\ \sum_{i=1}^n S_{j,i}(\tilde{\nu}_j)A_i \end{pmatrix} \quad (4.25)$$

Using the known calibration factors  $S_{j,i}$ , i.e. the sensitivity of the component  $i$  at the respective wavenumber  $j$ , the concentrations of the analyte  $A_i$  can be calculated, without the need for recording the whole spectrum.

A different, more resource-intensive, and time-consuming approach for analyte concentration retrieval is based on recording the whole spectrum and employing statistical evaluation algorithms, such as PLSR [5–7]. The reported applicability of this approach reaches from detection of multiple volatile organic compounds (VOCs) for breath analysis [5], to  $^{12}\text{C}$ ,  $^{13}\text{C}$  hydrocarbon isotopologue concentration retrieval [6] and simultaneous detection of tracegases in the atmosphere, e.g.  $\text{CH}_4$ ,  $\text{N}_2\text{O}$ ,  $\text{CO}$ , and  $\text{C}_2\text{H}_2$  [7].

In summary, the presented PA setup is well suited for the combined detection of methane and ethane in the ppbV range and water in the double digit ppmV range, using a single light source. Exploiting the photoacoustic detection of water could increase the resolution of traces of water and thus benefit the theoretical calculations of the relaxational effects of methane, presented in chapter 4.2. Although the first measurements have demonstrated promising results, regarding the achieved LoDs and compensation of spectral cross-sensitivities, further research is still required. The MCA, for example, should be investigated in more detail and tested for reliability against unknown gas samples, before the PA sensor is ready for use in environmental monitoring applications.

## References

- [1] J. J. Harrison et al. “Infrared absorption cross sections for ethane ( $\text{C}_2\text{H}_6$ ) in the  $3\mu\text{m}$  region”. In: *J. Quant. Spectrosc. Radiat. Transf.* 111.3 (Feb. 2010), pp. 357–363. ISSN: 00224073. DOI: 10.1016/j.jqsrt.2009.09.010 (cit. on p. 137).
- [2] H. Harde et al. “New optical analyzer for 13 C-breath test”. In: ed. by J. Popp et al. Apr. 2008, 69910T. DOI: 10.1117/12.781271 (cit. on p. 138).
- [3] D. C. Dumitras et al. “Laser photoacoustic spectroscopy: Principles, instrumentation, and characterization”. In: *J. Optoelectron. Adv. Mater.* 9.12 (2007), pp. 3655–3701. ISSN: 14544164 (cit. on p. 139).

- 
- [4] S. Weigl et al. “Scopes and Limits of Photoacoustic Spectroscopy in Modern Breath Analysis”. In: 2022, pp. 101–159. DOI: 10.1007/11663\_2022\_22 (cit. on p. 139).
- [5] Y. Saalberg and M. Wolff. “Multivariate Analysis as a Tool to Identify Concentrations from Strongly Overlapping Gas Spectra”. In: *Sensors* 18.5 (May 2018), p. 1562. ISSN: 1424-8220. DOI: 10.3390/s18051562 (cit. on p. 140).
- [6] A. Loh and M. Wolff. “Multivariate Analysis of Photoacoustic Spectra for the Detection of Short-Chained Hydrocarbon Isotopologues”. In: *Molecules* 25.9 (May 2020), p. 2266. ISSN: 1420-3049. DOI: 10.3390/molecules25092266 (cit. on p. 140).
- [7] A. Zifarelli et al. “Partial Least-Squares Regression as a Tool to Retrieve Gas Concentrations in Mixtures Detected Using Quartz-Enhanced Photoacoustic Spectroscopy”. In: *Anal. Chem.* 92.16 (Aug. 2020), pp. 11035–11043. ISSN: 0003-2700. DOI: 10.1021/acs.analchem.0c00075 (cit. on p. 140).



# Chapter 5

## Summary

This dissertation discusses the potential of photoacoustic spectroscopy (PAS) for the detection of methane and ethane in ambient air. The theoretical section is dedicated to the fundamentals of absorption spectroscopy and PAS in particular. Additionally, spectroscopic measurement methods relevant to this work such as Beer-Lambert absorption spectroscopy, cavity ring-down spectroscopy (CRDS) and wavelength-modulated spectroscopy (WMS) are presented and their respective advantages and disadvantages are discussed. The theory chapter also provides a detailed derivation of photoacoustic signal generation, including signal amplification by acoustic resonance amplification. Particular attention is given to the discussion of the influence of non-radiative relaxation on the photoacoustic signal, whereby the two dominant forms of collision-based energy transfer, vibrational-translation (VT) relaxation and vibrational-vibrational (VV) relaxation, are reviewed and discussed. A literature review completes the theoretical part, focusing on the influence of relaxation on the photoacoustic signal for different analytes.

Besides the characterization of the laser sources with respect to the emission wavenumber, an integrated system (Acoustic Resonance Monitoring System - ARMS) is presented, which allows fast quantification of acoustic parameters such as resonance frequency and  $Q$ -factor.

The photoacoustic methane sensor is evaluated in the results chapter regarding cross-sensitivities towards oxygen, humidity, carbon dioxide as well as photoacoustic cell temperature and pressure. Acoustic and relaxation-related effects were identified as the dominant parameters. The dependence of the photoacoustic amplitude and phase on the efficiency of the non-radiative relaxation can be calculated and compensated for using the developed algorithm *CoNRad*, which increases the reliability of the sensor. The concept of the digital twin combines theoretical calculations, ARMS measurements and the emitted optical laser power to calculate a fully theoretically expected photoacoustic signal and to compensate measured raw data for all cross influences. This approach was evaluated in a series of measurements over several days with a reference device for atmospheric methane monitoring. The results illustrate the potential of PAS for trace gas detection in the ambient air, but also emphasize the necessity of the digital twin for signal compensation.

Measurements with a quartz-enhanced PAS sensor also revealed relaxation-related signal distortions, which were compensated using an established statistical method of partial least squares regression (PLSR) and the digital twin. Both approaches achieved equally good results and reduced the mean relative error of the predicted analyte concentration to the single-digit percentage range.

Furthermore, a method for calculating spectral influences in terms of wavelength-modulated PAS was developed. Spectral influences on the measurement signal were also investigated for amplitude modulation.

In summary, this thesis is primarily dedicated to an in-depth analysis of relaxation-related, acoustic and spectral influences on the photoacoustic signal. Various novel approaches to quantify and compensate for these influences are presented, with the

objective of significantly increasing the accuracy and reliability of photoacoustic sensors in long-term field applications. The findings of this work not only demonstrate the capability of photoacoustic spectroscopy for the precise detection of trace gases in ambient air, but also emphasize the need for compensation techniques. Overall, this work provides a valuable contribution towards the application of photoacoustic sensors in continuous and long-term field applications.



## Chapter 6

# Zusammenfassung in deutscher Sprache

Die vorliegende Dissertation erörtert das Potenzial der photoakustischen Spektroskopie (PAS) für die Detektion von Methan und Ethan in der Umgebungsluft. Der theoretische Teil widmet sich zunächst ausführlich den Grundlagen der Absorptionsspektroskopie und insbesondere der PAS. Zusätzlich werden für diese Arbeit relevante Messmethoden wie die Absorptionsspektroskopie nach Lambert-Beer, Cavity ring-down Spektroskopie (CRDS) und Wellenlängen-modulierte Spektroskopie (WMS) vorgestellt und ihre jeweiligen Vor- und Nachteile erörtert. Im Theoriekapitel wird zusätzlich die photoakustische Signalgenerierung, einschließlich der Signalverstärkung durch akustische Resonanzverstärkung, detailliert hergeleitet. Besonderes Augenmerk liegt auf der Diskussion des Einflusses der nicht-strahlenden Relaxation auf das photoakustische Signal, wobei die zwei dominanten Formen der stoßbasierten Energieübergänge, Schwingungs-Translation (VT) Relaxation und Schwingungs-Schwingungen (VV) Relaxation, intensiv betrachtet und diskutiert werden. Eine Literaturzusammenfassung rundet den theoretischen Teil ab, wobei der Fokus auf dem Einfluss der Relaxation auf das photoakustische Signal für verschiedene Analyten liegt.

Neben der Charakterisierung der Laserquellen hinsichtlich der Emissionswellenzahl wird ein in die photoakustische Messzelle integriertes System (Acoustic Resonance Monitoring System - ARMS) präsentiert, welches eine schnelle Quantifizierung akustischer Parameter, wie Resonanzfrequenz und  $Q$ -Faktor ermöglicht.

Im Ergebnisteil wird der photoakustische Methansensor auf Quereinflüsse gegenüber Sauerstoff, Luftfeuchte, Kohlenstoffdioxid sowie Messzellentemperatur und -druck hin evaluiert. Dabei wurden akustische und relaxationsbedingte Effekte als dominierende Einflussgrößen identifiziert. Die Abhängigkeit der photoakustischen Amplitude und Phase von der Effizienz der nicht-strahlenden Relaxation lässt sich mithilfe des entwickelten Algorithmus *CoNRad* berechnen und kompensieren, wodurch die Zuverlässigkeit der Sensoren gesteigert wird. Das Konzept des digitalen Zwillings kombiniert theoretische Berechnungen, ARMS-Messungen und die emittierte optische Laserleistung, um ein vollständig theoretisch zu erwartendes photoakustisches Signal zu berechnen und gemessene Rohwerte für sämtliche Quereinflüsse zu kompensieren. Dieser Ansatz wurde in einer mehrtägigen Messreihe mit einem Referenzgerät zum atmosphärischen Methanmonitoring evaluiert. Die Ergebnisse verdeutlichen das Potenzial der PAS zur Spurengasdetektion in der Umgebungsluft, unterstreichen aber auch die Notwendigkeit des digitalen Zwillings zur Quereinflusskompensation.

Messungen mit einem quartz-enhanced PAS Sensor zeigten ebenfalls relaxationsbedingte Signalveränderungen, die mithilfe der etablierten statistischen Methode der Partial Least Squares Regression (PLSR) und dem digitalen Zwilling kompensiert wurden. Mit beiden Ansätzen konnten vergleichbar gute Ergebnisse erzielt werden und den mittleren relativen Fehler der vorhergesagten Analytkonzentration auf den einstelligen Prozentbereich verringert werden.

Darüber hinaus wurde eine Methode entwickelt, um spektrale Quereinflüsse in der Wellenlängen-modulierten PAS zu berechnen. Der Einfluss von spektralen

Überlappungen auf das Messsignal wurde zusätzlich für Amplitudenmodulation untersucht.

Zusammenfassend befasst sich diese Dissertation vorrangig mit der detaillierte Analyse von relaxationsbedingten, akustischen und spektralen Einflüssen auf das photoakustische Signal. Hierbei werden verschiedene innovative Ansätze zur Quantifizierung und Kompensation dieser Einflüsse präsentiert, mit dem übergeordneten Ziel, die Genauigkeit und Zuverlässigkeit photoakustischer Sensoren in langfristigen Feldanwendungen signifikant zu erhöhen. Die Erkenntnisse dieser Arbeit unterstreichen nicht nur das Potenzial der photoakustischen Spektroskopie zur präzisen Detektion von Spurengasen in der Umgebungsluft, sondern betonen auch die Notwendigkeit von Kompensationsmechanismen. Insgesamt trägt diese Arbeit entscheidend dazu bei, dass photoakustische Sensoren in kontinuierlichen Feldanwendungen eingesetzt werden können.



# Appendices

## A Miscellaneous

### A.1 Acoustic resonance modes

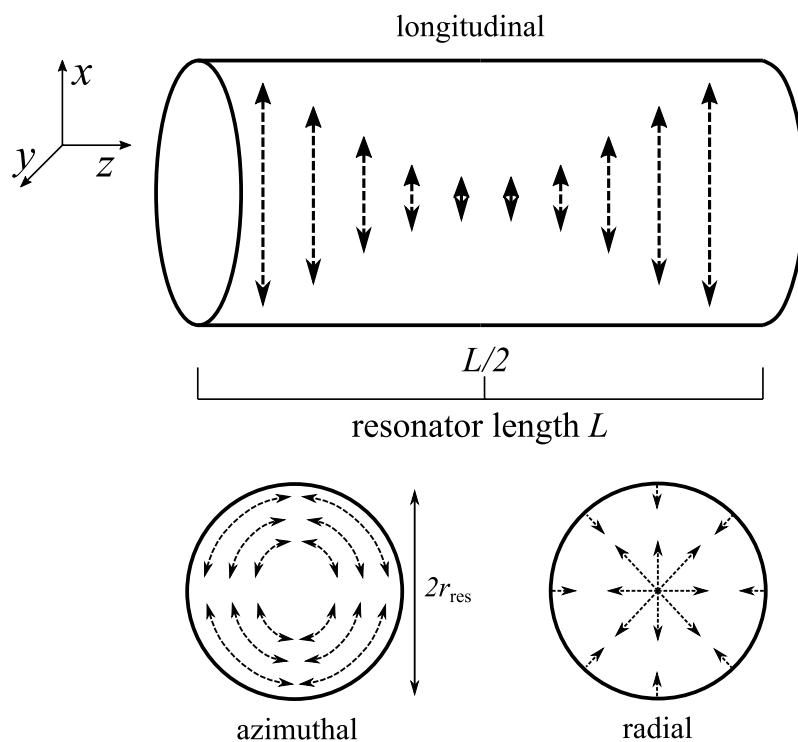


**Fig. A1.** Schematic representation of the longitudinal, radial and azimuthal acoustic resonances in a cylindrical acoustic resonator. The particle displacement for the individual resonances are represented by the dashed arrows. This figure has been adapted from [1].

## A.2 Ethan absorpction spectrum from different databases

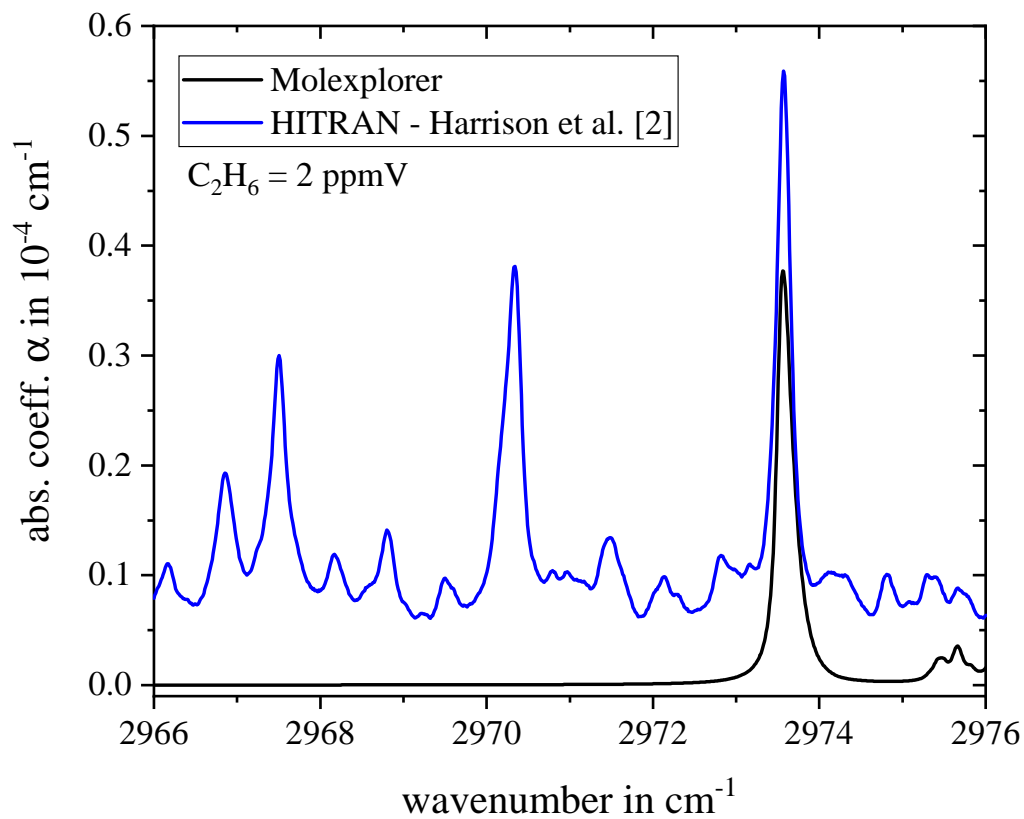


**Fig. A2.** Ethane absorption coefficient in the spectral range from  $2966 cm^{-1}$  to  $2976 cm^{-1}$  obtained from Molexplorer (black line) and HITRAN (blue line) [2]. The differences between the databases are clearly visible.

### A.3 Lock-in amplification

In photoacoustic spectroscopy, the frequency of the signal of interest is known exactly, i.e.  $f = f_{\text{mod}}$  in case of amplitude modulation, or  $f = 2f_{\text{mod}}$  in the case of wavelength modulation. Because of this feature the photoacoustic signal, even if the amplitude is much smaller than the background noise, can be retrieved via lock-in amplification. So-called dual-phase lock-in amplifiers (LIA) enable phase-sensitive detection of the measured signal, i.e. not only the amplitude but also the phase shift can be detected. Especially the phase shift is of importance, when investigating relaxation processes in photoacoustics, refer to chapter 4.2.

The measured signal  $u_s$  is multiplied by a cosine and a sine of the same frequency  $f_{\text{ref}} = f_{\text{mod}}$ , respectively. This yields an in-phase signal  $u_i(t)$ , as well as an quadrature signal  $u_q(t)$

$$u_i(t) = u_s(t) \cdot \hat{u}_{\text{ref}} \cdot \cos(2\pi f_{\text{ref}}t + \phi_{\text{ref}}) \quad (1)$$

$$u_q(t) = u_s(t) \cdot \hat{u}_{\text{ref}} \cdot \sin(2\pi f_{\text{ref}}t + \phi_{\text{ref}}) \quad (2)$$

The measured signal of interest  $u_s(t)$  can be expressed as

$$u_s(t) = \hat{u}_s \cdot \cos(2\pi f_s t + \phi_s) \quad (3)$$

Substituting equation (3) in equation (1) yields for the in-phase signal

$$u_i(t) = \hat{u}_s \hat{u}_{\text{ref}} \frac{1}{2} [\cos(2\pi t(f_{\text{ref}} - f_s) + (\phi_{\text{ref}} - \phi_s)) + \cos(2\pi t(f_{\text{ref}} + f_s) + (\phi_{\text{ref}} + \phi_s))] \quad (4)$$

Utilizing the condition  $f_{\text{ref}} = f_{\text{mod}} = f_s$  equation (4) is simplified, yielding

$$u_i(t) = \underbrace{\frac{\hat{u}_s \hat{u}_{\text{ref}}}{2} \cos(\phi_{\text{ref}} - \phi_s)}_{\text{DC}} + \underbrace{\frac{\hat{u}_s \hat{u}_{\text{ref}}}{2} \cos(4\pi f_{\text{mod}} t + \phi_{\text{ref}} + \phi_s)}_{\text{AC}} \quad (5)$$

Low-pass (LP) filtering the output of the in-phase modulation  $u_i(t)$  eliminates the AC component and leaves the DC component.

$$u_{i,\text{LP}}(t) = \frac{\hat{u}_s \hat{u}_{\text{ref}}}{2} \cos(\phi_{\text{ref}} - \phi_s) \quad (6)$$

As the amplitude of the reference signal  $\hat{u}_{\text{ref}}$  is known, it can be eliminated, resulting in the amplitude of the in-phase output

$$\hat{U}_i = \frac{\hat{u}_s}{2} \cos(\Phi) \quad (7)$$

with  $\Phi = \phi_{\text{ref}} - \phi_s$  being the phase difference of the photoacoustic signal and the reference signal. Performing the same procedure on the quadrature signal, i.e. multiplying and subsequent low-pass filtering, yields

$$\hat{U}_q = \frac{\hat{u}_s}{2} \sin(\Phi) \quad (8)$$

Combining both outputs the photoacoustic signal amplitude  $\hat{u}_s$  can be reconstructed

$$\hat{u}_s = 2\sqrt{\hat{U}_q^2 + \hat{U}_i^2} \quad (9)$$

while the phase difference is obtained via

$$\Phi = \arctan\left(\frac{\hat{U}_q}{\hat{U}_i}\right) \quad (10)$$

More detailed information about lock-in-amplification and implementation can be found in [3–5].

## A.4 Universal equation for heat production rate

The total heat production rate  $\dot{H}(t)$  of any system can be described as the sum of all individual heat rates released from the number  $n$  of all involved energy states. This total heat production rate can be directly linked to the photoacoustic pressure  $p_a$ .

$$\dot{H}(t) = \sum_i^n \dot{H}_i(t) \quad (11)$$

with

$$\dot{H}_i(t) = [\nu_i](t) \cdot \left[ hc_0 \cdot \left( \sum_j^m k_{i,j} \cdot (\tilde{\nu}_i - \tilde{\nu}_j) \right) \right] \quad (12)$$

According to Hunter et al. the population densities of every energy state involved in the relaxation process of any given system can be computed according to [6]:

$$[\nu_i](t) = \rho_A \sigma_A (\tilde{\nu}_{Ph}) \psi_0 \tau_i \frac{1}{\sqrt{1 + (\omega \tau_{\nu_i})^2}} e^{-i\phi_i} \left\{ \sum_{\text{all routes to } \nu_i} \left[ \prod_n^n \left( \frac{k_{n \rightarrow r}}{\sum k_n} \frac{1}{\sqrt{1 + (\omega \tau_{\nu_n})^2}} e^{-i\phi_n} \right) \right] \right\} e^{-i\omega t} \quad (13)$$

The product of photon flux  $\psi_0$ , volume number density  $\rho_A$  and absorption cross section  $\sigma_A(\tilde{\nu}_{Ph})$  of the analyte A accounts for the initial quanta of absorption per second and per unit volume in  $\text{s}^{-1}\text{m}^{-3}$ . This quantity acts as a starting point for the relaxation process. The sum in equation (13) for the population density of the involved energy states  $[\nu_i](t)$  adds up all individual relaxation routes starting from the initially excited state and resulting in the energy state  $\nu_i$  that is considered. The ratio  $(k_{n \rightarrow r} / \sum k_n)$  considers the fractions of molecules which undergo energy transition from the  $n$ -state to the  $r$ -state  $k_{n \rightarrow r}$ , before reaching the desired state  $\nu_i$ , with regards to all other transitions possibly performed by the  $n$ -state  $\sum k_n$ .

### A.5 The effect of pressure on the absorption coefficient

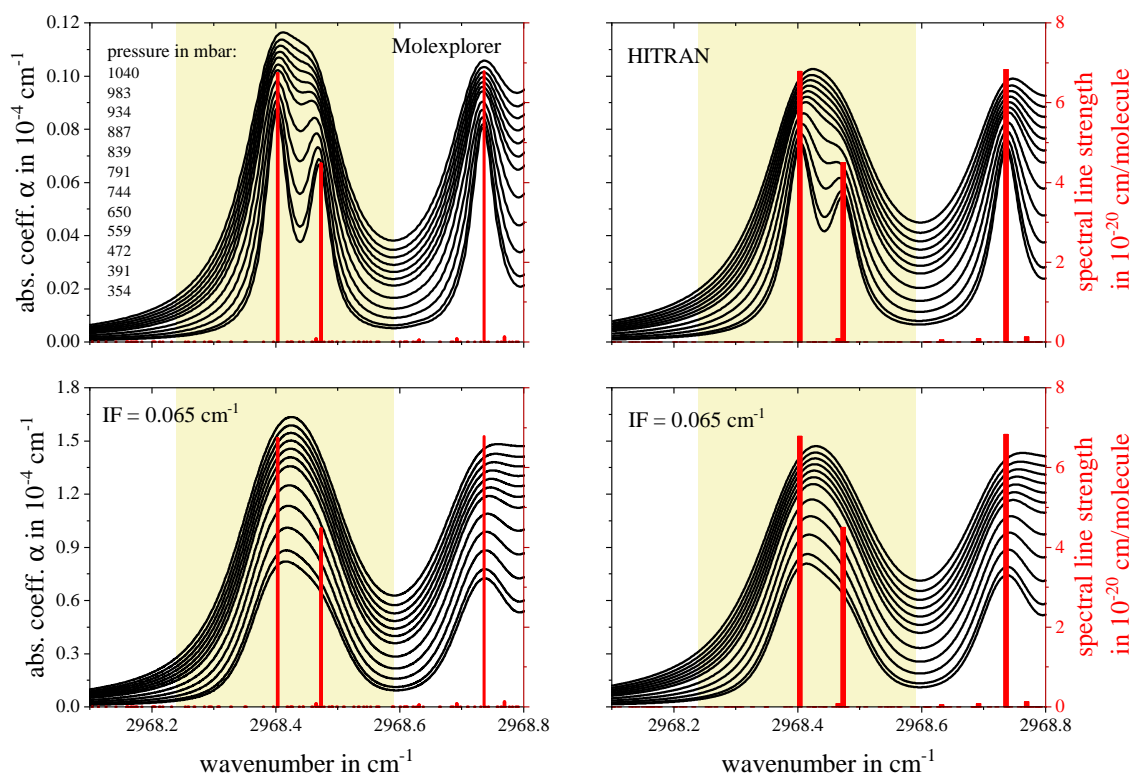


**Fig. A3.** Pressure dependency of the absorption coefficient of 15 ppmV CH<sub>4</sub> simulated using *HITRAN on the web* (left) and Molexplorer (right) database. The lower graphs show the effect of an applied IF of 0.065 cm<sup>-1</sup> on the spectral resolution. The highlighted light yellow area indicates the WM scanning range for the CH<sub>4</sub> on-peak detection results obtained in chapter 4.2, 4.3 and 4.4.

## A.6 AM PAS spectra of methane for different pressures

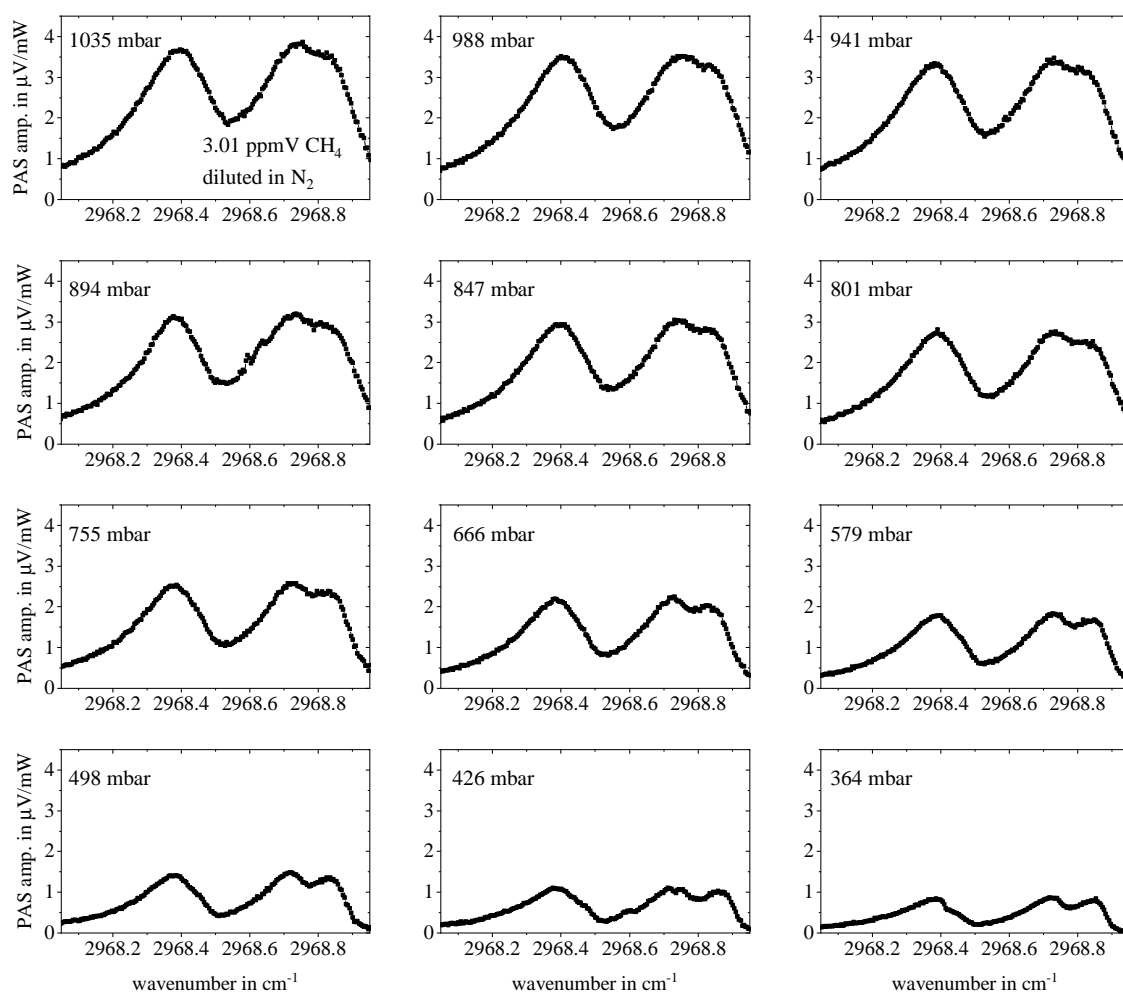


**Fig. A4.** Measured methane spectra for different pressures exploiting AM PAS used to obtain the results in chapter 4.6.3.

## A.7 Picarro G2301 temperature features with measured $\text{CH}_4$ readings

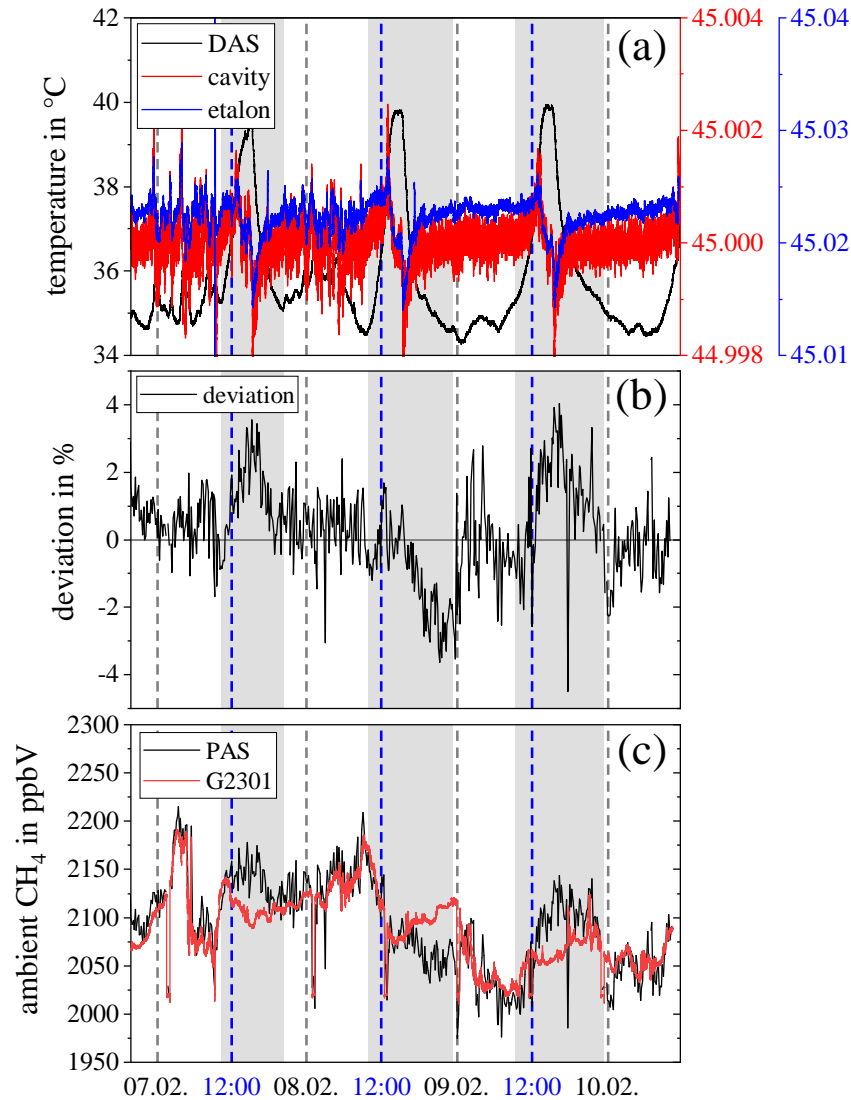


**Fig. A5.** Comparison of data acquisition system (DAS), cavity, and etalon temperature (a) of the Picarro G2301 CRDS over time, with the measured percentage deviation (b) and  $\text{CH}_4$  reading (c). The temperature spikes (highlighted grey areas) seem to correlate with the strongest deviations. The dashed blue lines indicate noon, which leads to the assumption that such spikes in temperature may be caused by direct sun exposure of the device.

## A.8 Work flow of the WM-2f FFT analysis

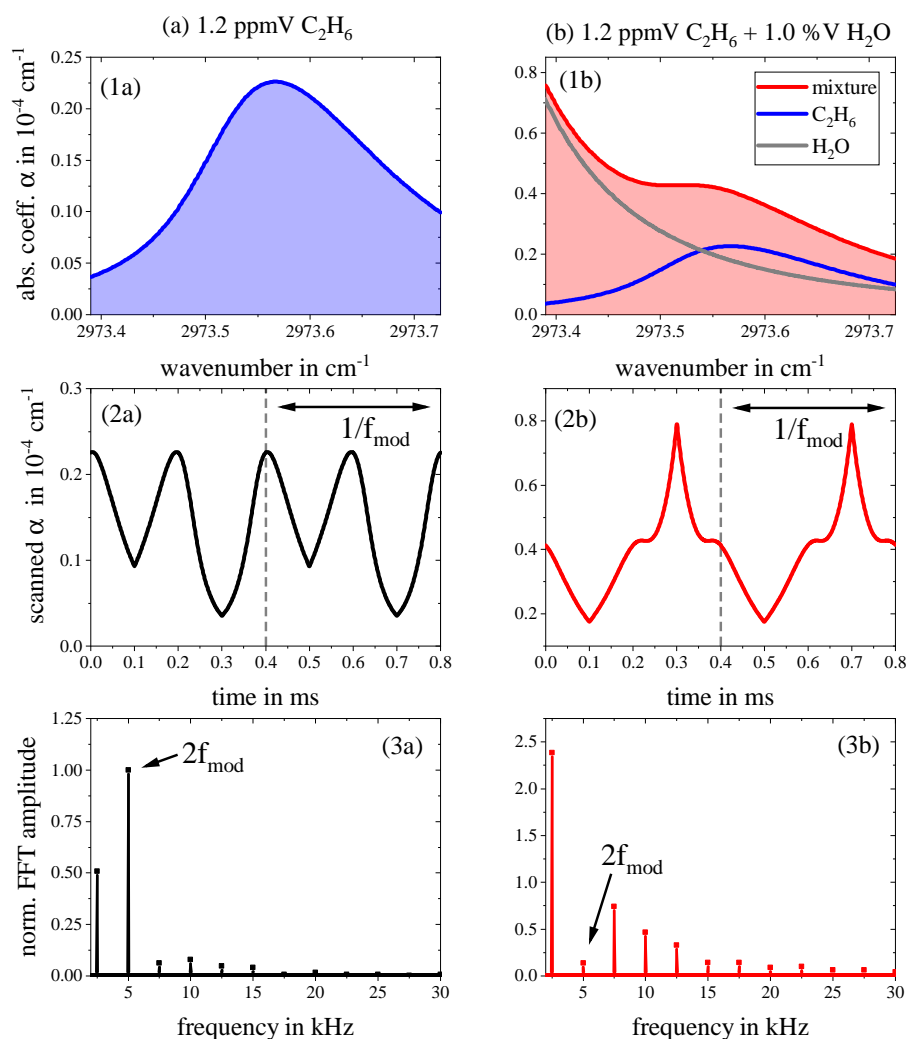


**Fig. A6.** Procedure of the WM-2f FFT simulation for 1.2 ppmV ethane in dry nitrogen (a) and for a humidified mixture (b). First, the spectrum of the sample gas is calculated, 1(a) and (b). Next, the laser modulation over the spectrum is simulated, 2(a) and (b). This is then used to perform a frequency analysis by FFT, recording the amplitude at  $2f_{\text{mod}}$  as an equivalent quantity to the photoacoustic amplitude, 3(a) and (b).

## References

- [1] A. Miklós et al. “Application of acoustic resonators in photoacoustic trace gas analysis and metrology”. In: *Rev. Sci. Instrum.* 72.4 (Apr. 2001), pp. 1937–1955. ISSN: 0034-6748. DOI: 10.1063/1.1353198 (cit. on p. 152).
- [2] J. J. Harrison et al. “Infrared absorption cross sections for ethane (C<sub>2</sub>H<sub>6</sub>) in the 3 $\mu$ m region”. In: *J. Quant. Spectrosc. Radiat. Transf.* 111.3 (Feb. 2010), pp. 357–363. ISSN: 00224073. DOI: 10.1016/j.jqsrt.2009.09.010 (cit. on p. 153).
- [3] J. H. Scofield. “Frequency-domain description of a lock-in amplifier”. In: *Am. J. Phys.* 62.2 (Feb. 1994), pp. 129–133. ISSN: 0002-9505. DOI: 10.1119/1.17629 (cit. on p. 155).
- [4] L. A. Barragán et al. “A modular, low-cost, digital signal processor-based lock-in card for measuring optical attenuation”. In: *Rev. Sci. Instrum.* 72.1 (Jan. 2001), pp. 247–251. ISSN: 0034-6748. DOI: 10.1063/1.1333046 (cit. on p. 155).
- [5] M. Hofmann et al. “Implementation of a dual-phase lock-in amplifier on a TMS320C5515 digital signal processor”. In: *2012 5th Eur. DSP Educ. Res. Conf.* IEEE, Sept. 2012, pp. 20–24. ISBN: 978-1-4673-4595-8. DOI: 10.1109/EDERC.2012.6532217 (cit. on p. 155).
- [6] T. F. Hunter et al. “Photophysical processes in the vapour-phase measured by the optic-acoustic effect. Part 1.—The model and apparatus for the study of radiationless processes”. In: *J. Chem. Soc., Faraday Trans. 2* 70 (1974), pp. 1010–1021. ISSN: 0300-9238. DOI: 10.1039/F29747001010 (cit. on p. 156).



# Erklärung

Ich erkläre hiermit an Eides statt, dass ich die vorliegende Arbeit ohne unzulässige Hilfe Dritter und ohne Benutzung anderer als der angegebenen Hilfsmittel angefertigt habe; die aus anderen Quellen direkt oder indirekt übernommenen Daten und Konzepte sind unter Angabe des Literaturzitats gekennzeichnet.

Andere Personen waren an der inhaltlich-materiellen Herstellung der vorliegenden Arbeit nicht beteiligt. Insbesondere habe ich hierfür nicht die entgeltliche Hilfe eines Promotionsberaters oder anderer Personen in Anspruch genommen. Niemand hat von mir weder unmittelbar noch mittelbar geldwerte Leistungen für Arbeiten erhalten, die im Zusammenhang mit dem Inhalt der vorgelegten Dissertation stehen.

Die Arbeit wurde bisher weder im Inland noch im Ausland in gleicher oder ähnlicher Form einer anderen Prüfungsbehörde vorgelegt.

Regensburg, 18.12.2023

Max Müller